Matériaux tubulaires biomimétiques en collagène : des mécanismes d'auto-assemblages aux applications in vitro

Isabelle Martinier

Sorbonne Université

Ecole doctorale 397 – Physique et Chimie des matériaux

Laboratoire de Chimie de la Matière Condensée de Paris (LCMCP)

Collagen-based biomimetic tubular materials: from self-assembly mechanisms during fabrication to *in vitro* applications

By Isabelle Martinier

Doctor of Philosophy thesis in Physics and Chemistry of Materials

Defended on the 7th of December 2023

In front of a jury composed of:

Dr. Francisco M. Fernandes, LCMCP, Sorbonne Université	**Supervisor**
Dr. Léa Trichet, LCMCP, CNRS	**Co-supervisor (invited)**
Dr. Teresa Simón-Yarza, LVTS, INSERM	**Referee**
Dr. Myriam Reffay, MSC, Université Paris Cité	**Referee**
Pr. Dominique Hourdet, SIMM, Sorbonne Université	**Examiner**
Pr. João Mano, CICECO, Universidade de Aveiro	**Examiner**
Pr. Carole Planes, H&P, Université Sorbonne Paris Nord	**Examiner**
Dr. Frederic Gobeaux, NIMBE, CEA	**Invited**

Remerciements

Cette thèse fait suite à un stage démarré au Laboratoire de Chimie de la Matière Condensée de Paris, d'abord plein de fougue et de bonnes intentions un peu naïves, puis terminé dans un lieu perdu de l'Ain, loin du laboratoire et ses expériences. La faute au Covid, et pourtant la route de la recherche a continué. Pour ça, merci à la confiance et l'attention portée tout d'abord par Francisco M. Fernandes, bientôt rejoint par Léa Trichet en thèse. Merci d'avoir été de si bon.nes guides dans cette réalisation, à la fois humainement et scientifiquement, et de m'avoir transfusé tout ce savoir. Merci pour le soutien, le temps infini passé à relire, corriger, remanier, repenser encore et encore, à manier mes humeurs parfois changeantes, à rire sur de la science puis après quelques années pas que. Merci de m'avoir poussée dans des directions nouvelles, merci d'avoir été là quand c'était bon, mais aussi quand je brassais de l'air et que les chiffres tournaient à vide.

Ce manuscrit est fait d'intensité, d'abord pas assez puis trop, de compromis, de paires d'yeux qui brillent à l'allure de courbes de graphes ou de striations au microscope. C'est porté par quatre mains sans lesquelles il n'existerait pas.

D'autres personnes se doivent d'être remerciées, particulièrement Gervaise Mosser, Patrick Davidson (LPS), Sylvain Deville (ILM), Abdul Barakat et Alessia Castagnino (LADHYX), Ilaria Onorati et Nicolas Dard (H&P). Merci pour tout ce que j'ai appris auprès de vous et pour le bout de chemin parcouru ensemble, je m'en sens très chanceuse.

Merci aussi aux personnes qui habitent le LCMCP d'en avoir fait un lieu si agréable. Une pensée particulière aux jeunes de MatBio : Alshaba, Florian, Minaine, Stéphanie, Daniel, Katsuya, Corentin et Clio. Et bien sûr aux copines de 1ere année : Fanny, Léna, Mariette et Agathe.

Enfin merci aux personnes de la vie hors du laboratoire, vous avez été, peut etre sans le savoir, essentielles !

Merci aux doctorant.es hors sciences « manuelles » pour toutes les discussions sur la recherche, ses hauts et ses bas, ses intensités et ses sombres désespoirs. Notre soutien mutuel tout au long de nos parcours ont été une aide précieuse. Merci à Camille, Etienne, Yvan, et Elisabeth. Je suis tellement fière de ce que vous êtes et de ce que vos têtes et mains ont su fabriquer.

Merci aux copain.es de Paris : Adri, Greg (& Sandra), Quentin, Kawtar, Albane. Merci aussi aux colocs et leur +1, Leslie, Mariette, Mathilde et Cécile, longue vie aux Zou' sur buttes et leurs 1000 plantes !

Merci aux artistes de la troupe de Stras d'etre si inspirant.es : Zoe, Mécistée, Léo.

Merci à la Fête, haut lieu de créativité complètement barje, de liberté, de ré-invention, et rempli de personnes toutes incroyables. Un grand merci surtout à Bastien, Julie, Abel et Fanny, et bien sûr Alba et Corail. Merci à Camille d'avoir été une complice tout ce temps.

Merci aux personnes qui sont là depuis plus de 10 ans maintenant : Lisa, Claire, Eva, Mathilde, Yoan, Julien, Jérémy, Camille, Marian, Nathan.

Merci à la première famille de science : Théo, Dam, Marion, Manon, Steph, Fab, Zilou, et tous les autres. Merci à la deuxième famille de science : Sarah, Louis-Aymard, à défaut d'etre rassemblé.es par un véritable amour de la chimie le fromage nous a eu et nous aura encore !

Merci à la famille, Michel et Flore, pour m'avoir fait grandir dans un monde un peu différent mais rempli de liberté. Merci à Alice et Cécile, et maintenant à ce petit bout de Paul. Et bien sûr merci à cette troupe de Belin, cette foutue 70aine de belles personnes !

Merci aux accompagnant.es les plus proches sur ce chemin, tout d'abord Ester et surtout Hector. Je crois que les mots n'auront ici jamais la force de mes sentiments.

Enfin merci à toutes les personnes qui prendront un temps à lire ces quelques 250 pages, j'espère qu'elles vous animeront autant qu'elles m'ont animées.

Table of contents

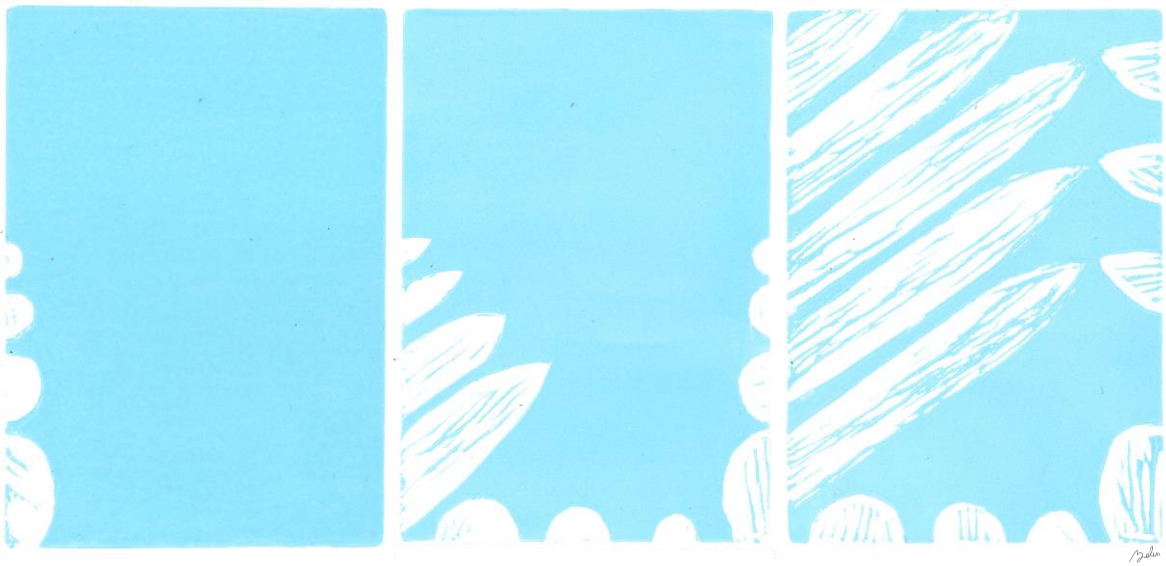

Introduction

Introduction

Type I collagen is the main building block of connective tissues. This structural protein provides the adequate strength and support to the various physiological functions across tissues and organs. Not only it is responsible for the tissue mechanical properties, but it also provides the necessary cellular microenvironment for adhesion and proliferation of the residing cells[1]. *In vivo*, the anisotropic supramolecular structure of collagen, namely fibrils, is a hallmark of the Extracellular Matrix (ECM). Fibrils are the result of the spontaneous self-assembly of collagen molecules, a process called fibrillogenesis, mediated by various physico-chemical conditions. Collagen molecules originate from cell-secreted procollagen, a triple-helix formed by three polypeptides alpha-chains. Following the cleavage of the terminal N- and C-telopeptides, procollagen turns into tropocollagen molecules, commonly named collagen[2]. Before forming mature collagen, molecules are gathering into early fibrils, either unipolar or bipolar. In unipolar fibrils all molecules point in the same direction, whereas in bipolar fibrils molecules display both orientations[3]. Supposedly, the terminal ends of the fibrils are shaped at an early stage of the self-assembly, and kept during fibril growth. Several hypotheses are still debated for the following growth mechanism of mature fibrils. One is based on the lateral fusion of the first formed filaments, another on the formation of a core filament with growing tips, on which the assembly continues[4]. The resulting fibrils display cross-striations, the fingerprint of this staggered arrangement. This characteristic axial D-period corresponds to 67 nm, which is the sum of the gap and overlap of adjacent molecules[5] (**Figure 1**).

In vitro, collagen molecules can be stabilized by chemical cross-linking or physical processes or by self assembly. Chemical cross-linking can form covalent bonds between collagen molecules or further stabilize fibrils[7]. However, cross-linking agents are known to be cytotoxic, which reduces interactions with cells. Physical treatments result in loss of the secondary structure of collagen, resulting in a denatured form of collagen, *i.e.* gelatin. In contrast, the soft-assembly routes offer to form native-like fibrils by simply tuning the initial collagen concentration, the pH and/or the ionic force[8]. The range of physiological physico-chemical conditions conducent to fibrillogenesis *in vivo* remains poorly described in the literature, which does not facilitate the handling of collagen *in vitro*. This is particularly challenging for the elaboration of biomimetic materials that aim at reproducing both the native structure and composition of tissues[9]. In the particular case of tubular tissues such as arteries, the trachea, the gut or urogenital tubes, their macroscopic geometry adds to the complexity of the fabrication. Many techniques have been developed to yield tubular collagen materials, including textile-inspired technique[10,11], ice-templating[12–15], and bioprinting[16–18], among others. However, these are challenged by the need to ensure cell colonization or biocompatibility of pre-seeded cells with the grafted site, as well as to preserve the attributes of molecular collagen in spite of harsh fabrication conditions usually required.

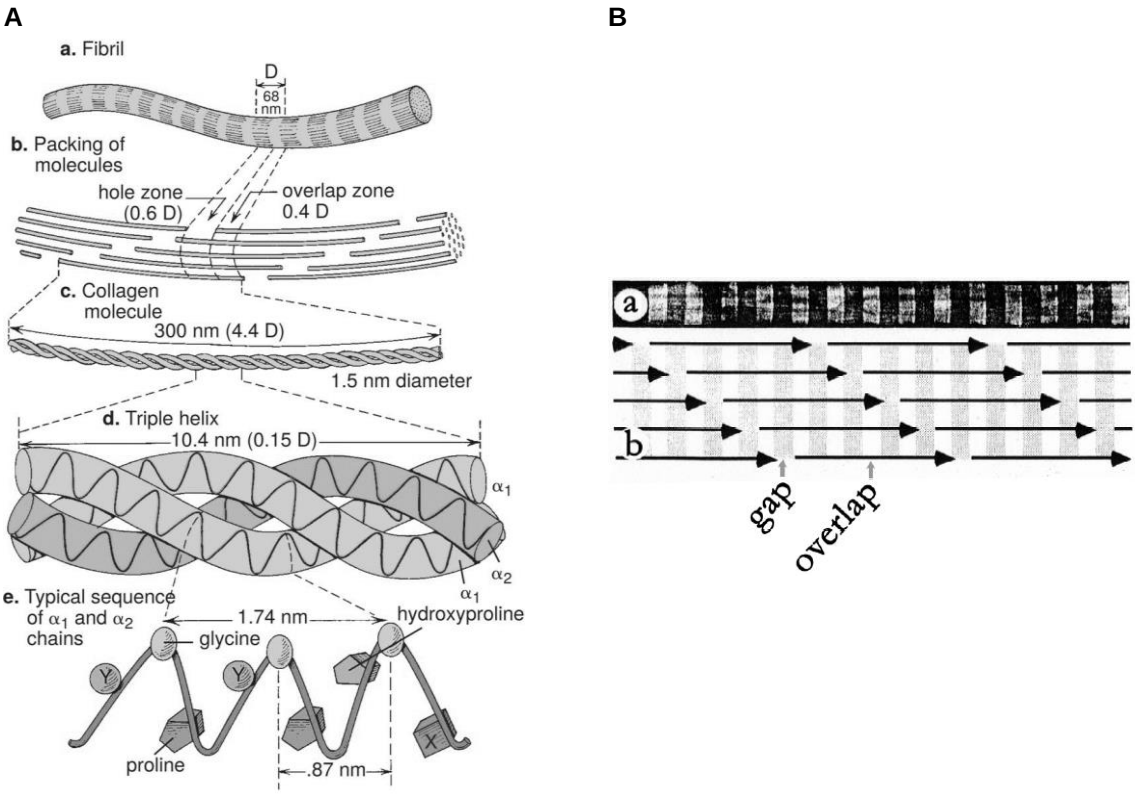

Figure 1. A. Single collagen fibril (**a**) reflecting the banding patterns with d–spacing (**b**, 67 nm). Each fibril is assembled by collagen molecules (**c**) featuring a triple helix. The triple helix (**d**), measuring about 300 nm in length and 1.5 nm in thickness, is made up of α -chains with every third amino acid of the chain being a glycine (**e**). The positions X and Y are predominantly proline and hydroxyproline, respectively. **B. a)** Transmission electronic micrography (TEM) of a collagen fibril, displaying the characteristic 67 nm periodicity, using negative staining. **b)** Two-dimensional model of the gap and overlap, due to the periodic arrangement of the triple helices. Images are adapted from Gueltekin[6] and Gobeaux[5] for A, and B, respectively.

This work addresses different aspects of the fabrication of collagen-based materials. It aims to picture the current knowledge of tubular tissues, and to propose an innovative rational approach to elaborate a new family of tubular collagen-based materials. The manuscript is divided in four chapters that cover the state of the art of biomimetic tubular materials, fundamental aspects of collagen organization, its impact on cell culture and a new approach to fabricate biomimetic tubular tissues through ice templating.

The first chapter introduces the structural and functional similarities of extracellular matrix (ECM) in tubular tissues. It proposes a simplified hierarchical model, based on a dual layer tissue constituted by the inner endothelial layer, and the outer muscular layer. The current existing strategies complying with a biomimetic approach are further described, and in particular, those based on type I collagen.

The second chapter is devoted to basic aspects of the molecular to fibrillar transition of collagen. Based on scattering, rheological, and thermodynamic experiments combined to transmission electron and polarized light microscopy, we describe for the first time the

organization of collagen as a function of temperature and concentration. These data are placed in state diagrams, drawn for type I collagen both in acidic solution and post-fibrillogenesis. In addition, we exemplify how these state diagrams can be powerful tools to tailor elaboration processes of biomimetic collagenous materials.

The third chapter focuses on the interactions of cells and collagen. Impact of collagen concentration and fibrillogenesis pathway on cell fate, largely neglected for *in vitro* models, is investigated by cell culture on flat samples of dense fibrillated collagen. We correlated the mechanical results, surface topography and fibrillar network to the cell adhesion and proliferation, to understand how endothelium reformation can be fostered by simple elaboration parameters.

The fourth chapter gathers this knowledge to elaborate biomimetic tubular collagen materials. Using a home-made ice templating set-up, we propose novel procedures that enable to tune properties of the hydrogels at various length scales and reach biomimetic features of native tissues. The proposed panel of porosity (geometry and size) and ultrastructure of collagen introduces a new family of materials, which demonstrate mechanical and biological properties in the range of tubular tissues.

References for the introduction

1. Peter Fratzl. *Collagen structure and mechanics*. (Springer, 2008).

2. Shoulders, M. D. & Raines, R. T. Collagen Structure and Stability. *Annu Rev Biochem* **78**, 929–958 (2009).

3. Kadler, K. E. Fell Muir Lecture: Collagen fibril formation in vitro and in vivo. *Int J Exp Pathol* **98**, 4–16 (2017).

4. Last, J. A. & Reiser, K. M. Collagen biosynthesis. *Environ Health Perspect* **55**, 169–177 (1984).

5. Gobeaux, F. Phases denses de collagène de type I: transition isotrope/cholestérique, fibrillogenèse et minéralisation. (Université Pierre et Marie Curie, 2008).

6. Gueltekin, O. Computational Inelasticity of Fibrous Biological Tissues with a Focus on Viscoelasticity, Damage and Rupture. (University of Technology, 2018).

7. Kadler, K. E., Holmes, D. F., Trotter, J. A. & Chapman, J. A. Collagen fibril formation. *Biochemical Journal* **316**, 1–11 (1996).

8. Giraud-Guille, M.-M. *et al.* Liquid crystalline properties of type I collagen: Perspectives in tissue morphogenesis. *Comptes Rendus Chimie* **11**, 245–252 (2008).

9. Giraud Guille, M. M., Nassif, N. & Fernandes, F. M. Collagen-based Materials for Tissue Repair, from Bio-inspired to Biomimetic. in *RSC Smart Materials - Materials Design Inspired by Nature: Function through Inner Architecture* (eds. Fratzl, P., W. C. Dunlop, J. & Weinkamer, R.) vol. 4 107–127 (The Royal Society of Chemistry, 2013).

10. Zhang, F. *et al.* A hybrid vascular graft harnessing the superior mechanical properties of synthetic fibers and the biological performance of collagen filaments. *Materials Science and Engineering C* **118**, (2021).

11. Magnan, L. *et al.* Human textiles: A cell-synthesized yarn as a truly "bio" material for tissue engineering applications. *Acta Biomater* **105**, 111–120 (2020).

12. Martinier, I. *et al.* Tunable biomimetic materials elaborated by ice templating and self-assembly of collagen for tubular tissue engineering. *biorXiv* (2023).

13. Ryan, A. J., Ryan, E. J., Cameron, A. R. & O'Brien, F. J. Hierarchical biofabrication of biomimetic collagen-elastin vascular grafts with controllable properties via lyophilisation. *Acta Biomater* **112**, 52–61 (2020).

14. Yin, K., Divakar, P. & Wegst, U. G. K. Freeze-casting porous chitosan ureteral stents for improved drainage. *Acta Biomater* **84**, 231–241 (2019).

15. Pawelec, K. M., Husmann, A., Best, S. M. & Cameron, R. E. Ice-templated structures for biomedical tissue repair: From physics to final scaffolds. *Appl Phys Rev* **1**, (2014).

16. Pati, F. *et al.* Printing three-dimensional tissue analogues with decellularized extracellular matrix bioink. *Nat Commun* **5**, 3935 (2014).

17. Suo, H., Zhang, J., Xu, M. & Wang, L. Low-temperature 3D printing of collagen and chitosan composite for tissue engineering. *Materials Science and Engineering C* **123**, (2021).

18. Griffanti, G., Rezabeigi, E., Li, J., Murshed, M. & Nazhat, S. N. Rapid Biofabrication of Printable Dense Collagen Bioinks of Tunable Properties. *Adv Funct Mater* **30**, (2020).

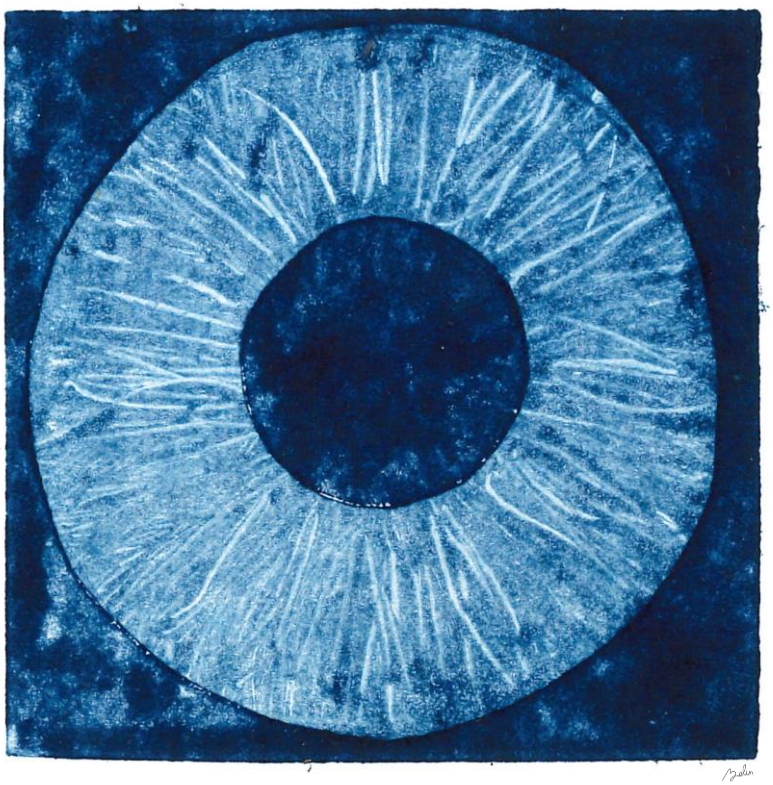

Chapter I

Biomimetic tubular organs

"I believe that the main thing in beginning a novel is to feel, not that you can write it, but that it exists on the far side of a gulf, which words can't cross: that it's to be pulled through only in a breathless anguish."

— Virginia Woolf

Review article, submitted

Biomimetic materials to replace tubular tissues

Isabelle Martinier, Léa Trichet and Francisco M. Fernandes**

Laboratoire de Chimie de la Matière Condensée de Paris, Sorbonne Université, UMR 7574, Paris 75005, France

Corresponding authors: lea.trichet@sorbonne-universite.fr and francisco.fernandes@sorbonne-universite.fr

Keywords: biomimetism, biomaterials, tubular tissues, tissue engineering.

Abstract

Repairing tubular tissues—the trachea, the esophagus, urinary and gastrointestinal tracts, and the circulatory system—from trauma or severe pathologies that require their replacement, calls for new, more effective graft materials. Currently, the relatively narrow family of materials available for these applications relies on synthetic polymers that fail to reproduce the biological and physical environments of native tissues. Mimicking the structure and the composition of native tubular tissues to elaborate functional grafts is expected to outperform the materials currently in use, but remains one of the most challenging goals in the field of biomaterials.

Despite their apparent diversity, tubular tissues share extensive compositional and structural features. Here, we propose a dual layer model common to all tubular tissues, which reduces each tissue to an inner epithelial layer and an outer muscular layer. Based on this model, we examine the current strategies developed to mimic each layer and we underline how each fabrication method stands in providing a biomimetic material for future clinical translation.

The analysis provided here, addressed to materials scientists, bioengineers and clinical staff alike, sets new guidelines to foster the elaboration of new biomimetic materials for effective tubular tissue repair.

Abbreviations

Col[roman numeral]: type [roman numeral] collagen

dECM: decellularized extracellular matrix

EC: epithelial cells

ECM: extracellular matrix

Fn: Fibronectin

GI: gastro-intestinal

Hep: heparin

iPSC: induced pluripotent stem cells

Ln: laminin

PET: poly(ethylene) terephthalate

PEG: poly(ethylene) glycol

SMC: smooth muscle cells

UC: urothelial cells

USC: urine stem cells

1. Introduction

In living organisms, the transport of gases and liquids through the body is imperative to ensure homeostasis and, ultimately, the organisms' viability. These transport mechanisms occur at different length scales in living systems. On the lower end, at the nanometer scale, specialized transmembrane proteins like aquaporins enable molecule-by-molecule water transport between the cytoplasm and the extracellular environment. On the other end of the fluid transport scale, the meters' long circulatory system of humans handles an incessant pulsatile flow of several liters of blood. The radically different transport phenomena—defined by the properties of the fluid, its volume or its flow rate—require different driving forces. Osmotic forces drive water molecules across the cell membrane whereas blood is pumped by the mechanical action of the muscles in the cardiovascular system. A detailed analysis of the different strategies favored by evolution to cope with all fluid transport needs in biological systems, falls beyond the scope of this review article. However, if we focus on native, large-scale fluid transport systems—such as gastrointestinal and urinary tracts or respiratory and circulatory systems—they all share common features: a three-dimensional concentric arrangement of sublayers around a luminal space, lined by a tightly bound layer of cells named the epithelium. At a first glance, the diversity of fluid properties—gases, liquids with variable viscosities and semi-solids—seems to play only a small role in the strategies selected by evolution to transport large volumes of fluids. **Figure 1** highlights the common concentric layered structures of five different tubular organs, with detailed electron microscopy observations of their epithelium. It illustrates that, despite their different physiological functions, they share a large array of

structural features—in particular three to four concentric layers, which compositions depend on each specific tubular organ[1] (Figure 1).

Tubular organs can adapt to some extent to moderate effects of stress[2], disease[3], aging[4,5] or environmental factors[6,7]. Clinical guidelines for the early treatment of damaged or malfunctioning tubular organs favor the use of drugs or other non-invasive procedures[8–11]. More severe cases require surgical replacement, using (a) autologous, (b) allogenic or (c) synthetic grafts. The most common procedure for tubular tissue grafting relies on allografts, *i.e.* native tissues harvested from another patient or obtained from a donor bank[12]. However, their availability is limited, either due to technical limitations to preserve the tissues on the long term, or due to plain shortage of suitable organs[13]. Synthetic tubular grafts are a promising solution to tackle these limitations, in particular because they are independent from most logistics limitations. Since the first grafts developed for vascular purposes using PVC (Vinyon) cloth in 1952[14], research efforts have extended this concept to a wide range of other synthetic polymers. Prosthetic grafts from polytetrafluoroethylene (PTFE (Teflon®), extruded PTFE (Gore-Tex®)), polyethylene terephthalate (PET (Dacron®)), or polyurethane (PU) have produced fruitful results as cardiovascular grafts, in particular for the replacement of large-diameter vessels (with an internal diameter above 6 mm)[20]. However, the unsatisfactory long-term clinical results* and the mismatch between the mechanical and biological properties of the living tissue and of those of the implanted biomaterial[15], have directed research towards alternative routes. Among these new approaches, biomimetic materials are expected to play a central role.

* Patency and viability, anastomotic leakage, obstruction of the grafts (thrombus or stenosis[12]).

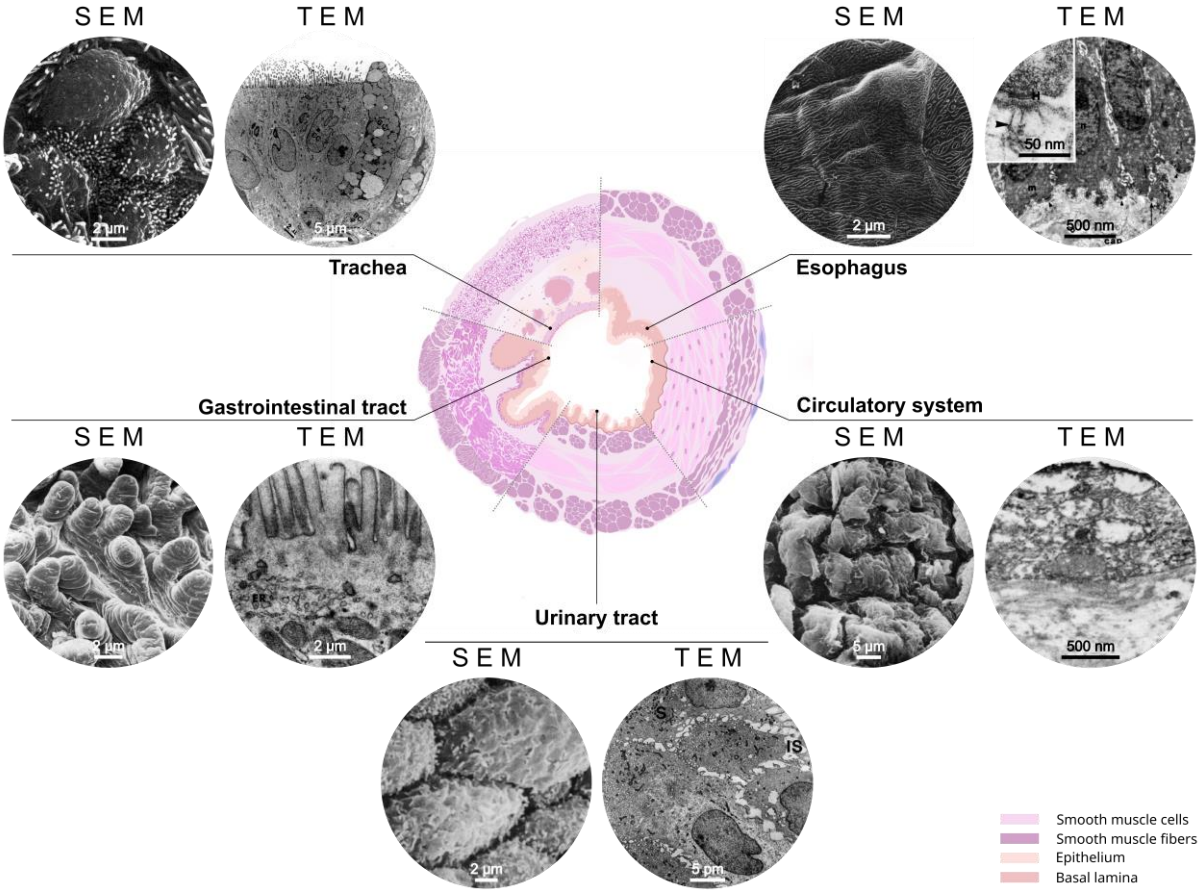

Fig 1. Similarities in the structural and compositional features across different tubular tissues. Center, schematic histological transversal cross-sections, associated with scanning electron microscopy (SEM) and transmission electron microscopy (TEM) images of epithelia for each tissue. **Trachea,** *chicken*†: (SEM) group of mature goblet cells on the luminal surface, exhibiting sparse microvilli on the peripheral surface[16]. (TEM) a mature goblet cell with a characteristic goblet shape releasing mucous granules (G) into the lumen of the trachea through pits or pores[16]. **Esophagus**, *human*: (SEM) individual squamous epithelial cells are separated by distinct intercellular ridges, and covered by varying arrangements of distinct micro-ridges forming a latticework[17]. (TEM) at low magnification, basal cells attached to the basal membrane (arrow heads) with hemidesmosomes (H). Nucleus (n) and intranuclear mitochondria (m) are observed. The inset at higher magnification details the basal membrane and shows anchoring fibrils (arrow heads) running into the lamina propria[18]. **Circulatory system**, *human*: (SEM, *saphenous vein* and TEM, *coronary artery*) high magnification of the luminal surface of a saphenous vein, ridges are covered with smooth-surfaced endothelium[19]. **Urinary tract**, *various origins*: (SEM, *human*) the transitional epithelium in the upper part of the prostatic urethra. Among the typical apices of the superficial cells, small apices provided with microvilli emerge[20]. (TEM, *sows*): basal cells (B), intermediate cells (I) and a few vesicles at the apical portion of cytoplasm close to the basal membrane (arrow)[21]. **Gastrointestinal tract**, *human*: (SEM) the majority of villi are fingershaped, but occasional bifid and leaf-shaped villi can be easily recognized[22]. (TEM) apical cytoplasm

† For tracheal epithelium electron microscopy observations, biopsies sourced from camel[296], rats[297], dogs[298] and porcine[299] were found, but not from humans.

of absorptive cells on a single villus located at the tip extremity, showing the length variations in the micro-villus lengths and the reticulum (R)[23].

The literature offers a wide range of definitions to the notion of biomimetic materials. Taken in a strict sense—as we do herein—a biomimetic material corresponds to an artificial material which structure and composition reproduces that of a natural tissue. Intuitively, reaching a high degree of similarity with a native material in its compositional and structural aspects, maximizes the chances that it equals its functions. For instance, in the case of gastrointestinal regeneration, it has been shown that cells attach and proliferate at a higher rate on biologically-based supports (biopolymers or ECM-derived materials) than they do on artificial ones[24]. This approach has resounding implications in the context of bioengineering and evidence of enhanced biointegration and low immune response of biomimetic materials has now been established in the medical field[25]. As a consequence, a detailed analysis of their anatomical structure, their composition and the relevant cell types, provides solid guidelines to conceive materials whose properties (mechanical, fluid transport, biocompatibility, etc) are comparable to those of original tissues and organs[1,5].

Despite their different physiological function, tubular organs share a large array of structural features—in particular three to four concentric layers, which compositions depend on each specific tubular organ (Figure 1)[1]. On the luminal side of tubular organs, cells adhere and form a tissue-specific epithelium that acts as a semipermeable interface between the transported fluid and the inner tissue wall. In the middle layer, smooth muscle cells—the effectors of motility—mediate the contraction of the lumen under specific physical or biological signals[26]. The outer layer provides mechanical support to the overall structure and favors the biochemical crosstalk between the implanted materials and their environment. In the outer layers, cells are embedded in the extracellular matrix (ECM), composed of macromolecules that include type I and IV collagens, elastin, proteoglycans and glycoproteins (laminin, fibronectin and nidogen). Each layer is composed of a different combination of components that determine the type and the density of binding sites that direct cell behavior. Type I collagen, the major component of the ECM in mammals, acts as a structural backbone for the whole tissues and as a support for cell adhesion, whereas elastin provides the tissues with resilience and elasticity[27].

Beyond type I collagen, other components play central roles in native tissues—laminin and fibronectin are involved in cellular adhesion and migration, and nidogen mediates biological responses of cells to laminin. In addition to the proteins mentioned above, proteoglycans ensure tissue hydration as well as an array of specific biological roles[28]. Despite the common traits between different tubular organs—that will be discussed further as a rationale for the elaboration of biomimetic grafts—the layers' composition is specific to each tissue[1].

The collective work of clinicians, biologists, materials chemists and physicists led to the creation of a variety of tubular grafts. The fabrication techniques involved in the elaboration of these materials can be classified according to their structure and composition, on a two-axis graph. The *biomimetic structure* axis refers to the degree of success in reproducing an adequate physical environment for cell colonization (macroporosity)[29] and the relevant number of concentric layers able to reproduce the macroscopic

tubular arrangement of the tissue. The *biomimetic composition* axis refers to the level of reproduction of the ECM composition, which determines interactions with cells. **Figure 2** depicts the wide spectrum of tubular biomaterials covered by the current fabrication techniques, which will be developed below (sections 2; 3). In addition, Figure 2 provides guidelines for the conception of future biomimetic grafts, while introducing currently developed techniques.

If biomimetic materials appeal for their capacity to recapitulate the structure and function of the native tubular tissues, the current panorama of materials is much broader. **Figure 2** depicts the main processing strategies, composition and geometry of the materials developed for tubular tissue engineering. Synthetic polymers are extremely versatile in their composition yet easily reproducible, which leads, respectively, to adjustable properties and steady quality[30]. These provide a high level of control over the mechanical properties, the cell spatial arrangement and differentiation by textural or topographic cues[31]. However, in the context of implantation procedures, synthetic scaffolds fail to recruit cells from anastomosis regions or from the surrounding environment due to the lack of specific cell-adhesion sites[12]. This results in poor cell proliferation substrates[17], with poor or absent epithelium. In addition, one should consider the possibility of materials to degrade *in vivo*, altering their structure and interactions with cells[32]. Polymers commonly used include polymethyl methacrylate (PMMA), silicones, polyvinyl chloride (PVC) and polyethylene terephthalate (PET), among others[33]. Polyesters and polyurethanes have also been investigated as replacement materials for the small intestinal submucosa, the esophageal submucosa, the gastric acellular matrix, or the aortic acellular matrix[34]. Current synthetic devices are now shifting from prosthetics towards scaffold materials to favor regeneration of tissues and long-term biocompatibility, by using biodegradable polymers such as: poly-lactic acid (PLA), polyglycolic acid (PGA), poly-l-lactic acid (PLLA), their copolymer poly(lactide-co-glycolide) and polycaprolactone (PCL)[35]. Another alternative route is to take benefit of the mechanical properties of synthetic polymers, and combine them to biologically derived components to enhance their biocompatibility. Entangled networks of PMMA and type I collagen, generated by co-electrospinning, provide a higher number of cellular anchoring sites that favors biointegration[36]. The addition of a biomimetic coating using proteins from the basal membrane—type III and IV collagens, fibronectin, laminin[37,30]—or the addition of active biomolecules[38] equally enables higher recruitment and adhesion rate of epithelial cells. Alternatively, biomaterials exclusively elaborated from ECM components, have proven efficient in promoting cell adhesion, proliferation and morphogenesis[39], ultimately leading to enhanced biointegration. In such case, the material performances depend mostly on the use of native biological components to reconstitute the tubular wall composition, and less on the structural and textural features of the material.

In this review, we describe the requirements to reconstitute the complexity of the native tissues, based on a thorough analysis of their specific biological and structural features (section 2), and we provide an overview of the existing methods to synthesized tubular tissue-analogs (section 3). We anticipate that the tissue-centered vision that we offer, restricted here to hollow architectures, will shift how the scientific community envisages the elaboration of new, more clinically-relevant biomimetic materials.

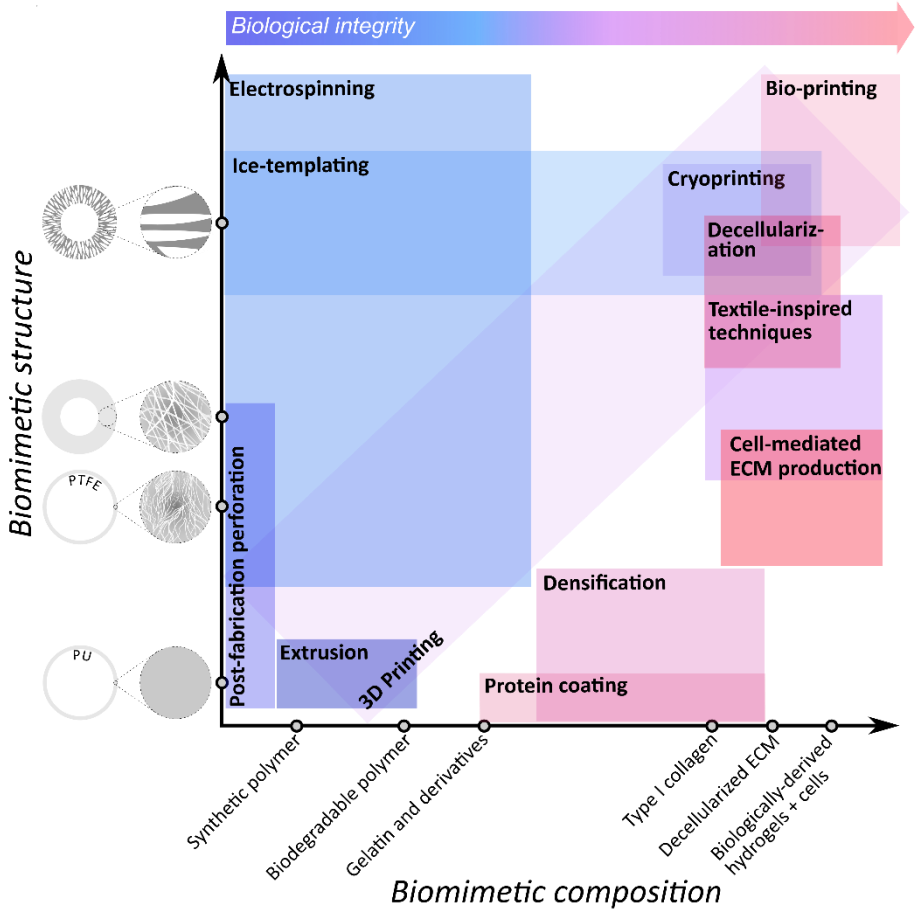

Fig. 2. Strategies to engineer biomimetic tubular tissues. Blue boxes refer to techniques for which the integrity of biological entities is hindered due to processing in the synthetic or biologically-derived composition. Pink-red boxes refer to techniques that preserve biologically-derived components, from biomolecules up to cells.

2. Structure and composition of tubular tissue layers

A detailed analysis of the native tissues enables to understand how each component holds a peculiar role in the tissues' structure and composition, giving guidelines for fabricating biomimetic materials that effectively replace damaged tissues. As mentioned above, tubular organs are multilayered structures, composed of three to four concentric layers, with specific cell arrangements and ECM architectures depending on their physiological function[40] (Figure 1). In the innermost layer, epithelial cells cover the lumen to form acellular sheet, the epithelium. Cells are anchored on a thin basal membrane, which separates the epithelium from the outer layers. Outer layers are populated by various type of cells—fibroblasts, nerve cells, smooth muscle cells, among others, depending on the tissue—embedded in a

protein-rich extra-cellular matrix. This arrangement can be depicted by a dual-layer model consisting of an epithelial inner layer and a muscular outer layer. Table 1 details the biological and physical properties of each of those simplified layers (epithelial and muscular layers) of tubular tissues, including the circulatory system, the trachea, the gastro-intestinal tract, the esophagus, and the urinary tract.

Following what was introduced above, **Table 1** highlights the predominance of type I collagen in the composition of tubular tissues. The structural conformation of collagen and its hierarchical arrangement are responsible for the anisotropy of tubular tissues and for their elastic properties[41], necessary to fulfill their physiological functions. *In vivo*, type I collagen can be described by four hierarchical levels: the amino-acid sequence, the triple helix (collagen molecule), the fibrils and the suprafibrillar structures. Generated by cells, amino-acids sequences self-assemble into triple-helices in the intracellular space and form fibrils upon extrusion from the cytoplasm. Interfibrillar proteoglycans, orthogonal to fibrils, bound them together to form fibers[42]. Fibrils display a typical staggering that results in an axial characteristic distance of 67 nm, named D-spacing, and observable exclusively under electron microscopy or by X-ray diffraction. Fibrils are arranged in higher ordered structures whose architecture are specific to each tissue (bone, skin, tendon…)[43]. These arrangements in tissues have been widely explored by microscopy techniques, in particular by TEM and polarized light microscopy[44]. The latter revealed a liquid crystal-like behavior, with the formation of lyotropic mesophases associated with specific tissues (cholesteric, nematic, plywood, among others)[45–47]. Mimicking *in vitro* the native motifs found *in vivo* requires a deep understanding of the physico-chemical conditions governing its emergence, notably during the fibrillogenesis step that encompasses the transition from acid solution to a fibrillar gel. However, the necessity of a high collagen density, and the structural modifications of collagen during the fabrication processes have received little attention and are most often disregarded in the literature. *In vitro*, fibrillogenesis can be triggered by increasing the pH or ionic force, collagen molecules are stabilized into fibrils that present the characteristic D-banding native fibrillar pattern of 67 nm[48]. Besides the use of soft fibrillogenesis pathways, a large part of the research using collagen relies on the use of chemical cross-linkers (EDC, genipin and glutaraldehyde), or physical treatment (dehydrothermal or UV treatment). However, controversy exists regarding the use of chemical crosslinkers. Bonds formed between collagen molecules differ from a cross-linker to another one[49], resulting in various biological responses that may not be conducive to tissue regeneration. Their potential toxicity and immunogenicity, even at low concentrations, has been reported to reduce cell proliferation and adhesion *in vitro*[49]. Physical treatments tend to denature collagen, forming gelatin that hinders the reformation of native-like fibrils. Despite the predominance of type I collagen in tissues, using it as a building block in tissue engineering requires a precise control over the elaboration conditions, to avoid its degradation that results in poorly biomimetic materials.

Table 1. Structural and compositional properties of tubular tissues based on a dual-layer model composed of an epithelial layer lining a muscular layer.

Tubular tissue in the human body	Epithelial inner layer		Muscular outer layer		Refs.
	Biological properties	Physical properties	Biological properties	Physical properties	
Circulatory system	*Endothelium*: endothelial cells aligned in the direction of the blood flow. *Basement membrane*: basal lamina[50], mainly composed of type III and IV collagens, along with laminin isoforms, entactin and fibronectin (see	*Permeability*[‡‡]: at a steady state, junctions in ECs originating from arteries and micro-vessels are tighter than those originating from veins. Diffusion distances of FITC-dextran deposited on monolayers of unstimulated cells, are reported at 8,3 % (arteries), 10,2 % (micro-vessels) and 15,8 % (veins) of the total wall thickness after 1 h. *Ultimate tensile stress*: in intima, 394 ± 223 kPa circumferentially and 391 ±	*Cells*: contractile SMCs, spindle shaped, and arranged circumferentially in a spiral shape within the matrix. On the outer part, a few fibroblasts and fibrocytes maintain the plasticity of the arterial wall, which allows remodeling upon mechanical stress or	*Ultimate tensile stress*: for the adventitia, 1,430 ± 604 kPa (circumferentially) and 1,300 ± 692 kPa (longitudinally). For the media, 446 ± 194 circumferentially and 419 ± 188 kPa longitudinally[51]. *Compliance*: average large and small arterial elasticity of 12.9 ± 4.2 mL/mmHg x 10 and 4.4 ± 2.3 mL/mm Hg x 100, measured on human patients [55].	50 to 55

‡‡ Caution should be taken with the permeability assessments. The measurement of epithelial permeability is an indicator of the tightness of the cellular network, necessary to withstand the physiological intraluminal pressure while allowing for molecular exchanges. *In vivo* direct measurement of arterial permeability is a procedure that is impossible to be done without harming patients. Hence, *in vitro* models have been developed to obtain an approximation of it, but the physiological micro-environment has not been fully reconstituted yet. For instance, permeability values show heterogeneity between different phenotypes of human ECs *in vitro*[83]. The EC permeability response upon stimulation with histamine, platelet activator factor (PAF), and thrombin is also modulated by the cells' origin[83]. The static conditions often used in the current models also influence junction response to stimuli. The use of thrombin or other permeability modulator can affect actin cytoskeleton, resulting in large gap junctions slowly forming overtime, compared to the discrete and rapid endothelial gaps observed *in vivo*. Finally, endothelial cells upregulate inflammatory genes in culture conditions, which might bias results. The permeability of vascular endothelium is a delicate measurement, and the value must not be taken as an absolute but be mitigated by the experimental conditions[59].

	section ***2.1.2*** for more details).	144 kPa longitudinally[51]. *Stiffness*: mean stiffness values in intima layer of human aorta is 24.04 ± 13.97 kPa, measured by AFM. Intimal collagen fibers stiffness was also measured by ultra-AFM and evaluated at 7.31 ± 3.5 MPa[40]. Collagen fibers angle[§]//***: 15.2° in the intima, with respect to the vessel axis[52].	biochemical stimuli[53]. *ECM*: fibrous, contains collagen, elastin and proteoglycans, in which SMCs are embedded. Tunica media is isolated from the other layers by elastic laminae[54]. The adventitia is a connective tissue composed of a dense network of collagen and elastin fibers arranged along the vessel axis. This layer is infiltrated with nerve fibers, lymphatic vessels, and the vasa vasorum.	*Stiffness*: for the *media* of human aorta the stiffness is 22.18 ± 5.54 kPa, and for the *adventitia* 22.54 ± 3.35 kPa[55]. *Collagen fibers angle*[§]: 28.8° for the media and 57.1° for the adventitia, with respect to the vessel axis[52].	
Trachea	*Epithelium*: pseudostratified ciliated epithelium containing ciliated cells (over 50 %), goblet cells, basal	*Permeability*: $1.05.10^{-14}$ $m^4.N^{-1}.s^{-1}$ towards water in porcine hyaline cartilage[59]. *Stiffness*: no data was found in the literature for tracheal apical surface	*Cells*: smooth muscle cells. ECM (*submucosa* and *adventitia*): connective tissue rich in elastin that	*Ultimate tensile stress*: longitudinal elastic modulus of 1.10 ± 0.68 MPa for porcine tracheal ring[62]. Circumferential elastic modulus of 4.6-13.6 MPa for human trachea.	57 to 64

§ Collagen fibers angle is an important feature of tissue, which guides cells migration along the axis of the fibers and provide binding sites. This angle particularly important in arterial tissue where collagen fibers have a circumferential arrangement.

	cells and neuroendocrine cells4o,[57]. *Basement membrane*: collagen type IV, V and laminin in the upper part (*lamina densa*), secreted by the epithelial cells. Fibronectin, type III and V collagens are secreted by subepithelial fibroblasts in the thicker *lamina reticularis*[58].	stiffness. Eventually, stiffness of cultured lung epithelial cells seeded on petri dish was reported at 8.70 ± 0.23 kPa by AFM[60]. *Mucus viscosity*: from 0,01 to 1000 Pa.s for healthy human tracheal mucus. Pathological conduits often lead to increased viscosity values[61].	also contains seromucous glands and cartilage rings. Horseshoe-shaped rings of hyaline cartilage (type II collagen and chondroitin sulfate) from the submucosa are encased.	*Compliance*: ranging from 0.046 to 0.101 cm.H_2O^{-1}, measured on a handmade setup. Sections were fixed and pre-strained, then pressure response to intraluminal injection of Dulbecco's PBS was measured[63]. *Stiffness*: tensile stiffness of cartilage from human tracheal sections varies from 1.8 ± 2.1 MPa to 10.1 ± 3.3 MPa depending on the age (17 to 81 years old), water content, and is inversely proportional to collagen content. The outer layer provides the higher stiffness (14 MPa) compared to the innermost layer (5 MPa)[64].	
Gastro-intestinal (GI) tract (stomach, large and small intestines, rectum)	*Epithelium*: simple columnar epithelium composed of enteroabsorptive cells, goblet cells, Paneth cells and neuroendocrine cells. The concentration of the mucus on the epithelium was reported at 19.9 ± 0.8 % (w/w) for human	*Permeability*: in the case of the GI tract, it relates to the porosity of the mucus (up to 200 nm diameter in purified porcine jejunal mucin network[65]). However, in human ileal mucus, 58.1 ± 4.7 % of 500 nm latex beads dispersed in bile salt at a physiological concentration (11 mM) are able to diffuse. Permeability of the mucus is thus not only depending on the pore size, but also on the interactions between the mucus and the diffusing particles and the	*Cells*: smooth muscle cells. ECM (*muscularis mucosa* and *adventitia* or *serosa*, depending if the gut is extra- or intra-peritoneal): vascularized tissue divided into longitudinal and circular muscle fiber layers[68], lying on the submucosa, a connective tissue containing type III	*Ultimate tensile stress and strain*: 0.57 ± 0.12 MPa transversally and 0.677 ± 0.19 longitudinally on surgically resected human stomach, with a maximum strain of 190 % for both[70]. *Compliance*: 1.49 ± 0.15 mL.mmHg^{-1} measured for canine ileum[71]. *Stiffness*: 0.641 ± 0.342 kPa measured for bovine ileum and 0.698 ± 0.463 kPa for bovine	65 to 71

	ileal mucus[65]. *Basement membrane*: mucosal folds and finger-like vili structures[66].	structural organization of the mucus. A model proposes that small non-mucoadhesive particles can diffuse through lamellae and create transient channels though which bigger particles can pass[65]. *Stiffness*: for colonic tissue and the ileum (a section of the small bowel), stiffness is respectively of 0.698 ± 0.463 kPa and 0.641 ± 0.342 kPa. Values were measured by a custom-cantilever based indenter[67]. *Mucus viscosity*: mean viscosity of 23.4 ± 8.2 mPa.s[65].	collagen[69].	colon[67].	
Esophagus	*Epithelium*: stratified squamous epithelium. *Basement membrane*: *lamina propria* and *muscularis mucosae* contains gland cells, endocrine cells, small blood vessels, nerve fibers and lymphatic cells. It is surrounded	*Permeability*: for healthy epithelium, biotin diffuses only into the superficial layers at a distance of 8.3 % ± 2.4 % to the lumen, compared to 100 % diffusion in the case of chronic epithelial inflammation (eosinophilic esophagitis)[73]. *Stiffness*: no data was found in the literature for esophageal apical surface stiffness. Data were only	*Cells*: the upper third of the esophagus is composed of striated muscle cells, and on the lower third of smooth muscle cells. *ECM (muscularis externa and adventitia)*: thick muscle layer consisting of an inner and outer	*Ultimate tensile stress and strain*: for human esophagus maximum stress is 1.2MPa and destructive strain is 140 %[70]. *Compliance*: mean value of 2.27 % volume/mmHg for children esophagi[75]. *Stiffness*: 2.24 ± 0.39 kPa and 12.2 ± 70.78 kPa in the circumferential	72 to 76

	by the submucosa layer which contains areolar connective tissue, blood and lymphatic vessels, and nerve fibers[72].	found for cells cultured on synthetic substrates. *Opening angle*[**]: 134.3 ± 19.1° measured for rat esophageal mucosa.	longitudinal layer, separated by a nervous layer (*myenteric plexus*). The outer layer contains blood vessels, veins and lymphatic vessels[74].	and longitudinal directions for rat esophagus[76]. No data was found in the literature for human esophagus. *Opening angle*[4]: 62.2 ± 7.0°, measured for intact rat esophagus.	
Urinary tract (ureter, urethra)	*Urothelium:* transitional epithelium for ureter, pseudostratified columnar and transitional epithelium for urethra. The epithelium is populated by a single layer of umbrella cells, followed by intermediate cells and a basal cell layer[77]. *Basement membrane (lamina propria):*	*Permeability*: no data was found for urinary tube. The same urothelium lines ureter, urethra and the bladder, hence we herein assume their properties equivalent. For the bladder, permeability to water and urea were estimated at P_D = 4.12 ± 0.29.10^{-5} cm.s^{-1} and 4.35 ± 0.65 .10^{-6} cm.s^{-1}. For smaller species like ammonia and protons, permeability values of 5.00 ± 0.48.10^{-4} cm.s^{-1} and 2.96 ± 1.86.10^{-3} cm.s^{-1} were measured. The epithelium only contributes for 80 % of the resistance to water flow and over 95 % of the resistance to fluxes of urea, ammonia, and	*Cells (mesothelium)*: layer of epithelial cells covering the *serosa*. *ECM (serosa, the visceral peritoneum)*: areolar connective tissue for ureter, and muscular layers (one longitudinal and one circular) for urethra.	*Stiffness, tensile stress and strain*: no data was found in the literature for urinary tubes, research focuses mainly on the bladder. *Compliance*: maximal urethral opening of 0.35 ± 0.2 mm^2/cmH_2O for human[80].	77 to 80

[**] The opening angle is a particularly relevant measurement of esophageal tissue. It is an indicator of the cartilaginous flexibility and the ability of the material to deform for swallowing purposes.

	loose connective and vascularized tissue with many elastic fibers.	protons[78]. *Stiffness*: 31 ± 0,5 Pa for the apical surface of mouse bladder urothelium, measured by AFM[79].			

A. Epithelial inner layer

The innermost surface of the tubular walls consists of an epithelium—a tight layer of cells—that covers the thin basal membrane of the lumen. Epithelia are widely spread throughout the body, covering most organs and body surfaces. They isolate the tissues from non-self or any other substances in the lumen, prevent direct contact of blood with ECM to avert thrombosis, and favor pathogens' evacuation[81]. Sensors and specific receptors at the cell surface participate to immune defense by generating host-pathogen signaling cascades, and maintain homeostasis. Depending on its permeability, the epithelium also allows exchanges with its environment[82].

The classification of epithelia is based upon cell organization (orientation and number of cell layers) and cell shape. Four types of organizations are commonly considered[81]. Simple epithelium consists in a single layering of tightly-bound cells. Oppositely, stratified epithelium is composed of two or more cell layers, with equivalent size and morphology. In pseudostratified epithelium, a single layer of cells covers the surface, but uneven cells' shape and size creates a layered or stratified effect. Transitional epithelium is a stratified epithelium, for which cell morphology adapts following the organ distention. For instance, under low pressured fluid cells are cuboidal, whereas if pressure increases they flatten and adopt a squamous morphology. In columnar epithelia, elongated cells arise from the basal membrane to the exposed surface in a compact arrangement. These cells often express motile projections named cilia on their surface, consisting in two central microtubules, encompassed by nine microtubule doublets. These small hair-like structures increase the sensitivity to fluid pressure and flow, and can move in coordinated waves to propel mucus or other fluids and eliminate foreign substances[57]. Permeability, one of the key functions regulated by epithelia, depends on the cellular arrangement and junctions mentioned above, in order to provide proper supply to the adjacent tissues' physiological needs.

Epithelial cells' shape and arrangement reflect the epithelium functions at a given site. Under the passage of blood, epithelium (namely endothelium) adopts a *simple squamous* structure. It acts as a semi-permeable barrier for rapid diffusion of gases or materials through cells membranes or junctions[83]. In gastro-intestine tract, *simple columnar* epithelium is responsible for the absorption and secretion of mucus and enzymes. Nutrients absorption is maximized by topographical specifications associated with increased surface area: mucosal folds, finger-like villi and columnar crypts[57]. The luminal surface is protected from damage by a mucin layer, responsible for lubrication, which is secreted by goblet cells[56]. In the GI tract, a deleterious consequence of loose epithelial cell junctions is increased permeability from the lumen, resulting in paracellular transport of water, nutrients and ions. In trachea, a single layer of columnar cells of various heights and shapes lines the lumen, giving the appearance of stratifications. This *pseudo-stratified* structure favors the entrapment of foreign particles (bacteria, pollutants) in the mucus. Cilia on the surface of the cells contribute to move the contaminated mucus out of the airway. Damaged or senescent cells are renewed by reserve cells migrating from the basal lamina to the mucosal surface. The tubular structures exposed to higher distension and stretch—esophagus and urethra—are endowed with multiple layers of cells that collectively form a *stratified squamous* epithelium. The extended number of cell layers limits the diffusion from and into the underlying tissue, and it prevents

erosion by acidic food and urine[81]. The constant replacement of cells ensures the dynamics required for repairing epithelial damages and the subsequent restoration of the physiological permeability. The epithelium of urethra and ureter, urothelium, differs slightly from those previously mentioned, since it needs to accommodate significant distension and stretch. Cells exhibit various shapes in their constitutive layers, forming a *transitional epithelium*. Thicker layers and tight arrangement of cells separate more efficiently the basal lamina from outer substances that might be toxic such as waste in urine. The thickness of the cellular layer and arrangement of cells in urothelium makes it almost impermeant under physiological conditions[56,84,85].

In native tissues, discriminating the mechanical properties of the cellular layer from those of the underlying tissue is technically challenging. It is however commonly accepted that the epithelial layer contributes poorly to the mechanical properties of tubular tissues. Lu *et al.* measured the radial Cauchy strain along a porcine coronary artery, and demonstrated that it increases gradually from the inner to the outer layers, as both smooth muscle cells and collagen fibers present in the latter absorb the deformation[66]. A sounder criterion to evaluate the physical properties of each type of epithelium relies on measuring the permeability of the cellular junctions and their resistance to hydraulic pressure. The respective data for each epithelium is reported in Table 1.

In vivo, re-epithelialization is vital for repairing damaged tissue. This process is mediated by different types of cell junction types: tight junctions, anchoring junctions, and gap junctions[85]. Tight junctions are responsible for the impermeability of the cellular layer by preventing intercellular infiltration. Anchoring junctions stabilize cells and allow cellular adaptation to mechanical or geometrical cues through lateral and basal connections: desmosomes (cell-cell link though cadherins), hemidesmosomes (cell-ECM link through integrins) and adherens (cell shape regulation due to intracellular link to actin cytoskeleton)[85]. The essential component of endothelial junctions, VE-cadherin, forms Ca^{2+}-dependent, homophilic interactions between adjacent endothelial cells to maintain a tight endothelial barrier[86]. Gap junctions are intercellular communication channels, through which ions and small molecules travel whereas macromolecules can cross the endothelial barrier in three ways: (1) between the cells, through cell junctions (paracellular); (2) through the EC, via pores (diaphragms or fused vesicles); and (3) transcellularly, via shuttling vesicles and specific receptors[86].

The type of cells that line the luminal part of tubular organs and their arrangement largely dictate the function of epithelia in each organ. Although cell-cell interactions are qualitative markers for the functionality of the epithelium there is an equally important aspect that determines the quality of this cell layer: the underlying support materials. The following section addresses the composition and the organization of the basal membrane (BM), the underlying supporting materials onto which epithelial cells adhere.

B. The interfacial layer: the basal membrane

The basal membrane is a thin and dynamic layer that separates the epithelium from the rest of the connective tissue. The BM is composed of tissue-specific proteins isoforms that dictate the phenotypes of cells able to anchor[87]. It is a critical layer for the formation of the epithelium, and it is also involved in its regulation and maintenance through biochemical signaling (hormones, growth factor, cell adhesion ligands) and mechanical support (roughness, pore size, tensile modulus).

Despite its small thickness ranging between 50 to 300 nm, the BM is structured in two distinct layers, the basal lamina—composed of the *lamina lucida* and the *lamina densa*—and the *lamina reticulata*. Fibrillar type IV collagen and laminin isoforms dominate the composition of the BM. Nidogen (also named entactin), perlecan, fibrinogen and fibrin, act as linkers between collagen and laminins to form a fibrillar network, often in the form of a 2D random mesh[88]. Interconnected pores cross the full thickness of the BM, and allow for the transport of solutes and for the transmigration of cells without requiring matrix degradation or remodeling. As an example, the tracheal basal membrane features an average density of 737–863 pores/mm² with a mean diameter of 1.76 m[50]. Mechanical properties of the BM vary with age, medical condition, anatomical site and species. Furthermore, the spatial heterogeneity in BM mechanical properties direct the cellular behavior locally and, at a larger scale, drive the tissue morphogenesis or expansion[89]. At the tip of a growing lung for instance, the alternance of a thicker region followed by micro-perforations and thinning in the BM promotes branching and cell proliferation. The thicker region—built by a rearward translocation of the BM—stabilizes and constrains the expansion, while at the growing tip, the perforations and thinning locally increase the compliance to facilitate the expansion of both epithelium and BM[90]. Combined with the topography, the BM also influences cell function and phenotype. For instance, in the intestine, the luminal surface is structured in finger-like projections (or villi, 0.5-1.2 mm in height, and 100 m in diameter) and well-like invaginations (crypts, 120-170 m in depth, and 50 m in diameter) located between the villi. Cells proliferate in the crypts, and, as they migrate to reach the top of the villi, they differentiate into enterocytes[91].

The examples above illustrate the key role of the BM in determining the fate of epithelial cells, in the same manner as it is now widely established that cells respond to the mechanics[92], composition, topography and roughness[93] of their environment.

The basal lamina is also a site where the crosstalk between the epithelium and the mesenchyme takes place. Epithelial and mesenchymal stem cells interact via secretory signaling molecules, ECM and direct cell-cell junctions. Cells on each side of the BM influence the development of cells on the other (*e.g.* mesenchymal cells are implicated in the formation of the epithelium, and epithelial cells induce smooth muscle cell differentiation). These cell types work thus concomitantly to define tissue morphology during organogenesis, as well as to ensure tissue regeneration and homeostasis[94]. For instance, in urinary and GI tracts epithelium Sonic hedgehog (Shh) mediates smooth muscle cell differentiation and promotes mesenchymal cell proliferation. On the other side, in the mesenchyme, fibroblasts' growth factor 7 (FGF-7) stimulates the differentiation, proliferation and arrangement of epithelial cells at their early stage, while transcription growth factor 1 (TGF-β1) plays a role in cell differentiation[95,96]. Cells from

the luminal layer provide growth regulatory signals for the underlying SMC[37]. For instance, Wei *et al.* revealed that the addition of epithelial cells on a scaffold enhances muscular regeneration[97], that depend on a biochemical cascade initiated by ECs. The release of lactate stimulates the promotion and the polarization of macrophages. Under their impulsion, myogenic progenitor cells (MPCs) activate to proliferate, differentiate and fuse into myofibers to restore the damaged muscle. ECs are thus a key player in muscle regeneration and revascularization[98] and their crosstalk with muscular cells should be fully considered in the development of the different cell types mentioned just above.

Basal membrane mediates epithelium formation and restoration through different biological and physical factors. However, its influence over the muscular layer has been poorly investigated. Although cellular behavior is probably guided by BM's physical (permeability and mechanics) and biological (growth factors and binding sites) properties, research has not been able to clarify this interdependence until now.

C. The muscular outer layer

In tissue engineering—and in particular when following a biomimetic approach to develop new materials—it is critical to reproduce the structural and compositional features of the targeted tissue. This is particularly relevant in the case of the muscular outer layer, since it is the first barrier against excessive expansion of the tubular tissues in cases where the luminal pressure increases, while the adventitia's role is mostly to prevent wall rupture. This layer is thus key for the biomechanical functions of tubular tissues. Structural fibrous proteins (collagens, elastin and laminin) as well as glycosaminoglycans (GAG) provide a robust skeleton to cells embedded in the matrix, mainly smooth muscle cells (SMC).

In arteries, the tunica media is a fibrous ECM layer mainly composed of type I collagen (ColI)[99](Table 1). In GI tract and esophagus, type III collagen is the main component of the mucosa, and forms a network that provides anchorage to smooth muscle cells[54]. In trachea, several types of collagen subtypes are involved and assume different roles, however 80 to 90 % of the total collagen moiety are represented by type I, II and III collagens. Type II is the main component of airway cartilage and facilitates chondrogenesis, whereas type III and especially type I collagens provide the ECM with mechanical stability[100]. Finally, type I collagen dominates the composition of the muscular layer of the ureter, with 83 % of the global wall composition[101]. Considering the predominance of collagens in native tubular tissues and in particular in the thickest and outer muscular layer, their use as a raw material is essential to fabricate biomimetic tissues. Still, the accurate quantification of their content in healthy tissues, about 100 to 200 $mg.mL^{-1}$,[102], remains imprecise which raises major challenges to design consistent strategies for the elaboration of biomimetic tubular tissues grafts. This aspect is of particular importance due to the lyotropic behavior of collagen in solution and its impact on the fibrillar architectures obtained after fibrillogenesis[44]. If the concentration of ColI has not been established for many tissues, its organization within these tissues has been widely described in the literature over the past decades, as described in the introduction. Variations in the conformation of the collagen molecules and network modulate interactions with cells, and the cellular responses might vary with the number of exposed binding sites, tightness of the network and fiber sizes, among other factors. For instance, residual proteoglycans in

collagen extracted from animal tissues is known to affect the antigenicity of the material[43]. Other studies showed that cell phenotype depends on the collagen conformation, in particular SMC that populate the muscular layer[103].

The SMC network is an active control system able to generate the contractile forces necessary to adapt the geometry and the mechanics upon physiological demands[69]. For example, in arteries, they respond to nervous and hormonal signals to modify the vessel volume and the blood pressure[72]. Their contraction is initiated by membrane depolarization, which activates voltage-gated calcium channels and leads to calcium (Ca^{2+}) influx into the cell, leading to its contraction[54]. Healthy contractile SMCs exhibit a spindle-shaped morphology, regulated by several signaling pathways and local environment cues[104]. Under certain conditions, for instance damaged tissue or *in vitro* culture, cells undergo phenotypic transitions that hamper the contractile behavior. Following the loss of their myofilaments, they flatten, lose their contractile function and become more proliferative. Regulation of their phenotype is a complex process that remains poorly understood due to its plasticity[105]. By identifying the conditions that favor one or another phenotype, these could be advantageously used to bioengineer tubular materials, generating phenotype-specific regions and guiding their reversibility. The composition of the tubular tubes could also be modulated to control the cellular behavior. On the one hand, it is known that fibronectin[106], monomeric type I collagen[26], or growth factors could promote the migration and proliferation in order to maximize the repopulation of the inner part of the material. Various growth factors are also known to favor SMC migration (transforming growth factor-β1 TGF-β1), proliferation (fibroblast growth factor bFGF), or both (platelet-derived growth factor PDGF)[74]. On the other hand, once SMCs are distributed in the material, favoring their subsequent transition into contractile SMCs could be achieved using laminin, elastin, heparin[106], hyaluronic acid (HA)[107], while fibrillar type I and IV collagens at high concentrations would enable to reconstitute the adventice[108,30]. This complex approach requires a fine control over the material composition, and no example of such system was found in the current literature.

SMCs are not only impacted by the surrounding layers, but also by their local environment, the topography and porosity of the substrate. While tailoring the external surface using coatings or textural motifs enhance the epithelial cell adhesion[109], for SMC the limiting factors reside more in the penetration into the material with sustainable access to nutrients[55]. Porosity is the most important feature to increase viability and proliferation rate in a non-vascularized biomaterial, but in the meantime, increased porosity can compromise mechanical properties. Well-balanced pore characteristics—enabling both cell migration, proliferation, nutrients diffusion as well as the maintenance of the structural stability—need to be found for each targeted tissue.

D. Recapitulating tubular tissues layers

Research efforts to fabricate tubular tissue grafts have focused on a large panel of techniques and compositions, ranging from synthetic up to cell-derived compounds. Although the design of grafts has progressively approached the characteristics of native tissues, they still fail in demonstrating the

physiological properties that should derive from biomimetic structure and composition. Some of these characteristics have become clear guidelines to rebuild environments favorable to cell migration, proliferation, and to provide accurate mechanical support. A general overview of such guidelines is presented in **Table 2** for each layer of the tubular tissues, dictated by their biological and mechanical properties summarized in Table 1.

As previously introduced in section 2.3, smooth muscle cells require access to the inner volume of the implanted material, as well as to nutrients to proliferate. In the absence of vascularization, these requirements can only be met by adjusting the porosity of the material. Size, shape and interconnectivity of the porous network determine cells migration kinetics. Parisi *et al.* compared the migration mechanisms of normal human dermal fibroblasts on a porous type I collagen matrix and an equivalent non-porous matrix. After 28 days, cells seeded on the porous matrix reached 6 times the depth through the material as compared to non-porous matrix (respectively ~700 m and 110 m from the seeding surface)[110]. A variety of methods allowing to modulate cell colonization is reported in section 3.2.2 of this review. One particularly important point in this context concerns the maintenance or induction of cell contractile phenotype which determine the materials' functionality but also could entail their loss of dimensional stability.

The processes involved in epithelium formation relies on diverse cell locomotion modes (collective, mesenchymal, amoeboid) that are regulated by textural, mechanical and biological cues. In this regard, the texture of the luminal surface should promote cell adhesion and minimize cell infiltration, suggesting that porosity—at the length scale of the cell—should be minimized. Textural motifs might facilitate adhesion and proliferation of cells[111]. Fabrication routes based on the coating of the luminal surface with proteins from the basement membrane (collagen IV and laminin isoforms) should allow reproduction of the complex biological cues that favor cell anchorage and subsequent epithelialization. Beyond biological cues, such an approach should cover and smoothen the luminal surface and thus minimize cell infiltration.

Numerous studies have shown that collagen is an ideal substrate to develop 3D biomimetic matrices[43,112]. Because type I collagen behaves as a lyotrope in solution, there is a strong link between its concentration and the formation of liquid crystal mesophases. Upon fibrillogenesis, these structures lead to a variety of suprafibrillar architectures that are crucial to understand the relationship between the graft and its environment, but also to achieve functional graft materials. Control over the collagen concentration in the physiological range, coupled to the ability to tailor its textural properties remain ultimate goals to the research community dealing with collagen-based biomaterials', and more generally with biomimetic approaches to the elaboration of functional grafts in tissue engineering. The following section discusses the strategies—their forces and their shortcomings—to tackle this goal.

Table 2. Biological and physical properties of the tubular tissue structural layers.

Layer	Structure	Composition	Functions
Epithelial inner layer	Layer of cells lining the luminal surface of the organ, *i.e.* the interfacial basal membrane (BM). The latter is a two-layered structure composed of the *basal lamina* and the *lamina reticulata*.	Tissue-specific epithelial cells tightly bound together to form the epithelium. In the BM, collagen IV and laminin isoforms predominate in a fibrillar network along with entactin, perlecan, fibrinogen and fibrin.	To control permeation of the different components of biological fluids between the luminal space and surrounding tissue. Exchanges with the fluids (air, mucus, blood) and evacuation of eventual contaminants. The BM brings mechanical support, signaling functions for epithelium anchorage, and acts equally as a selective barrier allowing exchanges between the epithelial and muscular layers.
Muscular outer layer	Porous fibrillar network, divided into two to three layers in tubular tissues.	Smooth muscle cells embedded in a protein macroporous matrix, dominated by type I collagen and elastin.	Responsible for the mechanical properties and structural integrity of tissues. Hosts the SMC network able to generate the contractile forces.

3. Biomimetic strategies to recapitulate tubular tissue layers

A. The epithelial inner layer

a. Challenges of epithelium replacement

The absence of epithelium, both in pathological tissues or in grafts currently used in clinical practice, is one of the major causes for tissue or graft failure. Such limitation results in bacterial colonization, occlusion of the construct or tissue, or leakage[81]. A focus on the reconstruction of this layer is thus crucial for the proper function of tubular tissues. One strategy to favor the generation of epithelia relies on *in situ* grafting of the epithelial layer harvested from an analogous tissue. Currently, buccal mucosa grafts are the most common substitutes in urology, with a success rate of 70 to 80 %[113]. However, autologous transplants of epithelial grafts are often associated with donor-site morbidity, slow dedifferentiation to match the host tissue epithelium, functional misfits (stenosis, fibrosis, and contraction[114]) as well as deleterious side effects at the harvesting site for patients. These procedures significantly reduce the quality of life of patients. Buccal mucosa harvesting, for instance, induces pain, bleeding, difficulties to swallow, reduced mouth movement (opening, smiling, whistling, speaking), as well as profound impact on of salivation, taste and diet[113]. Both the harvesting procedure of autologous transplant and the implantation procedure are challenging. Implanting epithelia harvested from a different tissue might also lead to undesired physiological features if cells are not able to dedifferentiate. It is often the case for oral mucosa replacement using skin grafts, associated with excessive mucus formation and more surprisingly, hair growth[115]. The inability of these advanced surgical grafting techniques to restore the physiological functions together with the non-negligible side effects both challenge the biomaterial community to develop new solutions for epithelization. The alternatives proposed by the tissue engineering community tend to reconstitute the native basal membrane, with simplified structure/composition. These approaches result in lesser specificity towards certain cell types, decreased number of anchoring sites and signaling functions. The following sub-sections address the current and future strategies to promote epithelium reformation, illustrated in **Figure 3**.

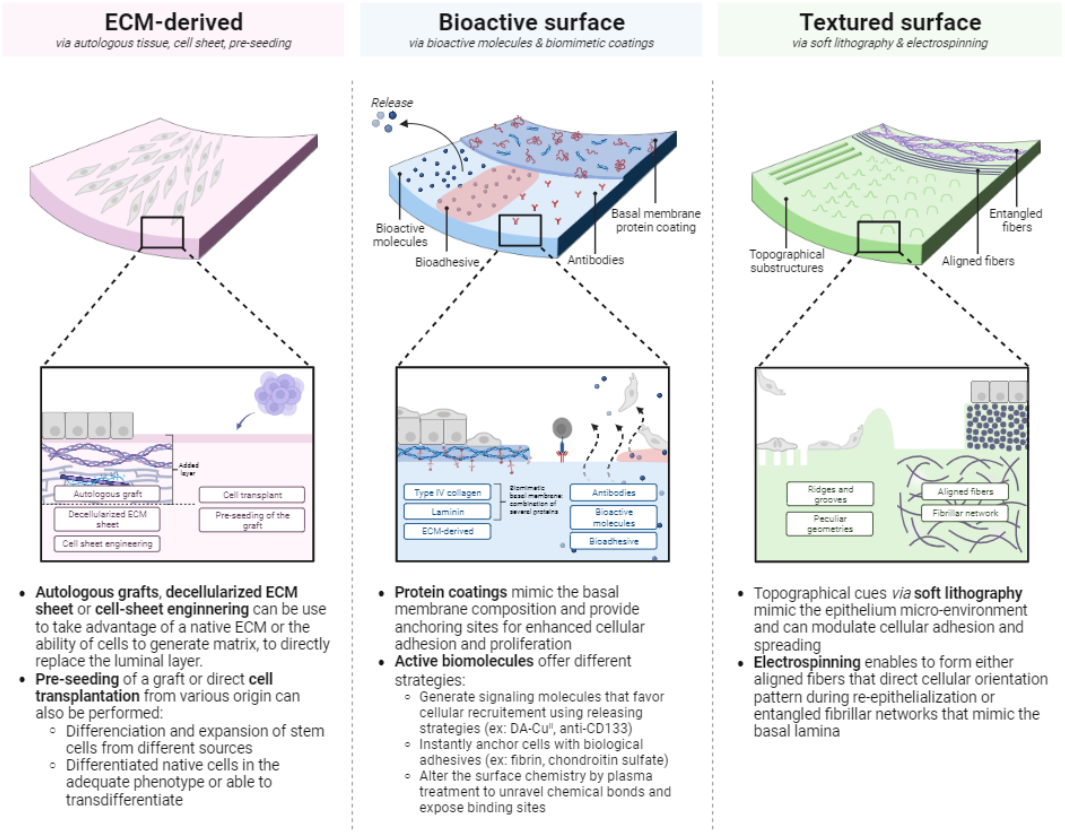

Fig. 3. Tubular tissue epithelium recapitulation. Strategies can be reduced to three main pathways: (a) ECM-derived epithelial layers, (b) bioactive surfaces and (c) textured surfaces.

b. Pre-seeding

A strategy for scaffolds unable to be quickly repopulated by cells, is to restore the epithelial layer by direct *in vitro* cell seeding prior to the graft implementation (**Fig.3**-ECM derived). The issue that dominates this approach is the reliability of the cell source. Collecting either autologous or allogenous cells able to differentiate is a difficult process, further adhesion on the scaffold is stochastic, and maintaining their phenotype and regeneration abilities require to provide the adequate environment. If cells are not able to do so, it results in graft rejection[116]. Additionally, due to the use of living cells, autologous tissue engineered products are subject to a severe regulatory framework that restrains the translation from the laboratory to the clinic[117].

Urothelium repair is currently the easiest and the most standardized epithelium replacement procedure. A new procedure was established for its repair in 2015, inspired by the conventionally used oral mucosa tissue for which a small number of autologous cells are expanded to form a cell sheet, later implanted for anterior urethroplasty[118]. The material, named MukoCell® is used for urethral stricture surgery with an efficiency of 84% treated patients, and is one of the few tissue-engineered products available in the European market. Replacement of the urothelium in urinary tracts is a minor field of research in

biomaterials and cell therapy, but pre-seeding techniques for the bladder replacement have been extensively studied. Because these tissues share the same urothelium it is likely that the methods developed for the bladder may be transposed to the epithelization of urinary tract. With a similar phenotype to mesenchymal stroma cells, urine-derived stem cells (USCs) can be reprogrammed into iPSCs[119]. Under appropriate cell culture conditions, it is possible to induce the differentiation of human iPSCs into bladder-associated cell types, including urothelial, endothelial and smooth muscle cell-like lineages[120], overcoming cell sourcing issues[113,120,121]. The potential of alternative sources like human bone marrow mesenchymal stem cells have also been studied to induce the simultaneous differentiation of both SMCs and UCs under appropriate culture conditions[122]. Urothelium bladder engineering currently relies on several sources of stem cells which enable relevant differentiation and proliferation *in vivo*[122]. The formation of a mature stratified bladder urothelium was shown by Suzuki *et al.* via a high primary dose administration of an inhibitor of the GSK-3 enzyme, implicated in inflammation and cancer cell proliferation[123,124]. But so far, only one study was able to demonstrate the reformation of an urothelium *in vivo* following cell transplantation. This first successful transplant of UC into the bladder lumen was performed in 2019[124]. UCs were transdifferentiated from human dermal fibroblasts using four transcriptional factors (FOXA1, TP63, MYCL and KLF4) that are expressed *in vivo* during urothelium formation and support mesenchymal-to-epithelial transition. After only 4 days of *in vitro* culture of the transdifferentiated fibroblasts, the transplantation into the bladder of a mice with damaged urothelium was performed and induced the conversion of the fibroblasts into UCs in the native environment. Overall, transplantation of cells is a possible and effective pathway for urothelium reformation, which allows variations in the cell source and transplantation method.

Regarding other tubular tissues, procedures are still experimental and no gold standard has been established. Airway epithelium reconstruction is limited by the difficulties of culturing primary human respiratory epithelial cells and maintaining their phenotype[116], partly due to the lack of mechanical resistance of the scaffold in the absence of cartilage. Attempts of replacement by autologous nasal squamous epithelium showed that the luminal epithelial surface can be recovered following transplantation[125,126]. Combined to the cell sheet method introduced by Kanzaki *et al.*[127] on pre-vascularized bioartifical grafts, Dang *et al.* developed sheets from those cells and incorporated them in partially decellularized grafts to improve re-epithelialization[126]. Noteworthy, they succeeded in preserving viable cartilage cellular components able to gradually restore the luminal architecture that still prevent immune rejection. While in most cases decellularization of trachea fail to retain cartilaginous components, impeding the restoration of the structural and mechanical properties that prevents luminal collapse. For the cell sheets, nasal epithelial cells were harvested in rabbits and expanded onto type I collagen-coated petri dish. At confluence, cells were seeded on thiol-modified HA-PET insert, and after three weeks, cell sheets were detached and harvested. The method enables to generate a multilayered mucosal epithelial structure with the characteristics features of airway epithelium, *i.e.* tight intercellular junctions, rounded morphology of the cells and low expression of anti-vimentin antibodies. Autograft transplantation in rabbit model following tracheal partial resection demonstrate the rehabilitation of the tracheal functions after 2 months, with a thin tracheal wall devoid of fibroproliferation, stenosis and granulation, displaying a lustrous and smoother appearance.

Esophagus epithelium replacement by cell therapy is still poorly investigated, and if so, mostly by pediatric surgeons. From the few articles available in the literature on this topic, the same strategies used for urothelium reconstruction prevail: either a generation of cell sheets further inserted in the scaffold lumen[128], or the seeding of autologous cells[129]. Differently from the previous approach, Saxena *et al.* studied the insertion of epithelial cell sheets onto a biomaterial rather than a decellularized matrix[113]. Epithelial cells were harvested in rat esophagus and transferred onto OptiMaix-3D®, a porous collagen matrix fabricated via solidification and freeze-drying of 1.5 wt% of collagen (mainly ColI) and elastin, previously sewed into a tube and pre-coated with 25 mg/mL ColI. After 8 weeks *in vitro*, cells exhibited the characteristics of mature epithelium (CK-14 markers) and formed a continuous layer on the lumen. Similar to the urothelium, both differentiated native epithelial cells and stem cells were studied and the two cell lineages were able to adhere on the substrate, proliferate and maintain or differentiate into the appropriate phenotype to reconstitute a mature epithelium[129].

The gastro-intestinal epithelium possesses outstanding regeneration abilities, with the fastest renewability. Formation of the crypt-villus units—epithelium included—is a self-organized process, able to originate from a single stem cell[130]. In homeostatic conditions, renewal is initiated by the transcription factors of the quiescent reserve stem cells in the crypts, the *leucine-rich repeat-containing G-protein coupled receptor 5*-stem cells (Lgr5+). Their proliferation leads to the spontaneous formation of multicellular 3D clusters named organoids. *In vivo,* new cells arise from these organoids, which proliferate and differentiate while migrating towards the crypt-villus axis[131]. Organoids also provide specific intestinal luminal cells, such as goblet and enteroendocrine cells, as well as mitotic cells[132]. Expanded *in vitro*, Lgr5+ cells produce organoids able to self-organize into an epithelial microvilli architecture with complex junctions, similar to what is observed in histology section of native tissues. The high potential of Lgr5+ to retain self-renewal properties and the ability to form organoids to repair damaged epithelium *in vivo* was confirmed for the first time in 2018, with a successful transplant of human colon organoids onto mice[133].

To the best of our knowledge, no cell transplant from autologous or stem cells were developed for the circulatory system. However, cell sheet engineering has been extensively studied to build either the luminal layer or the complete biomaterial for vascular applications[36].

Overall, two cell-based strategies enable to restore the epithelial layer of tubular tissues. Cell deposition on scaffolds or directly on the injured site can be conducted using either differentiated cells or stem cells. Cells might originate from another epithelial tissue (for instance, the oral mucosa EC for the urothelium) or from other individuals (for instance, human organoids onto mice intestine). However, it requires a control over the kinetics of the proliferation and the appropriate phenotype induction. The insertion of cell sheets grown *in vitro* into decellularized matrices or into engineered scaffolds allows to provide a more complex composition to the luminal surface. Production of ECM components by cells increases the repairing kinetics and favors biointegration which results in increased mechanical stability of the tubular organs.

c. In vivo recruitment of cells through active coatings

Another approach to reconstitute the epithelium is to design a luminal environment that actively induces epithelial cell migration[81] (**Fig.3**-bioactive surface). *In vivo* epithelialization requires a control over the cell migration (textured surface, signaling pathways and native environment) and the interactions with the surrounding cells (smooth muscle cells and mesenchymal stem cells). In particular, controlling the speed of cell migration *in vivo* is pivotal to ensure the coverage of the luminal surface, and avoid any clinical issues arising from epithelia depletion. To do so, many strategies attempt to mimic the basal membrane by topographical patterns or local supply of substances to endow the scaffold with high epithelialization ability and SMC phenotype regulation[37,81,91,134,135]. Wrinkled surfaces in the intima layer favor adhesion, oriented growth and phenotype differentiation of cells[91]. Approaches based on the integration of signaling molecules in the composition of the substrate are more reliable, but regulation of their release kinetics remain challenging[91].

Active biochemical coatings to regulate cell adhesion

Recent strategies have demonstrated an increasing potential of using active biomolecules to promote epithelialization. A simple and efficient approach relies on the decoration of the surface of the tubular grafts with antibodies onto which cells' antigens bind. CD133 antibodies are a good example for their ability to promote adhesion of circulating hematopoietic and endothelial regenerating cells presenting CD133 antigen glycoprotein on their surface. Encapsulation of antibodies has been studied in porous scaffolds by Wu *et al.*[136]. The core/shell electrospun scaffold presented a porous yet mechanically resistant outer layer composed of poly(L-lactide-co-caprolactone) (PLCL) and type I collagen (ColI), and a smooth inner layer of PLCL/ColI nanofibers/Heparin. The encapsulated antibodies were efficiently released, and a significant increase in the recruitment of endothelial cells *in vitro* was observed compared to the control without antibodies. Further *in vivo* investigations in rat abdominal aorta for 2 months confirmed the inhibition of coagulation by Heparin in the early period of implantation, and the promotion of EPCs recruitment and maturation on the luminal surface.

Aside from antibodies, ions or biologically-derived molecules have been equally investigated. Wang *et al.* established that the addition of dopamine-mediated copper(II) ion (DA-Cu^{II}) system on electrospun films significantly modulate the cell fate of ECs and SMCs and the platelet adhesion via a catalytic production of (NO) *in situ*[91]. In contrast to the control –without Cu^{2+} ions–NO was generated over a long-term period, less platelets adhered, and no blood clot was formed. *In vivo* evaluation performed on rat abdominal aorta model demonstrated a high patency rate for DA-Cu^{II} of 66.7 % after 3 months whereas all controls were occluded after 15 days.

Addition of active complexes as DA-Cu^{II} and CD133 in the scaffold enables to modulate biological signaling in favor of epithelial cells' recruitment. Integrating these molecules into a bioadhesive layer yields even higher cellular adhesion rates. However, the challenge of maintaining the adhesive strength within the moist environment of native tissues remains to address. Bioadhesion is a mechanism spanning

the whole animal kingdom (gecko, frogs, mussels, among others)[137] that constitute an inspiration for its potential to influence (bio)materials science research. Numeros examples of applications are available, ranging from wound healing (sealants and hemostatic agents[138]) to surgical tools for specific treatments[139]. In the case of grafts, marine mussel byssal plaques have provided inspiration for enhanced adhesion thanks to their high proportion in 3,4-dihydroxyphenylalanine (DPA). The adhesive system, composed of electrostatically self-assembled lysine and DPA-functionalized poly(acrylic acid) (PAADPA), was studied as a new adhesive coating strategy to prevent restenosis in injured arteries[140]. *In vivo* assays revealed increasing presence of endothelial marker CD31 on cells at the neointimal surface from day 3 to 7 and 14, alongside with a thick epithelium reformation.

Altering the surface biochemistry of biomaterials by plasma treatment has also been recognized as an efficient pathway to enhance protein absorption, by tailoring the surface with carboxyl groups, immobilizing biomolecules such as ECM proteins, improving biocompatibility of porous surfaces and changing hydro- or oleo-phobic properties. This technique has produces interesting results for synthetic polymers, but its translation to biopolymers has not been reported yet and requires further research efforts[141].

Protein coatings to enhance epithelization

Using one or several components of the BM to line the luminal surface of biomaterials favors epithelial cell adhesion, biocompatibility and impermeability by providing native anchoring sites[134]. Biomaterials obtained from decellularized ECMs, can be efficiently used as a coating since they retain the macro- and micro-architecture of the original native tissue, as well as their complex composition (**Fig.3**-bioactive surface). Fayon *et al.* studied the coating of human decellularized Wharton's Jelly—mainly composed of type I collagen—on an arterial substrate[135]. Seven days after EC seeding, the material showed good hemocompatibility and a density of cells 3 times higher than the control, a non-coated ECM-derived material. The complex biological composition combined to the native conformation of the components offered by the decellularized ECM coating efficiently improved the endothelialization. However, the technique remains far from being translated into clinical settings, since it relies on tissue banks, it requires facilities to perform cell culture and there because concerns over compatibility persist[135]. Single proteins extracted from mammalian ECM are already available on the market and constitute an interesting alternative. However, native proteins from mammalian ECM remains a relatively marginal strategy in the field of research dealing with biomaterials' coatings. The zoology of these proteins includes laminin (Ln), fibronectin (Fn), heparin (Hep) and type III and IV collagen (ColII, ColIV). Opposite to ColI, ColIII is not thrombogenic because it lacks the sites for platelets, while it still favors the adhesion of ECs. Hence its use as a coating on a scaffold, either synthetic or biologically-based, effectively promotes re-endothelialization[34]. Similarly, hyaluronic acid (HA), a polysaccharide, is widely used to prevent coagulation that contributes to hinder luminal re-endothelialization[142]. This trend is supported by Luo *et al.*, who used materials patterned with HA to study the synergic effects of several BM protein coatings[134]. Ln coating and co-deposition of Ln and ColIV demonstrate the lowest platelet

adhesion and activation, along with enhanced proliferation rate for both ECs and SMCs. For SMCs, the contractile phenotype was maintained, further inhibiting hyperplasia, whereas the control—a non-coated surface—induced a shift toward a flat phenotype. Cytocompatibility studies demonstrated the ability of Ln and Ln+ColIV to promote the release of NO, inhibit the adhesion of macrophages while maintaining their anti-inflammatory phenotype (M_2), which was further confirmed by *in vivo* studies. After 1-month dorsal sub-cutaneous implantation in rat models, substrates with coatings exhibited lower inflammatory response, with a fibrous encapsulation layer 2 times thinner than the control. What emerges here is that the use of a protein coating with a single component favors the endothelialization process, but the combination of several proteins mimicking the BM enhances its efficiency and boosts the proliferation of both ECs and SMCs. The remaining challenge of coatings is their application to tubular tissues, in particular in terms of their homogeneous application and controlled position at the lumen of the constructs.

d. Patterned luminal architectures to guide cellular behavior

Soft lithography

Contact guidance[143] induced by microtopography is based on a controlled arrangement of fibers or textural motifs (grooves and ridges) to guide and orient cells[109,149]. While the technique has mostly been applied to elaborate microfluidic devices, soft lithography can be transposed to larger biomimetic tissues with the purpose of promoting contact guidance (**Fig.3**-textured surface). This technique is particularly adapted for peculiar geometries such as those of the gut, featuring crypt and villi structures. Wang *et al.* used it to form thin membranes of type I collagen at 5 $mg.mL^{-1}$ from a PDMS mold with micro-well arrays[68]. *In vitro* assays resulted in surprising conclusions: a biomimetic topography is not necessarily required for intestinal epithelium reformation. Reproducing the depth of the crypt structures found in native tissues led to confinement of an intestinal epithelial cell line (Caco-2) and poor cell-cell interactions with delay in spreading and inhibition of their differentiation.

The difficulty to translate the soft lithography from planar to tubular geometry was overcome for the first time in 2016 with a synthetic polymer[144]. Topographical niches of 2 mm were created by thermal-based nanoimprint lithography method on tubular PDMS molds. These were dipcasted several times in poly(vinylalcohol) (PVA) cross-linked solution and dried to obtain the final scaffolds. Implantation in infrarenal aorta of rats demonstrated that patterned surfaces induce self-endothelialization and no patency, in comparison to unpatterned grafts that were occluded after 20 days. Use of soft lithography techniques in biomaterials research remains scarce, but the results suggest that this easy and effective route to guide cell fate deserves more attention from the community.

Electrospun fibers

Electrospinning is a widespread method to create porous biomaterials, with tunable properties such as the polymer composition, number of layers, their thickness, the fibers' diameter and orientation. These parameters result in a diversity of materials with variable porous network. Generally, the system is composed of a polymer dissolved in a volatile solvent dispensed through a needle, a high voltage source and a target. Polymer is electrically charged and extruded into thin threads through the needle, and collected on the target thanks to their potential difference. The obtained polymer meshes exhibit fiber diameters ranging from nm to m in dry state, since the solvent evaporates during the process[145]. The use of synthetic polymers still dominates the field, but a few biopolymers have been processed by electrospinning, including chitosan, native and degraded type I collagen (gelatin)[146], or biodegradable polymers such as polycaprolactone (PCL) and polylactic acid (PLA). They efficiently promote cell adhesion[147] by providing biochemical cues similar to the ECM. The versatility of electrospinning can generate entangled protein networks that mimic the native BM by co-electrospinning several biopolymers to obtain core-shell structures or by the creation of double-layered structures by successive electrospinning of different components or by patterning techniques[148,149]. Biological materials such as decellularized ECM (dECM) of bovine aorta can be incorporated into a polymeric solution and electrospun to form tubular constructs. This combination is beneficial to mechanical properties with the use of the polymer and to cell adhesion and proliferation through increased hydrophilicity by the dECM[150]. Electrospinning also permits to align fibers that guide cell growth, positively affecting spreading, differentiation and formation of typical elongated epithelial patterns[151]. Orientation of the fibers in aligned wrinkled patterns similar to the arterial lumen can orient endothelial cells growth while limiting platelet adherence and activation[91]. PLA/silk fibroin (1:1) scaffolds with longitudinally oriented nanofibers enabled the formation of a dense layer of HUVEC after 5 days of culture, with a spindle shape morphology parallel to the motif's axis. The resulting material can encapsulate signaling molecules and gradually release them to promote cell adhesion and proliferation[91,149], however, the intrinsically porous structure cannot avoid cell infiltration within the scaffold wall, hindering epithelium reformation. Reduced porosity specifically on the luminal surface can be engineered by adjusting the process parameters (polymer concentration, speed, distance to the mandrel and voltage). Porosity can be modified by additional post-processing steps, for instance by the addition of a supplementary coating, with the dual advantage of filling the pores and exposing a higher number of binding sites for ECs adhesion. Many examples in the literature feature an outer porous layer of PCL, HA or PLA combined to a smoother inner layer integrating collagen or derived components (gelatin[146,152] and recombinant human collagen[108]. In most cases, collagen is electrospun with other polymers or crosslinked in a second step to preserve the shape and porosity. Both conditions preclude collagen self-assembly into fibrillar structures, hindering the formation of the characteristic structures found in native tissues. Moreover, crosslinking steps require the use of harsh chemicals (genipin or carbodiimides) that can be detrimental to cell survival. Dems *et al* demonstrated for the first time that pure collagen could be electrospun without any cross-linker, by replacing the crosslinking step with an ammonia-rich atmosphere to induce self-assembly. The resulting self-standing flat membrane exhibited the typical characteristics of collagen fibrils found in tissues, *i.e.* the D-banding pattern observed under TEM corresponding to native collagen

fibrils and a bi-refringent signal under cross-polarizers demonstrating the existence of liquid-crystal like motifs[153]. Briefly, collagen was dissolved in a mixture of hydrochloric acid (3 mM HCl, pH 2.5) and ethanol (75 %vol) with a final concentration of 1.7 $mg.mL^{-1}$. Solvent was evaporated overnight at room temperature, and fibrillogenesis of the collagen molecules was performed in ammonia vapor for 20 minutes. Samples were rinsed in culture medium 3x/day for 10 days to remove all ammonia residues, before cellularization. Long-term cytotoxicity assay performed with normal human dermal fibroblasts showed that the membrane promotes cell spreading with clear stress fibers distribution in the cellular body and spindle-like shape morphology. Further investigations are needed to clarify if these interactions are equally found in epithelial cells and thus if electrospun collagen could be used to line the inner part of a tubular biomaterial.

The examples mentioned above illustrate the relevance of electrospinning as a cost-effective and scalable process to reconstitute partial organ structures from entangled fibers, able to influence cell movement, proliferation and phenotype by topographical and compositional cues. Although the field is relatively new, we anticipate that electrospun materials composed of biomolecules from the ECM will play an increasingly relevant role in the development of functional tubular tissues.

e. Advantages & disadvantages of each technique

We discussed above a selection of fabrication methods able to reproduce the luminal layer of tubular tissues, with a focus on biomimetic approaches, and how they succeed in promoting epithelium reformation. Three major pathways and types of surfaces stand out: (a) ECM-derived (b) bioactive and (c) textured, as illustrated in Figure 3. Additionally, we compared in detail the methodologies within these 3 categories to provide guidance in their elaboration and present the key challenges that still need to be addressed (Table 3).

Table 3. Comparison of various methods for biomimetic tubular tissue epithelial layer elaboration. Advantages and disadvantages as well as key literature references are given for guidance in fabrication.

Approach	Method	Advantages	Disadvantages	Key references				
				Vascular	Trachea	GI tracts	Esophagus	Urinary tracts
ECM-based surfaces	Autologous grafts or allografts	Native structure and composition.	The harvest might be harmful to patients. Its implantation is associated with biocompatibility issues, undesired physiological features (ex: hair growth on the oral mucosa), or availability dependency to tissue banks.	36	116	N/A	N/A	86, 87 All references in this section were previously gathered by Ławkowska *et al* in 2023[113]. To our knowledge, there is no tissue engineering approaches at the clinical level specifically targetting the urothelium of ureter.
	Pre-seeding	Reconstitution of a mature and permeable epithelium displaying the typical immunohistological characteristics. Possibility to vary the cell	Long procedures that requires a relevant cell source. Difficult to implement in clinical context.	N/A	125–127,154	130,132,133,155	128,129	156 References for the bladder, which possess the same urothelium as urinary tract: 120–

		source, either specific to tissues or undifferentiated.						124,157
Bioactive surfaces	Active biomolecules	Simple procedure to promote cell recruitment through the addition of signaling molecules. Treatment of the surface by plasma enhances cell adhesion.	Requires a precise control over the releasing kinetics and identifying the ideal cell seeding concentration. Plasma treatment is difficult to apply at the luminal surface and has not been translated to biopolymer-based tubular materials yet.	140	28,91	N/A	N/A	N/A
	Biomimetic protein coatings	Efficiently promote cellular adhesion and proliferation by a single protein coating. Possibility to combine several proteins for enhanced adhesion.	Difficulty to deposit a coating on tubular structures and ensure its maintenance to endure the physiological functions (flow and mechanical stress).	N/A	19,28,89–91,93,95	28,50	N/A	N/A
Textured surface	Soft lithography	Straightforward method to create and tailor geometrical patterns.	Surprisingly the biomimetic topography is not necessarily an advantage in the epithelium reformation, in particular for intestine. If the	144,150	N/A	68,158	N/A	N/A

			designed wells follow the native architecture, cells are confined and cannot restore junctions but such behavior could be related to the composition of the materials that can be processed by soft lithography.					
	Electrospinning	Easily scalable, possibility to create an entanglement of several components to mimic the BM. Provides a porous network compatible with drug eluting systems.	The porous network can induce cell migration into the scaffold, hence limiting the epithelium formation kinetics. The technique requires biopolymers that can be electrospun.	152,153	147,151,153	91,153	151	146,149,153

B. The muscular outer layer

Research in the field of tubular organs' replacement revolves around bioengineering approaches to recreate the muscular layer. This requirement is often complemented by an engineered epithelial layer using the strategies described above. A large array of techniques has been explored to develop scaffolds with adequate structural and compositional features, which are commonly divided into two main approaches: acellular or cellularized scaffolds. Cellularized scaffolds have the benefit of proposing "ready-to-use" materials, simplifying its application. Moreover, they can be considered as platforms to

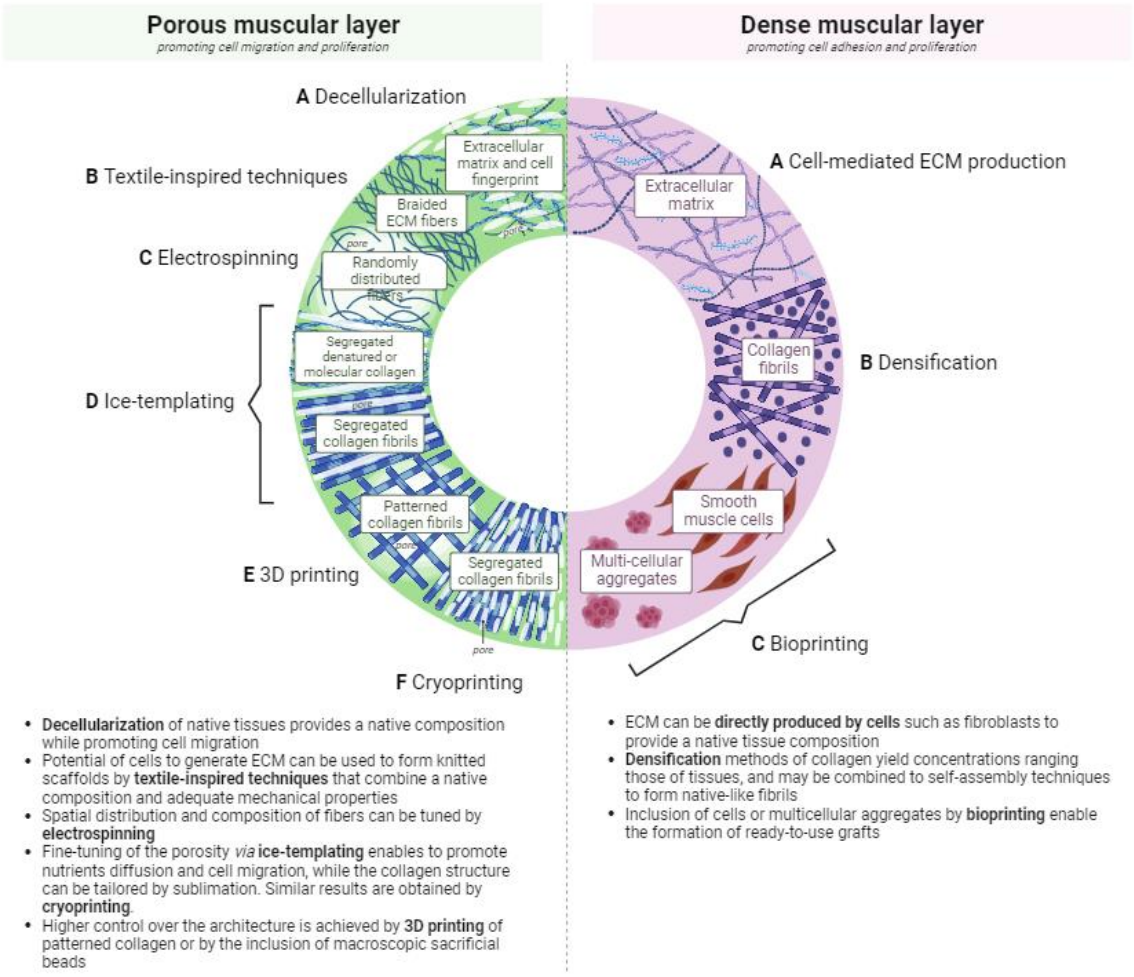

understand cell-material interactions and to study the materials' potential biointegration.

Fig. 4. Tubular tissue muscular layer recapitulation. Biomaterials can be reduced to two main pathways: *Porous* or *Dense*. Six techniques allow to generate porosity to promote cell migration including (**A**) decellularization, (**B**) textile-inspired techniques (**C**) electrospinning, (**D**) ice-templating, (**E**) 3D printing, and (**F**) cryoprinting. Three techniques allow to generate dense materials from biologically-derived components to favor cell adhesion and remodeling including (**A**) cell-mediated ECM production, (**B**) densification and (**C**) bioprinting.

However, they raise multiple issues regarding cell viability during processing, host cells compatibility and sourcing[159], and custody from fabrication to implantation. Although a few pre-cellularized muscular layer

models will be cited, this section will mostly focus on acellular scaffolds, in particular since these impose far less logistics hurdles. Acellular scaffolds rely on the assumption that the material will be repopulated by the cells of the host following implantation, either by means of a *porous* material facilitating cell migration, or via a *dense* material promoting cell adhesion and followed by material remodeling. The challenge of designing successful acellular porous scaffolds is to combine a porous network to promote cell migration, while achieving the required mechanical properties to restore the physiological functions. Dense materials offer a more complex composition, closer to native tissues, often integrating biologically-derived components such as cells, organoids or materials generated by cells[160]. The following sections aim at classifying the array of available manufacturing methods (advantages, disadvantages and challenges) to reproduce the muscular layer, illustrated in **Figure 4** and **Table 4.**

a. Promoting biointegration with acellular porous materials

Decellularized ECM providing a native composition

As discussed in the introduction, decellularization process enables to remove cellular components from a tissue, while preserving its micro and nano-structure, complex composition and eventually its mechanical properties[160]. Beyond mature tissues, embryonic and fetal-derived tissues may also be used for their ability to foster regeneration[161]. Decellularized chorion membrane shows encouraging results in arterial tissue regeneration[162]. Wrapping the decellularized chorion membrane into a tubular structure provides mechanical properties in the range of the saphenous vein and promotes ECs proliferation on the lumen. However, the exact reasons behind successful replacement using a certain type of decellularized tissue remain unknown. A striking example is allogenic decellularized trachea, which fails to replace itself whereas cryopreserved aortic allografts allow for complex tracheal and bronchial reconstruction[163]. Briefly, human cryopreserved (-80°C) aortic allografts are mounted on custom-made stents to prevent collapse, and transplanted into patients with severe cancers. Radical resections of the lesions were performed prior to implantation. The clinical study has been running for a few years, with now 44 patients treated with that technique. Other attempts of translational transplant have been done in arterial surgery using decellularized small intestinal submucosa (SIS), based on its high content in type I collagen (90 %). The local treatment of injured vascular tissues with SIS patches is efficient and shows good neovascularization and host cells infiltration[164]. However, if applied to larger structures such as a complete esophagus or an artery, it may lead to stenosis or thrombosis due to the loss of components during the decellularization process or to the thrombogenic effect of collagen in direct contact with blood[165]. To overcome the risk of blood clotting it is possible to seed endothelial cells at the luminal surface of the tubes to restore the physical separation between collagen and blood and thus avoid platelet adhesion[166]. To replace other tubular tissues, however, decellularized SIS matrices play an increasingly important role[39]. Pig-derived decellularized SIS has been tested for the reconstruction of the urethra of two patients. The follow up showed a continuous re-formation of the mucosa while the implants were progressively degraded. Post-operative assessment by intravenous urography at 12 months showed no anastomotic stenoses along the ureters[167].

Another strategy to favor the use of decellularized matrices in the context of tubular tissues' grafts relies on their application in presence of a stent. The use of stents reinforces the mechanical stability of the decellularized matrices and allows time for epithelial and muscular migration onto the cell-free scaffolds[168]. In this context the timing of stent removal has a strong impact on the scaffold cellularization and, more generally on clinical course after implantation[169].

Overall, using decellularized matrices offers suitable alternatives for a few tissues, providing native architecture and composition. However, the process involves high costs, may require several surgeries, and as for any biologically-derived tissue it raises standardization and industrialization issues[170]. Still, improvements of the regeneration process offer great perspectives. Optimization of the decellularization protocols to reach higher architecture and composition preservation rates is currently an active field of research with different techniques emerging rapidly[39]. The reduction of the number and the concentration of the chemical agents used for decellularization and the combination of physical and chemical treatments are the leading research avenues[24,168,171]. It would allow to extend the technique to more tissues, as urinary and GI tracts. Beyond the example mentioned above, urinary tubes are poorly studied despite the existence of extensive studies on the bladder—that holds comparable wall composition and architecture[172,173]. One of the most exciting challenges in the domain is to preserve intact villi in decellularized GI tracts, precluding the possibility for self-replacement. However, to the best of our knowledge, no reports have described the preparation of such a decellularized matrix[161].

Textile-inspired techniques

The use of textile-inspired techniques to mimic the architecture of native tubular tissues has attracted increased attention in the past decade. Zhang *et al.* proposed a fully reconstituted vessel, by combining electrospinning and braiding techniques[174]. Materials prepared from sequentially electrospinning silk fibroin (SF) and poly(L-lactide-co-ε-caprolactone) (PLCL) with a ratio of 30/70 were used to replicate the intima, while higher ratios of SF of 50/50 or 70/30 conveyed higher stiffness to replicate the media. The outer layer of the materials was composed of a braided silk fibroin structure to prevent wall rupture and to favor cell migration within the large spaces left between the yarns. The overall construct shows higher mechanical properties than native tissues, exhibiting a tensile strength of 5.5 ± 1.97 MPa and elongation at break of 3.34 ± 1.6 mm compared to 3.7 ± 2.0 MPa and 1.7 ± 0.7 mm for saphenous veins, respectively, for sample lengths of 1 mm. This outer braided membrane allowed for SMC percolation through the large pores, however SMCs seeding directly from the outside has not been studied.

More recently, the concept of textile-based biomimetic materials for vascular grafts has been extended to fully knitted collagen-based biomaterials[175]. Electrochemically aligned collagen threads were prepared by injecting a collagen solution (3 mg.mL^{-1}) between two parallel electrodes mounted on a rotating cylinder, and by imposing a constant electric potential (40 V) to induce the electro-compaction of collagen molecules into filaments (in the pH region corresponding to the isoelectric point). The obtained filaments were combined with PLA to improve mechanical properties and knitted into small-diameter vascular grafts using a circular-knitting machine. Porosity was optimized by adjusting the pull-down

tension and the number of filaments for a single thread. Using 3-ply threads (instead of 2-ply yarns) and imposing a higher tension by an increasing weight led to narrower pores. Mechanical properties were assessed and compared to pure collagen and PLA scaffolds. Both the bursting strength and suture retention strength of the hybrid vascular scaffolds were significantly improved compared to the pure collagen ones. Collagen incorporated in the matrix favored cell recruitment compared to pure PLA displaying more than 10 times the number of attached HUVECs, characterized by a more elongated morphology. Evaluation of the scaffold degradation evidenced a gradual loss of weight and tensile strength but displaying sufficient mechanical support at the early stage of cell recruitment, until the regenerated organ assumes this role. This same approach has been recently applied to fully biological knitted scaffolds. Magnan and colleagues developed a new kind of yarn by using cell-assembled extracellular matrix (CAM) sheets produced by normal adult skin fibroblasts[176] (Fig. 5). Tubular scaffolds could be directly formed by rolling sheets, or by slicing the CAM sheets into ribbons that were subsequently twisted into threads, dried, spooled and stored as ready-to use biological yarns. A weaving technique was implemented to obtain fully biological grafts, whose dimensional properties could be adapted to various assembling techniques (knitting, knotting, weaving or crocheting), leading to the presence of pores in between the yarns. The resulting material can endure surgical procedure and physiological pressure, with a suture retention strength and burst pressure of respectively 6 N and 6000 mmHg, compared to 1.4 N and 3000 mmHg for human internal mammary artery. These exciting performances correlate directly with the very dense collagen fibrils network composing the threads. TEM images show their arrangement in parallel bundles and the presence of the typical 67 nm striation of collagen, the hallmark of the physiological fibrillar structures in native tissues[177]. Furthermore, mass spectrometry identified 50 other components of the ECM in the CAM, propelling this material as one of the first biomimetic tubular graft from a compositional perspective. However, the concentration of the ECM components remains unknown. As a proof of concept, a tubular vascular graft was implanted in an ovine model, and even though fully *in vivo* results were not reported yet, suturability, arterial pressure resistance and transmural permeability were confirmed visually and by palpation[176].

1

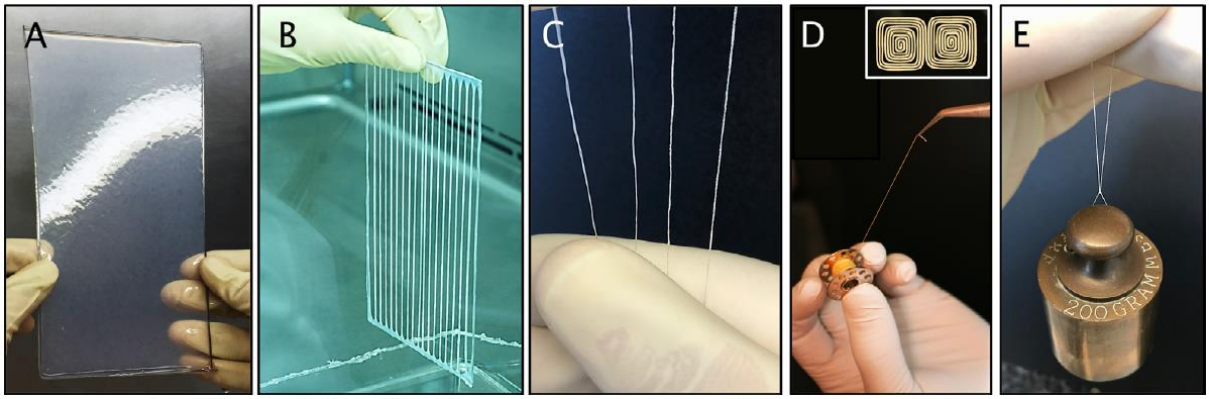

2

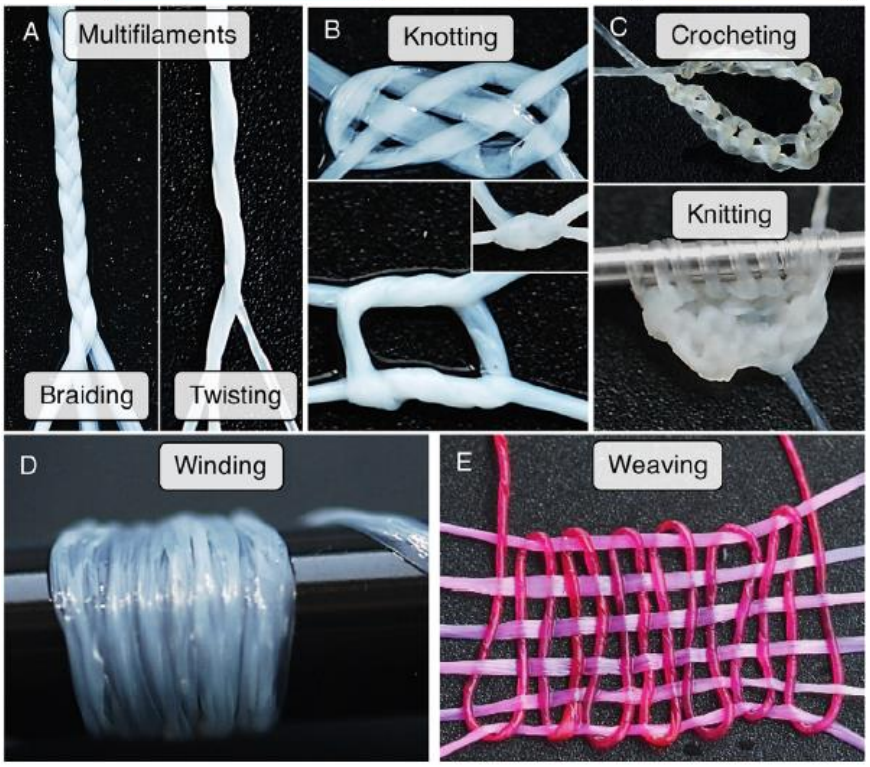

Figure 5. 1. Human yarn production. (**A**) A fresh sheet detached from the flask after 8 weeks of culture stretched over a frame. (**B**) Seventeen 5-mm-wide ribbons obtained by longitudinally cutting a CAM sheet. (**C**) Ribbons could be twisted to obtain threads. (**D**) One continuous 3-m-long ribbon was obtained by cutting a sheet in two connected spirals (inset). The biological yarn could be dried, spooled, and stored until needed. (**E**) A thread tied to, and lifting, a metal weight of 200g. **2. Human textiles.** (**A**) More complex yarn could be produced by braiding and twisting ribbons. (**B**) Complex or surgical knots could be tied and firmly tightened (inset) without breaking the yarn. (**C**) Crocheting and knitting could be used to produce complex structures. (**D**) One ribbon was wound around a mandrel to cover its surface. (**E**) A loose weave is shown with colored yarn to show the assembly principle. Six ribbons (light pink) were woven with a two-filament thread (dark pink). Images are reproduced from Magnan *et al.* [176]

The challenges of electrospinning labile biomolecules

As described in section *3.1.4.2*, electrospinning is a versatile method to elaborate different types of porous materials. Using electrospinning to reproduce the microenvironment around smooth muscle cells in the muscular layer of tubular tissues (*i.e.* highly concentrated collagen walls) is complex. The challenge arises from the use of harsh solvents from the dehydration occurring during the process. These parameters have a deleterious impact on the collagen ultrastructure, and need to be considered—and controlled—to elaborate materials that truly are biomimetic.

Most electrospun biomaterials combine biopolymers with synthetic counterparts to achieve a compromise between native biological properties and mechanical strength, respectively[175,178,179]. In particular, gelatin has attracted attention as a low-cost derivative of collagen. Lu *et al.* constructed a three-layered graft[180] composed of an inner PCL/ColI layer, a middle PCL-only layer and a PCL/gelatin outer layer. Spinning solutions were prepared at 10 %wt in 2,2,2-trifluoroethanol at a ratio of (3:1) for PCL/gelatin, and stirred for 24 h. Solutions were gradually spun on a rotating stainless-steel rod covered with aluminum foil, starting from the inner layer. After 4 h of electrospinning, grafts were collected and freeze-dried to remove the solvent. The addition of gelatin in the outer layer increased the hydrophilicity and the fiber diameter with respect to that composed of PCL alone. Although the mechanical properties of the composite material (maximum tensile stress and strain) were greater than those of native tissues (*n.b.* tensile testing was conducted in dry conditions and it is thus difficult to infer the material properties in physiological environment), neither the porosity nor the ability of SMCs to repopulate the scaffolds were evaluated. Despite the interesting properties and the layered structure that captures some features of native tissues reached by this material, questions remain regarding how closely gelatin allows to mimic the native ECM of tubular tissues. Gelatin is a denatured form of collagen as a product of hydrolysis or thermal denaturation, and it is associated with the irreversible loss of the triple-helix secondary structure[188]. The preservation—or not—of the secondary structure determines which recognition sites are accessible to antibodies. Cell-materials interactions are thus significantly different, and the use of gelatin may induce inflammation and fibrotic tissue formation[181]. Moreover, gelatin lacks the characteristic lyotropic properties of ColI and cannot form fibrillar structures, which are central building blocks responsible for the anisotropy of tubular tissues for the mechanical properties. In 2021 a review article quantified that 53 % of collagen-based electrospun scaffolds reported in the literature were produced exclusively out of ColI[182], the other 47 % being blended with mainly PCL[108,180,183,184]. A common step following electrospinning is the freeze-drying of the material to sublimate the solvent[136] and to obtain a foam or sponge. In the case of type I collagen, this process is known to result in decreased number of α-helices[185] and stiffening of the fibers[41]. The damaging effects inherent to freeze drying can be mitigated by optimizing the freeze-drying conditions (time, pressure, set temperature and temperature gradient)[186].

Choosing the most suitable solvent is also critical in retaining collagen ultrastructure throughout the process. Collagen has a poor solubility in the common organic solvents used in electrospinning, dichloromethane and chloroform, due to its hydrophilicity. Instead, fluoroalcohols are commonly used to dissolve collagen. However, Zeugolis *et al.* demonstrated that using this solvent results in the absence of triple-helix conformation and that the obtained materials exhibited a denaturation temperature lower

than fibrillar collagen, comparable to that of gelatin[187]. Resorting to fluoroalcohol-based dissolution created gelatin out of collagen, turning gold into lead. A few studies report the maintenance of collagen ultrastructure after electrospinning, by suspending collagen into acetic acid/DMSO at a ratio of 93/7[188] or 1,1,1,3,3,3 hexafluoro-2-propanol (HFP)[181,189]. Matthews *et al.* collected a concentrated solution of type I collagen (83 $mg.mL^{-1}$) on the mandrel after electrospinning from a short distance (125 mm between needle tip and mandrel)[189]. The short distance facilitated the collection of the spun fibers. Moreover, drying of the collected fibers could result in a concentration range that is comparable to that of native tissues. Cross-linking in presence of glutaraldehyde vapors for 24 h and rinsing in phosphate-buffered saline allowed to restore the fibrillar arrangement of collagen as confirmed by TEM observations, and the effective repopulation by aortic smooth muscular cells after 7 days. However, using cross-linkers results in a different fibrillar arrangement than *in vivo*. To avoid it, pioneering self-standing fibrillar pure collagen scaffolds without the resort to any cross-linker and polymer support were produced by electrospinning, depicted earlier for the recapitulation of the *epithelial inner layer*, page 28[153]. It demonstrates the relevance of electrospinning to elaborate fibrous biomaterials, however the process requires reaching native concentrations, lowering the toxicity by widening the range of solvents, and adjusting the porosity for increased cell migration kinetics.

Controlled porosity through freezing

The elaboration of multi-level hierarchical materials that offer pores, unaltered protein structure and concentration comparable to native tissues, combined with suitable mechanical properties is a gold standard that remains elusive. Freeze-casting or ice templating, is a mild process strategy initially used for the assembly of ceramic green bodies that provides excellent control over the porosity of the resulting materials. The technique has recently been transposed for the elaboration of biopolymer-based cellular architectures[190]. The principle is first to create pores *via* controlled freezing of the aqueous solvent, followed by a second step which consists in sublimating the formed ice crystals to reveal the macroporous structure composed by the solute. The physico-chemical parameters of the solution and the cooling system influence the initial freezing point. During freezing, at equilibrium, bulk water molecules converge to the surface of ice crystals (or nuclei), resulting in a gradual ice crystal growth. During this process, solutes are expelled from the growing ice crystals and concentrate between them[191]. Part of the water remains unfrozen and bound to the solute in a vitreous or glass-like phase[192,193]. Ice can adopt different morphologies that range from fully isotropic up to highly anisotropic lamellar crystals[190]. After sublimation of ice, the pores represent the negative imprint from such structures. As a consequence, the geometry, interconnectivity and orientation of the pores, as well as their size, can be tailored by adjusting the freezing process parameters. The ice growth mechanism is dictated by the thermal properties (thermal conductivity, cooling bath temperature and dipping speed on which depend the temperature gradient and the freezing front velocity), the design of the mold (shape[194], type of material and its thermal properties[195]) and the polymer solution properties (concentration, viscosity, particle size or molecular weight and carrier-particles interactions[196]). A straightforward parameter to tune is the cooling rate. A rapid cooling will translate into small ice crystals and symmetrical pores, whereas a slower cooling will

favor the growth of ice crystal along the vertical *c*-axis and yield to larger ice crystals[197,198]. To forecast the porous structure induced by thermal conditions in collagen samples, Cyr *et al.* created a theoretical model that is capable to predict the temperature fields and the corresponding ice growth[199]. The growth of ice-crystals can also be followed *in situ* to understand the impact of ice growth, using a confocal microscope set-up equipped with a cryoscopic stage a solution with a fluorophore[200]. Tailoring the porous structure enables to control the textural characteristics mentioned above. These parameters can be set to encourage cell infiltration and suitable mechanical properties for tissue regeneration[201]. Numerous methods have been developed to control ice formation and growth, including static copper platform[202], rotational freezing[196], controlled dipping[195,203], and translational plane freezing[193,204]. These methods offer to control the macroscopic geometry of the scaffolds (by the design of relevant molds) and, simultaneously allow for a fine adjustment of the macroporosity within the materials via a set of well-defined thermal boundary conditions. Beyond the elaboration of biomaterials, directional freezing techniques have found increasing relevance in the domain of cryopreservation[112]. A few techniques relying on cross-linking are worth mentioning for the ingenuity of the process, although these are not relying on ice-templating. Porogens may be integrated using for instance gelatin or pluronic F-127 as temporary beads to create pores or complex geometrical structures to support the collagen solution during solidification or cross-linking[205,206]. Foam technology is another efficient way to manufacture porous scaffolds by introducing nitrogen gas bubbles of various diameters in a solution, followed by cross-linking and degassing[207]. Finally, plastic compression methods have been explored to force molecules staggering and densify the material, resulting in increased mechanical properties[208].

The conventional method to sublimate ice crystals following ice-templating is freeze-drying or lyophilization, which results in porous dry materials named foams or sponges[209]. It was briefly introduced in the previous section as a possible additional step for solvent evaporation after electrospinning. However, it can also serve as a standalone fabrication process following freezing of a sample. The drying process can be split into two steps, primary drying (sublimation) and secondary drying (desorption). Yin *et al.* combined a simple ice-templating process and freeze-drying to manufacture highly porous chitosan stents for ureteral replacement[210]. Conductive molds were filled with 3.5% w/v and placed at -80°C to generate a radial bi-directional formation of ice crystals. Molds were subsequently removed and the samples were freeze-dried overnight. Structural analysis by SEM revealed an anisotropic arrangement composed of aligned lamellar pores radially oriented imposed by the mold's conductivity and the homogeneous thermal gradient. The same group of researchers investigated the influence of longitudinal versus radial freezing generated with PTFE or aluminum molds respectively, as well as slow versus fast cooling rate, on pore dimensions[211]. The lamellar spacing, pore area and wall thickness increased with both radial and fast freezing. Poor mechanical performances of the resulting porous materials were compensated by use of chemical cross-linking—a strategy that has equally been applied to collagen-based materials obtained by freeze-drying[212]. Collagenous biomaterials based on ice-templating and freeze-drying are currently used in the clinical, for skin wound healing (extensive burns[213], ulcers[214] and skin defects[215]), osteo-reconstruction[216] or dura matter repair[217].

The challenge after ice-templating lies in removing the ice-crystals by another means than freeze-drying, while inducing the self-assembly of collagen molecules into native-like fibrils. A recent study from Rieu *et al.* introduced for the first time the concept of topotactic fibrillogenesis for the self-assembly of collagen molecules[202]. The strategy is to trigger type I collagen fibrillogenesis after ice-templating, by combining two effects simultaneously: cryoscopic depression of ice in contact with a solute, and the physicochemical conditions (pH rise, ionic force change, etc) able to induce the self-assembly of collagen molecules into fibrils. By exposing the ice-templated scaffolds to ammonia vapors at 0°C, ice was allowed to slowly thaw while the increasing pH forced collagen molecules to form fibrils. Macroporous and anisotropic fibrillar collagen scaffolds were obtained, with regular ridges and pore size. Mechanical performances in the wet state were excellent compared to common cross-linking techniques and close to mammalian soft tissues (33 kPa). Normal human dermal fibroblasts and myoblasts demonstrate high bioactivity (cell adhesion, spreading and myotubes formation) after 11 days of culture without any additional physical, chemical or biological cues. Similar results were obtained on collagen matrices seeded with fibroblasts for 3D cell culture applications, allowing good proliferation and colonization 7 times further than in equivalent non-porous yet fibrillated matrices at day 28[110]. Moreover, the macroporous matrices presented high dimensional and compositional stability in long-term experiments, reaching up to 60 days of cell culture without noticeable changes. Recently, our team was able to transpose this approach to the fabrication of a variety of collagen-based biomimetic tubular tissues[195]. The ability to control the porosity of both the luminal surface and the muscular layer exclusively using type I collagen yields materials that can accommodate a wide range of cell types and that present elastic properties comparable to hydrated native arteries (from 10 to 58 kPa measured in longitudinal traction). Epithelial and endothelial cells were able to line the luminal side, whereas SMCs and MSCs could effectively migrate from the adventitial side to colonize the tubular sample. The exciting results *in vitro*, together with the mechanical properties and the recapitulation of the fibrillar structures found in native tissues, propel topotactic fibrillogenesis to the most promising strategy to combine with ice-templating for the development of biomimetic tubular tissues.

3D printing

Three-dimensional printing enables the manufacturing of a variety of biomaterials through a gradual building process using hydrogels that allow for geometrical, structural and compositional tunability. The three techniques commonly used are micro-extrusion, inkjet and laser assisted printing[218]. In the context of elaborating soft tissue biomimetic materials, one of the major concerns is to formulate hydrogels that combine printability and high resolution with biocompatibility. Adequate rheological properties of the hydrogels (or of the respective ink prior to hydrogel formation) are central to do so, and include shear thinning, yield stress, viscosity and molding ability. The shear-thinning behavior is characterized by a decrease in the viscosity at high shear ratios, which encompasses a transition from a high-viscosity gel to a low-viscosity fluid during printing. It is followed by a rapid restoration of the gel state to maintain the structural integrity. For each printer-hydrogel combination, the parameters must be carefully adjusted to optimize the structural characteristics of the resulting printed biomaterial. These adjustments include

tuning the molecular weight and concentration of polymer, add modifiers, or modifying the bioprinters parameters such as the speed, layering, needle size, among others[219]. Differently from synthetic polymers, ECM-derived bio-inks are studied to optimize the cellular microenvironment and to avoid eliciting an immune response. These factors are deemed essential to promote tissue growth in newly engineered organ[220,221]. It is expected that 3D printing may tackle the issues related with direct implantation of decellularized ECM, by modulating the structure and mechanics of the materials while preserving the native composition. As already mentioned, various sources of ECM are decellularized and processed into inks, mainly from porcine tissues[221]. One interesting feature of 3D printing is the possibility to perform dual printing and combine several tissue types, as well as to integrate cells

Formulation of dECM bioinks is also investigated for gastrointestinal tract from porcine small intestinal submucosa[222]and urinary tract[223]. To our knowledge, dECM bioinks formulated for vascular tissues are poorly explored[224]—although a few researchers studied the mix of alginate with dECM[225,226]—or rather focused on cardiac tissues[227].

A significant body of work has been devoted to the elaboration of collagen-based bioinks. The major concern with these is their low mechanical properties during the printing process that require additional support to stabilize the printed geometry. To do so, collagen can be printed in molds that are subsequently removed[195], by using printing baths[228,229], or cross-linked following printing[230–232]. An interesting alternative to chemical crosslinking is to increase the ink viscosity by associating it to other biologically derived components (chitosan[233] or gelatin[234]) or by increasing its concentration[235]. However, according to Osidak and co-workers, 90% of the studies carried out on collagen 3D (bio)printing until now use concentrations limited to 10 mg.mL^{-1}. These values lay substantially below the concentration of collagen in tissues and fail to provide suitable gel stiffness to ensure geometric fidelity of the printed structure[236]. To tackle this shortcoming, Nociera *et al.* reported the formulation of a collagenous ink at 60 mg.mL^{-1} of lyophilized collagen in PBS, prepared at pH 7[237], that exhibited high viscosity and shear thinning behavior. The low resolution imposed by the high viscosity was skirted by delay times in-between each layer. Two different fibroblastic cell lines demonstrated good adhesion and proliferation on (and later within) the macroporous 3D constructs obtained with a viability of 70%. Another approach was developed by Camman *et al.* to model skeletal muscle ECM, where the acidic solvent of a collagen solution was evaporated until the solution reaches a concentration of 30 mg.mL^{-1}, [238]. This approach avoids damaging the collagen during the drying step of freeze-drying while still reaching the suitable rheological properties to allow its use as an ink. 3D matrices were printed with a porous architecture (pores of 100 m). Due to the shearing effect during printing, collagen molecules aligned along the direction of printing when conducted directly in a PBS (5X) bath—to ensure both the geometry stabilization and the collagen fibrillogenesis. Additional channels of 600 m were created by adding needles in the printed matrix after 30 min fibrillation. After 24 h, an ammonia vapor bath was applied to consolidate the fibrillogenesis and increase mechanical properties. The measured Youngs' moduli ranged from 8 to 25 kPa, which are in the same order of magnitude as that of native ECM. Along with the nutrients' supply provided by the porous network, the matrix stiffness induced the formation of myotubes inside the channels after the seeding with C_2C_{12} muscle cells in Matrigel®. Finally, a recent

work may be mentioned for the interesting processing method that it proposes. Named drop-on-demand (DOD), it can effectively generate porosity in a collagen matrix by printing drops directly inside the hydrogel and remove them after stabilization of the structure[239]. Although the two last techniques mentioned above have not been transposed into the elaboration of tubular tissues, they provide important leads to further develop of biomimetic tubular tissues via 3D printing. An emerging technology named 4D printing could also bring additional properties that enable the formation of tubular structures. The technique relies on the printing of materials with shape-memory properties that respond to external stimuli. The triggers can be either light, temperature or magnetic field, to induce swelling, curvature, self-assembly or disassembly. These features could bring dynamic performances to biomaterials, an interesting perspective to better mimic native tissues[240].

Cryoprinting: coupling 3D-printing and ice-templating

3D printing and ice-templating have been combined to create cryoprinting (also named ice-printing) for the first-time in 2015 by Adamkiewicz and Rubinsky using liquid nitrogen[241], using home-made printing and cooling systems[242]. A custom cryogenic platform was mounted in place of the original printing stage and maintained at a constant temperature and controlled humidity, generally with liquid nitrogen. The substrate was able to move in the Z-axis while the printer head could move in X-Y axes. The molten material was gradually solidified during deposition, forming a well-defined and tunable frozen structure. On the one hand, 3D printing allows to control the macrostructure and adjust the composition of the printout with several inks or cells. On the other hand, the freezing events allow to fix the printed geometry and to form macropores inside the walls, adding a supplementary hierarchical level at the cell length scale. The main challenge with cryoprinting is to find a solvent able to both dissolve the solute and freeze within the temperature range reached by the modified printer, generally between 0 and -80 °C. Ice might also be used as a sacrificial platform or mold,[243,244] instead of a way to create pores. Studies started with synthetic polymers such as PLLA[245], polyhydroxymethylene and polyvinyl carbonate[246], but the field is likely to be extended to biologically-derived material. A few studies have already explored these with coaxial cryoprinting of a core-shell structure using alginate and PCL, respectively[247], or PCL only dissolved in glacial acetic acid[248]. Several set-ups have been reported as suitable for cryoprinting, including printing in a cooling fluid[241], in a cryogenic chamber with liquid nitrogen-filled walls surrounding the printing stage[243], or atop different cooled platforms (provided with a solid CO_2 in isopropanol reservoir[246,249], an inner circuit filled with alcohol at -20°C[247], or simply a cooled copper plate[244]). Removal of ice while preserving the porosity has been done by phase separation based on DMSO polymeric solution/water bath interactions[246] or by standard freeze-drying[247,248]. The cryoprinted materials exhibit a well-defined structure providing different levels of organization, proven to enhance cellular proliferation compared to traditional printed technique[248], especially if using additional biocompatible fillers such as crosslinked gelatin nanofibers[246]. Considering the narrow research field of cryoprinting, type I collagen has taken very little attention. Concentration of 4.5% w/v in acetic acid was used by Kim *et al.* on a home-made set-up named "3D plotted system" that was basically a 3D printer equipped with a cryogenic stage, to create squared porous samples[242]. After freeze-drying, authors

investigated the structural features and mechanical properties, and the influence of process parameters on the obtained materials. Extensive research using cryoprinted collagen combined to softer fibrillogenesis methods, as detailed in the previous section, seems promising in the field of tissue engineering.

b. Dense materials promoting cell adhesion and material remodeling

Cell-mediated ECM shaped into dense tubular structure

Some cell types are able to produce ECM under adequate culture conditions. This property has been exploited to produce cohesive cell sheets both *in vivo*[250] and *in vitro*[176], to engineer epithelial layers as discussed above and larger 3D structures. These sheets are comprised of living cells in a complex mix of biological material, which can be detached from the culture plate for further modeling. Methods to shape these sheets into thick tubes include wrapping[251], layer-by-layer assembly[30], ring-stacking[252] and textile-inspired techniques[176] (read section *3.2.1.1* for more details). Most cell sheets are generated *in vitro* for practical reasons, but it is also possible to generate matrices by relying on the capacity of living tissues to generate biological substrates. Yamanami *et al.* implanted molds sub-cutaneously in dog dorsal skin for 4 weeks, and obtained tubular connective tissues after harvesting[250]. However, this technique is ethically questionable in an industrial context in view of the current regulatory framework. Aside from commercialized commodity, cells can also be sourced directly from patient biopsies and expanded *ex vivo*. This was demonstrated for the first time by L'Heureux *et al.* who fabricated a biological and clinically effective material from autologous cells for small-diameter arterial replacement[253]. They used fibroblast-derived ECM sheets, which were simply wrapped around a temporary Teflon®-coated stainless-steel tube. After a maturation step of 10-weeks, layers were cohesive and formed a homogeneous tissue. The final material was fabricated with two thick layers based on this method. A living cell sheet was used as the external layer to provide stiffness while the middle layer consisted in a decellularized sheet to limit cell migration towards the lumen. Finally, ECs were seeded on the luminal side to form the endothelium. The final material was proven non-thrombogenic and featured mechanical properties in the range of native tissues *in vitro*. *In vivo* experiments in rat model confirmed the ability to regenerate an endothelium displaying a barrier function, promote SMC infiltration, and reform the characteristic *vasa vasorum* and the basal membrane. The materials thus seem to be able to replace arteries from autologous cells, but result in a particularly lengthy process. Another study succeeded in shortening the fabrication time by simplifying the model to directly produce a contiguous bi-cellularized sheet containing both SMCs and fibroblasts[254], and which can be further rolled. Biological properties were not assessed but the mechanical properties were higher than the standard association of two different cell line sheets, including burst pressure and linear modulus, enabling the material to sustain physiological vascular pressures.

A different study has focused on optimizing the balance between two cell lines, using a hybrid technique that combines sheet-stacking and reseeding[255] for urethra replacement application[256]. This method enables to solve the common unbalanced properties of cell-generated matrix, which provide adequate

mechanical properties but do not preserve the epithelial layer barrier function. In the case of urethra, it is crucial to avoid inflammation and fibrosis originating from urine extravasation. Two cell sources of fibroblasts were investigated to produce the stroma, vesical fibroblasts (VF) to support epithelium formation, and dermal fibroblasts (DF) to improve mechanical properties. These were used either as a single source, or mixed in various ratios (VF only, 90/10, 80/20, 70/30 corresponding to VF/DF, and DF only), and their impact on urothelium formation from seeded urothelial cells (UCs) was assessed. For the study, both fibroblasts and epithelial cells were extracted from human bladder biopsies, which provide similar UCs while avoiding the significant co-morbidities associated to urethral biopsies. Fibroblasts were seeded with ascorbate on well plates and cultured for 28 days with a reseeding at day 14 to obtain neosynthesized ECM sheets. After sheet stacking, the stromal sheets were subsequently seeded with urothelial cells. After 7 days, the substitutes were detached from the bottom of the plate to reach the air-liquid interface and induce mature urothelium differentiation. The final structures demonstrated that high concentrations of VF (80 to 90 %) significantly improve impermeability towards urea, mechanical properties, and the near-restoration of the endothelium and basal lamina. Interestingly, villi were observed for all samples comprised with VF. Tubularization of the flat materials was not tested as the common grafts implanted for urethroplasty are flat.

Instead of wrapping a single layer around a tube, multiple cell layers can be assembled by a layer-by-layer (LbL) process[30]. 3D dense tissues with high cell density are built by gradually overlaying multiple SMC layers from previously expanded SMCs brought to confluence. Between each deposition, a thin coating of ColI was applied to favor attachment between adjacent layers. After one week, a five layers-tube was fabricated, exhibiting elongated SMCs aligned in the direction of the microchannels. After two weeks, the thickness of a human coronary artery could be reached, corresponding to the equivalent of 10 assembled layers. Optimization of the technique was proposed by Xu *et al.*, who directly produced tubular material from cell expansion[257].

Patel et al. developed a ring stacking method to generate biomimetic arterial *tunica adventitia*[252]. Tissue rings were self-aggregated around center posts and stacked into a tubular structure. The base plate was fabricated using PDMS posts, coated with fibrin gel only (20 $mg.mL^{-1}$) or a combination in various ratios of fibrin and collagen (0.7 to 2.2 $mg.mL^{-1}$) . Expanded human dermal fibroblasts (hDF) were then seeded onto the posts and cultured for 7 days. Stimulation of the collagen production was not only explored through the supporting matrix, but also by continuous additions of factors. These cytokine stimulating agents included TGF-β, ascorbic acid (AA) and combinations of both at various timepoints. At day 7, the self-assembled fibroblasts mediated rings were removed from the plates and 6 of them were placed around a rod. Cohesion of the overall tubular construct was ensured by a simple sealing of the rings with fibrin glue composed of fibrinogen and thrombin, enabling the use of the grafts after 8 days only. The continuous stimuli by cytokines promoted collagen production associated with a significant increase in the mechanical properties. In particular, the combination of TGF- β and AA resulted in the thickest ring and highest cell density, associated with the highest elasticity, ultimate tensile strength, and failure strength. Compared to rings supported by fibrin alone, fibrin-0.7 $mg.mL^{-1}$ collagen mediated rings were significantly denser, with twice as much collagen content. The cell density was continuous along the

tube that demonstrated good cohesion in between the rings. The same method was applied to SMCs with the intention of forming a tubular muscular layer[258], which could be integrated as the *tunica media* for arterial replacement, or may be used alone for other tissue types. Versatility of the layering method allows to use various type or cells, orient cells differently for each layer or create various topographies. Xu *et al.* have illustrated the advantages of the technique by producing an arterial outer layer featuring helicoidally-oriented SMC, reproducing the native arrangement of muscular cells in the native tissue[257].

The cell-sheet engineering research community has mostly focused on vascular applications, hence the results presented here are mostly driven by this final application. However, similar techniques are used for other tubular tissues and a few examples are reported for each in **Table 4.**

Densification of collagen

Most tubular scaffolds fail to reach the concentration of ColI in native tissues. To address this issue, Justin *et al.* developed a densification method that generates a new type of highly concentrated collagenous tubular materials[259]. The resulting tubes are seamless, provided with relevant mechanical properties and display homogeneous fibril density along the tube. The authors used a funnel-shaped chamber composed of a central rod and an outer mold, laying on hydrophilic porous nylon membranes on top of paper-towel. Gradual withdrawal of the water from the bottom combined to water repelling from the pores thanks to collagen contraction anchorage in the membrane, enabled to reach a collagen concentration ranging from 120 to 190 $mg.mL^{-1}$, depending on the initial concentration and volume. Second harmonic generation (SHG) images revealed a network of collagen fibrils and fibers aligned along the axis of the walls. Upon crosslinking with genipin at low concentration (1 mM) the resulting materials displayed a 2 to 3-fold increase in tensile strength. The method has proven efficient in directly integrating cells and maintaining their viability and, more interestingly, in tailoring the cells' spatial distribution both for single and multiple-cell type experiments. This versatility may allow to recreate the distinct cellular spatial configuration of the aorta with endothelial cells in the luminal part and smooth muscle cells on the outer part for instance. Additionally, the central rod surface can be tailored to resemble native luminal patterns such as the wavy motifs of arteries of the crypt-villi texture of gastrointestinal tracts.

Another study developed a micro-fluidic device to extrude collagen sheets and increase collagen compaction[260]. The principle lies in the co-extrusion of a collagen solution in between two layers of a flow focusing buffer (FFB) inducing pre-fibrillogenesis (Fig. 6). Collagen fibrils are aligned in the direction of the extrusion by a continuous strain using a rotating mandrel, followed by a buffer bath to complete fibrillogenesis. Collagen solution was prepared by dissolving lyophilized ColI in deionized water at a concentration of 5 $mg.mL^{-1}$, and the FFB was composed of PEG and salts. An adjustment of the pH to 8 promoted the self-assembly of collagen molecules by increasing the pH close to their iso-electric point (*ca.* 7.4) and enabling increased hydrophobic interactions between the molecules. PEG, a crowding agent, was used to favor the expulsion of water by providing a hypertonic environment. Additionally, collagen sheet was strained by a rotating mandrel over which it passes to induce fibril

alignment, and fibrillogenesis was then completed by a buffer solution bath for 48 h. Finally, the sheet was washed and dried to increase compaction. Through shear, strain, macromolecular crowding and evaporation, this device enables to produce highly concentrated collagen layers with a native-like ultrastructure. Ability of the material to support cell proliferation was evaluated using ECs and SMCs, and influence of the degree of fibrillar alignment controlled by the extrusion speed was explored. Coordinated vasoconstrictive and vasorelaxation responses were only observed for co-aligned SMC-sheets, providing higher contractile and residual stresses. This approach proposes unprecedent features of native collagen found in the ECM, *i.e.* high compaction and native ultrastructure, while being an easy and fast process.

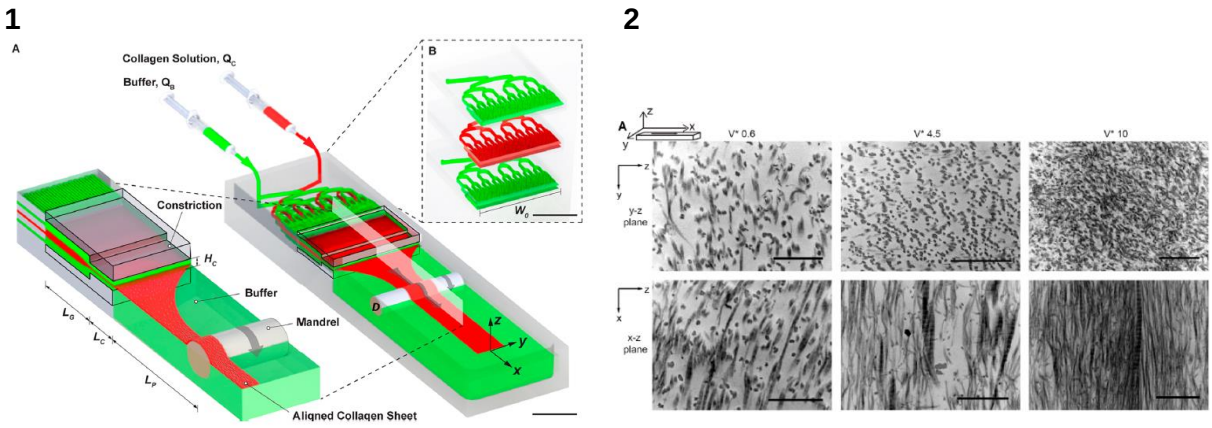

Figure 6. 1.A) Schematic of a biofabrication approach for continuous formation of ultrathin collagen sheets. Collagen (red) and buffer solutions (green) are delivered to a three-layered microfluidic device. A collagen sheet emerges at the device exit, hydrodynamically focused between buffer solutions, and guided through a geometric constriction. The emerging collagen sheet undergoes fibrillogenesis and further strain by passing over a rotating mandrel. Continued incubation, washing and drying results in the production of multicentimeter-wide, meter-long, ultrathin collagen sheets. (**B**) Focus on the three-layered microfluidic device containing hierarchical microchannel networks. Scale bars (A and B) 10 mm. **2.** Nanostructure and molecular features of collagen sheets, imaged by TEM, and produced at V* = 0.6, 4.5, and 10 in (y–z) and (x–z) planes. Image retaken from Malladi *et al.* [276]

Loy *et al.* developed a novel technique based on a rotational bioreactor that expels water and densifies collagen to produce tubular scaffolds[261]. The method consists in filling a tubular mold with 2 mg.mL^{-1} ColI solution, dissolved in acetic acid, Dulbecco's modified Eagle's medium (DMEM), NaOH and Hepes to induce fibrillogenesis. The outer mold was further removed to place the matrix on a homemade rotating bioreactor in an incubator at 37°C for 1 h. Rotation enabled to align fibrils in the longitudinal direction while expelling water. A four-fold increase in concentration was measured, resulting in significant improvement in the mechanical properties. The possibility to incorporate cells in the process was evaluated using fibroblasts, and demonstrated steady cell viability before and after rotation. This versatile technique is particularly adapted to prepare tubular matrices. Moreover, it allows for the assembly of biomimetic components of the ECM into hierarchical or multi-layered structures capable of hosting various cell types.

Collagen as a bioink to generate cellularized tubular grafts

In parallel with the control over the geometry of the printed objects, the possibility to use biomimetic components as printing inks and the capacity to co-print different compositions, 3D printing has the ability to directly integrate cells during the fabrication process, a now widespread technique called bioprinting[29]. Bioprinting enables to incorporate cells in a hydrogel with a precise control over their spatial distribution in a material. For tracheal tissue engineering, it opens up an exciting opportunity to create alternating rings of tissue-specific bioinks that promote either cartilage (C) or vascularized fibrous (VF) tissue regeneration[262]. Photocrosslinkable inks were developed by incorporating cells into dedicated ECM-derived inks both sourced from pigs. For the C-ink, chondrocytes were loaded in a hydrogel composed of methacryloyl-modified gelatin, chondroitin sulfate, and cartilage acellular matrix. For VF ink, fibroblasts were loaded in a vascularized fibrous tissue bioink composed of methacrylate-modified hyaluronic acid, 8-arm-polyethylene glycol-succinic acid ester (8-PEG-NHS), and methacryloyl-modified dermal acellular matrix. Upon photo-initiation, the temperature-sensitive C ink became stiffer while the highly viscous VF ink remained soft, forming a stiff-to-soft ring staggered structure. Seamless interfacial fusion of adjacent rings was ensured by amidation of the 8-PEG-NHS. The resulting tracheal analogs demonstrated good mechanical properties and suitable cellularization. The alternating structure, with cartilaginous and vascularized fibrous tissue rings, offers a combination of mechanical resistance (compressive resistance, tensile and bending ability) and sufficient nutrients supply. It enabled the restoration of its functionality following tracheal implantation in a rabbit model. Using a comparable approach, Nam *et al.* proposed a modified bioprinting set up for esophageal reconstruction, with an inner mucosal layer and a muscular outer layer[263]. The main difference relies in the possibility to create pores in the material to favor cell migration. To achieve this, the authors developed a dragging technique able to print altered lines with adjustable width and pore size in a single step. The resulting esophagus mime facilitates cell proliferation thanks to its multilayered porous structure, as confirmed by *in vitro* experiments using SMC.

The central challenge in bioprinting is to ensure the survival of cells, which face confinement in the syringe as well as exposure to isostatic pressure and shear forces during printing. Through modulation of the type, source and density of cells, diverse heterogeneous constructs can be fashioned to mimic various native tissues, for instance arterial tissue by combining human aortic SMCs and HUVECs[264].

Diamantides *et al.* studied cell viability and activity using chondrocytes in a 8 $mg.mL^{-1}$ type I collagen bioink directly after bioprinting, and up to 14 days[265]. Assays demonstrated cell viability over 90% from day 0 until the end of the culture period. By day 11, noticeable shape retraction of the matrices was observed, highlighting the biological activity of cells but also the insufficient collagen concentration to ensure dimensional stability. Authors also demonstrated that cell density impacts rheological properties of the bioink. The shear-thinning behavior was steady across all cell concentrations, however increased cell density led to higher storage modulus prior to printing, but reduced moduli in the gel state (following printing and gelation at 37°C). The introduction of cells into the ink also led to improved resolution compared to acellular ink, resulting in reduced dot footprint and narrower line widths. However, as rheological properties depend on the cell type due to variations in cell size and their

interactions with the chosen hydrogel, these findings should be taken cautiously. Multicellular spheroids may also be used instead of single cell lines to replicate the native cellular population[266].

The examples just above point out to the relevance of collagen as a bioink in terms of cell viability. This same argument has equally drawn attention in the context of tubular tissue applications [267]. Nevertheless, collagen-based bioinks often require pre- or post-processing: either a crosslinking step, lyophilization prior to dissolution[268], or a modification of the composition by the addition of components that are not part of native tissues such as alginate, methacrylated gelatin, PEG or PCL[269]. These changes participate to increasing the mechanical stability of the printed constructs and, in most cases, to lowering the cost of fabrication and explain the scarcity of research projects focusing solely on pure collagen[270].

Rué *et al.* developed a core-shell structure composed of an inner alginate-ColI-HUVECs layer and an outer ColI-human aortic SMCs layer using a triple coaxial nozzle to mimic arteries[264]. For the luminal layer, HUVECs were simply suspended at a density of 15.10^6 cells.mL^{-1} in a 5 mg.mL^{-1} collagen solution. For the outer layer, SMC were encapsulated at a density of $10x10^6$ cells.mL^{-1} into a solution of alginate (2%wt) and collagen (3 mg.mL^{-1}). The two layers were co-printed with a central pluronic F-127 ink to create the lumen, directly in a Ca^{2+} solution at 37°C. Maintenance and stiffening of the scaffolds were secured by calcium ions that induced alginate crosslinking, and by the increased temperature that induced collagen gelation. Pluronic support was dissolved in water for co-culture of the scaffold over 14 days. The shear stress exerted during the process had no detrimental impact on cell viability and, by the fifth day, HUVECs had formed a monolayer whereas SMCs displayed a rounded morphology that deviated from the native contractile phenotype. The differences in behavior may be attributed to the lower collagen concentration in the outer layer. However, SMCs exhibited a diagonal-perpendicular alignment akin to the perpendicular alignment observed in native arteries. Another interesting result was that cells did not intermingle and remained in their respective layers. The comparable results obtained with dECM and ColI suggest that the single component ColI bioink could be advantageous[226]. A similar co-extrusion method increased mechanical strength by using eight-arm PEG acrylate and gelatin methacryloyl rather than ColI[271]. The scaffold effectively promoted bladder urothelial cells proliferation and urothelium reformation in the inner layer, meanwhile on the opposite side cells expressed α-smooth muscle actin, the predominant isoform in vascular smooth-muscle cells which plays a key role in fibrogenesis.

In a study by Kim *et al.*, the authors prepared a gastrointestinal model by loading cells into a pure collagen scaffold through bioprinting and crosslinked wih tannic acid (TA)[272]. To prepare the tubular construct, a 4%wt collagen bioink was loaded with HUVECs in the shell layer and with Caco-2 (epithelial) cells in the core layer, both at a cell density of $5x10^6$ cells.mL^{-1}. The high amount of added TA enabled to precisely build a stable intestine-like architecture and to obtain micro-vascular structures with the shell ink, while lower quantity of TA in the core ink ensured a good coverage by Caco-2 cells. The resulting co-cultured scaffold presented outstanding structural similarities with GI tracts, and the presence of the capillary network increased cell proliferation, enzyme expression, and barrier function.

Post-fabrication perforation to enhance dense materials biointegration

Alternatively, enhancing cell migration in a scaffold may be done by generating porosity with a post-fabrication perforation. A method was introduced by Marzaro *et al.* for esophageal replacement, using a patented microscopic robotic perforator. After decellularization and removal of the submucosa and mucosa of a porcine esophagus, the remaining muscular layer was perforated with a 150 m needle. An algorithm controlled the regularity of the pattern, to obtain about 1200 pores/cm² and a pore size ranging from 80 to 100 m with a similar interspace. The scaffold dimensions, thickness and ECM architecture were preserved, and no burns or damages of the connective tissue were observed. After culturing autologous bone marrow-derived mesenchymal stromal cells for 10 days, SEM images showed that cells adhered and diffused in the inner and outer layers of the scaffold. *In vivo* studies using pigs evidenced that after 3 months, the muscular layer was regenerated for pre-seeded scaffolds, while it was not the case for non-seeded scaffolds. However, half of the pigs suffered from non-practicable stricture in both groups, and substenosis occurred at a higher rate with pre-seeded scaffold[106].

Cell ingrowth can also be enhanced through laser micro-perforation, as demonstrated by Xu *et al* [273]. Trachea matrices were perforated with a laser, optimized to find the right balance between pore dimensions and structure conservation. Such parameters included output power, pulse width, and number of cycles. The resulting lattice-arranged conical pores were spaced 1 mm apart, with a maximum pore size of 800 m, and no significant damage on the ECM was evidenced by H&E staining. Pores enabled a rapid and efficient decellularization, and the interconnected network facilitatds infiltration and proliferation of chondrocytes in the micropores and bilateral surfaces. *In vivo*, after 3 months implantation on porcine models, this rapid cell infiltration led to a regenerated cartilage twice as thick as for a native trachea, and with higher mechanical strength.

c. Advantages & disadvantages of each technique

In this section, we described various fabrication methods to reproduce the muscular layer of tubular tissues with a focus on pure type I collagen materials. We identified two main approaches, either *porous* materials facilitating cell migration or *dense* materials promoting cell adhesion and matrix remodeling, illustrated in **Figure 4** and detailed in **Table 4**.

Table 4. Comparison of various methods for biomimetic tubular tissue muscular layer elaboration. Advantages and disadvantages as well as referenced research work are given to provide guidance in its fabrication.

Method	Advantages	Disadvantages	Ref. for the circulatory system	Ref. for trachea	Ref. for GI tracts	Ref. for esophagus	Ref. for urinary tracts	Non-tissue specific
Porous materials								
Decellularization	Preservation of the native tissue architecture and composition	Materials are not always compliant, fail to reach mechanical properties comparable to native tissues.	165,166,171,274,275	163	276,277	278,279	Bladder: 280	N/A
Textile-inspired	Composition similar to the ECM, tunable geometry.	Long process to obtain the threads or ribbons. Compliance not suitable for physiological function.	175,176,281	N/A	N/A	N/A	N/A	N/A
Electrospinning	Easily scalable, possibility to create an entanglement of several components, tunability of the porous network (size, orientation, interconnectivity).	Difficulties to electrospun pure collagen and maintain its native structure throughout the process. The solvents, drying, freeze-drying, and/or cross-linking can induce collagen denaturation or limit the molecular self-assembly.	108,179,180,184	N/A	282	N/A	146	153,178,189
Freezing	(a) Freeze-drying	(a) Freeze-drying	283	(a) 284,285	(a) 286	(a) 287	(a) 210	(a) 190,209,211

techniques	Easy and tailorable process to generate porous structures, with pore size suitable for cell colonization. (b) Topotactic fibrillogenesis Porous network combined to dense collagen walls with a native-like fibrillar ultrastructure.	Weak mechanical properties associated with walls too thin to support SMCs colonization and contraction. Additionally, collagen is not in a fibrillar form, requiring chemical cross-linking. (b) Topotactic fibrillogenesis The competition between the kinetics of ice thawing and collagen self-assembly may lead to pore size and volume reduction. Recent method, with no *in vivo* results yet.						(b) 202
3D-printing	Tunable geometry, possibility to use several inks in the same material to create layers or rings.	The bioink should enable high resolution printing, and adequate mechanical properties that are often yield by using cross-linkers. The high viscosity of dense collagen also hamper printing in the	225,226	262	222	263	223	221,237–239,275

		physiological concentration range.						
Cryoprinting	High-resolution fabrication technique, enabling to tune the porosity, the number of layers and the complex composition.	Requires to build a homemade set-up controlling both temperature and humidity to ensure printability. Removal of ice without compromising the printed structure is challenging	N/A	N/A	N/A	N/A	N/A	241–244,246–249
Dense materials								
Cell-mediated ECM fabrication	Self-assembly process that generates endogenous biological materials with a composition and an architecture almost equal to native tissues, as opposed to any other process.	Cell sourcing issues (biocompatibility and availability) associated with long production times.	47, 262,263,266,295	289	290	291	159,256	N/A
Densification	Easy method to provide increased mechanical properties and a physiological concentration range,	Require to develop homemade setups.	259,261	N/A	N/A	N/A	N/A	259–261

	while preserving the ability of molecules to self-assemble.							
Bio-printing	Biocompatible, suitable for cell integration and easily printable.	Long optimization of the bioink rheological properties, due to printability issues and insufficient mechanical properties.	264,269,292	293,294	272	266,295	271	Reviews on collagen-based bioinks: 236,265,267,270

Conclusions

Tubular tissues share common structural and compositional features. Their structure can be described with a simplified dual-layer model, comprising the epithelial inner layer and the muscular outer layer. While the first provides impermeability towards the inner wall, as well as absorption and exchange properties, the latter is responsible for structural stability, hosting the smooth muscle cells, and for the overall mechanical properties.

Type I collagen is the main building block of native tubular tissues. The arrangement of this protein is governed by self-assembly processes of the molecules, mediated by physico-chemical parameters that include concentration, pH and ionic strength. The ability to reproduce its conformation and concentration as found in vivo, is the leading pathway to mimic and eventually to replace native tissues. We have thus devoted a large part of this review article to methods based on type I collagen or ECM-derived material. Besides, the shape of tubular tissues poses substantive challenges to many materials processing techniques, which required a myriad of adaptation strategies. Formulating a material that combines both the native structure and composition defines the biomimetic approach, a term that we clarified in the introduction. Strategies to yield both a biomimetic composition and a biomimetic structure can be placed in a two-axis graph, drawn to guide the fabrication as well as a framework to compare different approaches reported in the literature.

To reform an epithelium, we identified three main strategies relying on structural or biological modifications of the luminal surface. ECM-derived surfaces, bioactive surfaces, and textured surfaces propose methods with similar results in terms of cellular adhesion and proliferation, which promote the material biointegration. ECM-derived surfaces are based on native ECM from autologous grafts, decellularized ECM, or cell-mediated ECM production. In addition, pre-seeding of grafts or in situ transplantation of cells enables an efficient re-epithelialization. In order to enhance epithelialization in situ, strategies that take inspiration from the basal membrane—by the addition of luminal protein coatings or active biomolecules—have proven efficient. The increased number of binding sites improves cell adhesion and proliferation, resulting in enhanced epithelialization with respect to the nude material. Finally, textured materials featuring fibers or specific topographies can direct cells spreading and improve their adhesion in vivo.

Multiple strategies have been developed to mimic the muscular outer layer as it is the constitutive layer of tubular organs. We classified these methods into two approaches: one relies on a porous network that facilitates cell and nutrients diffusion for the reconstitution of the entire tissue complexity, while the other hinges on dense matrices with increased compositional complexity. These two visions stand opposite, with the former that seems to show greater success, ease of process, and fewer biocompatibility issues. Porous materials can be achieved by decellularizing native tissues, braiding cell-derived ECM sheets, or building 3D porous materials from type I collagen via electrospinning, ice-templating, 3D-printing, or

cryoprinting. Dense muscular layers, on the contrary, rely on the cells ability to remodel the surrounding matrix. The latter can be either produced directly by cells (i.e. fibroblasts), or resulting from densification or bioprinting methods. These processing methods are particularly interesting since they allow introduction of relevant cell lines for each layer, for instance epithelial cells and smooth muscle cells.

The question that motivated this review is twofold. i) What are the key characteristics that remain unaddressed in the attempts to mimic and to replace native tubular tissues? ii) Which processing techniques are expected to tackle the current shortcomings and produce next-generation of biomaterials for clinical applications? In terms of technical means, building biomaterials, particularly those that encompass biological components—living or extracted from mammals—poses significant challenges in terms of their translation to clinical use, owing to the regulatory framework and the lengthy steps prior to clinical studies. Despite significant progresses in emulating living tissues in the lab, the intricate native cellular microenvironment, the structural and mechanical features, and the need to consider the organisms' homeostatic mechanisms raises many questions about the significance of in vitro models and their relevance in vivo. Approaches based solely on the use of biopolymers have demonstrated superior outcomes, particularly porous materials. In that sense, the techniques of ice-templating, electrospinning, and cryoprinting emerge as versatile tools with good reproducibility. Regarding the epithelium restoration, textured surfaces or protein coatings are straightforward routes to foster ECs adhesion and proliferation. Future developments of tubular tissues should combine a porous network with an engineered luminal surface, in a matrix composed of native-like type I collagen or ECM-derived material. Furthermore, it is worth noting that some tubular tissues, such as respiratory and urinary tract and notably urethra and ureter, have received relatively limited attention from both the biomaterials' community for their reproduction and the basic biology community for their in-depth description. However, there is a growing clinical demand for effective treatment of these tissues. We believe that this will push the scientific community to delve further into these tissues, propelling these as the next topics of biomaterials research in the upcoming years.

Conflicts of interest

There are no conflicts to declare.

References

1 A. Góra, D. Pliszka, S. Mukherjee and S. Ramakrishna, *J Nanosci Nanotechnol*, 2016, **16**, 19–39.

2 P. G. Camici, C. Tschöpe, M. F. Di Carli, O. Rimoldi and S. Van Linthout, *Cardiovasc Res*, 2020, **116**, 806–816.

3 B. W. Warner, *Cell Mol Gastroenterol Hepatol*, 2016, **2**, 429–438.

4 Z. Ungvari, S. Tarantini, A. J. Donato, V. Galvan, A. Csiszar, C. Impairment, N. Program, O. City, O. City, A. Medical, C. L. City, S. L. City, A. Studies and S. Antonio, *Mechanisms of Vascular Aging*, 2018, vol. 123.

5 S. Bruhin-feichter, W. Meier-ruge, G. Martucciello and E. Bruder, .

6 J. P. Richalet, *Rev Mal Respir*, 2021, **38**, 395–403.

7 B. Amadi, K. Zyambo, K. Chandwe, E. Besa, C. Mulenga, S. Mwakamui, S. Siyumbwa, S. Croft, R. Banda, M. Chipunza, K. Chifunda, L. Kazhila, K. VanBuskirk and P. Kelly, *Nat Microbiol*, 2021, **6**, 445–454.

8 M. D. Gerhard-Herman, H. L. Gornik, C. Barrett, N. R. Barshes, M. A. Corriere, D. E. Drachman, L. A. Fleisher, F. G. R. Fowkes, N. M. Hamburg, S. Kinlay, R. Lookstein, S. Misra, L. Mureebe, J. W. Olin, R. A. G. Patel, J. G. Regensteiner, A. Schanzer, M. H. Shishehbor, K. J. Stewart, D. Treat-Jacobson and M. E. Walsh, *Circulation*, 2017, **135**, 686–725.

9 H. Wessells, A. Morey, L. Souter, L. Rahimi and A. Vanni, *Journal of Urology*, 2023, **210**, 64–71.

10 H. Kuwano, Y. Nishimura, T. Oyama, H. Kato, Y. Kitagawa, M. Kusano, H. Shimada, H. Takiuchi, Y. Toh, Y. Doki, Y. Naomoto, H. Matsubara, T. Miyazaki, M. Muto and A. Yanagisawa, *Esophagus*, 2015, **12**, 1–30.

11 F. Matsumoto and K. Ikeda, *Cancers (Basel)*, 2021, **13**, 1–13.

12 M. Carrabba and P. Madeddu, 2018, **6**, 1–12.

13 J. Sánchez-Ibañez, C. Humphreys, M. Lomero, M. Escoto, M. J. Weiss, M. Wilson and M. López-Fraga, *Transplant Direct*, 2023, **9**, e1466.

14 A. H. Blakemore, A. B. And, N. Voorhees and N. Y. York, .

15 N. Pien, S. Palladino, F. Copes, G. Candiani, P. Dubruel, S. Van Vlierberghe and D. Mantovani, *Cells Tissues Organs*, 2022, 128–154.

16 M. C. Lai and A. Latif Ibrahim, *Physiology and reproduction*, 1982, **63**, 1425–1431.

17 H. M. Shields, R. A. Sawhney, F. Zwas, J. A. Boch, S. Kim, D. Goran and D. A. Antonioli, *Microsc Res Tech*, 1995, **31**, 248–256.

18 D. Hopwood, G. Milne and K. R. Logan, *J Pathol*, 1979, **129**, 161–167.

19 J. J. Barboriak, D. L. Van Horn and K. Pintar, *Journal of Thoracic and Cardiovascular Surgery*, 1976, **71**, 673–679.

20 Orlandini G. E., S. Z. Orlandini, A. F. Holstein, R. Evangelisti and R. Ponchietti, *Andrologia*, 1987, **19**, 315–321.

21 M. Woldemeskel, W. Drommer and M. Wendt, *Anat Histol Embryol*, 1998, **27**, 51–55.

22 P. G. Toner, K. E. Carr, A. Ferguson and C. Mackay, *Gut*, 1970, **11**, 471–481.

23 J. S. Trier and C. E. Rubin, *Gastroenterology*, 1965, **49**, 574–603.

24 K. N. Bitar, S. Raghavan and E. Zakhem, *Gastroenterology*, 2014, **146**, 1614–1624.

25 F. Taraballi, M. Sushnitha, C. Tsao, G. Bauza, C. Liverani, A. Shi and E. Tasciotti, *Adv Healthc Mater*, 2018, **17**, 1–13.

26 S. S. M. Rensen, P. A. F. M. Doevendans and G. J. J. M. Van Eys, *Netherlands Heart Journal*, 2007, **15**, 100–108.

27 J. H. Kristensen and M. A. Karsdal, *Chapter 30 - Elastin*, Elsevier Inc., 2016.

28 N. K. Karamanos, A. D. Theocharis, Z. Piperigkou, D. Manou, A. Passi, S. S. Skandalis, D. H. Vynios, V. Orian-Rousseau, S. Ricard-Blum, C. E. H. Schmelzer, L. Duca, M. Durbeej, N. A. Afratis, L. Troeberg, M. Franchi, V. Masola and M. Onisto, *FEBS Journal*, 2021, **288**, 6850–6912.

29 C. Parisi, K. Qin and F. M. Fernandes, *Philosophical Transactions of the Royal Society A: Mathematical, Physical and Engineering Sciences*, DOI:10.1098/rsta.2020.0344.

30 Y. L. Mary B. Chan-Park, Jin Ye Shen, Ye Cao, Yun Xiong and H. P. G. Shahrzad Rayatpisheh, Gavin Chun-Wei Kang, DOI:10.1002/jbm.a.32318.

31 L. Chen, C. Yan and Z. Zheng, *Materials Today*, 2018, **21**, 38–59.

32 L. S. Nair and C. T. Laurencin, *Progress in Polymer Science (Oxford)*, 2007, **32**, 762–798.

33 M. Vert, *Progress in Polymer Science (Oxford)*, 2007, **32**, 755–761.

34 L. Yang, H. Wu, L. Lu, Q. He, B. Xi, H. Yu, R. Luo, Y. Wang and X. Zhang, *Biomaterials*, DOI:10.1016/j.biomaterials.2021.121055.

35 E. Jones, T. Jensen, I. Sharma, H. Wanczyk, A. Mitchell, C. Foster, W. Sayej and C. Finck, DOI:10.1016/B978-0-08-102561-1.00023-3.

36 L. Elomaa, M. Lindner, R. Leben, R. Niesner and M. Weinhart, *Biofabrication*, , DOI:10.1088/1758-5090/ac9433.

37 J. Li, K. Zhang, H. Chen, T. Liu, P. Yang, Y. Zhao and N. Huang, *Materials Science and Engineering C*, 2014, **38**, 235–243.

38 Z. Wang, M. Li, B. Wang, Y. Xu, J. Li, S. Zhang, Q. Qin and J. Wang, .

39 X. Zhang, X. Chen, H. Hong, R. Hu, J. Liu and C. Liu, *Bioact Mater*, 2022, **10**, 15–31.

40 M. Asgari, N. Latifi, F. Giovanniello, H. D. Espinosa and M. Amabili, *Adv Nanobiomed Res*, 2022, **2**, 2100159.

41 Peter Fratzl, *Collagen structure and mechanics*, Springer, 2008.

42 J. A. Last and K. M. Reiser, *Environ Health Perspect*, 1984, **VOL. 55**, 169–177.

43 L. Salvatore, N. Gallo, M. L. Natali, A. Terzi, A. Sannino, M. Madaghiele and M. G. Raucci, , DOI:10.3389/fbioe.2021.644595.

44 M.-M. Giraud-Guille, E. Belamie, G. Mosser, C. Helary, F. Gobeaux and S. Vigier, *Comptes Rendus Chimie*, 2008, **11**, 245–252.

45 G. Mosser, A. Anglo, C. Helary, Y. Bouligand and M. M. Giraud-Guille, *Matrix Biology*, 2006, **25**, 3–13.

46 M. M. Giraud-Guille, *Int Rev Cytol*, 1996, **166**, 59–101.

47 J. Charvolin and J. F. Sadoc, *Interface Focus*, 2012, **2**, 567–574.

48 F. Portier, C. Teulon, A. Nowacka-Perrin, F. Guenneau, M.-C. Schanne-Klein and G. Mosser, 2017, 12916–12925.

49 S. Gorgieva and V. Kokol, *Biomaterials Applications for Nanomedicine*, , DOI:10.5772/24118.

50 D. A. Knight and S. T. Holgate, *Respirology*, 2003, **8**, 432–446.

51 S. Mishani, H. Belhoul-Fakir, C. Lagat, S. Jansen, B. Evans and M. Lawrence-Brown, *Quant Imaging Med Surg*, 2021, **11**, 3494–3505.

52 G. A. Holzapfel, , DOI:10.1016/j.jtbi.2005.05.006ï.

53 S. Singh and M. Torzewski, *Biomolecules*, 2019, 9.

54 S. R. and E. Z. Khalil N. Bitar, 2015, **146**, 1614–1624.

55 B. Syeda, M. Gottsauner-Wolf, S. Denk, P. Pichler, A. Khorsand and D. Glogar, *Am J Hypertens*, 2003, **16**, 356–362.

56 N. Shashikanth, S. Yeruva, M. L. D. M. Ong, M. A. Odenwald, R. Pavlyuk and J. R. Turner, *Compr Physiol*, 2017, **7**, 1497–1518.

57 K. L. Edelblum and J. R. Turner, *Epithelial Cells: Structure, Transport, and Barrier Function*, Elsevier, Fourth Edi., 2015, vol. 1–2.

58 G. A. Holzapfel, T. C. Gasser and R. W. Ogden, *J Elast*, 2000, **61**, 1–48.

59 L. Claesson-Welsh, E. Dejana and D. M. McDonald, *Trends Mol Med*, 2021, **27**, 314–331.

60 M. Lasalvia, S. Castellani, P. D'Antonio, G. Perna, A. Carbone, A. L. Colia, A. B. Maffione, V. Capozzi and M. Conese, *Exp Cell Res*, 2016, **348**, 46–55.

61 S. K. Lai, Y.-Y. Wang, D. Wirtz and J. Hanes, *Adv Drug Deliv Rev*, 2009, **61**, 86–100.

62 M. A. Jankowska, M. Bartkowiak-Jowsa and R. Bedzinski, *J Mech Behav Biomed Mater*, 2015, **50**, 1–12.

63 B. Hoffman, M. Martin, B. N. Brown, L. J. Bonassar and J. Cheetham, *Laryngoscope*, 2015, 1–7.

64 J. K. Rains, J. L. Bert, C. R. Roberts and P. D. Pare, *J Appl Physiol*, 1992, **72**, 219–225.

65 L. Krupa, B. Bajka, R. Staroń, D. Dupont, H. Singh, K. Gutkowski and A. Macierzanka, *Sci Rep*, DOI:10.1038/s41598-020-77129-4.

66 Y. Lu, H. Wu, J. Li, Y. Gong, J. Ma, G. S. Kassab, Y. Huo, W. Tan and Y. Huo, *Sci Rep*, 2017, **7**, 1–12.

67 D. C. Stewart, D. Berrie, J. Li, X. Liu, C. Rickerson, D. Mkoji, A. Iqbal, S. Tan, A. L. Doty, S. C. Glover and C. S. Simmons, *PLoS One*, DOI:10.1371/journal.pone.0200377.

68 L. Wang, S. K. Murthy, G. A. Barabino and R. L. Carrier, *Biomaterials*, 2010, **31**, 7586–7598.

69 G. A. Holzapfel, G. Sommer, M. Auer, P. Regitnig and R. W. Ogden, *Ann Biomed Eng*, 2007, **35**, 530–545.

70 V. I. Egorov, I. V Schastlivtsev, E. V Prut, A. O. Baranov and R. A. Turusov, *J Biomech*, 2002, **35**, 1417–1425.

71 C.-C. Chou and J. M. Dabney, *Intestinal Compliance*, 1967, vol. 12.

72 F. V Brozovich, C. J. Nicholson, C. V Degen, Y. Z. Gao, M. Aggarwal and K. G. Morgan, 2016, 476–532.

73 J. Chen, T. Oshima, X. Huang, T. Tomita, H. Fukui and H. Miwa, *J Clin Med*, DOI:10.3390/jcm11144246.

74 H. Shen, X. Hu, H. Cui, Y. Zhuang, D. Huang, F. Yang, X. Wang, S. Wang and D. Wu, *J Mater Chem B*, 2016, **4**, 7689–7696.

75 M. Hassan, S. Aceves, R. Dohil, A. Gharibans, R. Newbury, J. Proudfoot and H. Mousa, *J Pediatr Gastroenterol Nutr*, 2019, **68**, 559–565.

76 J. Yang, J. Zhao, D. Liao and H. Gregersen, *J Biomech*, 2006, **39**, 894–904.

77 M. G. Dalghi, N. Montalbetti, M. D. Carattino and G. Apodaca, *Physiol Rev*.

78 H. O. Negrete, J. P. Lavelle, J. Berg, S. A. Lewis and M. L. Zeidel, *American Journal of Physiology-Renal Physiology*, 1996, **271**, F886–F894.

79 J. C. Mathai, E. H. Zhou, W. Yu, J. H. Kim, G. Zhou, Y. Liao, T. T. Sun, J. J. Fredberg and M. L. Zeidel, *Biophys J*, 2014, **107**, 1273–1279.

80 J. S. Walter, J. S. Wheeler, C. Morgan, P. Zaszczurynski and M. Plishka, *Neurourol Urodyn*, 1993, **12**, 273–276.

81 N. E. Vrana, P. Lavalle, M. R. Dokmeci, F. Dehghani, A. M. Ghaemmaghami and A. Khademhosseini, *Tissue Eng Part B Rev*, 2013, **19**, 529–543.

82 R. Saksena, C. Gao, M. Wicox and A. de Mel, *J Tissue Eng*, 2016, 7.

83 K. T. Callesen, A. Yuste-Montalvo, L. K. Poulsen, B. M. Jensen and V. Esteban, *Biomedicines*, , DOI:10.3390/biomedicines9040439.

84 N. Yu. Ignat'eva, N. A. Danilov, S. V. Averkiev, M. V. Obrezkova, V. V. Lunin and E. N. Sobol', *Journal of Analytical Chemistry*, 2007, **62**, 51–57.

85 C. M. Niessen, *Journal of Investigative Dermatology*, 2007, 127, 2525–2532.

86 M. N. Yu. Ignat'eva, NA Danilov, SV Averkiev, V. Obrezkova and Lunin, 2007, **62**, 59–65.

87 C. D. Devillard and C. A. Marquette, *Front Bioeng Biotechnol*, 2021, 9.

88 P. Jain, S. B. Rauer, M. Möller and S. Singh, *Biomacromolecules*, 2022, 23, 3081–3103.

89 G. A. Stooke-Vaughan and O. Campàs, *Curr Opin Genet Dev*, 2018, 51, 111–119.

90 N. Khalilgharibi and Y. Mao, *Open Biol*, 2021, 11.

91 Z. Wang, M. Li, B. Wang, Y. Xu, J. Li, S. Zhang, Q. Qin and J. Wang, *Chemical Engineering Journal*, 2023, **451**, 138805.

92 A. J. Engler, S. Sen, H. L. Sweeney and D. E. Discher, *Cell*, 2006, **126**, 677–689.

93 H. Schweikl, R. Müller, C. Englert, K. A. Hiller, R. Kujat, M. Nerlich and G. Schmalz, *J Mater Sci Mater Med*, 2007, **18**, 1895–1905.

94 M. Barrera-Velázquez and L. D. Ríos-Barrera, *Biol Open*, DOI:10.1242/bio.058760.

95 U. D. Jerman, M. E. Kreft and P. Veranič, *Tissue Eng Part B Rev*, 2015, 21, 521–530.

96 G. R. Cunha and L. Baskin, *Differentiation*, 2016, 91, 20–27.

97 Z.-M. Y. Ren-Qian Wei, Bo Tan, Mei-Yun Tan, Jing-Cong Luo, Li Deng, Xiao-He Chen, Xiu-Qun Li, Xiao Zuo, Wei Zhi, Peng Yang, Hui-Qi Xe, 2009, 453–461.

98 J. Zhang, J. Muri, G. Fitzgerald, T. Gorski, R. Gianni-Barrera, E. Masschelein, G. D'Hulst, P. Gilardoni, G. Turiel, Z. Fan, T. T. Wang, M. Planque, P. Carmeliet, L. Pellerin, C. Wolfrum, S. M. Fendt, A. Banfi, C. Stockmann, I. Soro-Arnáiz, M. Kopf and K. De Bock, *Cell Metab*, 2020, **31**, 1136-1153.e7.

99 R. Fitridge and M. Thompson, *Mechanisms of Vascular Disease*, Adelaide, 2011.

100 L. Liu, B. Stephens, M. Bergman, A. May and T. Chiang, 2021, 1–13.

101 B. R. Lee, R. I. Silver, A. W. Partin, J. I. Epstein and J. P. Gearhart, *Elsevier*.

102 T. J. McKee, G. Perlman, M. Morris and S. V. Komarova, *Sci Rep*, , DOI:10.1038/s41598-019-46896-0.

103 J. C. Ribeiro-Silva, P. Nolasco, J. E. Krieger and A. A. Miyakawa, *Int J Mol Sci*, DOI:10.3390/ijms221810175.

104 N. Shi and S. Y. Chen, *J Cell Physiol*, 2016, 231, 777–787.

105 B. C. Isenberg, C. Williams and R. T. Tranquillo, *Circ Res*, 2006, 98, 25–35.

106 M. Marzaro, M. Algeri, L. Tomao, S. Tedesco, T. Caldaro, V. Balassone, A. C. Contini, L. Guerra, G. F. D. Abriola, P. Francalanci, M. E. Caristo, L. Lupoi, I. Boskoski, A. Bozza, G. Astori, G. Pozzato, A. Pozzato, G. Costamagna and L. D. Oglio, 2020, 1–12.

107 J. Li, K. Zhang, W. Ma, F. Wu, P. Yang, Z. He and N. Huang, *Regen Biomater*, 2016, **1**, 149–157.

108 T. M. Do, Y. Yang and A. Deng, *Polymers (Basel)*, DOI:10.3390/polym13224042.

109 A. Ray, O. Lee, Z. Win, R. M. Edwards, P. W. Alford, D. H. Kim and P. P. Provenzano, *Nat Commun*, , DOI:10.1038/ncomms14923.

110 C. Parisi, B. Thiébot, G. Mosser, L. Trichet, P. Manivet and F. M. Fernandes, *Biomater Sci*, 2022, **10**, 6939–6950.

111 C. A. Dessalles, C. Leclech, A. Castagnino and A. I. Barakat, *Commun Biol*, 2021, **4**, 764.

112 K. Qin, C. Parisi and F. M. Fernandes, *J Mater Chem B*, 2021, **9**, 889–907.

113 K. Ławkowska, C. Rosenbaum, P. Petrasz, L. Kluth, K. Koper, T. Drewa, M. Pokrywczynska and J. Adamowicz, *Front Bioeng Biotechnol*, DOI:10.3389/fbioe.2022.1040987.

114 S. Bhargava, J. M. Patterson, R. D. Inman, S. MacNeil and C. R. Chapple, *Eur Urol*, 2008, **53**, 1263–1271.

115 A. I. Toma, J. M. Fuller, N. J. Willett and S. L. Goudy, *Translational Research*, 2021, 236, 17–34.

116 E. Maurizi, D. Adamo, F. M. Magrelli, G. Galaverni, E. Attico, A. Merra, M. B. R. Maffezzoni, L. Losi, V. G. Genna, V. Sceberras and G. Pellegrini, *Front Bioeng Biotechnol*, , DOI:10.3389/fbioe.2021.652214.

117 G. Ram-Liebig, J. Bednarz, B. Stuerzebecher, D. Fahlenkamp, G. Barbagli, G. Romano, U. Balsmeyer, M.-E. Spiegeler, S. Liebig and H. Knispel, *Adv Drug Deliv Rev*, 2015, **82–83**, 181–191.

118 G. Ram-Liebig, G. Barbagli, A. Heidenreich, D. Fahlenkamp, G. Romano, U. Rebmann, D. Standhaft, H. van Ahlen, S. Schakaki, U. Balsmeyer, M. Spiegeler and H. Knispel, *EBioMedicine*, 2017, **23**, 185–192.

119 Y. Xue, X. Cai, L. Wang, B. Liao, H. Zhang, Y. Shan, Q. Chen, T. Zhou, X. Li, J. Hou, S. Chen, R. Luo, D. Qin, D. Pei and G. Pan, *PLoS One*, DOI:10.1371/journal.pone.0070573.

120 J. Lu, L. F. Zhu, Y. M. Cai, H. Y. Dong, L. Zhu and J. M. Tan, *Mol Med Rep*, 2019, **19**, 187–194.

121 M. Culenova, A. Nicodemou, Z. V. Novakova, M. Debreova, V. Smolinská, S. Bernatova, D. Ivanisova, O. Novotna, J. Vasicek, I. Varga, S. Ziaran and L. Danisovic, *Int J Mol Sci*, , DOI:10.3390/ijms222212503.

122 H. Tian, S. Bharadwaj, Y. Liu, P. X. Ma, A. Atala and Y. Zhang, *Tissue Eng Part A*, 2010, **16**, 1769–1779.

123 K. Suzuki, M. Koyanagi-Aoi, K. Uehara, N. Hinata, M. Fujisawa and T. Aoi, *Sci Rep*, DOI:10.1038/s41598-019-46848-8.

124 Y. Inoue, T. Kishida, S. ichiro Kotani, M. Akiyoshi, H. Taga, M. Seki, O. Ukimura and O. Mazda, *Sci Rep*, DOI:10.1038/s41598-019-50388-6.

125 J. P. Koo, C. H. Kim, J. G. Lee, K. S. Kim and J. H. Yoon, *Laryngoscope*, 2007, **117**, 1750–1755.

126 L. Huu Dang, S.-H. Hung, Y. Tseng, L. Xuan Quang, N. Thao Ngoc Le, C.-L. Fang and H. Tseng, *International Journal of Molecular Sciences Article Int. J. Mol. Sci*, 2021, **22**, 10322.

127 M. Kanzaki, M. Yamato, H. Hatakeyama, C. Kohno, J. Yang, T. Umemoto, A. Kikuchi, T. Okano and T. Onuki, *Tissue Eng*, 2006, **12**, 1275–1283.

128 A. K. Saxena, H. Ainoedhofer and M. E. Höllwarth, *J Pediatr Surg*, 2009, **44**, 896–901.

129 T. Jensen, H. Wanczyk, I. Sharma, A. Mitchell, W. N. Sayej and C. Finck, *J Pediatr Surg*, 2019, **54**, 1744–1754.

130 T. Sato, R. G. Vries, H. J. Snippert, M. Van De Wetering, N. Barker, D. E. Stange, J. H. Van Es, A. Abo, P. Kujala, P. J. Peters and H. Clevers, *Nature*, 2009, **459**, 262–265.

131 J. Sprangers, I. C. Zaalberg and M. M. Maurice, *Cell Death Differ*, 2021, **28**, 95–107.

132 S. Yui, T. Nakamura, T. Sato, Y. Nemoto, T. Mizutani, X. Zheng, S. Ichinose, T. Nagaishi, R. Okamoto, K. Tsuchiya, H. Clevers and M. Watanabe, *Nat Med*, 2012, **18**, 618–623.

133 S. Sugimoto, Y. Ohta, M. Fujii, M. Matano, M. Shimokawa, K. Nanki, S. Date, S. Nishikori, Y. Nakazato, T. Nakamura, T. Kanai and T. Sato, *Cell Stem Cell*, 2018, **22**, 171-176.e5.

134 X. Luo, C. Han, P. Yang, A. Zhao, D. Zou, L. Jiang, P. Gao, B. Yin and N. Huang, *Colloids Surf B Biointerfaces*, , DOI:10.1016/j.colsurfb.2020.111307.

135 A. Fayon, D. Helle, G. Francius, J. B. Vincourt, V. Regnault, D. Dumas, P. Menu and R. El Omar, *Front Bioeng Biotechnol*, DOI:10.3389/fbioe.2022.884069.

136 T. Wu, J. Zhang, Y. Wang, B. Sun, M. Yin, G. L. Bowlin and X. Mo, *ACS Appl Bio Mater*, 2018, **1**, 833–844.

137 L. M. van den Boogaart, J. K. A. Langowski and G. J. Amador, *Biomimetics*, 2022, **7**, 134.

138 W. Li, Y. Zheng, W. Pang and P. Lai, *Biomedical Technology*, 2023, **1**, 65–72.

139 W. Xie, V. Kothari and B. S. Terry, *Biomed Microdevices*, DOI:10.1007/s10544-015-9972-7.

140 C. Xu, Y. Chen, Y. Si, Y. Yan, A. B. Kayitmazer, Y. Ding, W. Qian, Z. Zheng, S. Cao and Y. Xu, *Adv Mater Interfaces*, , DOI:10.1002/admi.202001955.

141 R. R. Pillai and V. Thomas, *Polymers (Basel)*, 2023, 15.

142 Y. Jiang, H. Wang, X. Wang and Q. Li, *Int J Biol Macromol*, 2022, **219**, 1146–1154.

143 H. Lai, B. Gong, J. Yin and J. Qian, *Mater Des*, 2022, **218**, 110663.

144 M. F. A. Cutiongco, S. H. Goh, R. Aid-Launais, C. Le Visage, H. Y. Low and E. K. F. Yim, *Biomaterials*, 2016, **84**, 184–195.

145 S. Yunoki, E. Kondo and K. Yasuda, in *Collagen Biomaterials*, IntechOpen, 2022.

146 J. Hu, B. Ai, S. Zhu, Z. Wang, H. Xia and W. Jia, *J Biomater Appl*, 2022, **36**, 956–964.

147 O. A. Romanova, T. H. Tenchurin, T. S. Demina, E. V. Sytina, A. D. Shepelev, S. G. Rudyak, O. I. Klein, S. V. Krasheninnikov, E. I. Safronova, R. A. Kamyshinsky, V. G. Mamagulashvili, T. A. Akopova, S. N. Chvalun and A. A. Panteleyev, *Cell Prolif*, , DOI:10.1111/cpr.12598.

148 P. Jain, S. B. Rauer, M. Möller and S. Singh, *Biomacromolecules*, 2022, **23**, 3081–3103.

149 K. Zhang, M. A. Bhutto, L. Wang, K. Wang, J. Liu, W. Li, W. Cui and Q. Fu, *Advanced Fiber Materials*, 2023, **5**, 662–680.

150 J. A. Reid and A. Callanan, *J Biomed Mater Res B Appl Biomater*, 2020, **108**, 910–924.

151 J. Dolgin, S. N. Hanumantharao, S. Farias, C. G. Simon and S. Rao, *Fibers*, 2023, **11**, 39.

152 Y. Niu, M. Galluzzi, M. Fu, J. Hu and H. Xia, *J Nanobiotechnology*, DOI:10.1186/s12951-021-01091-0.

153 D. Dems, J. Rodrigues Da Silva, C. Hélary, F. Wien, M. Marchand, N. Debons, L. Muller, Y. Chen, M. C. Schanne-Klein, C. Laberty-Robert, N. Krins and C. Aimé, *ACS Appl Bio Mater*, 2020, **3**, 2948–2957.

154 M. Ghosh, S. Ahmad, C. W. White and S. D. Reynolds, *Am J Respir Cell Mol Biol*, 2017, **56**, 1–10.

155 H. A. Khalil, S. N. Hong, J. D. Rouch, A. Scott, Y. Cho, J. Wang, M. S. Lewis, M. G. Martin, J. C. Y. Dunn and M. G. Stelzner, *PLoS One*, 2019, **14**, e0216326.

156 G. Barbagli, I. Akbarov, A. Heidenreich, V. Zugor, R. Olianas, M. Aragona, G. Romano, U. Balsmeyer, D. Fahlenkamp, U. Rebmann, D. Standhaft and M. Lazzeri, *Journal of Urology*, 2018, **200**, 448–456.

157 G. Bento, A. K. Shafigullina, A. A. Rizvanov, V. A. Sardão, M. P. Macedo and P. J. Oliveira, *Cells*, 2020, **9**, 573.

158 Samuel S. Hinman, Yuli Wang, Raehyun Kim and Nancy L. Allbritton, *Nat Protoc*, 2021, **16**, 352–382.

159 E. Elia, D. Brownell, S. Chabaud and S. Bolduc, *Int J Mol Sci*, 2022, **24**, 9.

160 A. Atala, F. Kurtis Kasper and A. G. Mikos, *Sci Transl Med*, DOI:10.1126/scitranslmed.3004890.

161 A. Porzionato, E. Stocco, S. Barbon, F. Grandi, V. Macchi and R. De Caro, *Int J Mol Sci*, 2018, **19**, 4117.

162 L. P. Frazão, A. M. Fernandes, C. Oliveira, A. Martins, T. H. Silva, J. Vieira De Castro, C. Nogueira-Silva and N. M. Neves, *ACS Biomater Sci Eng*, 2021, **7**, 3423–3433.

163 E. Martinod, K. Chouahnia, D. M. Radu, P. Joudiou, Y. Uzunhan, M. Bensidhoum, A. M. Santos Portela, P. Guiraudet, M. Peretti, M. D. Destable, A. Solis, S. Benachi, A. Fialaire-Legendre, H. Rouard, T. Collon, J. Piquet, S. Leroy, N. Vénissac, J. Santini, C. Tresallet, H. Dutau, G. Sebbane, Y. Cohen, S. Beloucif, A. C. D'Audiffret, H. Petite, D. Valeyre, A. Carpentier and E. Vicaut, *JAMA - Journal of the American Medical Association*, 2018, **319**, 2212–2222.

164 S. F. Badylak, B. Kropp, T. Mcpherson, H. Liang and P. W. Snyder, *Tissue Eng*.

165 T. W. Jernigan, M. A. Croce, C. Cagiannos, D. H. Shell, C. R. Handorf, T. C. Fabian, D. V. Feliciano, E. E. Cornwell and B. A. Pruitt, *Ann Surg*, 2004, **239**, 733–740.

166 J. Negishi, Y. Hashimoto, A. Yamashita, Y. Zhang, T. Kimura, A. Kishida and S. Funamoto, *J Biomed Mater Res A*, 2017, **105**, 1293–1298.

167 Q. Xu, C. Chen, Z. Xu, F. Chen, Y. Yu, X. Hong, S. Xu, J. Chen, Q. Ding and H. Chen, *Asian J Urol*, 2020, **7**, 51–55.

168 G. Totonelli, P. Maghsoudlou, J. M. Fishman, G. Orlando, T. Ansari, P. Sibbons, M. A. Birchall, A. Pierro, S. Eaton and P. De Coppi, *World J Gastroenterol*, 2012, **18**, 6900–6907.

169 Y. Takimoto, T. Nakamura, Y. Yamamoto, T. Kiyotani, M. Teramachi and Y. Shimizu, *General thoracic surgery*.

170 M. A. Rodríguez-Soto, C. A. Polanía-Sandoval, A. M. Aragón-Rivera, D. Buitrago, M. Ayala-Velásquez, A. Velandia-Sánchez, G. Peralta Peluffo, J. C. Cruz, C. Muñoz Camargo, J. Camacho-Mackenzie, J. G. Barrera-Carvajal and J. C. Briceño, *Polymers (Basel)*, 2022, 14.

171 H. Omid, S. Abdollahi, S. Bonakdar, N. Haghighipour, M. A. Shokrgozar and J. Mohammadi, *J Mater Sci Mater Med*, DOI:10.1007/s10856-023-06716-4.

172 O. M. El-Taji, A. Q. Khattak and S. A. Hussain, *Oncol Lett*, 2015, 3–10.

173 M. Garriboli, K. Deguchi, G. Totonelli, F. Georgiades, L. Urbani, M. Ghionzoli, A. J. Burns, N. J. Sebire, M. Turmaine, S. Eaton and P. De Coppi, *Pediatr Surg Int*, 2022, **38**, 665–677.

174 Y. Zhang, X. S. Li, A. G. Guex, S. S. Liu, E. Müller, R. I. Malini, H. J. Zhao, M. Rottmar, K. Maniura-Weber, R. M. Rossi and F. Spano, *Biofabrication*, , DOI:10.1088/1758-5090/aa6bae.

175 F. Zhang, T. Bambharoliya, Y. Xie, L. Liu, H. Celik, L. Wang, W. College and N. Carolina, *Materials Science & Engineering C*, DOI:10.1016/j.msec.2020.111418.

176 L. Magnan, G. Labrunie, M. Fénelon, N. Dusserre, M. P. Foulc, M. Lafourcade, I. Svahn, E. Gontier, J. H. Vélez V., T. N. McAllister and N. L'Heureux, *Acta Biomater*, 2020, **105**, 111–120.

177 F. Gobeaux, Université Pierre et Marie Curie, 2008.

178 P. Kuppan, S. Sethuraman and U. M. Krishnan, *J Biomed Mater Res A*, 2015, **103**, 2236–2250.

179 H. A. Strobel, E. L. Calamari, A. Beliveau, A. Jain and M. W. Rolle, *J Biomed Mater Res B Appl Biomater*, 2018, **106**, 817–826.

180 X. Lu, H. Zou, X. Liao, Y. Xiong, X. Hu, J. Cao, J. Pan, C. Li and Y. Zheng, *Biomedical Materials (Bristol)*, , DOI:10.1088/1748-605X/aca269.

181 D. G. Simpson, B. S. Jha, C. E. Ayres, J. R. Bowman, T. A. Telemeco, S. A. Sell and G. L. Bowlin, *J Nanomater*, DOI:10.1155/2011/348268.

182 B. N. Blackstone, S. C. Gallentine and H. M. Powell, *Bioengineering*, 2021, **8**, 39.

183 J. Venugopal, L. L. Ma, T. Yong and S. Ramakrishna, *Cell Biol Int*, 2005, **29**, 861–867.

184 T. Wu, J. Zhang, Y. Wang, B. Sun, M. Yin, G. L. Bowlin and X. Mo, *ACS Appl Bio Mater*, 2018, **1**, 833–844.

185 I. Roy and M. N. Gupta, *Biotechnol Appl Biochem*, 2004, **39**, 165–177.

186 R. Polak and R. N. M. Pitombo, *Cryobiology*, 2011, **63**, 61–66.

187 D. I. Zeugolis, S. T. Khew, E. S. Y. Yew, A. K. Ekaputra, Y. W. Tong, L. Y. L. Yung, D. W. Hutmacher, C. Sheppard and M. Raghunath, *Biomaterials*, 2008, **29**, 2293–2305.

188 A. Elamparithi, A. M. Punnoose and S. Kuruvilla, *Artif Cells Nanomed Biotechnol*, 2016, **44**, 1318–1325.

189 J. A. Matthews, G. E. Wnek, D. G. Simpson and G. L. Bowlin, *Biomacromolecules*, 2002, **3**, 232–238.

190 U. G. K. Wegst, M. Schecter, A. E. Donius and P. M. Hunger, *Philosophical Transactions of the Royal Society A: Mathematical, Physical and Engineering Sciences*, 2010, **368**, 2099–2121.

191 S. Deville, E. Saiz and A. P. Tomsia, *Acta Mater*, 2007, **55**, 1965–1974.

192 V. Kocherbitov, *Carbohydr Polym*, 2016, **150**, 353–358.

193 K. Qin, C. Eschenbrenner, F. Ginot, D. Dedovets, T. Coradin, S. Deville and F. M. Fernandes, *Journal of Physical Chemistry Letters*, 2020, **11**, 7730–7738.

194 L. Buttafoco, A. A. Poot, P. J. Dijkstra, W. F. Daamen, T. H. Van Kuppevelt, I. Vermes and J. Feijen, 2005, 357–368.

195 I. Martinier, F. Fage, A. Kakar, A. Castagnino, E. Saindoy, J. Frederick, I. Onorati, V. Besnard, A. I. Barakat, N. Dard, E. Martinod, C. Planes, L. Trichet and F. M. Fernandes, *bioRxiv*, DOI:10.1101/2023.08.30.555553.

196 J. Seuba, J. Leloup, S. Richaud, S. Deville, C. Guizard and A. J. Stevenson, *J Eur Ceram Soc*, 2017, **37**, 2423–2429.

197 H. Joukhdar, A. Seifert, T. Jüngst, J. Groll, M. S. Lord and J. Rnjak-Kovacina, *Advanced Materials*, DOI:10.1002/adma.202100091.

198 D. Dedovets, C. Monteux and S. Deville, *Science (1979)*, 2018, 303–306.

199 J. A. Cyr, A. Husmann, S. M. Best and R. E. Cameron, *Acta Biomater*, 2022, **153**, 260–272.

200 M. Marcellini, C. Noirjean, D. Dedovets, J. Maria and S. Deville, *ACS Omega*, 2016, **1**, 1019–1026.

201 K. M. Pawelec, A. Husmann, S. M. Best and R. E. Cameron, *Appl Phys Rev*, , DOI:10.1063/1.4871083.

202 C. Rieu, C. Parisi, G. Mosser, B. Haye, T. Coradin, F. M. Fernandes and L. Trichet, *ACS Appl Mater Interfaces*, 2019, **11**, 14672–14683.

203 M. C. Gutiérrez, M. L. Ferrer and F. Del Monte, *Chemistry of Materials*, 2008, **20**, 634–648.

204 M. W. Pot, K. A. Faraj, A. Adawy, W. J. P. Van Enckevort, H. T. B. Van Moerkerk, E. Vlieg, W. F. Daamen and T. H. Van Kuppevelt, *ACS Appl Mater Interfaces*, 2015, **7**, 8495–8505.

205 X. Liu and P. X. Ma, *Biomaterials*, 2009, **30**, 4094–4103.

206 J. Lee and G. Kim, *ACS Appl Mater Interfaces*, 2018, **10**, 35801–35811.

207 H. W. Liu, W. T. Su, C. Y. Liu and C. C. Huang, *Int J Mol Sci*, , DOI:10.3390/ijms23158449.

208 J. L. Zitnay, S. P. Reese, G. Tran, N. Farhang, R. D. Bowles and J. A. Weiss, *Acta Biomater*, 2018, **65**, 76–87.

209 C. Katrilaka, N. Karipidou, N. Petrou, C. Manglaris, G. Katrilakas, A. N. Tzavellas, M. Pitou, E. E. Tsiridis, T. Choli-Papadopoulou and A. Aggeli, *Materials*, 2023, **16**, 4425.

210 K. Yin, P. Divakar and U. G. K. Wegst, *Acta Biomater*, 2019, **84**, 231–241.

211 P. Divakar, K. Yin and U. G. K. Wegst, *J Mech Behav Biomed Mater*, 2019, **90**, 350–364.

212 N. Davidenko, C. F. Schuster, D. V. Bax, N. Raynal, R. W. Farndale, S. M. Best and R. E. Cameron, *Acta Biomater*, 2015, **25**, 131–142.

213 D. K. Chang, M. R. Louis, A. Gimenez and E. M. Reece, *Semin Plast Surg*, 2019, **33**, 185–189.

214 O. Kloeters, F. Unglaub, E. de Laat, M. van Abeelen and D. Ulrich, *Int Wound J*, 2016, **13**, 1231–1236.

215 J. H. Min, I. S. Yun, D. H. Lew, T. S. Roh and W. J. Lee, *Arch Plast Surg*, 2014, **41**, 330–336.

216 S. Govender, C. Csimma, H. K. Genant and A. Valentin-Opran, *J Bone Joint Surg*, 2002, **84-A**, 2123–2134.

217 P. K. Narotam, S. José, N. Nathoo, C. Taylon and Y. Vora, *Spine (Phila Pa 1976)*, 2004, **29**, 2861–2867.

218 X. Cao, S. Maharjan, R. Ashfaq, J. Shin and Y. S. Zhang, *Engineering*, 2021, **7**, 832–844.

219 Y.-C. Hou, X. Cui, Z. Qin, C. Su, G. Zhang, J.-N. Tang, J.-A. Li and J.-Y. Zhang, *Int J Bioprint*, 2023, **9**, 0.

220 F. Pati, J. Jang, D.-H. Ha, S. Won Kim, J.-W. Rhie, J.-H. Shim, D.-H. Kim and D.-W. Cho, *Nat Commun*, 2014, **5**, 3935.

221 K. Dzobo, K. S. C. M. Motaung and A. Adesida, *Int J Mol Sci*, 2019, **20**, 4628.

222 Z. Y. Xu, J. J. Huang, Y. Liu, C. W. Chen, G. W. Qu, G. F. Wang, Y. Zhao, X. W. Wu and J. A. Ren, *Bioeng Transl Med*, DOI:10.1002/btm2.10327.

223 Y. Zhao, Y. Liu, Y. Dai, L. Yang and G. Chen, *Micromachines (Basel)*, 2022, **13**, 1073.

224 C. Norotte, F. S. Marga, L. E. Niklason and G. Forgacs, *Biomaterials*, 2009, **30**, 5910–5917.

225 M. M. De Santis, H. N. Alsafadi, S. Tas, D. A. Bölükbas, S. Prithiviraj, I. A. N. Da Silva, M. Mittendorfer, C. Ota, J. Stegmayr, F. Daoud, M. Königshoff, K. Swärd, J. A. Wood, M. Tassieri, P. E. Bourgine, S. Lindstedt, S. Mohlin and D. E. Wagner, *Advanced Materials*, DOI:10.1002/adma.202005476.

226 G. Gao, J. H. Lee, J. Jang, D. H. Lee, J. Kong, B. S. Kim, Y. Choi, W. B. Jang, Y. J. Hong, S. Kwon and D. Cho, *Adv Funct Mater*, DOI:10.1002/adfm.201700798.

227 Z. Wang, L. Wang, T. Li, S. Liu, B. Guo, W. Huang and Y. Wu, *Theranostics*, 2021, **11**, 7948–7969.

228 S. Liu, T. Wang, S. Li and X. Wang, *Polymers (Basel)*, 2022, **14**, 2182.

229 A. Lee, A. R. Hudson, D. J. Shiwarski, J. W. Tashman, T. J. Hinton, S. Yerneni, J. M. Bliley, P. G. Campbell and A. W. Feinberg, *Science (1979)*, 2019, **365**, 482–487.

230 C. Z. Liu, Z. D. Xia, Z. W. Han, P. A. Hulley, J. T. Triffitt and J. T. Czernuszka, *J Biomed Mater Res B Appl Biomater*, 2008, **85**, 519–528.

231 Y. B. Kim, H. Lee and G. H. Kim, *ACS Appl Mater Interfaces*, 2016, **8**, 32230–32240.

232 M. K. Włodarczyk-Biegun and A. del Campo, *Biomaterials*, 2017, **134**, 180–201.

233 H. Suo, J. Zhang, M. Xu and L. Wang, *Materials Science and Engineering C*, DOI:10.1016/j.msec.2021.111963.

234 A. Nagaraj, A. E. Etxeberria, R. Naffa, G. Zidan and A. Seyfoddin, *Biology (Basel)*, 2022, **11**, 1561.

235 S. O. Sarrigiannidis, J. M. Rey, O. Dobre, C. González-García, M. J. Dalby and M. Salmeron-Sanchez, *Mater Today Bio*, 2021, **10**, 100098.

236 E. O. Osidak, V. I. Kozhukhov, M. S. Osidak and S. P. Domogatsky, *Int J Bioprint*, 2020, **6**, 270.

237 A. D. Nocera, R. Comín, N. A. Salvatierra and M. P. Cid, *Biomed Microdevices*, , DOI:10.1007/s10544-018-0270-z.

238 M. Camman, P. Joanne, J. Brun, A. Marcellan, J. Dumont, O. Agbulut and C. Hélary, *Biomaterials Advances*, DOI:10.1016/j.bioadv.2022.213219.

239 W. L. Ng, M. H. Goh, W. Y. Yeong and M. W. Naing, *Biomater Sci*, 2018, **6**, 562–574.

240 S. Shakibania, L. Ghazanfari, M. Raeeszadeh-Sarmazdeh and M. Khakbiz, *Drug Dev Ind Pharm*, 2021, **47**, 521–534.

241 M. Adamkiewicz and B. Rubinsky, *Cryobiology*, 2015, **71**, 518–521.

242 G. Kim, S. Ahn, H. Yoon, Y. Kim and W. Chun, *J Mater Chem*, 2009, **19**, 8817–8823.

243 A. Moghanizadeh, *Manuf Lett*, 2022, **31**, 116–118.

244 A. Garg, S. S. Yerneni, P. Campbell, P. R. LeDuc and O. B. Ozdoganlar, *Advanced Science*, DOI:10.1002/advs.202201566.

245 C. Wang, Q. Zhao and M. Wang, *Biofabrication*, , DOI:10.1088/1758-5090/aa71c9.

246 B. Stolz, M. Mader, L. Volk, T. Steinberg and R. Mülhaupt, *Macromol Mater Eng*, , DOI:10.1002/mame.202000541.

247 T. Liu, B. Yang, W. Tian, X. Zhang and B. Wu, *Polymers (Basel)*, , DOI:10.3390/polym14091722.

248 W. Zhang, I. Ullah, L. Shi, Y. Zhang, H. Ou, J. Zhou, M. W. Ullah, X. Zhang and W. Li, *Mater Des*, 2019, **180**, 107946.

249 Z. Tan, C. Parisi, L. Di Silvio, D. Dini and A. E. Forte, *Sci Rep*, , DOI:10.1038/s41598-017-16668-9.

250 M. Yamanami, K. Kanda, T. Kawasaki, D. Kami, T. Watanabe, S. Gojo and H. Yaku, *Artif Organs*, 2019, **43**, 773–779.

251 T. Shin'oka, Y. Imai and Y. Ikada, *New England Journal of Medicine*, 2001, **344**, 532–533.

252 B. Patel, Z. Xu, C. B. Pinnock, L. S. Kabbani and M. T. Lam, *Sci Rep*, 2018, **8**, 1–13.

253 N. L'Heureux, N. Dusserre, G. Konig, B. Victor, P. Keire, T. N. Wight, N. A. F. Chronos, A. E. Kyles, C. R. Gregory, G. Hoyt, R. C. Robbins and T. N. Mcallister, *Nat. Med.*, 2006, **12**, 361–365.

254 R. Gauvin, T. Ahsan, D. Larouche, P. Lé, J. Dubé, F. O. A. Auger, R. M. Nerem and L. Germain, *Tissue Eng Part A*.

255 W. Jakubowska, S. Chabaud, I. Saba, T. Galbraith, F. Berthod and S. Bolduc, *Tissue Eng Part A*, 2020, **26**, 811–822.

256 C. Caneparo, S. Chabaud, J. Fradette and S. Bolduc, *Sci Rep*, , DOI:10.1038/s41598-022-25311-1.

257 W. Xu, M. Yao, M. He, S. Chen and Q. Lu, *ACS Appl Mater Interfaces*, 2023, **15**, 19966–19975.

258 C. B. Pinnock, E. M. Meier, N. N. Joshi, B. Wu and M. T. Lam, *Methods*, 2016, **99**, 20–27.

259 A. W. Justin, F. Cammarata, A. A. Guy, S. R. Estevez, S. Burgess, H. Davaapil, A. Stavropoulou-Tatla, J. Ong, A. G. Jacob, K. Saeb-Parsy, S. Sinha and A. E. Markaki, *Biomaterials Advances*, 2023, **145**, 213245.

260 S. Malladi, D. Miranda-Nieves, L. Leng, S. J. Grainger, C. Tarabanis, A. P. Nesmith, R. Kosaraju, C. A. Haller, K. K. Parker, E. L. Chaikof and A. Günther, *ACS Biomater Sci Eng*, 2020, **6**, 4236–4246.

261 C. Loy, A. Lainé and D. Mantovani, *Biotechnol J*, 2016, **11**, 1673–1679.

262 Y. Huo, Y. Xu, X. Wu, E. Gao, A. Zhan, Y. Chen, Y. Zhang, Y. Hua, W. Swieszkowski, Y. S. Zhang and G. Zhou, *Advanced Science*, DOI:10.1002/advs.202202181.

263 H. Nam, H. J. Jeong, Y. Jo, J. Y. Lee, D. H. Ha, J. H. Kim, J. H. Chung, Y. S. Cho, D. W. Cho, S. J. Lee and J. Jang, *Sci Rep*, , DOI:10.1038/s41598-020-64049-6.

264 E. Bosch-Rué, L. M. Delgado, F. J. Gil and R. A. Perez, *Biofabrication*, DOI:10.1088/1758-5090/abbd27.

265 N. Diamantides, C. Dugopolski, E. Blahut, S. Kennedy and L. J. Bonassar, *Biofabrication*, DOI:10.1088/1758-5090/ab3524.

266 Y. Takeoka, K. Matsumoto, D. Taniguchi, T. Tsuchiya, R. Machino, M. Moriyama, S. Oyama, T. Tetsuo, Y. Taura, K. Takagi, T. Yoshida, A. Elgalad, N. Matsuo, M. Kunizaki, S. Tobinaga, T. Nonaka, S. Hidaka, N. Yamasaki, K. Nakayama and T. Nagayasu, *PLoS One*, DOI:10.1371/journal.pone.0211339.

267 Z. Li, C. Ruan and X. Niu, *Med Nov Technol Devices*, 2023, **17**, 100211.

268 L. R. Versteegden, K. A. van Kampen, H. P. Janke, D. M. Tiemessen, H. R. Hoogenkamp, T. G. Hafmans, E. A. Roozen, R. M. Lomme, H. van Goor, E. Oosterwijk, W. F. Feitz, T. H. van Kuppevelt and W. F. Daamen, *Acta Biomater*, 2017, **52**, 1–8.

269 X. Zhou, M. Nowicki, H. Sun, S. Y. Hann, H. Cui, T. Esworthy, J. D. Lee, M. Plesniak and L. G. Zhang, *ACS Appl Mater Interfaces*, , DOI:10.1021/acsami.0c14871.

270 J. M. Lee, S. K. Q. Suen, W. L. Ng, W. C. Ma and W. Y. Yeong, *Macromol Biosci*, DOI:10.1002/mabi.202000280.

271 Q. Pi, S. Maharjan, X. Yan, X. Liu, B. Singh, A. M. van Genderen, F. Robledo-Padilla, R. Parra-Saldivar, N. Hu, W. Jia, C. Xu, J. Kang, S. Hassan, H. Cheng, X. Hou, A. Khademhosseini and Y. S. Zhang, *Advanced Materials*, , DOI:10.1002/adma.201706913.

272 W. Kim and G. Kim, *ACS Appl Mater Interfaces*, 2018, **10**, 41185–41196.

273 Y. Xu, D. Li, Z. Yin, A. He, M. Lin, G. Jiang, X. Song, X. Hu, Y. Liu, J. Wang, X. Wang, L. Duan and G. Zhou, *Acta Biomater*, 2017, **58**, 113–121.

274 B. C. Isenberg, C. Williams and R. T. Tranquillo, *Circ Res*, 2006, **98**, 25–35.

275 M. Kamaraj, P. S. Giri, S. Mahapatra, F. Pati and S. N. Rath, *Int J Biol Macromol*, 2022, **223**, 1405–1419.

276 P. Maghsoudlou, G. Totonelli, S. P. Loukogeorgakis, S. Eaton and P. De Coppi, *J Vis Exp*, , DOI:10.3791/50658.

277 F. Grandi, E. Stocco, S. Barbon, A. Rambaldo, M. Contran, F. Fascetti Leon, P. Gamba, P. P. Parnigotto, V. Macchi, R. De Caro and A. Porzionato, *Biomed Res Int*, DOI:10.1155/2018/7824757.

278 G. Luc, G. Charles, C. Gronnier, M. Cabau, C. Kalisky, M. Meulle, R. Bareille, S. Roques, L. Couraud, J. Rannou, L. Bordenave, D. Collet and M. Durand, *Biomaterials*, 2018, **175**, 1–18.

279 S. Barbon, A. Biccari, E. Stocco, G. Capovilla, E. D'Angelo, M. Todesco, D. Sandrin, A. Bagno, F. Romanato, V. Macchi, R. De Caro, M. Agostini, S. Merigliano, M. Valmasoni and A. Porzionato, *Cells*, DOI:10.3390/cells11192945.

280 M. Garriboli, K. Deguchi, G. Totonelli, F. Georgiades, L. Urbani, M. Ghionzoli, A. J. Burns, N. J. Sebire, M. Turmaine, S. Eaton and P. De Coppi, *Pediatr Surg Int*, 2022, **38**, 665–677.

281 Y. Zhang, X. S. Li, A. G. Guex, S. S. Liu, E. Müller, R. I. Malini, H. J. Zhao, M. Rottmar, K. Maniura-Weber, R. M. Rossi and F. Spano, *Biofabrication*, 2017, **9**, 029501.

282 O. Syed, J.-H. Kim, Z. Keskin-Erdogan, R. M. Day, A. El-Fiqi, H.-W. Kim and J. C. Knowles, *Acta Biomater*, 2019, **99**, 181–195.

283 A. J. Ryan, E. J. Ryan, A. R. Cameron and F. J. O'Brien, *Acta Biomater*, 2020, **112**, 52–61.

284 M. Tamaddon, R. S. Walton, D. D. Brand and J. T. Czernuszka, *J Mater Sci Mater Med*, 2013, **24**, 1153–1165.

285 Z. Nematollahi, M. Tafazzoli-Shadpour, A. Zamanian, A. Seyedsalehi, S. Mohammad-Behgam, F. Ghorbani and F. Mirahmadi, *Iran Biomed J*, 2017, **21**, 228–239.

286 V. Shabafrooz, M. Mozafari, G. A. Köhler, S. Assefa, D. Vashaee and L. Tayebi, *J Biomed Mater Res A*, 2014, **102**, 3130–3139.

287 M. Saito, T. Sakamoto, M. Fujimaki, K. Tsukada, T. Honda and M. Nozaki, *Surg Today*.

288 M. B. Chan-Park, J. Y. Shen, Y. Cao, Y. Xiong, Y. Liu, S. Rayatpisheh, G. C. Kang and H. P. Greisler, *J Biomed Mater Res A*, 2009, **88A**, 1104–1121.

289 M. Yang, J. Chen, Y. Chen, W. Lin, H. Tang, Z. Fan, L. Wang, Y. She, F. Jin, L. Zhang, W. Sun and C. Chen, *Adv Healthc Mater*, , DOI:10.1002/adhm.202202022.

290 Y. Kobayashi, C. E. J. Cordonier, Y. Noda, F. Nagase, J. Enomoto, T. Kageyama, H. Honma, S. Maruo and J. Fukuda, *Sci Rep*, , DOI:10.1038/s41598-019-46801-9.

291 H. Okuyama, S. Umeda, Y. Takama, T. Terasawa and Y. Nakayama, *J Pediatr Surg*, 2018, **53**, 223–226.

292 F. Fazal, F. J. Diaz Sanchez, M. Waqas, V. Koutsos, A. Callanan and N. Radacsi, *Med Eng Phys*, 2021, **94**, 52–60.

293 J. H. Park, M. Ahn, S. H. Park, H. Kim, M. Bae, W. Park, S. J. Hollister, S. W. Kim and D. W. Cho, *Biomaterials*, DOI:10.1016/j.biomaterials.2021.121246.

294 J. Y. Park, H. Ryu, B. Lee, D. H. Ha, M. Ahn, S. Kim, J. Y. Kim, N. L. Jeon and D. W. Cho, *Biofabrication*, DOI:10.1088/1758-5090/aae545.

295 W. Farhat, F. Chatelain, A. Marret, L. Faivre, L. Arakelian, P. Cattan and A. Fuchs, *Biomaterials*, 2021, **267**, 120465.

296 A. R. Raji and M. Naserpour, *Journal of Veterinary Medicine Series C: Anatomia Histologia Embryologia*, 2007, **36**, 10–13.

297 P. K. Jeffery and L. Reid, *J. Anat*, 1975, **120**, 295–320.

298 J. M. Frasca, O. Auerbach, V. R. Parks and J. D. Jamieson, *Exp Mol Pathol*, 1968, 363–379.

299 W. S. Kim, J. W. Chang, W. S. Jang, Y. J. Seo, M. L. Kang, H. J. Sung, D. H. Kim, J. M. Kim, J. H. Park, M. J. Ban, G. Na, S. H. Shin, H. K. Byeon, Y. W. Koh, S. H. Kim, H. K. Baik and E. C. Choi, *Sci Rep*, DOI:10.1038/s41598-017-10733-z.

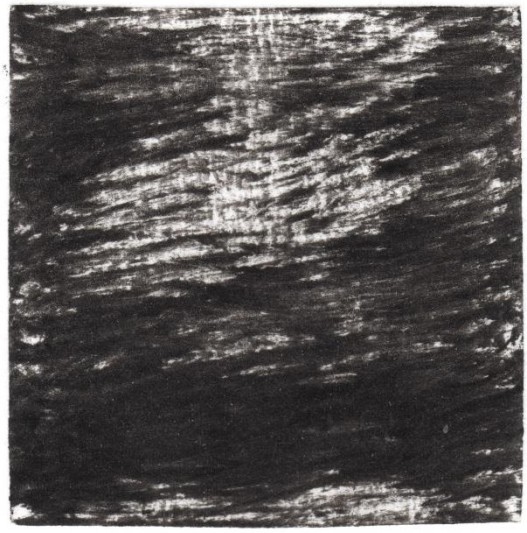

Chapter II

State diagrams of collagen

“*Le monstre est celui qui vit en transition. Celui dont le visage, le corps et les pratiques ne peuvent encore être considérés comme vrais dans un régime de savoir et de pouvoir déterminés.***”**

— Paul B. Preciado

1. Introduction

Type I collagen type is the first "brick" of the ECM, and constitutes its most abundant element. In particular in tubular tissues, collagen—paired with other biological components—provides mechanical support, hierarchical structure, and a suitable environment for the adhesion and proliferation of several cell types. Recapitulating the characteristics of native collagen promises to provide the necessary biological and mechanical properties to the biointegration and functionality of new tissue-engineered materials. A vast array of elaboration techniques is reported in the literature to design collagenous materials for this purpose. Understanding the underlying mechanisms that trigger the formation of fibrillar collagen, *i.e.* the physico-chemical parameters that regulate the self-assembly of collagen molecules *in vitro*, is thus of paramount importance in the design of innovative fabrication protocols.

The process of self-assembly describes the spontaneous organization of molecules into well-defined structures that display enhanced stability. At thermodynamic equilibrium, the creation of non-covalent bonds between collagen molecules leads to the formation of supramolecular assemblies, under precise conditions of temperature, concentration. This phenomenon is further modulated by other factors such as pH, osmotic pressure, and ionic strength. Historically, the analysis of the supramolecular assemblies of collagen molecules has been anchored on the analogy to liquid-crystals, explaining how collagen behaves under certain physicochemical conditions and how these result in materials that mimic the properties of a given tissue[1]. The dependence of tissue properties on the collagen arrangement has been largely demonstrated, with a wide spectrum of structures depicted, from plywood (cornea), helicoidal (compact bone), to a random distribution (dermis)[1]. These conformations were shown to be regulated by the acid[2] and the collagen concentrations[3], among other parameters. A local change of these conditions *in vivo* may be the reason of dysfunctional self-assemblies, leading to local pathologies (keratoconus[4] and fibrotic tissue[5]) to extended and more severe diseases (cancer[6], diabetes and Ehler-Danlos syndrome[7]).

However, in the domain of biomaterials, the structural complexity of collagen fibrils is rarely reconstituted. The delicate self-assembly mechanism spreads at every hierarchical level, from the amino acid sequence to the formation of fibrillar patterns. Reproducing such complexity during material processing requires a precise control over each step, physicochemical parameters, as well as relevant characterization techniques. The fabrication methods described in the previous chapter, including electrospinning, ice-templating, or 3D-printing, involve harsh processing conditions. In most cases, they lead to the degradation of collagen molecules, hindering their ability to reform native-like fibrils. This underlines the lack of knowledge regarding the critical parameters affecting collagen integrity and physicochemical state, resulting in current biomaterials that do not mimic tissues in their

entire complexity. In this chapter, we propose to partially bridge this gap, by delving into how concentration, temperature, and physico-chemical parameters act on the self-assembly of collagen molecules. From our experiments, we draw the state diagrams of collagen that propose clear guidelines in the elaboration of biomimetic materials. We describe the organization of collagen as a function of temperature and concentration for the first time, in both acido-soluble and fibrillar type I collagen. We depict the thermal boundaries based on differential scanning calorimetry measurements, as well as scattering experiments and transmission electron microscopy. These tools deepen the understanding of the self-assembly mechanisms in dense solutions and fibrillar conditions, and present the relation between molecular staggering, fibril size and arrangement, and well-defined conditions of pH, ionic force, concentration and temperature. Unveiling this might set new frameworks in the elaboration of collagenous biomaterials, which enables to reach properties of a target tissue. Beyond the fundamental aspects that this work has uncovered, it promises the development of better biomimetic *in vitro* models and prosthetic grafts.

2. Manuscript to be submitted *Nature Materials*

State diagrams of type I collagen for the rational design of biomimetic materials

Isabelle Martinier[1], Sylvain Deville[2], Gervaise Mosser[1], Léa Trichet[1], Patrick Davidson*[3] and Francisco M. Fernandes*[1]

[1]Chemistry of Condensed Matter Laboratory (LCMCP), Materials and Biology group - Sorbonne Université, Paris, France

[2]Institut Lumière Matière (ILM), Université Claude Bernard Lyon 1 - CNRS, Villeurbanne, France

[3]Laboratoire de Physique des Solides (LPS) - Paris-Saclay Université, Orsay, France

e-mails: patrick.davidson@universite-paris-saclay.fr, francisco.fernandes@sorbonne-universite.fr

A. Introduction

In vivo, the supramolecular assembly of type I collagen molecules into fibrils underpins the formation of the Extracellular Matrix (ECM), a central aspect of tissue morphogenesis and remodeling. This process occurs in a narrow range of physicochemical conditions (temperature, concentration, and ionic strength) that are defined by the physiology of the cells and by the composition of the extracellular environment. We will henceforth refer to this set of conditions as the *physiological physicochemical range.* The current paradigm in collagen-based biomimetic materials states that reproducing the same physicochemical conditions *in vitro* as *in vivo*, is the key to mimicking the architecture—and functions—of biological tissues[1]. This approach is gaining traction as it promises to tailor materials for applications such as 3D cell culture models[2] or prosthetic grafts[3,4].

The state of the art is rich in reports describing biomaterials built with collagen as the central building block to mimic the ECM. *In vitro*, fibrillogenesis, the transformation of collagen solutions into fibrillar gels, is an entropy-driven process that occurs above 1 nM through a change in pH or ionic strength[5]. This step triggers the formation of fibrils, which are the building blocks recognized by cells and that contribute to the mechanical properties of tissues. In fibrils, hydrated type I collagen molecules are arranged in a regular staggered parallel pattern, with an axial periodicity of 67 nm known as the D-banding period[6]. Preserving this subtle self-assembly in material fabrication techniques requires a deep understanding of its mechanisms. Molecular and supramolecular order is determined by weak interactions between collagen molecules—electrostatic, van der Waals, hydrophobic, and hydrogen-bonds[7]—and follows a liquid-crystal-like behavior, as first described by Y. Bouligand[8]. Since then, the fluid phases of collagen (isotropic, nematic, cholesteric), which occur in the vicinity of the physiological physicochemical range, have been explored for a wide

range of collagen concentrations[9], acid types and their respective concentrations[10,11], using microscopy tools (polarized light optical microscopy, PLOM, and transmission electron microscopy, TEM[9,12–14]).

In parallel, the development of biomimetic collagenous materials has increasingly been coupled with materials processing techniques such as ice-templating[15–21], electrospinning[22,23], spray-drying[24,25], 3D bioprinting[26–30], electrochemically aligned collagen (ELAC)[31] or cell-mediated tissue engineering[32,33]. Many of these reports refer to concentrations below those of native tissues and processing temperatures above the denaturation temperature of collagen molecules, resulting in particularly expensive gelatin-based materials as discussed elsewhere[34]. The native structures of collagen are thus rarely achieved by most of materials engineering strategies, due to a large gap between the bioengineering community and the basic research community focused on biological self-assembly mechanisms (structural biologists, biochemists and biophysicists). As a result, there is a significant lack of guidance on how to preserve the *physiological physicochemical range* in harsh processes aimed at mimicking biological tissues[35]. Incorporating the conditions that ensure collagen self-assembly into harsh processing strategies that rely on drastic temperature and concentration changes (e.g. evaporation or phase separation induced by ice growth) remains a major challenge. Simply put, the underlying question can be formulated as follows:

How can the weak interactions that govern the supramolecular assembly of collagen be preserved under the harsh conditions of material shaping processes?

To answer this question, we have carried out a comprehensive investigation of the molecular and supramolecular states of acid-soluble collagen over a wide range of concentrations and temperatures. We draw, for the first time, a state diagram of collagen that encompasses the extreme concentrations and temperatures that characterize materials fabrication processes. Here, we explore the thermal events that determine the different state transitions of acid-soluble collagen, such as denaturation (on heating), crystallization and vitrification (on cooling), together with a concentration-dependent molecular to fibrillar transition. Using differential scanning calorimetry (DSC), rheological analysis, small- and wide-angle X-ray scattering (SAXS and WAXS, respectively) together with TEM, we have determined the characteristic temperatures of the system, as well as the supramolecular order of collagen molecules and fibrils.

The new constitutive state diagrams, both in solution and after fibrillogenesis, are novel tools to rationalize the design of collagen-based biomimetic materials. We anticipate that the fundamental insights drawn in this work will guide the processing strategies to develop materials with features that will approach, to a further extent, the outstanding properties of the ECM.

B. Results and Discussion

a. The state diagram of type I collagen in acidic solution

The state diagram of collagen in solution was studied over a wide range of concentrations, between 5.6 mg.mL^{-1} and 1350 mg.mL^{-1} (Fig. 1-A and B), and temperatures, between -80 and 80 °C. To investigate the collagen supramolecular arrangement as a function of the concentration samples at 40, 200, 400 and 900 mg. mL^{-1} were observed by PLOM between cross polarizers. At 40 mg.mL^{-1} samples showed no birefringence, confirming the isotropic arrangement of collagen molecules in solution at low concentration. The birefringence of samples at concentrations of 200 mg.mL^{-1} and above (Fig. S1) confirmed the presence of domains of aligned collagen molecules, in agreement with the widely described lyotropic liquid crystalline behavior of acid-soluble collagen[14,35,36]. Although the birefringence can be clearly observed above 200 mg.mL^{-1}, the large sample thickness, around 200 m, hindered the visualization of the fingerprint patterns characteristic of collagen mesomorphic phases. Phase contrast microscopy images (Fig. S1) confirm that the system is already heterogeneous at 200 mg.mL^{-1}, with the detection of bundles that become increasingly intertwined and crowded at higher concentrations. These observations confirm the formation of complex aggregates of aligned collagen molecules, which are birefringent and have an optical refraction index different from that of the solution, as previously demonstrated for different acidic conditions[11].

To probe the D-banding period and the intermolecular packing distance, we performed respectively SAXS and WAXS experiments over the whole collagen concentration range (Fig. 1-C). No diffraction peaks appear in the SAXS signal at 40 mg.mL^{-1} and only two weak peaks are observed at 200 mg.mL^{-1}, demonstrating the lack of long-range order. A different behavior is observed at 400 and 900 mg.mL^{-1} where twelve equidistant diffraction peaks are detected, a signature of the 67 nm axial period found in native collagen fibrils[37]. Regardless of the dimensions and organization of the measured objects—fibril-like, pre-fibrils, or fibrils—these data demonstrate that 3D objects with a hierarchical organization are directly formed from collagen solution without pH or ionic strength variation. To our knowledge, this is the first report of a spontaneous transition from a molecular to a supramolecular organization of collagen molecules in hydrochloric acid solution[vi].

We probed the molecular packing between adjacent collagen molecules, and thus the compacity of the fibrillar units, using WAXS. As collagen concentration increased the peak shifted to higher scattering angles, indicating that the molecules become more tightly packed, reaching a final distance of 1.36 nm at 900 mg.mL^{-1}. The molecular crowding resulting from increasing collagen

[vi] However, SAXS experiments conducted in acetic acid at a concentration of 500 mM, have revealed the presence of the characteristic 67 nm period at 145 mg.mL^{-1}. The shift in the concentration at which collagen assembles to form supramolecular objects is known to be modified by the type of acid and its concentration[10].

concentration induces the formation of ordered molecular aggregates that reproduce the characteristic distances of native collagen fibrils, both in their D-banding pattern and in their intermolecular distances[10]. These changes at the molecular scale are accompanied by a sharp increase in the G' and G'' values above 430 mg.mL^{-1} (Fig. S2). In addition to the characteristic distances deduced from the scattering experiments and the emergence of a gel-like behavior, ultrathin sections of 200, 400, and 900 mg.mL^{-1} samples were observed by TEM (Fig. 1-D). At 200 mg.mL^{-1}, low-contrast objects are observed, with a section of 30 nm, suggesting the formation of supramolecular assemblies of collagen molecules. This observation confirms the WAXS data showing the lateral packing of collagen molecules. At higher concentrations (400 and 900 mg.mL^{-1}), the observation of dense networks of nanofibrils confirms the characteristic 67 nm period measured by SAXS.

The results above, obtained at room temperature, were inserted in the temperature *vs* concentration state diagram of type I collagen in acidic solution (Fig. 2). In this diagram, we report the molecular organization of collagen as a function of concentration and temperature, both in a vast range. Contrary to the phase diagrams of collagen solutions reported to date—based on the characterization of the different mesophases as a function of acid concentration and ionic strength[10,38]—here we consider non-thermodynamic transitions like the molecular to fibrillar transition and vitrification, and other transformations, such as collagen denaturation. In solution collagen triple helices are thermally denatured when heated above ~37 °C and between 50 °C and 60 °C for fibrillar collagen. Upon heating, the dissociation of the triple helices—assimilated to a melting process[39]—produces gelatin, which prevents the re-formation of the native fibrillar ultrastructure. Up to 100 mg.mL^{-1}, the denaturation temperatures are close to 40 °C, corresponding to the denaturation of collagen in its molecular form[40]. For concentrations between 200 and 400 mg.mL^{-1}, two denaturation processes were detected (Fig. S3-A). In this range, the upper denaturation temperature values are close to those found for collagen in its fibrillar form, confirming the existence of an ordered phase arising in solution, as inferred from the SAXS measurements. We hypothesize that for 200 and 400 mg.mL^{-1}, the lowest denaturation temperature corresponds to the denaturation of collagen under its molecular form and the highest to an acidic fibrillar form. These observations lead to five distinct domains in the phase diagram of type I collagen in solution. A region, above the denaturation temperature, corresponds to the denatured form of collagen (D), *i.e.* gelatin, and three adjacent regions below the denaturation line, correspond to molecular collagen (M), the coexistence of fibrillar collagen and denatured collagen (F+D), and a single acidic fibrillar collagen phase (F). The existence of a domain composed of F and D phases (between 40 and 60 °C), suggests that, below the denaturation temperature of collagen in its molecular form, there is a domain where collagen in its molecular and fibrillar form coexist. This domain, not previsouly reported, is limited by an upper temperature corresponding to the denaturation of molecular collagen, a lower temperature defined by the liquidus line in a concentration regime between 200 and 400 mg.mL^{-1}. A large array of materials processing techniques applied to collagen in solution results in a progressive increase of collagen concentration. Based on the different concentrations reached during these fabrication processes,

awe are now able to pinpoint the supramolecular state of collagen, opening a rational path do design biomimetic materials.

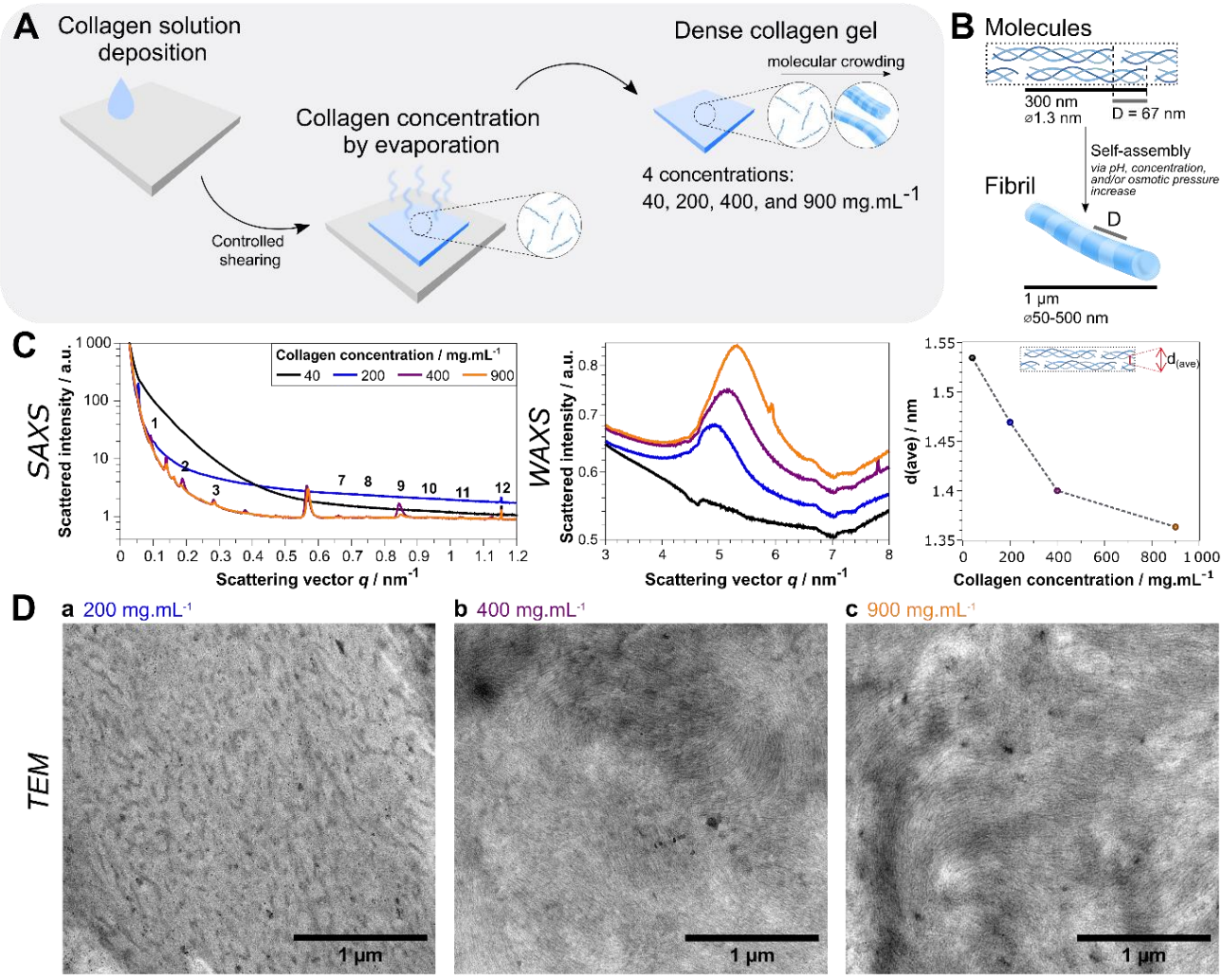

Fig. 1. The supramolecular organization of type I collagen is determined by its concentration. Preparation and characterization of dense collagen samples at four concentrations: 40 (**a**-black), 200 (**b**-blue),400 (**c**-purple), and 900 mg.mL^{-1}(**d**-orange). **A**) Thin films of dense collagen were prepared by drop casting, followed by shearing and controlled evaporation of the solvent. **B**) Scheme of the fibrillogenesis process *in vitro*. Characteristic dimensions were taken from Fratzl and Weinkamer[41]. **C**) Varying the concentration of collagen yields a range of different ultrastructures, characterized by small angle (left) and wide-angle X-ray scattering (middle). The dependence of the intrafibrillar lateral packing distance $d_{(ave)}$ (extracted from WAXS data) with concentration is shown on the right-hand side. (The artefacts observed at q = 7 nm^{-1} are due to the multichip nature of the detector.) **D**) TEM images of collagen in 3 mM HCl solution, as a function of the collagen concentration.

DSC experiments were also carried out to investigate the interactions of the solvent-solute system during freezing, a temperature regime that has been largely neglected in the literature. Solutions of different concentrations were frozen from 20 °C down to -80 °C to assess the crystallization temperature of free water (Fig. S3-B). When cooling down collagen samples, in a concentration range between 5.6 and 530 mg.mL^{-1}, the formation of ice nuclei and their subsequent

growth occurs at the solvent crystallization temperature lowered by the corresponding cryoscopic depression, defining the *liquidus* line. Since collagen, like most molecular and ionic species, is insoluble in ice, molecules are progressively expelled from the ice phase and concentrated in between the ice crystals at a *critical collagen concentration.* This concentration can be determined by DSC, as it results in the absence of an exothermic water crystallization peak, and was measured at 530 mg.mL^{-1} (Fig. S3-C). We consider this concentration as the point at which all remaining water is bound to collagen and cannot be further displaced to form ice crystals even at temperatures as low as -80°C. The absence of crystallization above this concentration suggests that a single phase composed of collagen and bound water exists between the denaturation temperature and -80°C.

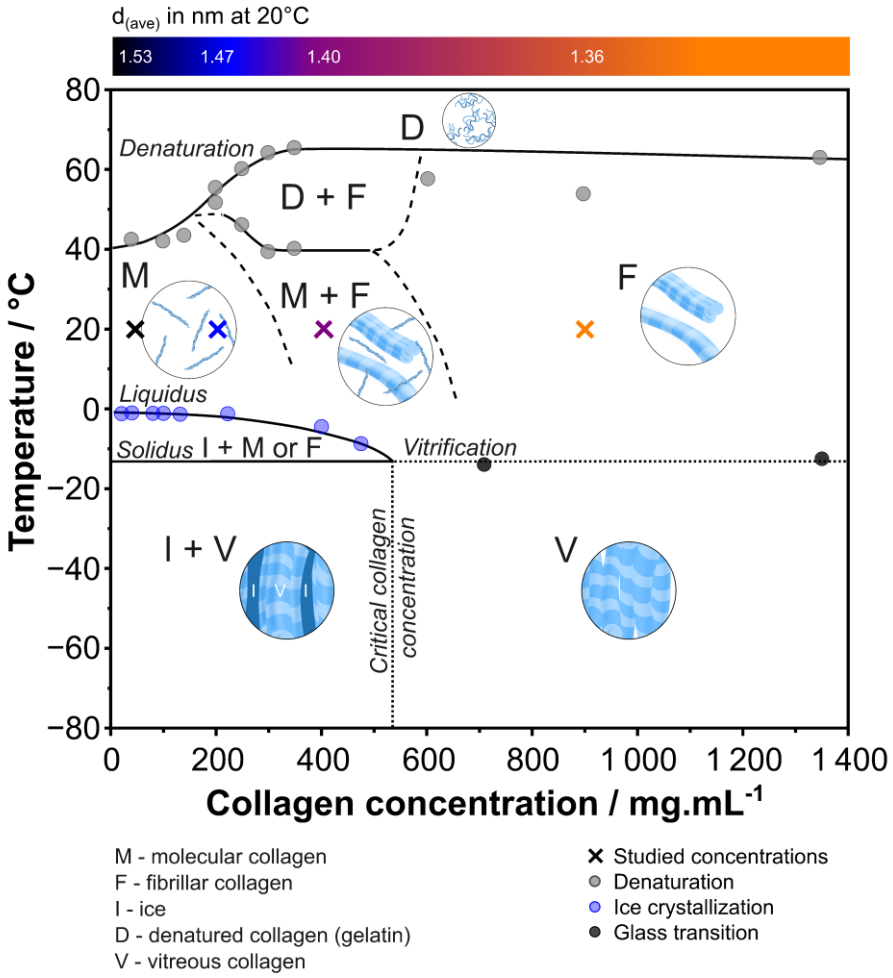

Fig. 2. State diagram of acid-soluble type I collagen. The diagram combines data obtained from DSC, mDSC, SAXS, and WAXS. Details of the measurements used to describe the various state transitions are given in Fig. S3.

We hypothesize that cooling collagen solutions above the critical concentration results in the formation of a vitreous state composed of collagen fibrils and disordered bound water. To verify this hypothesis, we measured the glass transition temperature (T_g) by modulated DSC (mDSC).

The T_g for 704 mg.mL^{-1} was measured at $T_{g,704}$ = -13.9 °C (Fig. S3-D.b), a value remarkably close to that measured for dry collagen, at $T_{g,1350}$ = -12.5 °C, measured by dynamic mechanical analysis (DMA). Taken together, the data set obtained by SAXS, WAXS, DSC, mDSC and DMA lead, for the first time, to a complete picture of the different organization states of collagen over a wide range of concentrations (from 5.6 to 1350 mg.mL^{-1}) and temperatures (from -80 to 80 °C). The state diagram provides a fundamental tool to describe collagen in solution, and it unveils the temperature and concentration-dependent self-assembly mechanisms that can prove instrumental in designing processing strategies to obtain materials that mimic the ECM.

b. The state diagram of fibrillar collagen

Collagen fibrils are the central building block of native tissues. The previous results establish guidelines for handling collagen in solution, but they are insufficient to provide insights for collagen in its fibrillar form. Moreover, some materials processing techniques deal with previously fibrillated collagen materials, notably by compression[42,43]. To build a state diagram for fibrillar collagen, we immersed the collagen samples into PBS 10x for 24 hours to induce fibrillogenesis (Fig. 3-A). Observed under the TEM, negatively stained samples prepared at room temperature revealed fibrils with the typical D-banding pattern for all concentrations (Fig. 3-B). At low concentrations, small randomly dispersed fibrils are observed, whereas at 200 and 400 mg.mL^{-1} the resulting network is denser and composed of large striated fibrilsAt 900 mg.mL^{-1}, a tight network of nanofibrils forms, with barely visible striations. The reduced size of the fibrils is ascribed to the limited mobility of collagen molecules in solution at increasingly high concentrations, as confirmed by rheology measurements (Fig. S2). Such hindered mobility during fibrillogenesis results in the formation of smaller fibrils, featuring a smaller number of repeating units.

Observation of the samples by PLOM shows that, qualitatively, the birefringence increases with increasing concentration (Fig. S4). Moreover, samples at lower concentration (40 and 200 mg.mL^{-1}) show a large contrast in light transmission depending on the angle between the substrate and the polarizer direction, indicating that the collagen is macroscopically aligned by surface effects. We hypothesize that, due to the higher packing and therefore limited mobility at high concentration, the chirality-induced twist of the collagen fibrils would be confined to the boundaries between domains, as suggested by de Sa Peixoto *et al*[11]. This would lead to sharp twists in molecular alignment between domains, as found in plywood models.

At all concentrations investigated, the SAXS patterns of the samples show diffraction peaks corresponding to the characteristic D-banding of collagen fibrils. The positions of the diffraction peaks remain constant, but the peaks become sharper above 40 mg.mL^{-1} until 400 mg.mL^{-1}, while at 900 mg.mL^{-1} the reflection width becomes larger. Altogether, the SAXS data correlate with the observations made by TEM. The relative intensities of the 67 nm harmonics depend on the concentration. In particular, at a concentration of 400 mg.mL^{-1}, extinctions are observed for many peaks, such as the 4th and 5th orders, while the 6th order has an exceptionally high intensity. This

peculiar behavior is reminiscent of previous observations of pathological fibrotic tissues (scars, burns or diabetic patients' skin[44–46], which show similar atypical patterns. In contrast to acid-soluble collagen, the average distance between the centers of the molecules, calculated from WAXS experiments at $d_{(ave)}$ = 1.36 nm, is independent of the concentration. This observation suggests that fibrillogenesis results in a robust supramolecular assembly irrespective of the concentration. Interestingly, these values perfectly match the one found for collagen in solution at 900 mg.mL^{-1}, proving that the crowding effect in solution suffices to assemble collagen molecules into tightly packed fibrils in the absence of a pH increase and at low osmolarity.

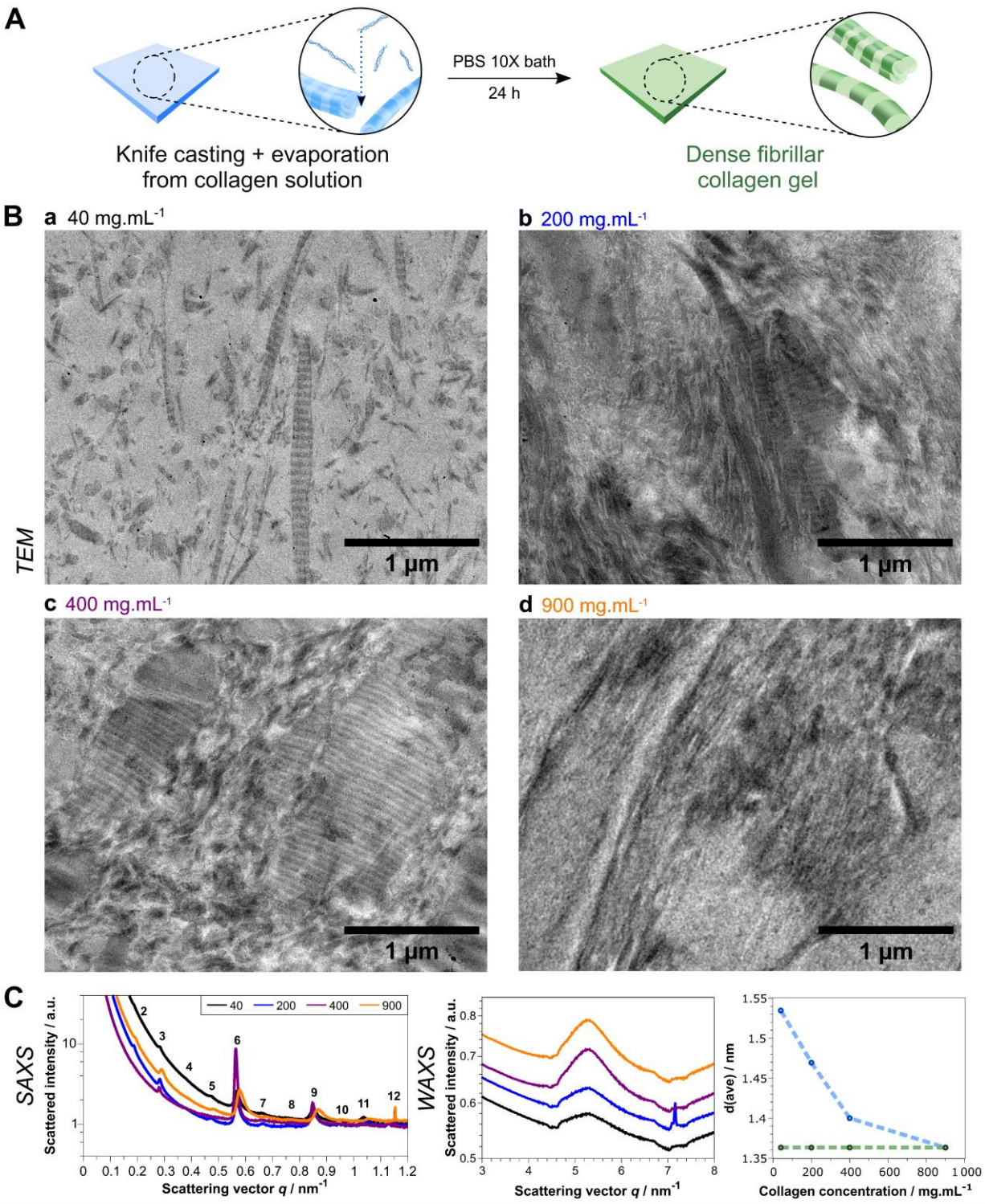

Fig. 3. Elaboration and characterization of self-assembled dense collagen samples. A) Samples were immersed in a PBS 10x for 24 h. Four concentrations were studied: 40 (**a**-black), 200 (**b**-blue), 400 (**c**-purple), and 900 mg.mL^{-1} (**d**-orange). **B**) TEM images of the samples displaying fibrils, and their arrangement as a function of collagen concentration. **C**) Left: Fibril formation was confirmed for all collagen concentrations by the native-like long-range order measured by SAXS. Middle: The molecular packing studied by WAXS is characterized by a constant average distance between fibrils, $d_{(ave)}$ = 1.36 nm, independent of the initial concentration. Right: concentration dependence of $d_{(ave)}$ for collagen in solution (blue points) and in fibrillar form (green points).

In parallel to the state diagram built for acid soluble type I collagen, we have built the state diagram of fibrillar collagen based on thermal analysis conducted by DSC and mDSC. The denaturation temperature, T_d, of fibrillar collagen is approximately 55°C, which is similar to that of collagen in acidic solution at high concentrations. This similarity further supports the idea that a fibrillar state of collagen can be obtained from solution at high concentrations.

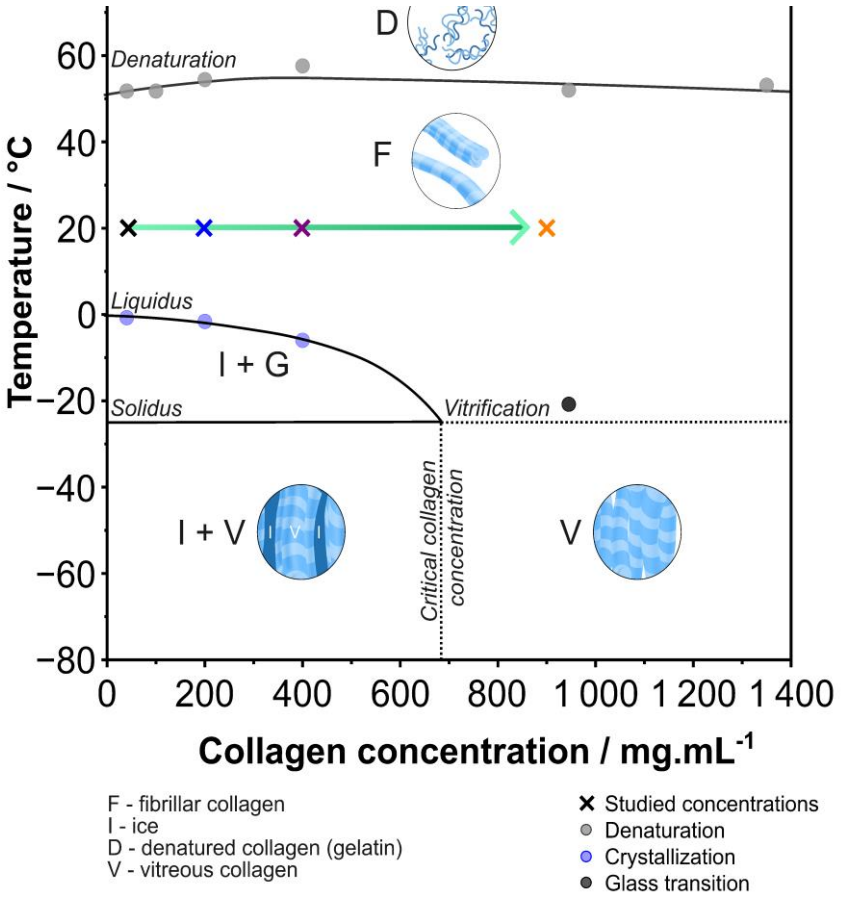

Fig. 4. State diagram of fibrillar type I collagen. Dense collagen samples were fibrillated by immersion in 10x PBS. Details of the measurements used to describe the various state transitions are given in Fig. S5. Green arrow: path describing compression-based processing tachniques[47].

As for the state diagram of collagen at low temperature, we have followed the heat exchanges during freezing using DSC, which allows to determine the characteristic crystallization temperatures of collagen gels. The crystallization events, measured up to 400 mg.mL^{-1}, were fitted with the modified Schroder-van Laar equation[48]. We estimated that the critical collagen concentration for fibrillar collagen should be somewhere above 400 mg.mL^{-1}, the highest concentration at which water crystallization was observed. Above this critical concentration, fibrillar collagen solutions will turn directly into a vitreous state at a temperature T_g of -25 °C (Fig. S5-C). We have estimated the collagen critical concentration in its fibrillar form from the intersection of the T_g line and the fit of the liquidus data points, which should be close to $[col_{gel}]_{crit} = 680\, mg.mL^{-1}$. Fibrillar collagen, due to the lateral association between adjacent collagen molecules, exposes fewer sites for interaction with bulk (or free) water molecules than its

molecular counterpart. As a consequence, for the same analytical concentration, fibrillar collagen has a higher content of free water than collagen in solution. This explains why a larger quantity of free water can be frozen in fibrillar collagen gels than in the solvated counterpart. The critical collagen concentration scales in proportion to the amount of frozen water, $[col_{gel}]_{crit} = 680\ mg.mL^{-1}$ for fibrillar collagen and $[col_{sol}]_{crit} = 530\ mg.mL^{-1}$ for collagen in soulution.

Upon heating or cooling, all the characteristic temperatures of the state diagram are constant regardless of the collagen concentration, except for the *liquidus* curve, which depends on the cryoscopic depression induced by the solutes. The invariance of the temperatures with collagen concentration, in particular the denaturation temperature T_d, indicates that the collagen fibrils have comparable thermal stability, irrespective of the concentration, contrary to what has been previously reported[49].

These observations clarify the effects on the thermal stability of collagen fibrils of two variables that are usually intertwined: their size and their intrafibrillar molecular packing. The data collected here, in which the fibril size is variable (as observed by TEM) but the intermolecular packing is constant (as observed by WAXS), allow to pinpoint the primordial role of the molecular packing on the thermal stability of collagen fibrils. In addition to the fundamental aspects of collagen fibril stability discussed above, it seems clear that post-fibrillogenesis processing of collagen does not affect its molecular packing and thus the thermal stability of the resulting materials. This observation is particularly relevant to shaping processes such as compression (Fig. 4, green arrow)[50].

c. Application of collagen state diagrams to the rational design of biomimetic materials

Taken together, the state diagrams described above define the conditions of temperature and concentration that control the molecular integrity and hierarchical organization of collagen, from the molecular packing distances up to the emergence of discrete fibrillar objects. This knowledge provides a new framework for building biomimetic materials that recapitulate the cellular micro-environment, both in terms of composition and functional properties. By tuning temperature and collagen concentration, and by considering the various state transitions mentioned above, the processes required to achieve the properties of native collagenous tissues can be rationalized. To illustrate this approach, we have used the state diagram of acid-soluble collagen to follow the events that occur during ice templating of a collagen solution at 40 mg. mL^{-1}, in 3 mM HCl.

On cooling, from the first moments of ice formation, the local collagen concentration gradually increases along the *liquidus* line until it reaches the *critical concentration* of 530 $mg.mL^{-1}$, at -12 °C. To visualize the events associated with this process, we have conducted controlled freezing of a collagen solution containing Rhodamine-B enclosed in a Hele-Shaw cell by sliding the sample from a hot plate at 20 °C to a cold plate at -30 °C under a cryoconfocal microscope[51] (Fig. 5-C.a and Video

S1). This series of events was plotted on the state diagram of collagen in solution to illustrate how the local composition of the collagen-rich fraction during freezing evolves (blue line in Fig. 5-A).

After the freezing process we stabilized the collagen phase by topotactic fibrillogenesis[15–17]. Holding the sample at -5 °C after freezing allows the ice phase to remain stable until it comes in contact with the PBS solution. At this point, the pH change and the cryoscopic depression caused by the buffer triggers the fibrillogenesis of the collagen-rich fraction and the thawing of ice crystals, respectively. The relative kinetics of these events determines the ability of the process to stabilize the collagen walls and prevent their swelling. These two events were captured as image sequences (Video S2), allowing to measure their local velocity (Fig. 5-D.b,c). Fig. 5-E shows the progression of the ice thawing front (1st front) and the PBS diffusion front into the collagen walls (2nd front), as a function of time. Comparing these two fronts reveals that the ice thawing proceeds slightly faster than the PBS diffusion within the collagen walls. Although this difference seems modest, it has a significant impact on the interstitial zone, which undergoes partial swelling and redilution, bringing the local collagen concentration from 530 mg.mL^{-1} reached after freezing (Fig. 5-C,D) to 230 mg.mL^{-1} after fibrillogenesis.

The stabilization of collagen molecules into fibrils was confirmed by TEM (Fig. 5-F). The resulting gel shows a dense network composed of tightly packed fibrils of different sizes, reminiscent of the features observed at 200 mg.mL^{-1}(Fig. 3-B.b). Larger bundles are found at the interface with the pores (bottom-right of the TEM image), where the re-dilution provides greater mobility for the molecules to self-assemble into larger supramolecular structures. A few cross-striated fibrils were also found across the walls. However, most assemblies are too small to generate the D-banding pattern, owing to the high density of collagen molecules. It is noteworthy that the harsh conditions of freezing do not alter the ability of collagen to form native-like fibrils when combined with appropriate fibrillogenesis conditions.

In addition to the ice templating process, the impact on the state of collagen can be assessed for other material processing strategies using the state diagrams described above. Electrospinning[22], electroconcentration[31], and spray drying[24,25] are evaporation-based processes that have been successfully applied to the production of collagen materials at ambient temperature. In both cases, these transformations can be described as a horizontal line in the state diagram of collagen in solution, starting from the initial concentration (Fig. 5, blue arrow). We therefore anticipate that these processes have led to a sol-gel transition associated with tighter molecular packing during evaporation. Post-fibrillogenesis processes can also be interpreted as specific trajectories in the state diagram of fibrillar collagen. Among these, one of the most important is compression, where a mechanical constraint is applied to increase the concentration of fibrillar collagen gels to a desired value[43,50] (Fig. 4, green arrow). Unlike solution-based processes, compression-based processes do not impose a significant change in the collagen organization in terms of molecular packing. The ability to interpret the effects of different processing strategies on the state of collagen using the diagrams described above provides an instrumental tool to guide the design of new collagen-based biomimetic materials.

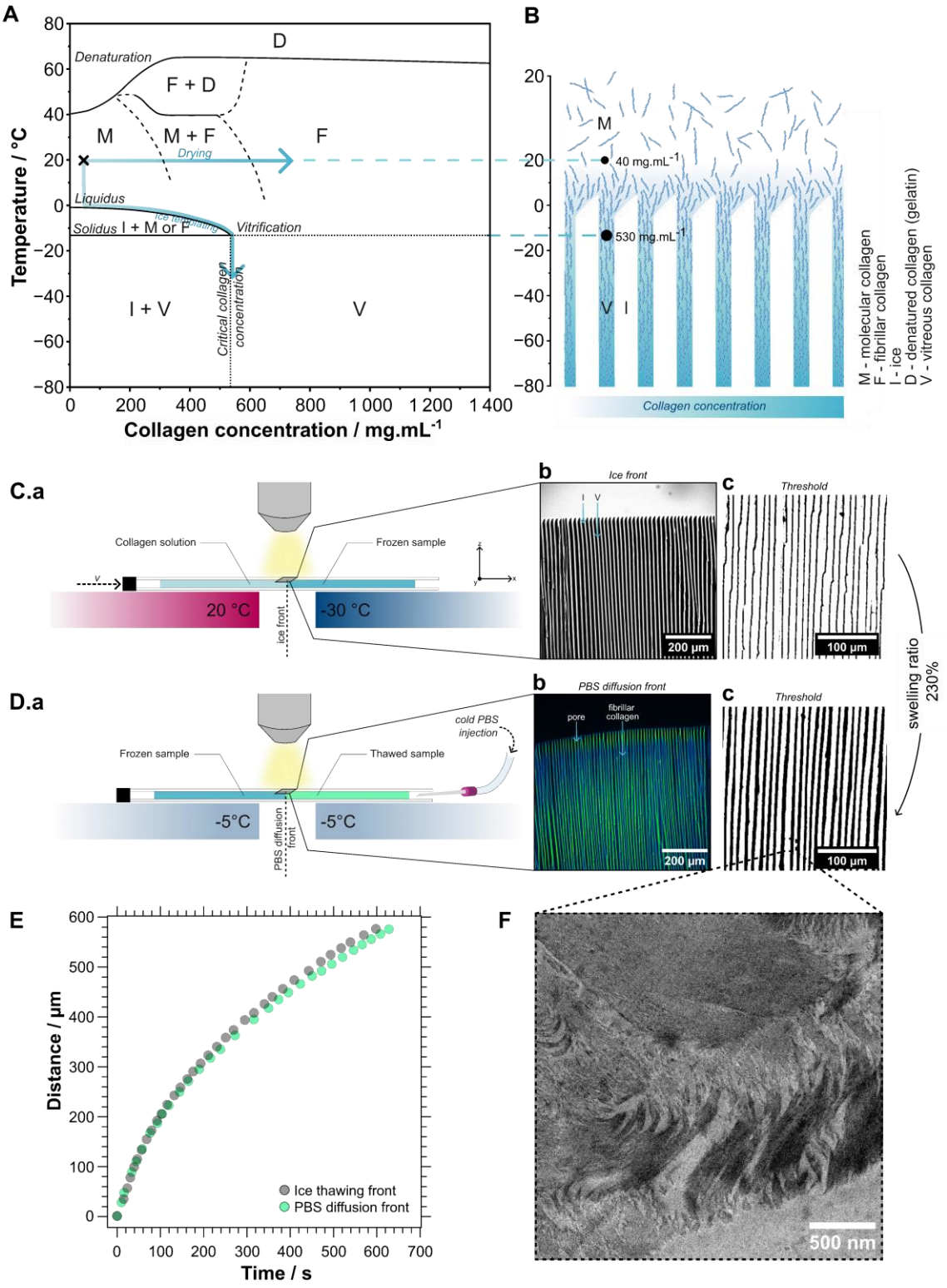

Fig. 5. ***In situ*** **cryoconfocal analysis of directional freezing and fibrillogenesis of a collagen sample at 40 mg.mL^{-1}. A)** Blue arrows track the fate of collagen in solution during drying (upper horizontal arrow) and ice templating (lower arrow). **B)** At 40 mg.mL^{-1} and 20 °C, collagen is in a molecular state. Below -1 °C, ice nucleates and grows into lamellar structures that expel collagen. In the interstitial space, collagen concentration increases, reaching the critical concentration of 530 mg.mL^{-1}. **C) a.** The cryoconfocal set-up allows to freeze a solution by sliding samples between defined thermal boundary conditions (from 20 to -30 °C, 2 mm apart). **b.** Fluorescence image of a frozen sample showing the collagen solution (light gray) and the

ice (black) fraction. **c.** Segmented image depicting the extent of phase separation. **D) a.** *In situ* topotactic fibrillogenesis of frozen collagen using PBS 10x solution, at a constant temperature of -5 °C, under the cryoconfocal microscope. **b,c.** Fluorescence and segmented image obtained after in situ fibrillogenesis. **E)** In situ measurement of the topotactic fibrillogenesis process allows to identify the kinetics of ice melting (1st front) and fibrillogenesis (**E**-2nd front). The TEM image of the fibrillated collagen wall (**F**) shows a dense network of small fibrils and demonstrates that the collagen can still self-assemble into fibrils by exposure to PBS 10x after ice templating.

C. Conclusions

To the best of our knowledge, our study is the first to report the state diagrams of collagen in solution and in its fibrillar form in a particularly wide range of concentrations and temperature, from 40 to 900 mg.mL^{-1} and from -80 to 80 °C.

In solution, at temperatures above 40 °C, collagen molecules denature into gelatin, preventing spontaneous self-assembly. Upon freezing, collagen segregates between ice crystals along the *solidus* line and gradually concentrates until a solubility limit, called the *critical collagen concentration*, at 530 mg.mL^{-1} is reached. While crossing this vertical line at low temperature, collagen reaches a vitreous state. At higher temperatures, above the *solidus*, increasing the concentration of collagen induces the formation of fibril-like structures. Scattering experiments, combined with microscopy techniques (PLOM, TEM), confirmed the self-assembly of molecules at concentrations ranging from 200 to 530 mg.mL^{-1}.

Similarly, we built the state diagram of fibrillar collagen, induced by immersion in PBS 10x. For each concentration, the formation of cross-striated native-like fibrils was confirmed by both SAXS experiments and TEM imaging. In addition, immersion in PBS 10x results in a constant intrafibrillar packing distance across the entire concentration range. This fibrillogenesis process therefore leads to the formation of well-ordered supramolecular organizations, regardless of the initial concentration.

We anticipate that the state diagrams of collagen will provide guidance for the rational design of biomimetic materials built from the main protein of the ECM, ensuring that the features responsible for achieving the native ultra-structure of collagen are preserved. For example, ice templating provides a convenient way to segregate collagen between ice crystals, locally reaching very high concentrations. In addition, it allows for control over the material texture, which combined to topotactic fibrillogenesis ensures the formation of fibrillar collagenous materials, a step forward in mimicking organ structure and function. The state diagram of collagen in solution allowed to follow these events in detail and to describe the organization of the protein throughout the different stages of fabrication. The state diagrams obtained in this work also provide keys to rationalize fibrillar collagen compression processes. Finally, our approach can be extended to other biomolecules, including fibroin, fibrin/fibrinogen, chitin/chitosan and keratin. Such diagrams would improve our understanding of the conditions that govern their organization, and thus how

close they are able to mimic the native tissues they derive from. We expect that such a predictive power will become instrumental in designing new materials processing strategies in the field of biomaterials.

D. Acknowledgements

The authors kindly acknowledge C. Djédiat for the preparation of TEM samples, and SOLEIL for provision of synchrotron radiation facilities (under the approved proposal #20221057) and thank Thomas Bizien for assistance with the X-ray scattering experiments at the SWING beamline. IM acknowledges the PhD fellowship from the Physics and Chemistry of Materials' graduate school (ED397). This work was supported by Agence Nationale de la Recherche (ANR) under grant agreement ANR-20-CE19-0029.

Keywords: dense collagen · state diagram · fibrillar collagen · self-assembly · biomaterials

E. References

1. Giraud Guille, M. M., Nassif, N. & Fernandes, F. M. Collagen-based Materials for Tissue Repair, from Bio-inspired to Biomimetic. in *RSC Smart Materials - Materials Design Inspired by Nature: Function through Inner Architecture* (eds. Fratzl, P., W. C. Dunlop, J. & Weinkamer, R.) vol. 4 107–127 (The Royal Society of Chemistry, 2013).

2. Yuan, Z. *et al.* Development of a 3D Collagen Model for the In Vitro Evaluation of Magnetic-assisted Osteogenesis. *Sci Rep* **8**, (2018).

3. Salvatore, L. *et al.* Mimicking the Hierarchical Organization of Natural Collagen: Toward the Development of Ideal Scaffolding Material for Tissue Regeneration. *Frontiers in Bioengineering and Biotechnology* vol. 9 Preprint at https://doi.org/10.3389/fbioe.2021.644595 (2021).

4. Sorushanova, A. *et al.* The Collagen Suprafamily: From Biosynthesis to Advanced Biomaterial Development. *Advanced Materials* vol. 31 Preprint at https://doi.org/10.1002/adma.201801651 (2019).

5. Kadler, K. E., Holmes, D. F., Trotter, J. A. & Chapman, J. A. Collagen fibril formation. *Biochemical Journal* **316**, 1–11 (1996).

6. Streeter, I. & De Leeuw, N. H. A molecular dynamics study of the interprotein interactions in collagen fibrils. *Soft Matter* **7**, 3373–3382 (2011).

7. Israelachvili & Jacob N. *Intermolecular and Surface Forces*. (Academic Press, 2011).

8. Charvolin, J. & Sadoc, J. F. About collagen, a tribute to Yves Bouligand. *Interface Focus* **2**, 567–574 (2012).

9. Mosser, G., Anglo, A., Helary, C., Bouligand, Y. & Giraud-Guille, M. M. Dense tissue-like collagen matrices formed in cell-free conditions. *Matrix Biology* **25**, 3–13 (2006).

10. Gobeaux, F. *et al.* Fibrillogenesis in dense collagen solutions: a physicochemical study. *J Mol Biol* **376**, 1509–1522 (2008).

11. De Sa Peixoto, P., Deniset-Besseau, A., Schanne-Klein, M. C. & Mosser, G. Quantitative assessment of collagen i liquid crystal organizations: Role of ionic force and acidic solvent, and evidence of new phases. *Soft Matter* **7**, 11203–11210 (2011).

12. Giraud-Guille, M.-M. Liquid crystalline phases of sonicated type I collagen. *Biol Cell* **67**, 97–101 (1989).

13. Gobeaux, F. *et al.* Cooperative ordering of collagen triple helices in the dense state. *Langmuir* **23**, 6411–6417 (2007).

14. Bouligand, Y. Liquid crystals and biological morphogenesis: Ancient and new questions. *Comptes Rendus Chimie* vol. 11 281–296 Preprint at https://doi.org/10.1016/j.crci.2007.10.001 (2008).

15. Martinier, I. *et al.* Tunable biomimetic materials elaborated by ice templating and self-assembly of collagen for tubular tissue engineering. *bioRXiv* (2023) doi:10.1101/2023.08.30.555553.

16. Rieu, C. *et al.* Topotactic Fibrillogenesis of Freeze-Cast Microridged Collagen Scaffolds for 3D Cell Culture. *ACS Appl Mater Interfaces* **11**, 14672–14683 (2019).

17. Parisi, C. *et al. Porous yet Dense Matrices: Using Ice to Shape Collagen 3D Cell Culture Systems with Increased Physiological Relevance.*

18. Cyr, J. A., Husmann, A., Best, S. M. & Cameron, R. E. Complex architectural control of ice-templated collagen scaffolds using a predictive model. *Acta Biomater* **153**, 260–272 (2022).

19. Mohee, L., Offeddu, G. S., Husmann, A., Oyen, M. L. & Cameron, R. E. Investigation of the intrinsic permeability of ice-templated collagen scaffolds as a function of their structural and mechanical properties. *Acta Biomater* **83**, 189–198 (2019).

20. Ryan, A. J., Ryan, E. J., Cameron, A. R. & O'Brien, F. J. Hierarchical biofabrication of biomimetic collagen-elastin vascular grafts with controllable properties via lyophilisation. *Acta Biomater* **112**, 52–61 (2020).

21. O'Brien, F. J. *et al.* The effect of pore size on permeability and cell attachment in collagen scaffolds for tissue engineering. *Technology and Health Care* **15**, 3–17 (2007).

22. Dems, D. *et al.* Native Collagen: Electrospinning of Pure, Cross-Linker-Free, Self-Supported Membrane. *ACS Appl Bio Mater* **3**, 2948–2957 (2020).

23. Elamparithi, A., Punnoose, A. M. & Kuruvilla, S. Electrospun type 1 collagen matrices preserving native ultrastructure using benign binary solvent for cardiac tissue engineering. *Artif Cells Nanomed Biotechnol* **44**, 1318–1325 (2016).

24. Lama, M. *et al.* Biomimetic Tough Gels with Weak Bonds Unravel the Role of Collagen from Fibril to Suprafibrillar Self-Assembly. *Macromol Biosci* **21**, (2021).

25. Lama, M. *et al.* Self-Assembled Collagen Microparticles by Aerosol as a Versatile Platform for Injectable Anisotropic Materials. *Small* **16**, (2020).

26. Camman, M. *et al.* Anisotropic dense collagen hydrogels with two ranges of porosity to mimic the skeletal muscle extracellular matrix. *Biomaterials Advances* **144**, (2023).

27. Pati, F. *et al.* Printing three-dimensional tissue analogues with decellularized extracellular matrix bioink. *Nat Commun* **5**, (2014).

28. Kim, Y. B., Lee, H. & Kim, G. H. Strategy to achieve highly porous/biocompatible macroscale cell blocks, using a collagen/genipin-bioink and an optimal 3D printing process. *ACS Appl Mater Interfaces* **8**, 32230–32240 (2016).

29. Kim, W. & Kim, G. Intestinal Villi Model with Blood Capillaries Fabricated Using Collagen-Based Bioink and Dual-Cell-Printing Process. *ACS Appl Mater Interfaces* **10**, 4185–4196 (2018).

30. Suo, H., Zhang, J., Xu, M. & Wang, L. Low-temperature 3D printing of collagen and chitosan composite for tissue engineering. *Materials Science and Engineering C* **123**, (2021).

31. Younesi, M., Islam, A., Kishore, V., Panit, S. & Akkus, O. Fabrication of compositionally and topographically complex robust tissue forms by 3D-electrochemical compaction of collagen. *Biofabrication* **7**, (2015).

32. Magnan, L. *et al.* Human textiles: A cell-synthesized yarn as a truly "bio" material for tissue engineering applications. *Acta Biomater* **105**, 111–120 (2020).

33. Zhang, F. *et al.* A hybrid vascular graft harnessing the superior mechanical properties of synthetic fibers and the biological performance of collagen filaments. *Materials Science and Engineering C* **118**, (2021).

34. Gorgieva, S. & Kokol, V. *Collagen-vs. Gelatine-Based Biomaterials and Their Biocompatibility: Review and Perspectives*. www.intechopen.com.

35. Giraud-Guille, M. M. *et al.* Liquid crystalline properties of type I collagen: Perspectives in tissue morphogenesis. *Comptes Rendus Chimie* vol. 11 245–252 Preprint at https://doi.org/10.1016/j.crci.2007.05.005 (2008).

36. Giraud-Guille, M. M. Twisted liquid crystalline supramolecular arrangements in morphogenesis. *Int Rev Cytol* **166**, 59–101 (1996).

37. Masunaga, H. *et al.* Multipurpose soft-material SAXS/WAXS/GISAXS beamline at SPring-8. *Polym J* **43**, 471–477 (2011).

38. Hafner, A. E., Gyori, N. G., Bench, C. A., Davis, L. K. & Šarić, A. Modeling Fibrillogenesis of Collagen-Mimetic Molecules. *Biophys J* **119**, 1791–1799 (2020).

39. Flory, P. J. & Garrett, R. R. Phase Transitions in Collagen and Gelatin Systems. *J Am Chem Soc* **80**, 4836–4845 (1958).

40. Mu, C., Li, D., Lin, W., Ding, Y. & Zhang, G. Temperature induced denaturation of collagen in acidic solution. *Biopolymers* **86**, 282–287 (2007).

41. Fratzl, P. & Weinkamer, R. Nature's hierarchical materials. *Progress in Materials Science* vol. 52 1263–1334 Preprint at https://doi.org/10.1016/j.pmatsci.2007.06.001 (2007).

42. Abou Neel, E. A., Cheema, U., Knowles, J. C., Brown, R. A. & Nazhat, S. N. Use of multiple unconfined compression for control of collagen gel scaffold density and mechanical properties. *Soft Matter* **2**, 986–992 (2006).

43. Brown, R. A., Wiseman, M., Chuo, C. B., Cheema, U. & Nazhat, S. N. Ultrarapid engineering of biomimetic materials and tissues: Fabrication of nano- and microstructures by plastic compression. *Adv Funct Mater* **15**, 1762–1770 (2005).

44. Jiang, Y. *et al.* Exploring nanoscale structure change of dermal tissues suffering injury by small angle X-ray scattering and transmission electron microscopy. *Mol Biol Rep* **46**, 67–76 (2019).

45. Zhang, Y. *et al.* Investigating the Fibrillar Ultrastructure and Mechanics in Keloid Scars Using In Situ Synchrotron X-ray Nanomechanical Imaging. *Materials* **15**, (2022).

46. Tian, F., Niu, Y. & Jiang, Y. Exploring the collagen nanostructure of dermal tissues after injury. *Burns* **45**, 1759–1764 (2019).

47. Brown, R. A., Wiseman, M., Chuo, C. B., Cheema, U. & Nazhat, S. N. Ultrarapid engineering of biomimetic materials and tissues: Fabrication of nano- and microstructures by plastic compression. *Adv Funct Mater* **15**, 1762–1770 (2005).

48. Kocherbitov, V. The nature of nonfreezing water in carbohydrate polymers. *Carbohydr Polym* **150**, 353–358 (2016).

49. Friess, W. & Lee, G. Basic thermoanalytical studies of insoluble collagen matrices. *Biomaterials* **17**, 2289–94 (1996).

50. Griffanti, G., Rezabeigi, E., Li, J., Murshed, M. & Nazhat, S. N. Rapid Biofabrication of Printable Dense Collagen Bioinks of Tunable Properties. *Adv Funct Mater* **30**, (2020).

51. Dedovets, D., Monteux, C. & Deville, S. Five-dimensional imaging of freezing emulsions with solute effects. *Science (1979)* **360**, 303–306 (2018).

52. Gobeaux, F. Phases denses de collagène de type I : transition isotrope/cholestérique, fibrilllogenèse et minéralisation. (Université Pierre et Marie Curie, 2008).

53. Dedovets, D., Monteux, C. & Deville, S. A temperature-controlled stage for laser scanning confocal microscopy and case studies in materials science. *Ultramicroscopy* **195**, 1–11 (2018).

54. Schneider, C. A., Rasband, W. S. & Eliceiri, K. W. NIH Image to ImageJ: 25 years of Image Analysis HHS Public Access. *Nat Methods* **9**, 671–675 (2012).

F. Supporting Information

State diagrams of type I collagen for the rational design of biomimetic materials

Isabelle Martinier[1], Sylvain Deville[2], Gervaise Mosser[1], Léa Trichet[1], Patrick Davidson[3,*] and Francisco M. Fernandes[1,*]

a. Experimental section

Fabrication of the collagen scaffolds

Type I collagen was extracted from the tendons of young rat tails according to a protocol adapted from that of Gobeaux *et al.*[52]. Tendons were thoroughly cleaned with phosphate buffered saline (PBS) 1X and 4 M NaCl solutions and dissolved in a 3 mM HCl solution. Differential precipitation with 300 mM NaCl and 600 mM NaCl, followed by redissolution and dialysis in 3 mM HCl, provided collagen of high purity. The final collagen concentration was determined using hydroxyproline titration and quantified at 5 $mg.mL^{-1}$. The extracted collagen solution was then concentrated to 40 $mg.mL^{-1}$ by centrifugation. The initial solution was transferred into Vivaspin tubes with 300 kDa filter and centrifuged at 3000g at 10 °C, until the final concentration was reached. Handling higher concentrations by centrifugation is technically challenging, since the increasing viscosity that follows collagen concentration hinders its use. To compensate this limitation, samples were concentrated by evaporation at ambient temperature, under sterile conditions, to reach concentrations of 200, 400, and 900 $mg.mL^{-1}$, after deposition on a glass slide using a Doctor Blade® knife. The concentration after evaporation was calculated based on mass difference. The initial deposited volume was determined to reach a final weight of 50 mg for each concentration. As evaporation is faster at the sides of the sample, all characterizations in this study were performed near the center of the samples.

Two types of experimental conditions were compared: (a) collagen in solution, and (b) collagen fibrillated in PBS buffer. For (a), samples were simply stored in hermetically sealed petri dishes at 4 °C to minimize evaporation. Previous tests confirmed that no significant mass change was observed over time under these conditions. For (b), samples were immersed in a sterile PBS 10x buffer bath for 24 h. After rinsing with PBS 5x, gels were placed in PBS 5x buffer and stored at ambient temperature for 2 weeks to secure fibrillogenesis. At the end of the process, collagen gels were stored at 4 °C.

Small angle X-ray scattering (SAXS) and wide angle X-ray scattering (WAXS)

Customized square frames were printed in acrylonitrile butadiene styrene (ABS) filament using a Zortrax M-200 3D-printer to prepare cells for collagen samples during scattering

experiments. First, a thin (*ca.* 23 m) layer of Mylar was glued to one side of the frame, then the collagen solution or fibrillated sample was deposited on the Mylar layer. Finally, the cell was sealed by gluing a second layer of Mylar to the other side of the frame. Collagen solutions were concentrated directly in the (open) cell rather than on glass slides due to handling issues, as the gels were too sticky to be displaced, whereas fibrillar collagen samples were prepared aside and cut to fit in the frames.

To ensure the robustness of the measurements, X-ray scattering was recorded from 16 (4×4 grid) different points in each sample and three consecutive scattering images were recorded at each point. Since there was no difference between the first and last scattering pattern at each point, beam damage was ruled out.

SAXS and WAXS experiments were performed at the Swing beamline of SOLEIL, the French Synchrotron Radiation Facility (Saint-Aubin, France). The X-ray wavelength was λ = 0.1033 nm and the sample to detection distance was either 6.216 m (SAXS) or 0.518 m (WAXS). The scattered X-rays were collected with an Eiger-4M detector (pixel size of 150 m) and the exposure time was typically 1 s. The X-ray scattering data was azimuthally averaged and normalized using the Foxtrot software developed at the beamline, resulting in plots of the scattered intensity versus scattering vector modulus, q (q = (4 sinθ)/λ where 2 is the scattering angle) ranged between 2×10^{-2} and 8 nm^{-1}. The background was subtracted after fitting by a polynomial function. Considering a hexagonal packing of the molecules, the average distance between the center of the molecules, $d_{(ave)}$ was derived from the peak position, q_{max}, in WAXS by the relation $d_{(ave)} \approx 2 /q_{max}*(2/\sqrt{3})$.

Transmission electron microscopy (TEM)

Fibrillated and in solution samples were cross-linked with 2.5% paraformaldehyde (PFA), 2% glutaraldehyde, 0.18 M sucrose, and 0.1% picric acid for 12 h. The samples were then post-fixed with uranyl acetate in ethanol for 12 h, and dehydrated using baths of increasing concentrations in ethanol. Longitudinal sections of samples were embedded in SPURR-S resins prior to sectioning, transversal to the main axis. 70 nm ultrathin sections (Leica microtome) were contrasted with uranyl acetate and observed on a transmission electron microscope (FEI Tecnai Spirit G2) operating at 120 kV to observe the ultrastructural collagen features. Images were recorded with a CCD camera (Orius Gatan 832 ccdigital) at 6.5 kM.

Polarized light optical microscopy (PLOM) and phase contrast microscopy

Samples were embedded in 2.5% agarose and 200 m semi-thin sections were cut with a vibratome (Compresstome). The sections were examined under two Olympus BX51 microscopes. For the PLOM, the microscope was equipped with an Olympus U-POC-2 (NA:

0.9) condenser and a 50X objective (Olympus LMPlan50XFL (NA 0.50)), and crossed polarizers to observe the birefringence of the sections. The phase contrast microscope was equipped with an Olympus U-PCD-2 (NA: 1.1), with a 40X (Olympus PLCN40XPH (NA 0.65)).

In situ cryoconfocal microscopy

The confocal microscopy system designed to inspect the ice front during directional freezing[53] consisted of a temperature controller connected to two independent Peltier elements (ET-127-10-13, Adaptive, purchased from RS Components, France) coupled with a controlled XY stage. The distance between the thermal elements was 2 mm. The freezing process was observed under a Confocal Laser Scanning Platform Leica TCS SP8 (Leica Microsystems SAS, Germany) using a 20x objective. For the analysis of the collagen wall width resulting from ice templating and the assessment of the fibrillogenesis impact on it, rhodamine B (0.05 mg per mg of protein) was dissolved in 4 wt% collagen solution. The resulting fluorescent solution was deposited on a dedicated Hele-Shaw cell (glass slide covered with a coverslip and sealed with a 100 m-thick tape). The samples were moved from the ambient temperature to the cold Peltier elements (temperature range from 20 to -30 °C) by a stepper motor at 50 $m.s^{-1}$ linear velocities. The dimensions of the concentrated collagen walls were analyzed using FIJI software[54]. For fibrillogenesis imaging, the temperature was maintained at -5°C. Cold phosphate buffer solution (PBS) at a 10x concentration was injected with a needle in between the glass slide and the coverslip. The samples were then imaged during fibrillogenesis as the diffusion front progressed.

Differential scanning calorimetry (DSC)

The thermal transitions of collagen samples were measured by DSC. The samples (around 5 mg) were encapsulated in sealed aluminum pans and inserted in the chamber of a TA Instruments Q10 DSC under a dry nitrogen gas flow of 50 $mL.min^{-1}$, coupled with a cooling flange. The instrument was calibrated using an empty cell baseline and an indium sample for heat flow and temperature. All measurements were performed at a cooling or heating rate of 5 $°C.min^{-1}$. Denaturation temperatures (T_d) were measured by heating from 10 to 180 °C. Crystallization temperatures (T_c) were measured by coupling cooling and heating cycles to minimize the supercooling effects occurring in aqueous solutions. A first cycle led to complete freezing of the free water, followed by heating up and cooling down until crystallization no longer occurred from a supercooled state, but from ice crystal seeds remaining from incomplete melting. The return point at which the equilibrium is in favor of the melting was defined as the T_c. The *critical collagen concentration* was determined by freezing increasing concentrations of collagen in solution, until no freezing event was

observed. The glass transition temperature (T_g) was measured by heating solutions from -80 to 20 °C, using the temperature-modulated mode DSC (mDSC), and analyzing it in the *reversing* component. The experimental conditions (amplitude, frequency, and heating rate) were optimized and set at a temperature amplitude of ±1 °C with a period of 60 s.

Establishing the liquidus lines

In solution the solvent crystallization temperatures decrease from -0.6 °C at 5.6 mg.mL^{-1} to -8.7 °C at 475 mg.mL^{-1}, due to the cryoscopic depression of the collagen solution, which allows the positioning of the *liquidus* line of the diagram, a transition line from one phase (collagen solution, S) to two phases (ice and concentrated collagen solution, I+S). This transition can be described theoretically by a modified Schroder-van Laar equation[48] (eq. S1), established for synthetic polymers, which was fitted to the experimental data:

$$T_f = \frac{1}{\frac{1}{T^0} - \frac{R}{H}\left(\ln(1-\phi_p) + \phi_p\right)} \qquad \text{(eq. S1)}$$

where T_f is the freezing temperature in Kelvin, ϕ_p is the collagen volume fraction (Table S1), T^0 is the solvent freezing temperature, R is the molar gas constant, H is the solvent melting enthalpy ($H_{(3\ mM\ HCl)}$ = 5752.2 J.mol^{-1}), and N is the degree of polymerization of the polymer, which was considered here as $N = \infty$.

Dynamic mechanical analysis (DMA)

The measurement of the T_g of dry collagen, was measured by DMA instead of DSC, since this technique could not detect the limited heat flow associated with this transition. Small-amplitude linear oscillations were applied to measure the dynamic moduli E, E' and tanδ of a dry collagen solution brought to its solubility limit, on a DMA 850 from TA Instruments. A 3-point bending clamp of 17.5 mm was used. The strain rate was fixed at 2% per minute, with a frequency from 1 to 10 Hz. Measurements were repeated 3 times to confirm the glass transition temperature value (data not shown).

Rheology

Shear-strain oscillatory measurements were performed on collagen solutions with an Anton Paar rheometer MCR-302. An 8 mm plane-plane geometry (PP08/S) was fitted with a rough surface to prevent gel slippage. All measurements were performed at ambient temperature. The storage modulus G' and loss modulus G" were recorded during a frequency sweep from 0.1 to 10 Hz with an imposed strain of 1%. The gap was set to ensure a minimal normal force of 0.01 N. Three samples of each solution were tested and averaged.

b. Limitations of the study

This study is the first to establish the collagen state diagrams as a function of concentration and temperature, both in solution and in the fibrillated state. However, several limitations must be taken into account:

i. Accuracy of the determination of the concentration after evaporation. The concentration of the samples after solvent evaporation in ambient air was simply quantified by weighing. The concentration homogeneity of the samples at 40 and 900 $mg.mL^{-1}$ is reliable, since in the the first case the sample is not dried at all and, in the second case, the sample is completely dry, as no further evaporation can take place in air. However, for the intermediate concentrations of 200 and 400 $mg.mL^{-1}$, the final concentrations are only average values that were determined by ignoring any potential concentration gradient at the sample edges resulting from the partial drying process. To limit concentration errors, measurements were systematically made at the center of the samples (*i.e.* in the least evaporated part).

ii. State diagram boundaries. The intersection of the fitted liquidus line with the T_g line is an approximation. For acid-soluble collagen, the line describing the transition from molecular to fibrillar state has only been determined from ambient temperature experiments and is therefore also approximate. More experimental data at different temperatures would be needed to determine this transition precisely, in particular using *in-situ* SAXS measurements during freezing.

State diagrams are drawn for a given concentration and type of acid. Varying these parameters can modulate the self-assembly process[11] and shift the phase transitions. The change in position of the boundaries can also occur due to changes in heating and cooling rates, especially for the T_g line which is kinetics dependent. As they depend on the T_g line, the dotted lines are also kinetic-dependent transitions and therefore their positions are likely to shift under different temperature rate analysis conditions.

iii. Determination of the denaturation temperature. Due to the coexistence of two states in solution and the overlap of the denaturation temperature peaks, the T_d were measured on the peak maxima rather than on the onset, as classical measured.

iv. Three-state intersection. The intersection of the regions of denatured fibrils (T_d line), fibrillar collagen and denatured collagen (F+D), and fibrillar collagen (F), is not precisely known due to the lack of measured T_d points and the difficulty in resolving thermal transitions with small temperature differences by DSC. Care must be taken in this region regarding the exact state of collagen.

v. Liquid-crystalline phases. In this work, we have focused on the state transitions of collagen rather than those involving liquid-crystalline phases. These have already been extensively described in terms of collagen and acid concentrations[9]. Extending their study

over a range of temperatures would require equilibrium conditions, unlike material processing techniques which are mostly carried out under out-of-equilibrium conditions. An assessment of the liquid crystal-like organization of collagen as a function of temperature was therefore simply not within the scope of this study.

c. Figures

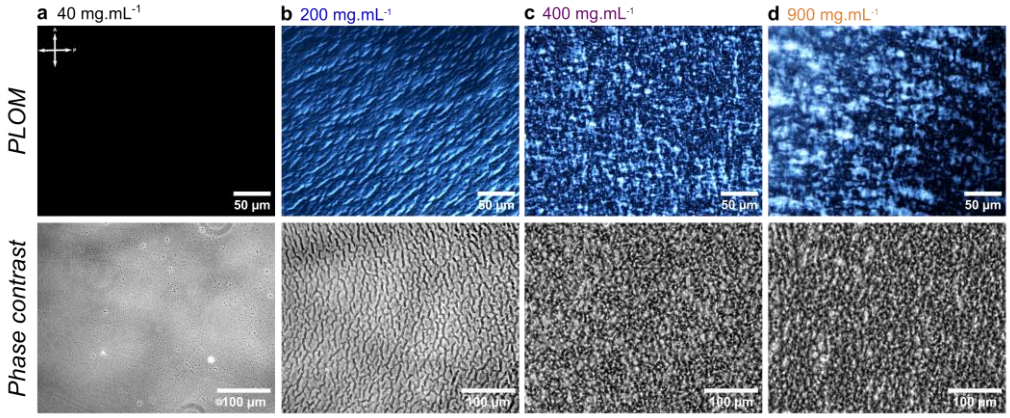

Fig. S1. Observations of dense collagen samples from acid-soluble type I collagen at four concentrations: 40 (**a**), 200 (**b**), 400 (**c**), and 900 mg.mL^{-1}(**d**). Increasing the collagen concentration leads to the appearance of birefringence and an increased complexity in the patterns observed by polarized optical microscope (PLOM, 50X objective) and phase contrast microscopy (40X objective).

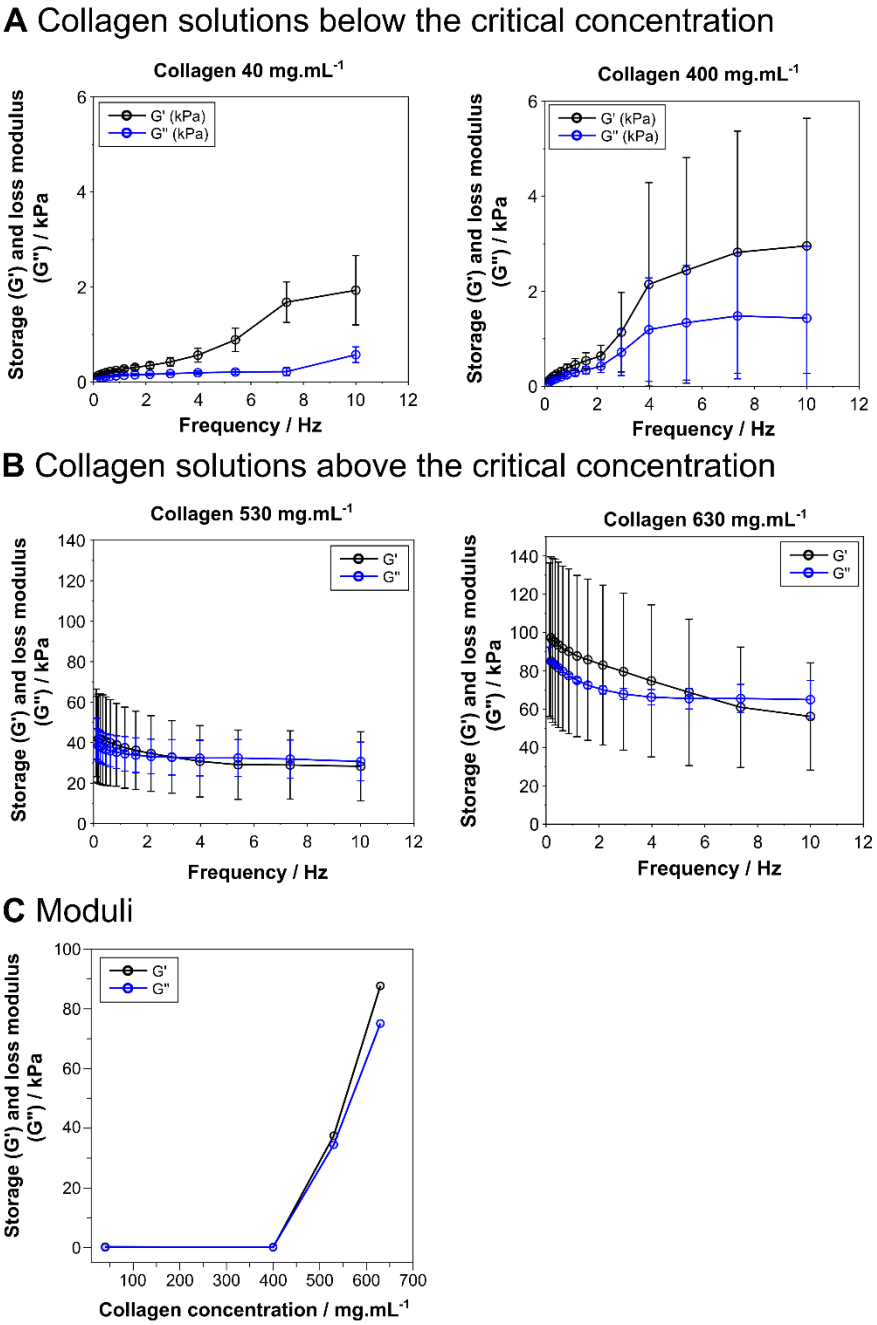

Fig. S2. Variation of storage modulus G' and loss modulus G'' with frequency and collagen concentration for solutions below (**A**) and above (**B**) the critical concentration of 530 mg.mL^{-1}. The G'/G'' ratio, calculated for a frequency of ω = 7.36 Hz, shows a change in the rheological behavior associated with the sol-gel transition.

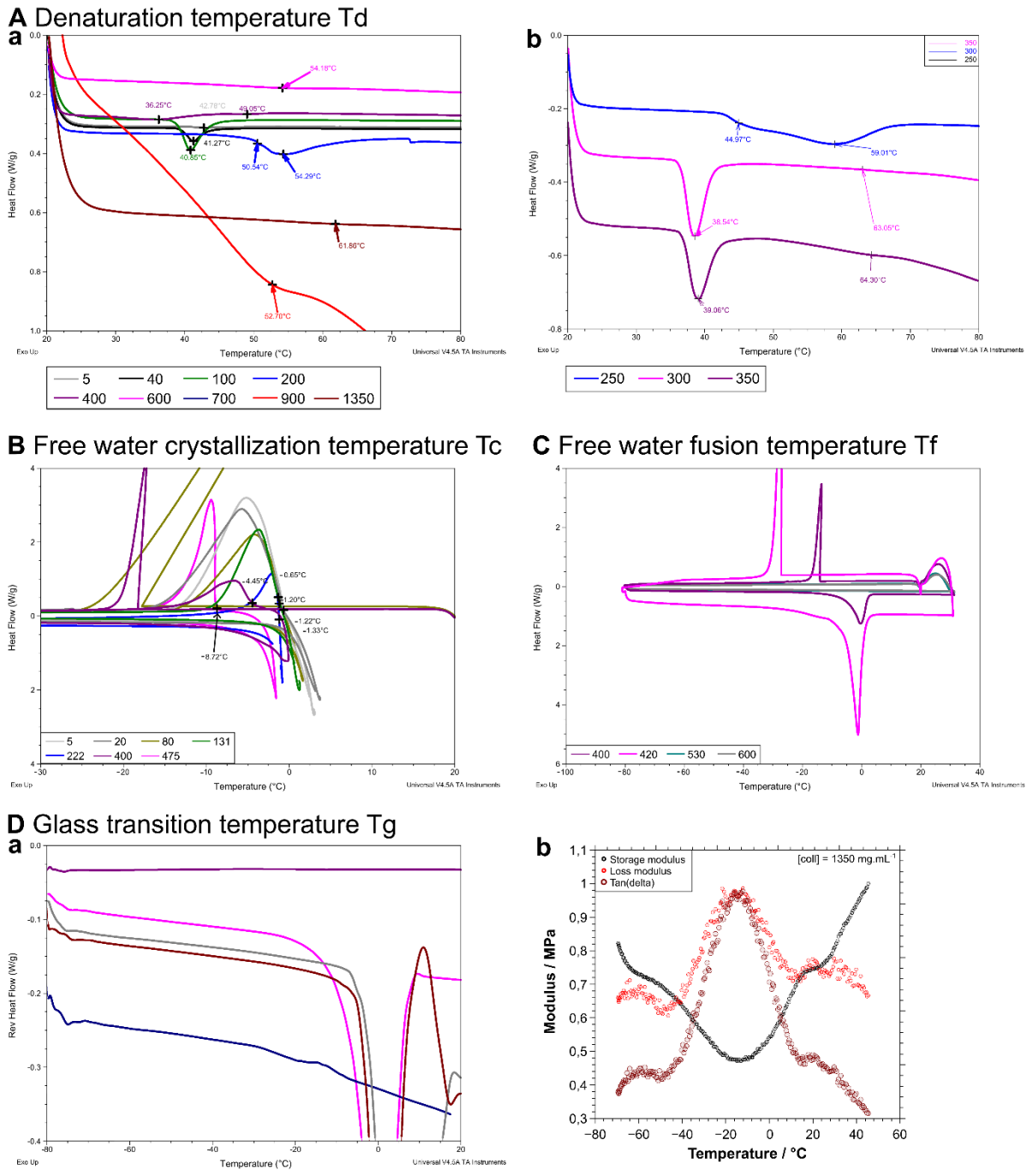

Fig. S3. Analysis of the thermodynamic phase boundaries by DMA, DSC, and mDSC of collagen in solution. All measurements were performed at a rate of 5 °C.min^{-1}. (**A**) Denaturation temperature T_d, (**B**) free water crystallization temperature T_c, (**C**) free water melting temperature measurements used to determine the *critical collagen concentration*, and (**D**) glass transition temperature T_g measured by mDSC (**D-a**) and DMA (**D-b**).

Table S1. Collagen volume fraction ϕ_p used in the modified Schroder-van Laar equation to fit crystallization temperature values.

	Collagen concentration / mg.mL^{-1}	Collagen volume fraction ϕ_p	T / K	T / °C
Collagen in acidic solution	475	0.352	264.43	-8.72
	400	0.296	268.7	-4.45
	222	0.164	271.93	-1.22
	131.7	0.098	271.82	-1.33
	100	0.074	272.03	-1.12
	80	0.059	272.04	-1.11
	40	0.030	272.14	-1.01
	20.5	0.015	271.95	-1.20
	5.6	0.004	272.54	-0.61
Collagen fibrillated in PBS 10x	0	0.000	273.15	0
	400	0.296	267.17	-5.98
	200	0.148	271.55	-1.60
	40	0.030	272.42	-0.73

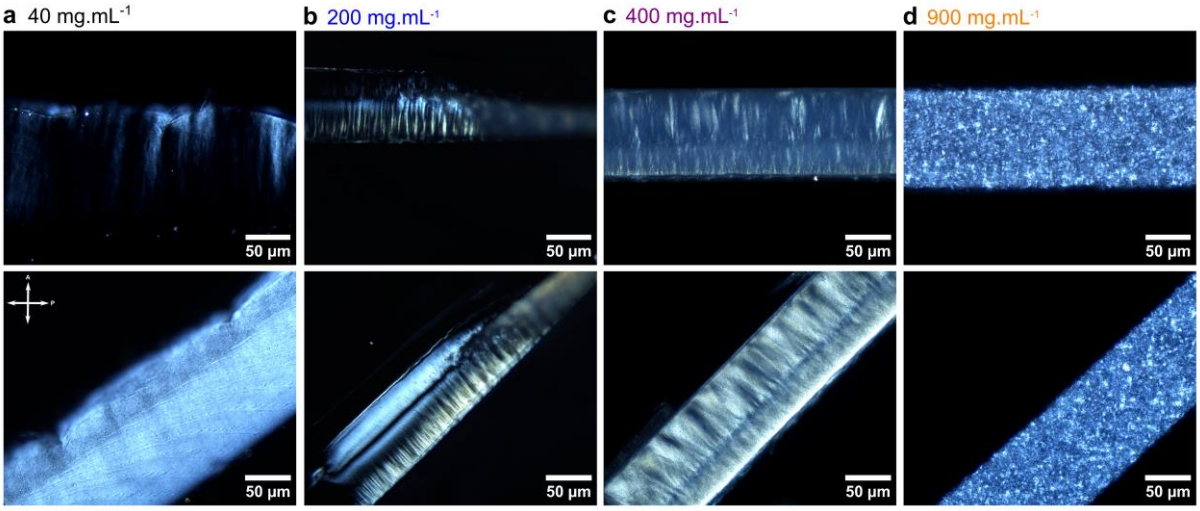

Fig. S4. Polarized light optical microscopy images of transverse cross-sections of dense collagen samples fibrillated in 10x phosphate buffer solution at different concentrations. The sample surface was set parallel (resp. at 45°) to the polarizer direction in the top (resp. bottom) row. (In the top row, the free surface of the samples is at the top.)

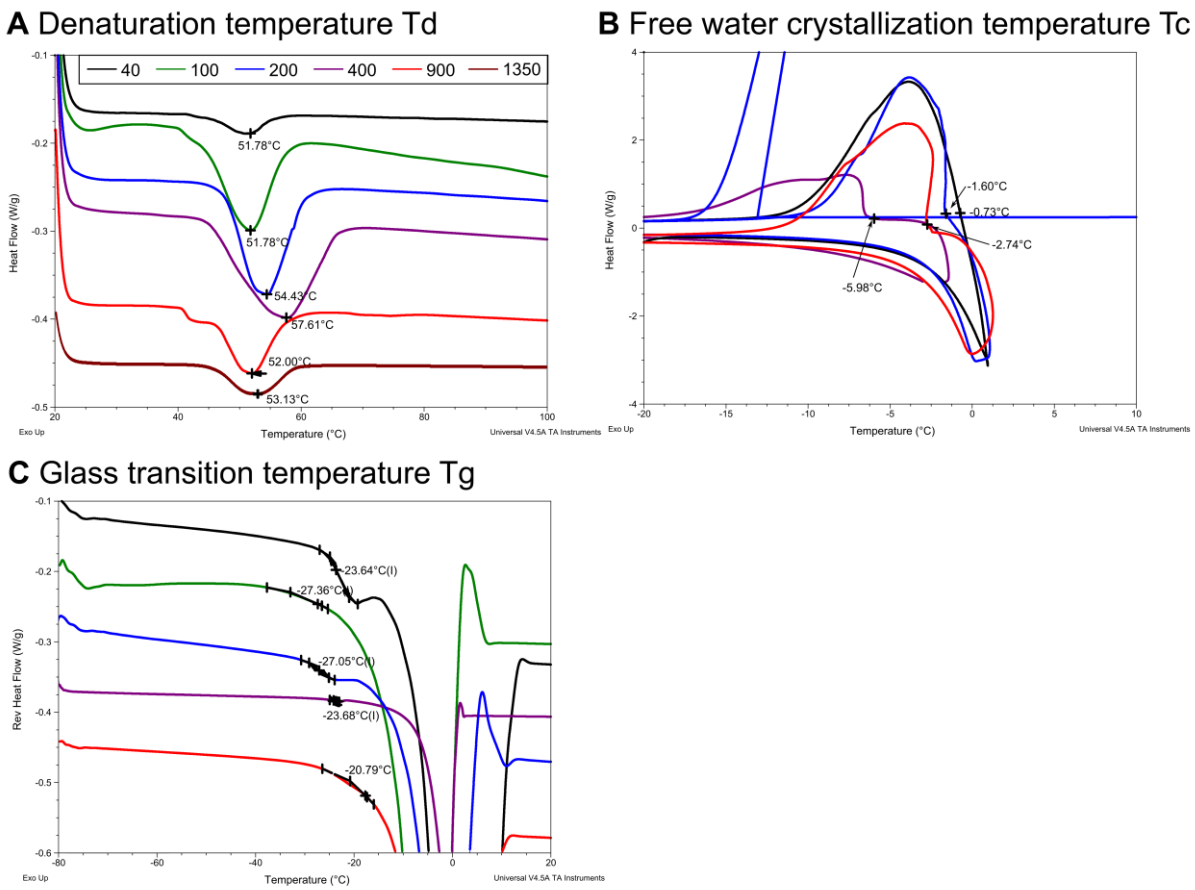

Fig. S5. Analysis of the thermodynamic phase boundaries by DSC and mDSC of collagen samples fibrillated by immersion in phosphate buffer solution. All measurements were performed at a rate of 5 °C.min^{-1}. (**A**) Denaturation temperature T_d, (**B**) free water crystallization temperature T_c, and (**C**) free water melting temperature measurements used to determine the *critical collagen concentration*.

Video S1. Sequential 2D fluorescence imaging of the freezing front of a 40 mg.mL^{-1} collagen solution frozen at 50 m.s^{-1}. The collagen solution (light gray) is segregated in the interstices between ice crystals (black). Link: https://dropsu.sorbonne-universite.fr/s/KdGmpdwzrJPnBs3

Video S2. Sequential 2D fluorescence imaging of the fibrillogenesis medium diffusion front in the previously ice-templated collagen solution, at a constant temperature of -5°C. The first front corresponds to the melting of ice (black), which occurs before the self-assembly of the collagen molecules in the wall (green-blue). Link: https://dropsu.sorbonne-universite.fr/s/aeM5wTxaxmTmrEM

3. Additional results

A. Impact of the concentration of acid on the collagen segregation

The state diagrams depicted above provide information on the collagen organization as a function of the temperature and concentration. However, they were built with a constant HCl concentration of 3 mM, the solvent composition being an essential parameter expected to shift the positions of the transition boundaries in both the *x*-*y* axes. Notably, upon freezing, limited information is available regarding the exact collagen concentration value reached in the interstices following segregation, and its dependency to acid concentration. We tackle that question by monitoring the freezing event and the melting enthalpy of free water within collagen solutions of varying HCl concentrations, using DSC. The collagen concentration was set at a constant low value to ensure a substantial amount of water molecules able to freeze.

Collagen was dissolved at 5 $mg.mL^{-1}$ in various concentrations of HCl, including 3mM (the commonly used acid concentration), 6, 10, 30 and 150 mM, and these binary mixtures were frozen from room temperature to -80°C at 5°$C.min^{-1}$ freezing rate (**Fig.8-A**). From the dataset acquired through DSC, we quantified the free water volume fraction $\phi_{w,f}$ of the collagen solutions from the integral of the ice melting enthalpy (**Appendix B-Fig.S3**). The volume fraction of non-frozen water $\phi_{w,b}$, corresponding to water that remains associated to collagen during cooling, was simply calculated by subtracting $\phi_{w,f}$ to the total water-HCl fraction. This fraction is referred to as the bound water. Based on this remaining volume, the segregation ratio was quantified to determine the fraction of collagen segregated in the interstices.

Figure 8-B depicts the evolution of collagen concentration during a cooling process, as a function of the acid concentration. At 3 mM, during freezing, collagen yields an average concentration of 114 $mg.mL^{-1}$. At higher acid concentrations, the local collagen concentration is lower, reaching values of 16 and 29 $mg.mL^{-1}$ for 30 and 150 mM HCl, respectively. These findings demonstrate that an increasing concentration of acid reduces the availability of water for freezing, owing to the redistribution of the water molecules interactions between HCl and collagen. However, the relationship between the fraction of frozen water and the HCl concentration is not linear. In the context of porous collagen materials fabrication, a higher acid concentration translates to a lower fraction of ice crystals and, consequently, smaller pores. Further exploring that relationship holds the potential of a higher control during freezing processes, for tailoring pore morphology and surface area.

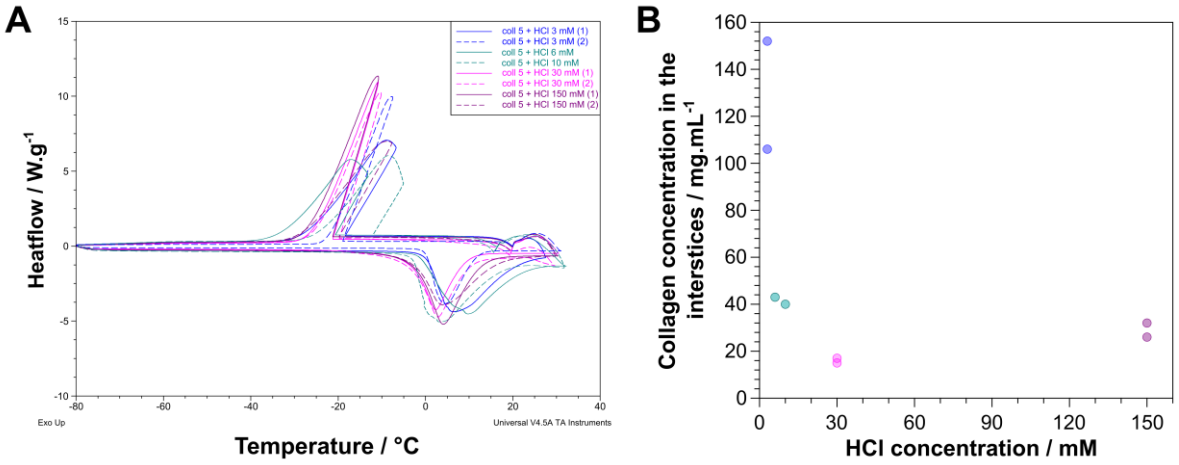

Figure 8. A) Analysis of the free water fusion enthalpy in collagen solutions at various concentrations of HCl (3, 30, 6, 10 and 150 mM). All measurements were performed by DSC at a speed of 5°C.min^{-1}. **B)** Local collagen concentration in the interstices between ice crystals, depending on the concentration of hydrochloric acid.

Table 1. Measurements of the free water fusion enthalpy of collagen solutions at various concentrations of HCl. From the enthalpy, the free water and bound water fractions were calculated, and allowed to obtain the collagen concentration in the interstices between ice crystals.

HCl concentration / mM	Collagen concentration / mg.mL^{-1}	Fusion enthalpy / J.g^{-1}	Free water fraction $\phi_{w,f}$	Bound water fraction $\phi_{w,b}$	Collagen concentration in the interstices / mg.mL^{-1}
3	5	308.8	0.967	0.028	152
3	5	304.3	0.953	0.047	106
6	5	282.4	0.884	0.111	43
10	5	279.6	0.816	0.119	40
30	5	224.1	0.702	0.298	17
30	5	213.1	0.668	0.328	15
150	5	258.3	0.809	0.191	26
150	5	269.5	0.844	0.156	32

Additionally, we delved into the dependence of the collagen concentration in the interstices to the initial concentration, resulting from a freezing process. Using a constant concentration of acid (3 mM HCl), we conducted a series of DSC experiments, run using similar protocol to the one described above. Analysis covering a wide spectrum of concentrations, ranging from 5 to 530 mg.mL^{-1}, and details of the thermograms can be found in **Appendix A-Fig.S1**. **Figure 9** illustrates the segregation phenomenon occurring during the ice templating of dense collagen solutions, depending on the initial concentration of the protein in solution. From an initial concentration of 5 mg.mL^{-1}, the concentration in the interstices directly yields a value of 499 mg.mL^{-1} (**Table 2**), which slightly increases with the initial collagen concentration. Below 530 mg.mL^{-1}, upon cooling, a phase separation occurs

between free water and collagen molecules. Above 530 mg.mL^{-1}, no crystallization event were measured (**Appendix A-Fig.S2**), demonstrating the presence of a single phase of collagen. The concentration of 530 mg.mL^{-1} indicates the shift from a two-phase to a single phase system.

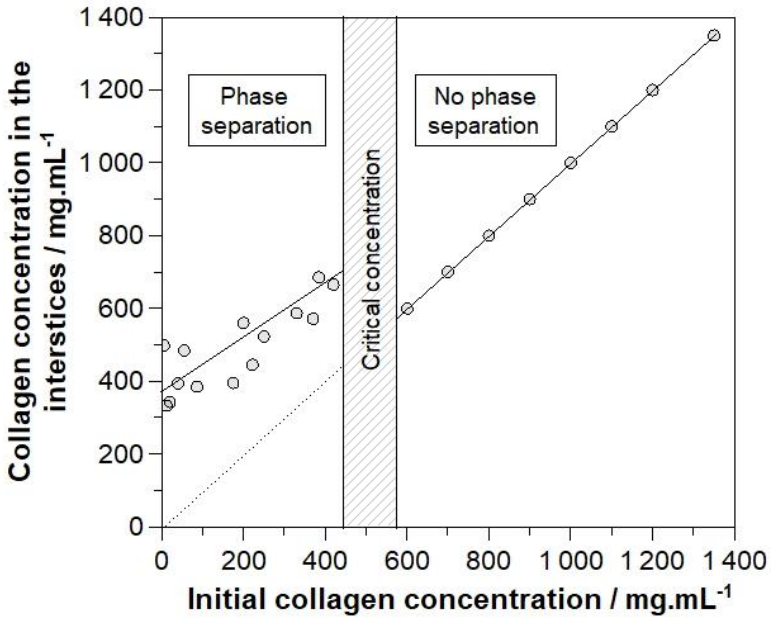

Figure 9. Local collagen concentration in the interstices between ice crystals depending on the initial collagen concentration, ranging from 5 to 1350 mg.mL^{-1}. Below 530 mg.mL^{-1}, the critical concentration, the system is biphasic (free water and collagen molecules). Above this value, the system is composed of a single phase (bound water and collagen molecules).

Table 2. Local collagen concentration segregated between ice crystals, calculated from the fusion enthalpy of ice, and as a function of the initial collagen concentration being frozen. Calculations are detailed in **Appendix A-Fig.S3**.

Collagen concentration / mg.mL^{-1}	Fusion enthalpy / J.g^{-1}	Free water fraction $\phi_{w,f}$	Collagen fraction	Total water fraction ϕ_{wT}	Bound water fraction $\phi_{w,b}$	Collagen concentration in the interstices / mg.mL^{-1}
1350	0	0	0.574	0.426	0.426	1350
1200	0	0	0.545	0.455	0.455	1200
1100	0	0	0.524	0.476	0.476	1100
1000	0	0	0.500	0.500	0.500	1000
900	0	0	0.474	0.526	0.526	900
800	0	0	0.444	0.556	0.556	800
700	0	0	0.412	0.588	0.588	700
600	0	0	0.375	0.625	0.625	600
420	117.6	0.368	0.296	0.704	0.336	665
384	140.3	0.439	0.277	0.723	0.283	685
370	112.9	0.354	0.270	0.730	0.376	572

330	139.9	0.438	0.248	0.752	0.314	587
250	166.8	0.522	0.200	0.800	0.278	523
222	160.0	0.501	0.182	0.818	0.317	445
200	205.2	0.643	0.167	0.833	0.191	560
175	177.9	0.557	0.149	0.851	0.294	395
86	247.9	0.776	0.079	0.921	0.144	385
55	283.0	0.886	0.052	0.948	0.062	484
40	286.9	0.899	0.038	0.962	0.063	394
20	300.7	0.942	0.020	0.980	0.039	343
12	307.8	0.964	0.012	0.988	0.024	333
5	316.1	0.990	0.005	0.995	0.005	499

B. Extended state diagram of fibrillar collagen using a different self-assembly route

In addition to establishing the state diagram for collagen fibrillated in a buffer solution, we conducted a parallel study using instead ammonia vapors, for the same collagen concentrations. While the fibrillogenesis in PBS 10x was based on both a change in pH and an increase in ionic strength within a liquid phase, the alternative ammonia fibrillogenesis occurs in gaseous atmosphere, based exclusively on a pH increase. The four studied concentrations, 40, 200, 400, and 900 mg.mL^{-1} were prepared as described above, and fibrillated for 24 h using NH_3 instead of PBS 10x (**Fig.10-A**).

Transmission electron micrographs of the samples reveal the formation of fibrils at each concentration, with the presence of the characteristic D-banding pattern (**Fig.10-B**). The observed collagen networks resemble those obtained by means of PBS fibrillogenesis, particularly for the lowest and highest concentrations, at 40 and 900 mg.mL^{-1}. In the first case, fibrils are cross-striated and randomly dispersed (**Fig.10-B, a**), and in the second case, nanofibrils are densely packed (**Fig.10-B, d**). The high density is responsible for the nano-size of fibrils and in turn, hinder the observation of striations. In contrast, collagen self-assembly in NH_3 at intermediate concentrations, *i.e.* 200 and 400 mg.mL^{-1}, result in different network arrangements. The 200 mg.mL^{-1} sample exhibits large cross-striated fibrillar domains, whereas at 400 mg.mL^{-1}, smaller cross-striated fibrils form in a dense network of nanofibrils. The arrangement of fibrils in NH_3 appears more compact than in PBS, which suggests a swelling and redilution of the collagen solution during the fibrillogenesis in PBS. This observation aligns with the shift from a liquid- to a gas-gel diffusion, which decreases molecular mobility and consequently, results in tighter fibrillar domains.

The SAXS experiments result in similar diffraction patterns for both fibrillogenesis routes and each collagen density. As for the case of PBS, in NH_3 the fibrillar collagen samples exhibit diffraction peaks that correspond to the 67 nm period of native collagen fibrils

(**Fig.10-C**, left panel), which confirms the observations made on the TEM images. The harmonic peaks remain at a constant position, with a higher intensity and a sharper appearance for concentrations above 40 mg.mL^{-1}.

The molecular packing calculated from WAXS experiments (**Fig.10-C**, central panel) varies with the concentration. The interdistance between fibrils decreases with the increasing concentration, until it reaches a $d_{(ave)}$ value of 1.36 nm at 400 mg.mL^{-1}. The concentration-dependency of that structural characteristic differs from the behavior observed in PBS, for which fibril centers have a constant $d_{(ave)}$ of 1.36 nm, regardless of the concentration (**Fig.10-C**, right panel, purple point for NH_3 *versus* green points for PBS). In comparison to collagen in solution, the highest $d_{(ave)}$ value of 1.40 nm obtained at 40 mg.mL^{-1} in NH_3, is reached in solution at a concentration 10x greater, for 400 mg.mL^{-1}.

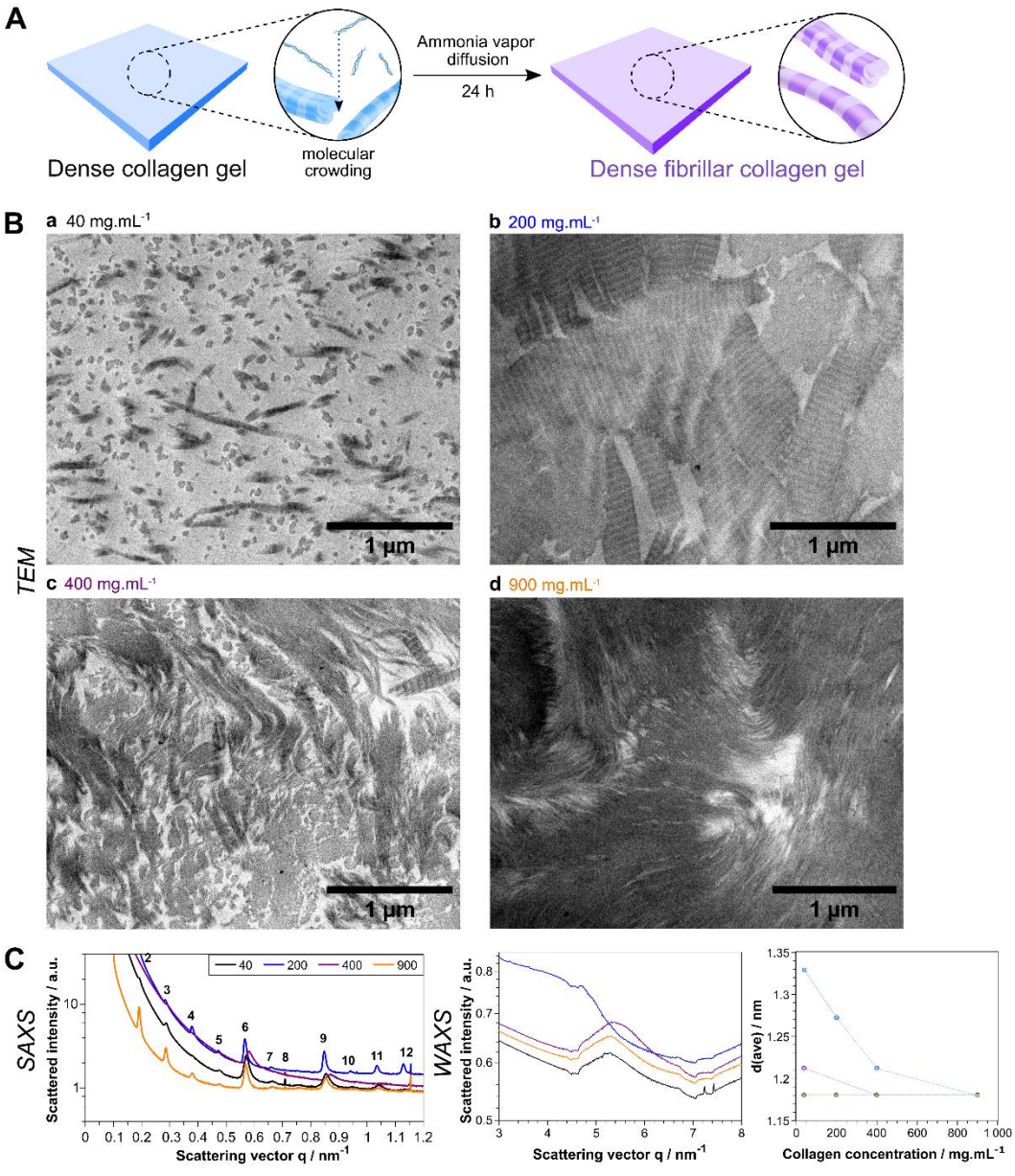

Figure 10. Self-assembly of dense collagen samples induced by an increase of the pH. **A**) Conditions were imposed by exposing the samples to ammonia vapors for 24 h, followed by a rinsing step and two weeks in PBS 5X bath. Four concentrations were studied: 40 (**a**-black), 200 (**b**-blue), 400 (**c**-purple), and 900 mg.mL^{-1} (**d**-orange). **B**) TEM images of the cross-striated fibrils and their organization as a function of the collagen concentration. **C**) The presence of a long-order range of native fibrils in SAXS measurements confirm the formation of fibrils for all collagen concentrations (left panel). The average distance between adjacent fibril centers, calculated from WAXS experiments, as a function of collagen concentration is compared to acidic collagen solution (blue points) and another fibrillogenesis route (PBS, purple points) (right panel).

Such differences in the fibrils interdistance highlight the impact of the chosen fibrillogenesis pathway on the self-assembly of collagen, owing to the different physico-chemical parameters. We hypothesize that the immediate tightness of the fibrils in PBS may be due to the combination of two force factors, both ionic strength and pH increase, in comparison to a pH increase only in NH_3.

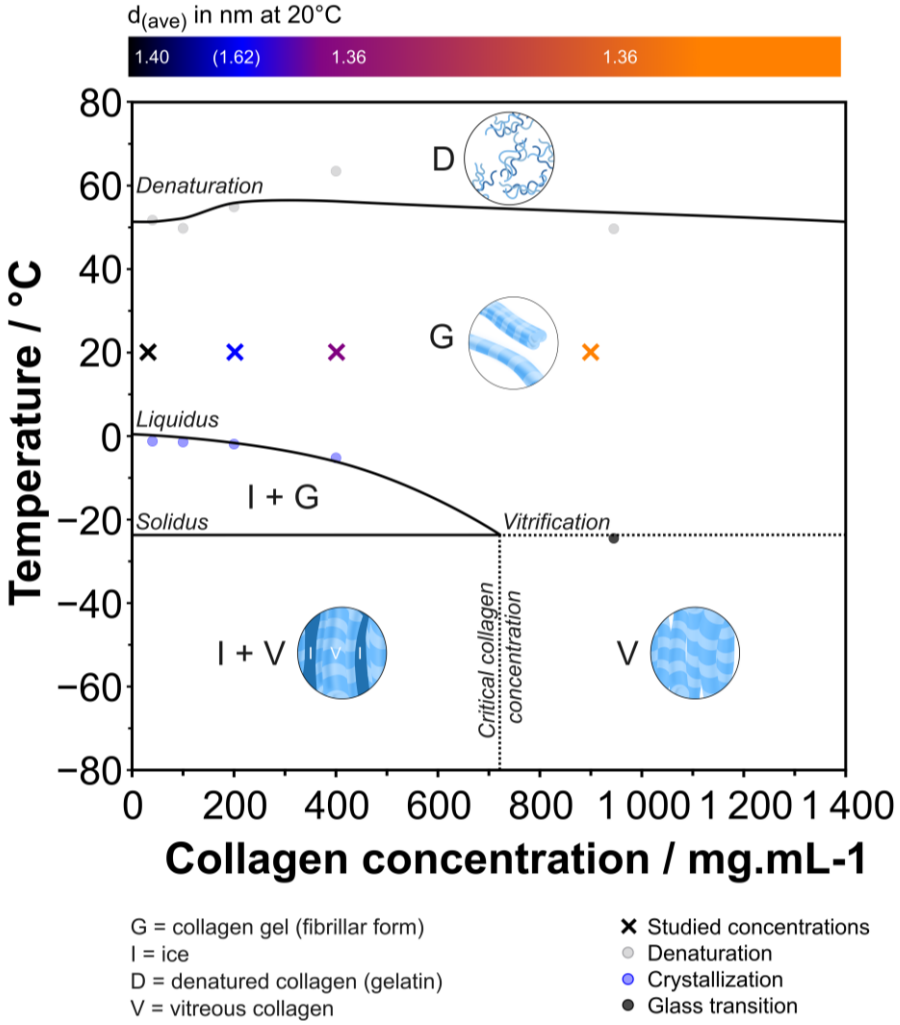

Figure 11. State diagram of fibrillated type I collagen, based on exposure to ammonia vapors of acid-soluble collagen. Details of the measurements used to describe the various state transitions are given in **Appendix B-Fig. S4.**

Not only we built the state diagram of fibrillar collagen self-assembled by PBS, but we also drew the corresponding state diagram of fibrillar collagen using NH_3 (**Fig.11**). We applied the same methods to those developed for PBS-fibrillated collagen and acido-soluble collagen, based on thermal analysis by DSC and mDSC (*Result and discussion,* section 1 and 2 of the article). The various phase transitions describe the conditions of concentration and temperature behind the obtention of denatured, gel, and vitreous states of a collagen solution. The denaturation and glass transitions temperatures are equivalent to those obtained for PBS-fibrillated collagen, with average values of T_d = 53.9°C and T_g = -24.5°C, compared to 55°C and -25°C in PBS, respectively. Once again, the characteristic crystallization temperatures T_c were fitted with the modified Schroder-van Laar equation to define the *liquidus* curve. The intersection between the *liquidus* and the T_g lines depicts the collagen critical concentration, above which collagen turns into a vitreous state below -24.5°C. We estimated this concentration at $[col_{gel}]_{crit} = 730\, mg.mL^{-1}$. This value is higher than for acid-soluble collagen and PBS-fibrillated collagen, found at 530 and 680 mg.mL^{-1}, respectively. We can hypothesize that increasing tightness of the fibrillar network, as observed by TEM (**Fig.10** of the article) is able to stabilize a lesser amount of water molecules per collagen molecule. As a consequence, more water is able to freeze in NH_3 than in PBS. These findings highlight how important is the choice of the fibrillogenesis route, and reveal how it tunes the size of collagen fibrils, the molecular packing, and the interactions with water molecules. In the context of biomaterials fabrication, this implicates that during freezing, using NH_3-fibrillated samples rather than PBS-fibrillated samples yield slightly higher concentration values, resulting in stiffer collagen domains.

Owing to the slight differences observed in the PBS and NH_3-fibrillated collagen state diagrams, and based and the different diffusion routes of the fibrillogenesis media, we hypothesized that the kinetics of topotactic fibrillogenesis may be different. To assess it, we used the *in situ* cryoconfocal set-up depicted earlier in **Figure 5-D.a**. After freezing a collagen solution in a Hele-Shaw cell (**Fig.12-A**), we exposed it to ammonia vapors and followed the diffusion front (**Fig.12-B** and **Appendix B-Video S1**). The drastic change of pH imposed by ammonia induced both the self-assembly of the molecules and the melting of the ice crystals. However, the local velocity of these two events differs from those measured in PBS, as illustrated in **Figure 12-C**. While in PBS the melting of ice occurs prior the fibrillogenesis, in NH_3 the fibrillogenesis is occurring before ice melts. This inversion is ascribed to the different diffusion routes, since gas molecules have a higher mobility than molecules dispersed in a liquid. Moreover, NH_3 vapors impose a higher pH than PBS 10x. The interstitial critical concentration of 530 mg.mL^{-1}, determined in the state diagram of acid-soluble collagen, is modulated by a 140% swelling of the collagen walls during fibrillogenesis (**Fig.12-B,a** and **c**). Consequently, the concentration is rediluted at a concentration of 379 mg.mL^{-1}, calculated from the average percentage of swelling.

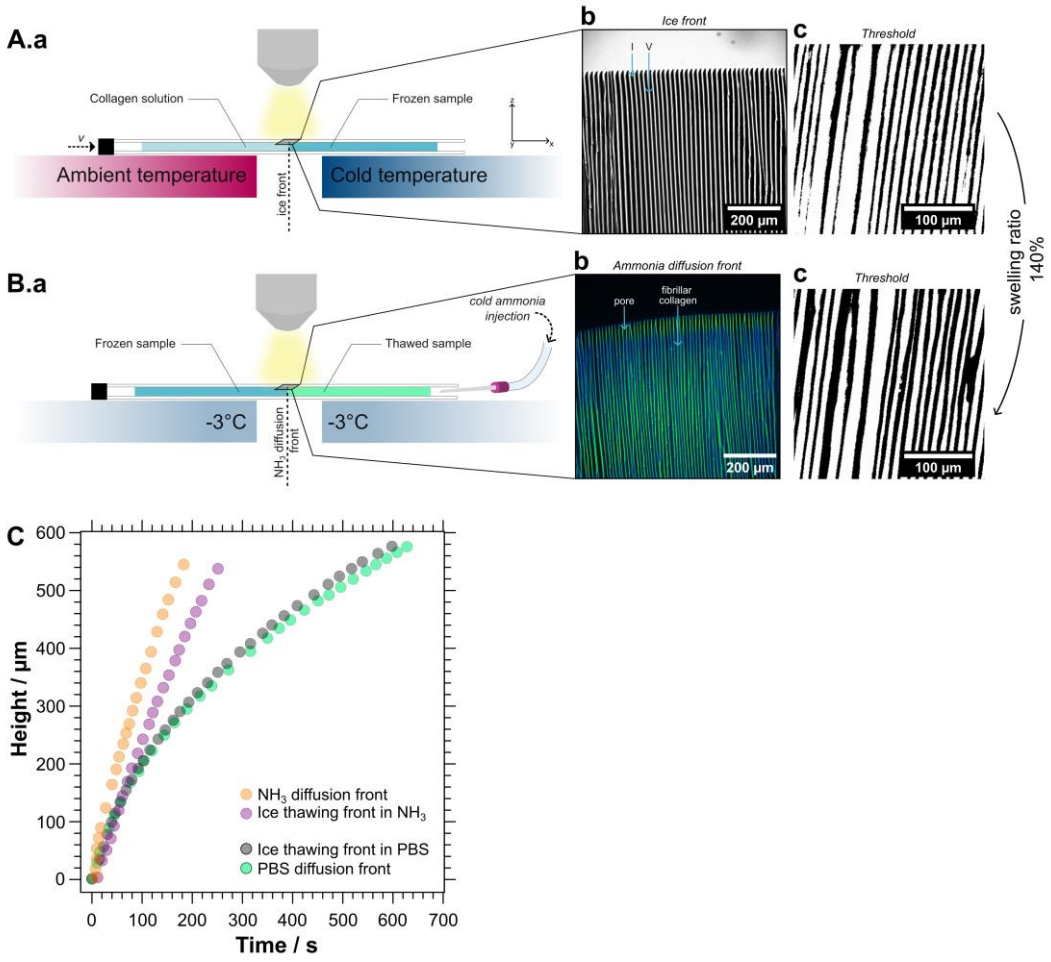

Figure 12. *In situ* cryoconfocal analysis of the freezing and fibrillogenesis of a collagen sample at a concentration of 40 mg.mL^{-1}. **A) a.** The cryoconfocal set-up allows to freeze a solution and to follow the freezing front at a velocity of 50 µm.s^{-1}. The segregation process occurring in between the collagen solution (light gray) and the growing ice (black) is observed. **b,c.** Image thresholding of a segment allowed to measure the width of the collagen walls. **B) a.** Topotactic fibrillogenesis of frozen collagen using ammonia vapors, at a constant temperature of -3°C. The diffusion front is followed by the *in situ* cryoconfocal microscope. **b,c. C)** A 140% swelling of the collagen walls was measured, lower than in PBS fibrillogenesis, due to the different kinetics of fibrillogenesis (orange-1st front) and ice melting (purple-2nd front).

In this study, we demonstrate the distinct ultrastructural characteristics and phase boundaries of two fibrillogenesis pathways. The resulting self-assembly phenomena and kinetics observed during a cooling process differ. The fibrillogenesis in NH_3 demonstrates a remarkable ability to limit the swelling of segregated collagen, due to an instant self-assembly of the molecules, resulting in a higher local collagen concentration of 379 mg.mL^{-1}. In contrast, the fibrillogenesis in PBS yields materials with a lower concentration of 230 mg.mL^{-1}.

4. Conclusions

In the context of biomimetic materials fabrication, collagen type I is, by far, seen as the most relevant building block. We evaluated the possibility to mimic collagen's *in vivo* organization in drastic conditions of temperature and concentration, often used in current processing techniques. The state diagrams, built for both collagen in solution and fibrillated collagen, are powerful tools to guide the fabrication of biomimetic materials, either for grafting applications or as *in vitro* models. Throughout our experiments, we verified a few specific features of the collagen molecules. In solution, the lyotropic behavior of collagen leads to spontaneous self-assembly of the molecules into native-like fibrils, from a concentration of 200 $mg.mL^{-1}$ onwards. Inducing fibrillogenesis inevitably induce molecular lateral packing, with a minimal interdistance that falls down to 1.36 nm. Depending on the chosen pathway, in ammonia vapors or buffer bath, the resulting organization differs both at a molecular and supramolecular level, offering an additional tool to tune collagen structure.

These tools also predict the sol-gel transition of collagen and how it can be triggered. Despite this, variations of the conditions in which the results were obtained (kinetics, acid type and concentration) will modulate the position of the boundaries. In particular, we have shown that an increasing concentration of acid lowers the critical collagen concentration. Consequently, designing an experiment based on the diagrams require to use comparable conditions of acid type and concentration as well as analysis kinetics.

From a basic research perspective, the next step would be to understand the relation between the mesophases and the states of collagen. Assessing the liquid crystal-like transitions by birefringence as a function of the temperature require out-of-equilibrium situations, which are difficult to combine with observations under cross-polarizers. The development of an *in situ* cryomicroscope equipped with cross-polarizers could unveil such transitions.

The methodology described here opens an exciting pathway for unveiling the state diagrams of other biopolymers, such as fibroin, fibrin/fibrinogen, chitin/chitosan, and keratin. In an effort to deepen the knowledge of natural materials, we provide an easy method to understand the impact of several conditions (concentration, temperature, and self-assembly routes) on their structure.

Finally, from a biomaterial fabrication standpoint, we provide new guidelines to design biomimetic materials. Beyond this, the question of the precise conditions resulting in the formation of healthy or pathological collagen organizations is raised. A first step would be to integrate the—largely unknown—physico-chemical conditions found *in vivo* that lead to specific collagen organizations in both physiological and pathological contexts.

5. References of Chapter II

1. Giraud-Guille, M. M. *et al.* Liquid crystalline properties of type I collagen: Perspectives in tissue morphogenesis. *Comptes Rendus Chimie* vol. 11 245–252.

2. Gobeaux, F. Phases denses de collagène de type I: transition isotrope/cholestérique, fibrilllogenèse et minéralisation. (Université Pierre et Marie Curie, 2008).

3. Mosser, G., Anglo, A., Helary, C., Bouligand, Y. & Giraud-Guille, M. M. Dense tissue-like collagen matrices formed in cell-free conditions. *Matrix Biology* **25**, 3–13 (2006).

4. McKay, Priyadarsini & Karamichos. Mechanisms of Collagen Crosslinking in Diabetes and Keratoconus. *Cells* **8**, 1239 (2019).

5. Moretti, L., Stalfort, J., Barker, T. H. & Abebayehu, D. The interplay of fibroblasts, the extracellular matrix, and inflammation in scar formation. *Journal of Biological Chemistry* **298**, (2022).

6. Fang, M., Yuan, J., Peng, C. & Li, Y. Collagen as a double-edged sword in tumor progression. *Tumor Biology* **35**, 2871–2882 (2014).

7. Mao, J.-R. & Bristow, J. The Ehlers-Danlos syndrome: on beyond collagens. *J Clin Invest* **107**, 1063 (2001).

8. Giraud Guille, M. M., Nassif, N. & Fernandes, F. M. Collagen-based Materials for Tissue Repair, from Bio-inspired to Biomimetic. in *RSC Smart Materials - Materials Design Inspired by Nature: Function through Inner Architecture* (eds. Fratzl, P., W. C. Dunlop, J. & Weinkamer, R.) vol. 4 107–127 (The Royal Society of Chemistry, 2013).

9. Yuan, Z. *et al.* Development of a 3D Collagen Model for the In Vitro Evaluation of Magnetic-assisted Osteogenesis. *Sci Rep* **8**, (2018).

10. Salvatore, L. *et al.* Mimicking the Hierarchical Organization of Natural Collagen: Toward the Development of Ideal Scaffolding Material for Tissue Regeneration. *Frontiers in Bioengineering and Biotechnology* vol. 9 (2021).

11. Sorushanova, A. *et al.* The Collagen Suprafamily: From Biosynthesis to Advanced Biomaterial Development. *Advanced Materials* vol. 31 (2019).

12. Kadler, K. E., Holmes, D. F., Trotter, J. A. & Chapman, J. A. Collagen fibril formation. *Biochemical Journal* **316**, 1–11 (1996).

13. Streeter, I. & De Leeuw, N. H. A molecular dynamics study of the interprotein interactions in collagen fibrils. *Soft Matter* **7**, 3373–3382 (2011).

14. Israelachvili & Jacob N. *Intermolecular and Surface Forces*. (Academic Press, 2011).

15. Charvolin, J. & Sadoc, J. F. About collagen, a tribute to Yves Bouligand. *Interface Focus* **2**, 567–574 (2012).

16. Gobeaux, F. *et al.* Fibrillogenesis in dense collagen solutions: a physicochemical study. *J Mol Biol* **376**, 1509–1522 (2008).

17. De Sa Peixoto, P., Deniset-Besseau, A., Schanne-Klein, M. C. & Mosser, G. Quantitative assessment of collagen i liquid crystal organizations: Role of ionic force and acidic solvent, and evidence of new phases. *Soft Matter* **7**, 11203–11210 (2011).

18. Giraud-Guille, M.-M. Liquid crystalline phases of sonicated type I collagen. *Biol Cell* **67**, 97–101 (1989).

19. Gobeaux, F. *et al.* Cooperative ordering of collagen triple helices in the dense state. *Langmuir* **23**, 6411–6417 (2007).

20. Bouligand, Y. Liquid crystals and biological morphogenesis: Ancient and new questions. *Comptes Rendus Chimie* vol. 11 281–296 (2008).

21. Martinier, I. *et al.* Tunable biomimetic materials elaborated by ice templating and self-assembly of collagen for tubular tissue engineering. *biorXiv* (2023) doi:10.1101/2023.08.30.555553.

22. Rieu, C. *et al.* Topotactic Fibrillogenesis of Freeze-Cast Microridged Collagen Scaffolds for 3D Cell Culture. *ACS Appl Mater Interfaces* **11**, 14672–14683 (2019).

23. Parisi, C. *et al. Porous yet Dense matrices: using ice to shape collagen 3D cell culture systems with increased physiological relevance.*

24. Cyr, J. A., Husmann, A., Best, S. M. & Cameron, R. E. Complex architectural control of ice-templated collagen scaffolds using a predictive model. *Acta Biomater* **153**, 260–272 (2022).

25. Mohee, L., Offeddu, G. S., Husmann, A., Oyen, M. L. & Cameron, R. E. Investigation of the intrinsic permeability of ice-templated collagen scaffolds as a function of their structural and mechanical properties. *Acta Biomater* **83**, 189–198 (2019).

26. Ryan, A. J., Ryan, E. J., Cameron, A. R. & O'Brien, F. J. Hierarchical biofabrication of biomimetic collagen-elastin vascular grafts with controllable properties via lyophilisation. *Acta Biomater* **112**, 52–61 (2020).

27. O'Brien, F. J. *et al.* The effect of pore size on permeability and cell attachment in collagen scaffolds for tissue engineering. *Technology and Health Care* **15**, 3–17 (2007).

28. Dems, D. *et al.* Native Collagen: Electrospinning of Pure, Cross-Linker-Free, Self-Supported Membrane. *ACS Appl Bio Mater* **3**, 2948–2957 (2020).

29. Elamparithi, A., Punnoose, A. M. & Kuruvilla, S. Electrospun type 1 collagen matrices preserving native ultrastructure using benign binary solvent for cardiac tissue engineering. *Artif Cells Nanomed Biotechnol* **44**, 1318–1325 (2016).

30. Lama, M. *et al.* Biomimetic Tough Gels with Weak Bonds Unravel the Role of Collagen from Fibril to Suprafibrillar Self-Assembly. *Macromol Biosci* **21**, (2021).

31. Lama, M. *et al.* Self-Assembled Collagen Microparticles by Aerosol as a Versatile Platform for Injectable Anisotropic Materials. *Small* **16**, (2020).

32. Camman, M. *et al.* Anisotropic dense collagen hydrogels with two ranges of porosity to mimic the skeletal muscle extracellular matrix. *Biomaterials Advances* **144**, (2023).

33. Pati, F. *et al.* Printing three-dimensional tissue analogues with decellularized extracellular matrix bioink. *Nat Commun* **5**, (2014).

34. Kim, Y. B., Lee, H. & Kim, G. H. Strategy to achieve highly porous/biocompatible macroscale cell blocks, using a collagen/genipin-bioink and an optimal 3D printing process. *ACS Appl Mater Interfaces* **8**, 32230–32240 (2016).

35. Kim, W. & Kim, G. Intestinal Villi Model with Blood Capillaries Fabricated Using Collagen-Based Bioink and Dual-Cell-Printing Process. *ACS Appl Mater Interfaces* **10**, 41185–41196 (2018).

36. Suo, H., Zhang, J., Xu, M. & Wang, L. Low-temperature 3D printing of collagen and chitosan composite for tissue engineering. *Materials Science and Engineering C* **123**, (2021).

37. Younesi, M., Islam, A., Kishore, V., Panit, S. & Akkus, O. Fabrication of compositionally and topographically complex robust tissue forms by 3D-electrochemical compaction of collagen. *Biofabrication* **7**, (2015).

38. Magnan, L. *et al.* Human textiles: A cell-synthesized yarn as a truly "bio" material for tissue engineering applications. *Acta Biomater* **105**, 111–120 (2020).

39. Zhang, F. *et al.* A hybrid vascular graft harnessing the superior mechanical properties of synthetic fibers and the biological performance of collagen filaments. *Materials Science and Engineering C* **118**, (2021).

40. Gorgieva, S. & Kokol, V. *Collagen-vs. Gelatine-Based Biomaterials and Their Biocompatibility: Review and Perspectives.*

41. Giraud-Guille, M. M. Twisted liquid crystalline supramolecular arrangements in morphogenesis. *Int Rev Cytol* **166**, 59–101 (1996).

42. Masunaga, H. *et al.* Multipurpose soft-material SAXS/WAXS/GISAXS beamline at SPring-8. *Polym J* **43**, 471–477 (2011).

43. Fratzl, P. & Weinkamer, R. Nature's hierarchical materials. *Progress in Materials Science* vol. 52 1263–1334 (2007).

44. Hafner, A. E., Gyori, N. G., Bench, C. A., Davis, L. K. & Šarić, A. Modeling Fibrillogenesis of Collagen-Mimetic Molecules. *Biophys J* **119**, 1791–1799 (2020).

45. Peter Fratzl. *Collagen structure and mechanics*. (Springer, 2008).

46. Flory, P. J. & Garrett, R. R. Phase Transitions in Collagen and Gelatin Systems. *J Am Chem Soc* **80**, 4836–4845 (1958).

47. Mu, C., Li, D., Lin, W., Ding, Y. & Zhang, G. Temperature induced denaturation of collagen in acidic solution. *Biopolymers* **86**, 282–287 (2007).

48. Kocherbitov, V. The nature of nonfreezing water in carbohydrate polymers. *Carbohydr Polym* **150**, 353–358 (2016).

49. Abou Neel, E. A., Cheema, U., Knowles, J. C., Brown, R. A. & Nazhat, S. N. Use of multiple unconfined compression for control of collagen gel scaffold density and mechanical properties. *Soft Matter* **2**, 986–992 (2006).

50. Brown, R. A., Wiseman, M., Chuo, C. B., Cheema, U. & Nazhat, S. N. Ultrarapid engineering of biomimetic materials and tissues: Fabrication of nano- and microstructures by plastic compression. *Adv Funct Mater* **15**, 1762–1770 (2005).

51. Jiang, Y. *et al.* Exploring nanoscale structure change of dermal tissues suffering injury by small angle X-ray scattering and transmission electron microscopy. *Mol Biol Rep* **46**, 67–76 (2019).

52. Zhang, Y. *et al.* Investigating the Fibrillar Ultrastructure and Mechanics in Keloid Scars Using In Situ Synchrotron X-ray Nanomechanical Imaging. *Materials* **15**, (2022).

53. Tian, F., Niu, Y. & Jiang, Y. Exploring the collagen nanostructure of dermal tissues after injury. *Burns* **45**, 1759–1764 (2019).

54. De Sa Peixoto, P., Laurent, G., Azaïs, T. & Mosser, G. Solid-state NMR study reveals collagen I structural modifications of amino acid side chains upon fibrillogenesis. *Journal of Biological Chemistry* **288**, 7528–7535 (2013).

55. Griffanti, G., Rezabeigi, E., Li, J., Murshed, M. & Nazhat, S. N. Rapid Biofabrication of Printable Dense Collagen Bioinks of Tunable Properties. *Adv Funct Mater* **30**, (2020).

56. Dedovets, D., Monteux, C. & Deville, S. A temperature-controlled stage for laser scanning confocal microscopy and case studies in materials science. *Ultramicroscopy* **195**, 1–11 (2018).

57. Schneider, C. A., Rasband, W. S. & Eliceiri, K. W. NIH Image to ImageJ: 25 years of Image Analysis HHS Public Access. *Nat Methods* **9**, 671–675 (2012).

Chapter III

On the importance of collagen concentration and ultrastructure on the endothelialization of biomimetic *in vitro* models

"*I am rooted, but I flow.*"
— Virginia Woolf

1. Context

In the preceding chapters, we established that type I collagen is one of the most promising components to replicate tubular organs, since it is the main constituent of the ECM. However, preserving its native conformation throughout the energy-intensive shaping processes is challenging. Collagen's secondary structure is necessary to trigger the molecular self-assembly into fibrils. Chapter II focused on how the supramolecular organization depends on the temperature and concentration, and proposed fabrication routes that enable to reach both a physiological concentration and the native ultrastructure of collagen in tissues. In this chapter, we report the development of biomimetic flat substrates made solely of type I collagen and we study the impact of the concentration and of the self-assembly route on the behavior of human umbilical vascular endothelial cells (HUVECs). Four different concentrations were studied, ranging from 40 to 900 $mg.mL^{-1}$, fibrillated by two different pathways based on pH and/or osmotic pressure increase. We investigated how the ultrastructure, the topography and local elastic properties of these substrates depend on the elaboration conditions, as well as their impact on the microenvironment met by cells. HUVECs cells were seeded to quantify their proliferation and actin coverage overtime, based on fluorescent image analysis. The correlation of the materials' attributes and the cell fate unveiled how the topography, fibril morphology, and stiffness modulate cell adhesion and proliferation. These results provide important guidelines to elaborate the luminal part of biomimetic tubular materials for vascular applications. Moreover, these results open an exciting pathway for the design of *ad hoc* biomaterials that may direct the cell behavior, providing relevant *in vitro* models of a wide range of tissues, both in physiological and pathological conditions.

2. Introduction

The extra-cellular matrix (ECM) is a complex and dynamic microenvironment, composed of multiple elements including collagens, proteoglycans, and polysaccharides that form a structural skeleton for cells and signaling molecules. The properties of the ECM depend on the composition, the arrangement, and interactions between their components, which vary drastically among different tissues, to provide various microenvironments that are adapted to the type of residing cells[1]. Cells interact with their environment, and respond to stimuli by engaging in different signaling cascades that regulate their growth, proliferation, motility, as well as their differentiation[2]. This active cross-talk between the mechanical, topographical, biological properties of the matrix and the cellular behavior has been observed for numerous

cell lines[3], and is driven *in vivo* by gradients within the tissue[4] Instead of following a Brownian movement, cell motility is directed by different cues in their environment. The spatial distribution and the nature of these cues are key to recapitulate tissue architecture and physiology, creating the tissue specificity for the respective cell types. Achieving their reconstitution promises to unlock biointegration of tissue grafts, and to provide accurate *in vitro* models to deepen our understanding of tissue homeostasis and regeneration. However, the complexity of the native cellular microenvironment has long limited the analysis of how individual component properties regulate the fate of cells[5].

Type I collagen is the most abundant component of the ECM and thus an important contributor to its structural properties[6]. Beyond the stiffness and the presence of the cell-anchoring sites, type I collagen (ColI) has the advantage of being both synthesized and degraded by cells, creating a dynamic environment that is prone to tissue homeostasis. Epithelial cells interact with ColI through different mechanisms such as the $\alpha_2\beta_1$ integrin receptor or Arg-Gly-Asp (RGD) recognizing integrins[7]. Tailoring the number of RGD sequences on a surface has proven efficient to modulate the spatial distribution of cells and to create gradients, resulting in a controlled migration across the materials *via* cell polarization[8,9]. Collagen concentration gradients also allow to modulate the number of exposed RGD sequences, leading to increased cell attachment[10]. Hale *et al.* demonstrated that cells migrate towards the highly concentrated areas, proving that cell motility is density-dependent[11]. Models with a homogenous concentration corroborate that a high collagen concentration enhances cell adhesion and proliferation overtime[12,13]. However, the few studies that explored this effect use collagen concentrations under 10 $mg.mL^{-1}$, a value way below the physiological concentration found in most native tissues, estimated between 100 and 200 $mg.mL^{-1}$[1,14]. Furthermore, the native-like fibrillar ultrastructure and the arrangement of fibrils are poorly reconstituted in the existing ECM models, a crucial shortcoming for a deeper understanding of cellular behaviors.

The local stiffness also plays an important role in the cellular fate. One of the most relevant attributes is the of elastic moduli of the ECM, which can vary according to the different body tissues. Cells perceive their environment through their actin cytoskeleton and actomyosin networks[15]. The mechanical stiffness of collagen is responsible for a large part of the overall mechanical properties of tissues. They result from both collagen local concentration and from the extension of cross-linking. *In vivo*, cross-linking is mediated by enzymes—lysyl oxidases—or by non-enzymatic components—glycation and trans-glutamination[16]. An increasing activity of these components triggers the formation of additional inter- and intramolecular crosslinks between the helical domain of tropocollagen, which stiffens the collagen network[17]. Increased proteoglycans concentration also promotes cross-linking and the formation of reactive oxidant species (ROS) responsible for cellular

signaling cascades[15]. Such situations are the hallmark of several pathologies, including fibrosis, diabetes, and cancer[16]. These pathologies can be modeled *in vitro*, by simply adjusting the collagen concentration that modulates the elastic properties[18]. In addition to textural properties, the topography of collagen fibrils regulates cell behavior[6]. The alignment of fibrils directs the cell migration, that migrate preferentially along the axis of fibrils[19].

The dependence of cells over the topography and mechanical properties of synthetic materials has been extensively studied[20,21]. However, there is a substantial lack of knowledge regarding the impact of these properties (topography and mechanical properties) on cells, in the case of biomimetic substrates. We focused on the influence of collagen concentration and ultrastructure on cell behavior. The models that we propose recapitulate the features of the ECM with a simplified composition, reduced to its main component, type I fibrillar collagen. Dense collagen materials were fabricated in concentrations of 40, 200, 400, and 900 $mg.mL^{-1}$ by evaporation. We induced the self-assembly of the molecules into fibrils in a second step, by exposing the collagen solutions to pH and/or osmotic pressure increase. The concentration of collagen, combined with the fibrillar network induced by fibrillogenesis, resulted in a wide range of local elastic moduli and textures, without using any physical or chemical cross-linking procedures, known for their intrinsic cytotoxicity[22]. Controlling the collagen network, in native-like conditions, enables to study the relationship between the concentration, self-assembly routes, and topographical cues over the cellular behavior. In particular, the chosen concentrations are not restricted to healthy physiological concentrations, evaluated in between 100 to 200 $mg.mL^{-1}$. Instead, they range between 40 $mg.mL^{-1}$ and 900 $mg.mL^{-1}$, covering a concentration range that could reproduce the characteristics of both healthy and pathological tissues. These substrates—designed here to reproduce the luminal part of tubular tissues—offer thus multiple possibilities to unveil cell-material or cell-cell interactions within a biomimetic framework, an absent feature in currently used *in vitro* models. These understandings pave the way for improved treatments of wound healing, skin aging, and several connective tissues pathologies.

3. Results and discussion

A. Self-assembly of the collagen molecules and their arrangement in the various models

To investigate the impact of the collagen network properties on cell behavior, we considered two parameters, concentration and self-assembly route. We prepared substrates at four concentrations, followed by a fibrillogenesis using two different routes, as illustrated in **Figure 1**. From an initial concentration of 40 $mg.mL^{-1}$, acido-soluble collagen deposited on glass slides were evaporated under sterile conditions to yield concentrations of 200, 400, and

900 mg.mL^{-1}. The self-assembly of collagen molecules into fibrils was induced by either increasing the pH and osmotic pressure through a 10x-phosphate buffer solution bath, or solely by increasing the pH upon exposure to ammonia vapors.

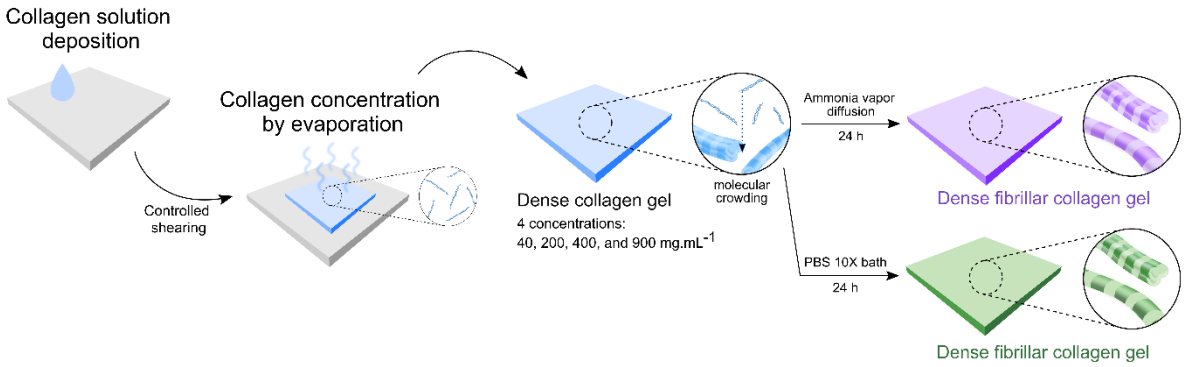

Figure 1. Elaboration of thin dense fibrillar collagen matrices. From an initial concentration of 40 mg.mL^{-1}, evaporation of collagen depositions enabled to yield various concentrations, including 200, 400, and 900 mg.mL^{-1}. Fibrillogenesis was induced by ammonia vapor diffusion or a 10X-phosphate buffer solution (PBS) bath for 24 h.

The fibrillar ultrastructure and organization of type I collagen networks can influence significantly the interactions with cells, by modulating the spatial distribution of active sites. Under the TEM, the negative staining of the samples revealed fibrils with the typical D-banding pattern in all concentrations below 900 mg.mL^{-1} (**Fig.2-A** and **B**). At low concentration and for both fibrillogenesis routes, small fibrils randomly dispersed are observed. At higher concentrations (200 and 400 mg.mL^{-1}), the resulting networks are denser and display large striated fibrils, close to those found in native connective tissues[23,24]. Such dense networks are rarely observed from reconstituted fibrils *in vitro*, since materials in literature mostly use concentrations below 10 mg.mL^{-1}. Interestingly, the large cross-striated fibrils formed at 400-PBS (**Fig.2-B.c**) share some features with those formed in 200-NH_3 (**Fig.2-A.b**). We hypothesize that this similarity originates from a re-dilution of the 400-PBS sample in the buffer solution during the fibrillogenesis step. This hypothesis is further supported by the observation made for 200-PBS, in which the arrangement of collagen fibrils represents an intermediate between 40-NH_3 and 200-NH_3. At 200-PBS, fibrils of similar dimensions to 40-NH_3 are surrounded by denser domains of small fibrils. At 900 mg.mL^{-1}, the collagen networks formed by both pathways appear similar, and exhibit tight bundles of nanofibrils for both fibrillogenesis routes (**Fig.2-A-B.d**). The high density limits the molecular mobility, resulting in smaller fibrils with a limited number of repeating units that hinder the observation of striations. We confirm here that increasing the concentration of collagen drastically changes the network organization regardless of the fibrillogenesis route. The differences observed between 200-NH_3 and 200-PBS—whilst 200-PBS and 400-NH_3 are alike—suggest that the concentration is modulated by the fibrillogenesis method. Switching

the fibrillogenesis route from ammonia vapor to PBS bath is expected to change the diffusion kinetics and result in a swelling of the collagen network[25]. These results are further explored in Chapter 4, as a tool to modulate the porosity of biomimetic tubular scaffolds. The ultrastructural features are thus controlled by both the initial concentration of ColI and by the self-assembly process.

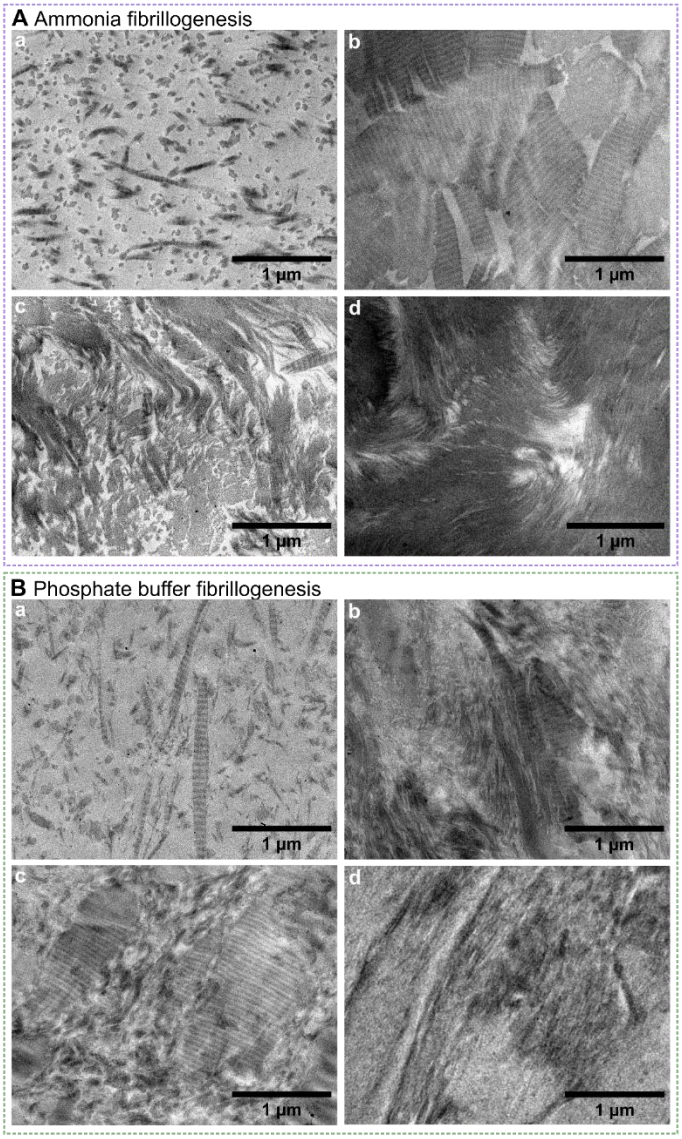

Figure 2. TEM images of dense collagen substrates at various concentrations of 40 (**a**), 200 (**b**), 400 (**c**), and 900 mg.mL^{-1} (**d**). Fibrillar networks formed under ammonia vapors conditions (**A**) display denser networks than those formed in 10x-phoshate buffer solution (**B**).

B. Dense collagen substrates providing a wide range of surface topography and local elastic properties

The ultrastructure of collagen discussed above describes the local composition encountered by cells when cultured on these substrates. However, and in particular for epithelial cell culture, the surface textural properties are equally determinant for cell processes, controlling adhesion, proliferation, and differentiation[26]. These characteristics are equally expected to play a key role on cell behavior *in vivo* and thus define the biomimetic grafts' relevance. We characterized the surface properties of the different materials prepared to quantify and to compare how these features affect cell adhesion, the cell-cell and cell-material interactions, and proliferation. First, surface topography was imaged by scanning electron microscopy (SEM). At low concentrations (40 $mg.mL^{-1}$), the formed collagen fibrils exhibit a small diameter for both fibrillogenesis routes, with 95 ± 21 nm and 107 ± 21 nm in ammonia and phosphate buffer solution, respectively (**Fig. 3** and **Table 1**). At 200 $mg.mL^{-1}$, larger fibrils are displayed in both NH_3 and PBS, with width of 225 ± 59 nm and 156 ± 64 nm respectively. SEM observations of 200 $mg.mL^{-1}$ samples prepared in ammonia show a dense network of large fibrils that display a visible striation (**Fig. 3-A.b**). Whereas PBS fibrillogenesis results in large fibrils that lay on a smooth surface formed by a dense network of tiny fibrils (**Fig. 3-B.b**). The coexistence of two fibrillar populations in PBS is confirmed by the polydispersity of fibril diameters, verified by the presence of two local maxima at ~10 nm and 180 nm. In contrast, in NH_3, the fibril width follows a monodisperse distribution. At 400 $mg.mL^{-1}$, fibrils are thinner, and exhibit a width of 108 ± 25 nm and 90 ± 17 nm in NH_3 and PBS, respectively. For the highest concentration, the two self-assembly routes lead to significantly different fibrillar morphologies on the surface (**Fig.3-A** and **B.d**). The use of PBS results in the formation of large fibrils that exhibit cross-striations, anchored on a smooth surface. Among all samples, this combination of conditions leads to formation of the largest fibrils, with a width of 390 ± 124 nm. We expect that performing fibrillogenesis in liquid media allows for higher molecular mobility than in gas phase diffusion conditions. This difference may explain the formation of wider supramolecular objects on the surface of the samples for PBS fibrillogenesis route. In comparison, fibrils formed in ammonia at 900 $mg.mL^{-1}$ do not show increased width, and display an equivalent size to the samples prepared at 40 and 400 $mg.mL^{-1}$, where small cross-striated fibrils appear, supported by a tighter fibrillar network.

The concentrations of 40 and 400 $mg.mL^{-1}$ result in similar networks, regardless of the fibrillogenesis route. However, fibrils formed by PBS tend to be larger at high concentration. The wider fibrils on the surface, are formed at 200 $mg.mL^{-1}$ for NH_3 and at 900 $mg.mL^{-1}$ in PBS. Overall, the fibrillar width is not only concentration-dependent, but is also controlled by the fibrillogenesis route, performed in this work either in liquid or gaseous phase. These

observations are valid for the fibrils present on the outer surfaces of the samples but, in comparison, the intrinsic collagen network observed under the TEM were more coherent for a given concentration irrespective of the fibrillogenesis route. This observation implies that we generated a gradient of fibril morphology across the sample thickness, that can be controlled through the self-assembly route regardless of the initial density. The choice of self-assembly route directs both the internal ultrastructure and the fibrils' morphology at the surface, features that are key to understand cellular interactions, in particular in the case of epithelial cells.

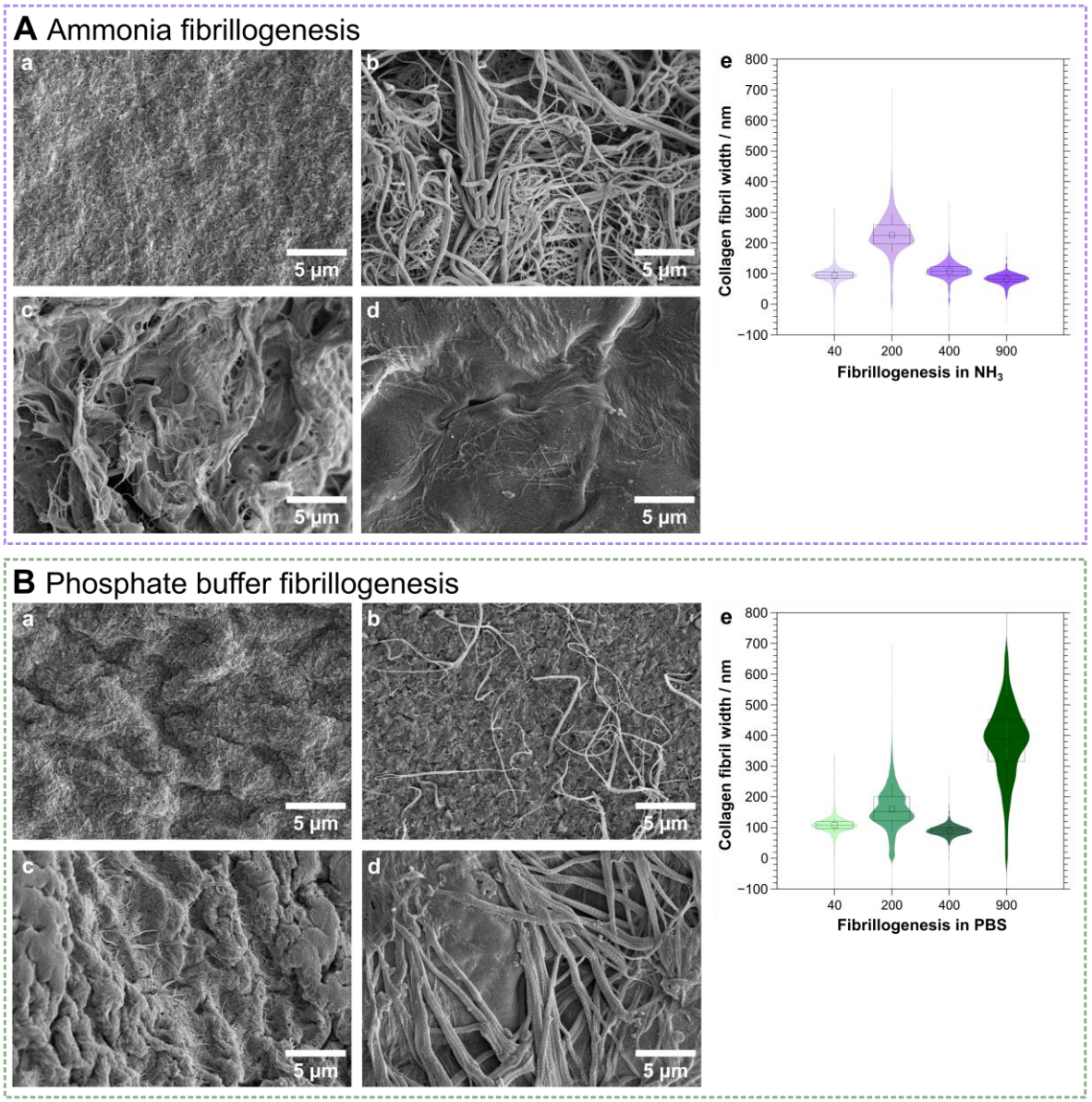

Figure 3. Topography of collagen ECM-models at various concentrations fibrillated in ammonia vapor (**A**) *versus* via phosphate buffer fibrillogenesis (**B**); **a.** 40 mg.mL^{-1}, **b.** 200 mg.mL^{-1}, **c.** 400 mg.mL^{-1}, and **d.** 900 mg.mL^{-1}). SEM analysis confirmed that the self-assembly routes regulate the formation of the

fibrils, that display various widths at the surface of the samples (**A** and **B-e**). Fibrils width was measured using the Ridge detection plugin on ImageJ (see **Appendix B-Fig.S1**). Box plots represent the first and third quartiles of the fibril width distribution, with the whiskers indicating the 10th to the 90th percentile range. The squares denote the average values, and the straight lines represent the median values.

Table 1. Influence of the collagen concentration and fibrillogenesis conditions on the fibril width in collagen substrates. Median values (± SD) of the widths were measured by Ridge detection ImageJ plugin for each sample.

	Collagen fibril width ± SD / nm	
Concentration / mg.mL^{-1}	NH_3 fibrillogenesis	PBS fibrillogenesis
40	95 ± 21	107 ± 21
200	225 ± 59	157 ± 64
400	108 ± 25	90 ± 17
900	83 ± 17	390 ± 124

Beyond their effect on collagen gels' textural properties, the physico-chemical conditions used for the preparation of the materials are also expected to play a decisive role in the matrices' elastic properties. The impact of collagen concentration (in the range studied here) and fibrillogenesis route on the elastic properties has not been previously investigated. To probe the elastic properties, we have conducted AFM indentation measurements, at the scale-length of a single cell (AFM, **Fig. 4 and Table 2**) in wet conditions. The resulting stiffness values range from 23 ± 211 kPa to 1415 ± 1171 kPa for 40 mg.mL^{-1} and 900 mg.mL^{-1}, respectively for samples fibrillated in ammonia. The local elastic moduli in samples fibrillated in PBS ranged from 36 ± 144 kPa to 1432 ± 1228 kPa for samples at concentrations equal to 40 mg.mL^{-1} and 900 mg.mL^{-1}, respectively. The engineered collagen models yield elastic moduli in the range of biological tissues—24 kPa for arteries intimal layer[27], 0.7 to 391 kPa for arteries adventitial layer[28], and 5.18 MPa for the bowel[29]—that are commonly reached with chemical cross-linking of collagen materials or synthetic polymers in biomaterials fabrication. The elastic moduli values determined by AFM (median values, **Table 2**) as well as the first and third quartiles of the distribution gradually increase with concentration; however, this relationship is linear for collagen self-assembled with NH_3 but not for samples fibrillated in PBS. Using ammonia, the increasing stiffness values correlate with the higher fibril diameters visualized by SEM. One descriptor that can account for the evolution of the samples' surface motifs is the height difference between the highest and lowest points on the AFM topographic images (**Fig.4**) of the samples (this descriptor is valid uniquely in case the samples are horizontally placed on the support). The maximum height distance variation of the samples, is higher at low concentration (with a height difference of 7.73 µm at 40 mg.mL^{-1}) and decreases progressively reaching 529 nm for samples at 900 mg.mL^{-1} fibrillated in NH_3.

The same trend is observed for samples fibrillated in PBS. We attribute this difference to the existence of large interstitial spaces in between fibrils for the lowest concentrations of collagen, whereas, as the concentration increases, the samples become increasingly dense, and the void spaces in between collagen fibrils become scarcer. Another interesting observation is the similar motifs observed at 900 $mg.mL^{-1}$ for both fibrillogenesis routes. In both cases, the texture observed is noticeably different from the lower concentrations. Alternating bright (high) and dark (low) zones with a round morphology in the micron range suggests a supramolecular organization of these materials that is distinct from the lower concentrations. The information on textures revealed by AFM is complementary to that obtained by SEM. Both techniques are prone to artifacts, but these artifacts are different in nature. SEM requires fixation and drying steps, which can encompass contraction of the samples. Topographic images obtained by AFM, on the other hand, are the result of a convolution between the tip geometry and the sample surface motifs, resulting in a widening of the fibrillar motifs. The technique can however be conducted in wet conditions, removing the risks of sample alteration due to drying.

The self-assembly of collagen induced by a PBS bath, results in different mechanical behavior over the range of concentrations studied here, in comparison to NH_3-fibrillogenesis. From 40 to 400 $mg.mL^{-1}$, stiffness values gradually increase, reaching a maximum at 900 $mg.mL^{-1}$. For the lowest collagen concentration, the local elastic moduli values for both fibrillogenesis are comparable, with median moduli of 23 ± 211 kPa in ammonia and 36 ± 144 in phosphate buffer solution. At 200 and 400 $mg.mL^{-1}$, stiffness is ~2.5x lower for collagen fibrillated in PBS than in NH_3. Moreover, the stiffness values and the height maps at 400-PBS are close to those of 200-NH_3. Based on values obtained for NH_3, the lower mechanical properties in PBS suggest a redilution of the collagen during the process. These observations confirm the swelling phenomenon expected for fibrillogenesis performed in a liquid media, described earlier in the analysis of the collagen ultrastructure by TEM. Interestingly, the moduli for the highest concentrations are in the same range for both routes, with values of 1414.96 ± 1170.77 kPa in NH_3 and 1431.75 ± 1227.77 kPa in PBS, suggesting that at this concentration no redilution takes place. Additionally, in PBS, the highest concentration displays two different regimes in the values distribution. This observation is confirmed by the coexistence of two distinct populations observed on SEM images (**Fig.2-B.d**), with large fibrils laying on a dense network of small fibrils.

It is important to note that the elastic moduli calculated here, based on the Hertz model, do not represent the properties of the individual fibrils (expected in the GPa range) nor those of the bulk matrix, but a combination of both that is modulated by the sample texture. The particularly wide distribution of elastic moduli values obtained reflect this combination of factors. However, the significance of the elastic properties discussed above is that they

provide an image of the cellular environment, at the cell length-scale. Consequently, these measurements provide an image of the mechanical environment of the cell, that we consider relevant to contextualize their adhesion and proliferation.

Here, using NH_3 vapors or PBS combined to high collagen concentration enables to reach a vast range of fibril size, roughness and stiffness of the surface. Their control leads to a precise recapitulation of the ECM, by both the ultrastructure of native type I collagen fibrils, and the elastic properties of native tissues. *In vivo*, these properties guide tissue morphogenesis and homeostasis through the regulation of the cell-specific environment. Tailored local fibrillar architecture and mechanical properties are expected to provide the adequate microenvironment at the cell length scale and support the physiological function at the tissue level for a wide range of applications in hard and soft tissue grafts.

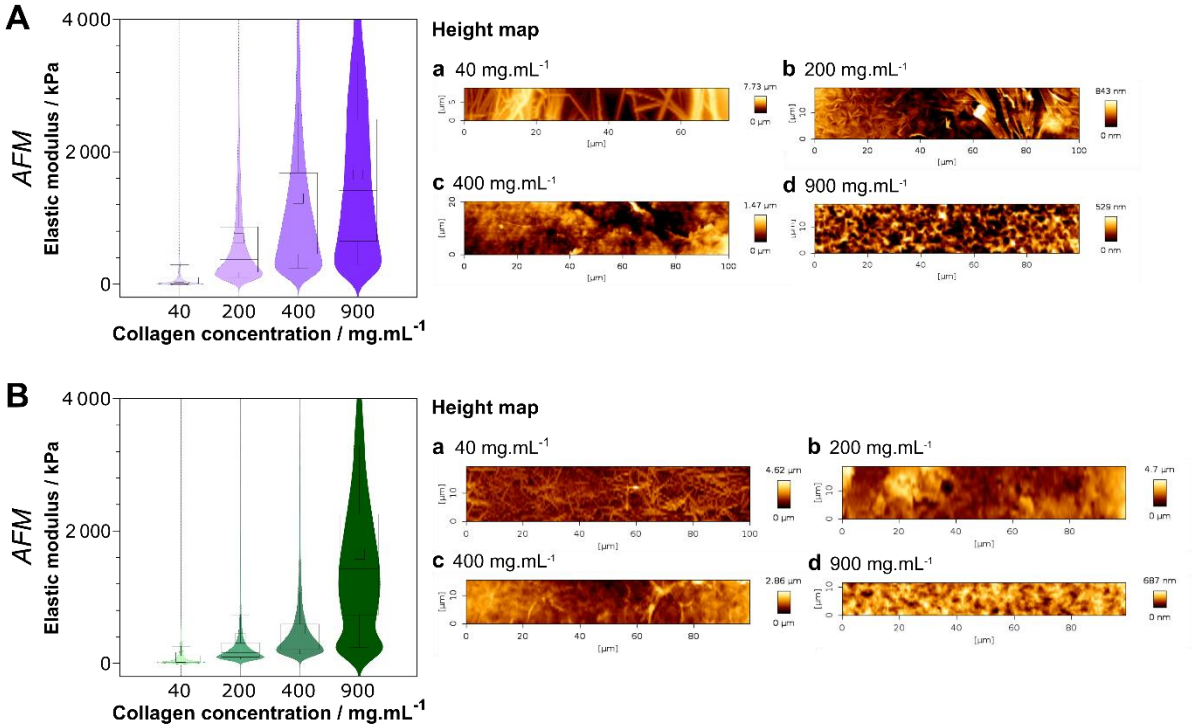

Figure 4. Nanomechanical properties of dense fibrillated collagen substrates measured by atomic force microscopy (AFM). At the microscale, collagen network density enables to reach a wide range of mechanical properties (elastic modulus) and fibrils diameter and network arrangement (height maps). Box plots represent the 25th to 75th percentile range of the modulus distribution, with the whiskers indicating the 10th to the 90th percentile range. The squares denote the average values, and the straight lines represent the median values. Measurements were performed by Dr. Joni Frederik and Dr. Florian Fage, in collaboration with the Laboratoire d'Hydrodynamique de l'X (LADHYX, Ecole Polytechnique, Palaiseau).

Table 2. Influence of the concentration and fibrillogenesis conditions on the mechanical properties of the collagen substrates. Median values (± SD) of the elastic modulus measured by AFM are reported for each sample.

	Median elastic moduli ± SD / kPa	
Concentration / mg.mL^{-1}	NH_3 fibrillogenesis	PBS fibrillogenesis
40	23 ± 211	36 ± 144
200	370 ± 898	164 ± 787
400	920 ± 1270	341 ± 573
900	1415 ± 1171	1432 ± 1228

C. Formation of an endothelial monolayer

The different cellular microenvironments described above, were used to contextualize the results of cell culture *in vitro*. We seeded HUVECs cells on the surface of our models and quantified their density as well as their spreading overtime, at day 3 and 5 (see full images in **Appendix B-Fig.S2**). The formation of tight intercellular junctions, identified by the presence of vascular endothelial (VE) cadherin, was scrutinized to assess the formation of an endothelial monolayer. Representative staining images in **Figure 5** illustrate the cell morphology (nuclei in white and actin in green) and the tightness of the cellular network (VE-cadherin in purple). Cell proliferation and actin stress fiber coverage (**Fig. 6**) measurements, realized on triplicates, revealed that at day 3, cells display a widely spread actin network is at low collagen concentration (40 mg.mL^{-1}) in both fibrillogenesis routes. A different tendency is observed for the highest concentrations, as actin is differently spread in NH_3 and PBS. According to the median coverage values, the concentrations that promote actin spreading are different for each fibrillogenesis route, at 200 mg.mL^{-1} and 900 mg.mL^{-1} in NH_3 and PBS, respectively. This observation cannot be directly correlated to the ultrastructure nor to the elastic moduli, as we assessed earlier that these samples display radically different features by TEM or AFM (*ca.* 370 kPa and 1432 kPa, respectively). However, the SEM images demonstrated that these samples have akin fibrillar morphologies. In both cases we observe the largest cross-striated fibrils among the range of surfaces. The wider actin cover may thus be explained by the presence of these large fibrils. We hypothesize that they provide an increased number of $\alpha_2\beta_1$ integrin receptor on the surface, or a specific and favorable spatial distribution of these, which results in higher cell spreading. Regarding the lowest concentration, the major difference compared to other conditions is the increased topographic height difference, a feature known to promote cell spreading. 40-NH_3 and 40-PBS substrates both provide a textured surface of peaks and valleys, with height differences of 7.73 µm and 4.62 µm respectively. At day 3 and for both self-assembly routes, the highest actin coverages also correlate with the highest cell density. This demonstrates that in the early time of culture, cellular adhesion and spreading are directly controlled by the

collagen fibril morphology and the surface topography, rather than by the local elastic properties of the surface and the intrinsic collagen ultrastructure.

Longer culture time revealed that the fibrillogenesis conditions affect the cell proliferation and cell spreading differently overtime. At day 5, the tendencies observed in PBS remain unchanged. Despite a decrease in the values of the cell density and actin coverage—which is also found in the control—the concentrations of 40 and 900 $mg.mL^{-1}$ still exhibit the highest values. Thus, it confirms that the adhesion and the expression of actin is favored on these surfaces, owing to the textured topography and the large collagen fibrils. Additionally, in contrast to NH_3, VE-cadherin seems more expressed on the periphery of cells in PBS (see white arrows in **Fig. 5**). This feature is characteristic of tight intercellular junctions, and is a hallmark of endothelium formation and maintenance in physiological conditions.

Overtime, a clear distinction is made on the behavior of cells on NH_3-fibrillated samples and PBS-fibrillated samples. At day 5 for NH_3, the cell density follows the concentrations values rather than the fibril width, as seen for day 3. Cell spreading also increases, with a peak at 400 $mg.mL^{-1}$ at a value close to the control (**Fig.6-A**, top). This demonstrates a dependence on the concentration and related stiffness overtime for NH_3-fibrillated substrates.

Overall, both fibrillogenesis pathways promote the formation of an endothelial monolayer, but under different conditions. The adhesion of cells is favored by the presence of large fibrils on the surface, occurring at 200 $mg.mL^{-1}$ and 900 $mg.mL^{-1}$ for NH_3 and PBS, respectively. The substrates textural features also promote the adhesion and spreading of cells in the early time of culture, conveyed by a low collagen concentration. Overtime, both the fibrillogenesis routes and the stiffness direct the cellular proliferation. In ammonia, incremental concentration and local stiffness promote the gradual increase of cell adhesion and actin spreading. In contrast, the PBS route provides steady tendencies through time, with the most favorable environments found for concentrations of 40 and 900 $mg.mL^{-1}$. The common concentration that provides a suitable environment for cell proliferation and spreading in both self-assembly routes, is the highest concentration at 900 $mg.mL^{-1}$ with the smoother, denser and stiffer surface. Furthermore, the cell density and the actin distribution are, on average, favored by PBS. It roots the formation of an endothelium-like layer of cells, characterized by tight intercellular junctions expressing high levels of VE-cadherin. Forming an endothelial monolayer is thus favored by PBS rather than ammonia, while the adhesion and migration rate can be tuned by the concentration.

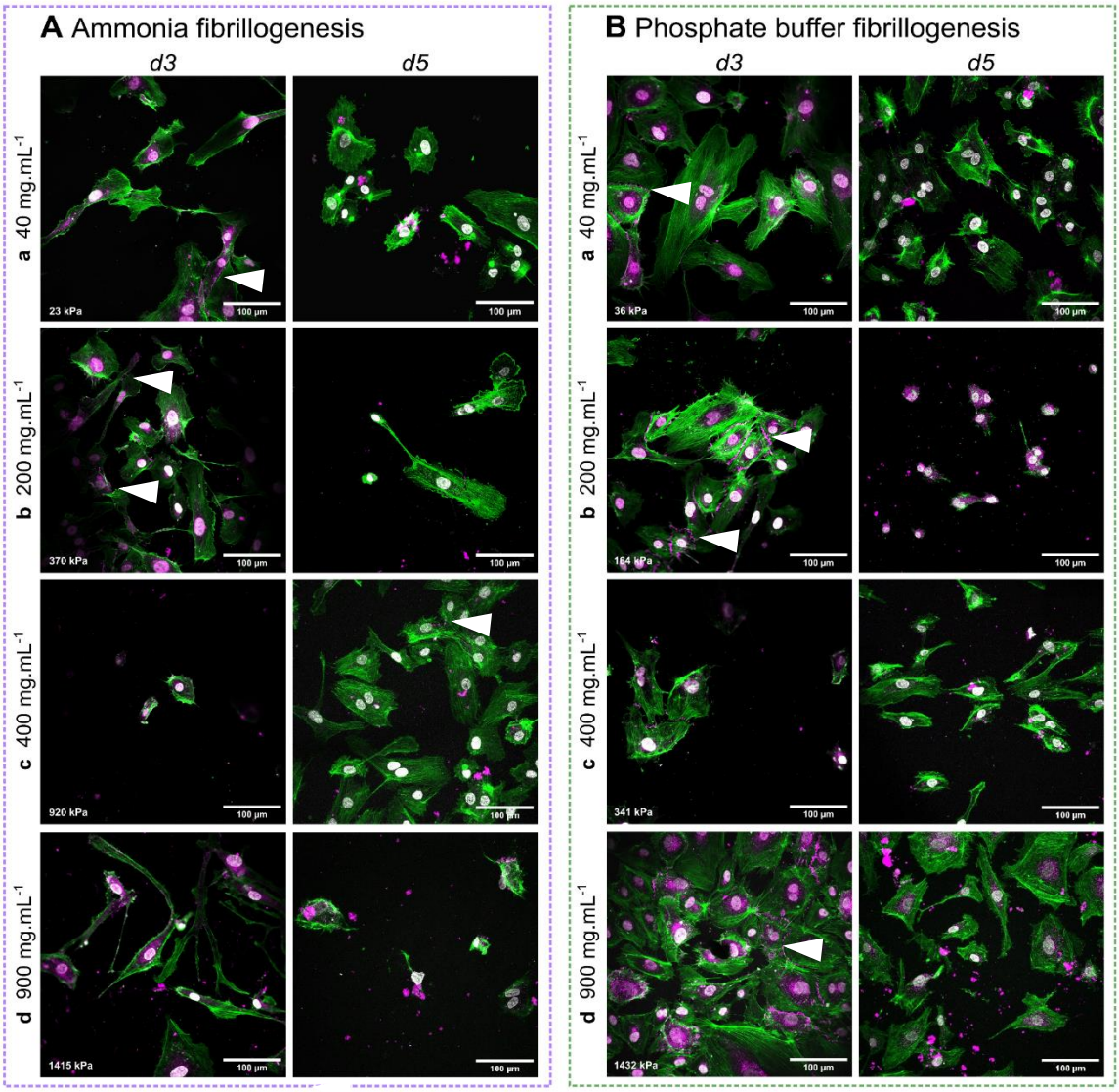

Figure 5. Cell proliferation and morphology after 3 and 5 days of culture on fibrillar collagen samples concentrated at 40 mg.mL^{-1} (**a**), 200 mg.mL^{-1} (**b**), 400 mg.mL^{-1} (**c**), and 900 mg.mL^{-1} (**d**). Samples were fibrillated using ammonia (**A**) or 10x-PBS (**B**). Upper values on the first image of each row correspond to the median local elastic moduli measured by AFM earlier. Images were acquired by confocal, following staining of cell nuclei (DAPI, white), actin (phalloidin, green), and cadherin (vascular endothelial (VE)-cadherin, purple). White arrows indicate tight junctions between cells that express VE-Cadherin in the intercellular space.

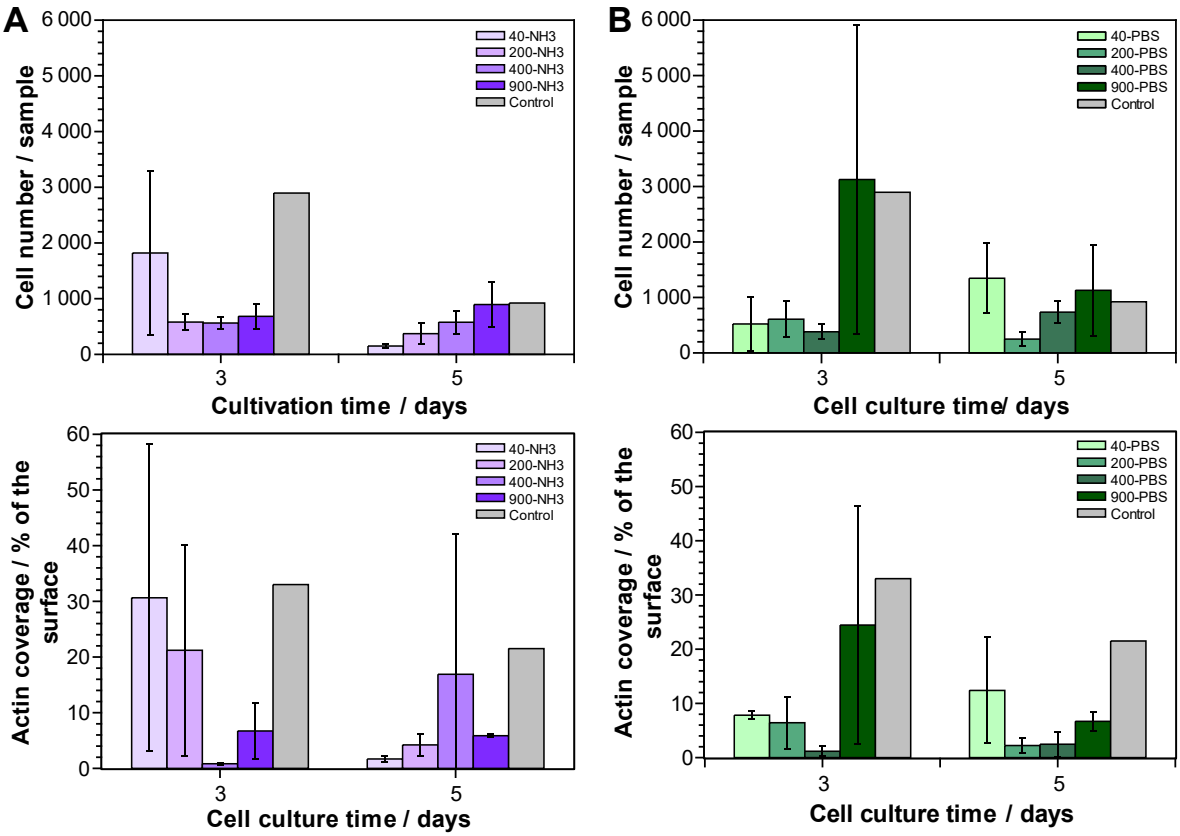

Figure 6. Cell proliferation and actin coverage after 3 and 5 days of culture on dense collagen substrates, fibrillated in ammonia vapor (**A**) or phosphate buffer solution (**B**). Controls were performed on plastic substrates. Error bars represent the standard deviations.

4. Conclusions

We elaborated thin substrates of fibrillar collagen at various densities, by mean of evaporation followed by ammonia or phosphate buffer solution-induced self-assembly. At low and high concentrations, the ultrastructure, fibril morphology, textural and mechanical cues are dictated by collagen concentration, with the fibrillogenesis pathway having a minimal impact. Low concentrations exhibit a surface composed of peaks and valleys, with small fibrils homogeneously distributed and a low elastic modulus of ~30 kPa. The highest concentrations provide a smooth and stiff environment, which favors cellular adhesion and spreading through time. These four samples enhanced cellular interactions, owing to either the textural cues or the high stiffness. In contrast, intermediate concentrations were revealed to be more sensitive to the fibrillogenesis route. PBS route induces a local dilution on the external surfaces, which leads to decreased mechanical properties and higher molecular

mobility in comparison to NH_3. The range of fibril morphology provided by the samples suggests that, in the early stage of culture, the presence of large collagen fibrils on the surface is responsible for significantly higher adhesion and spreading of endothelial cells. Furthermore, samples with a high concentration and stiffness could maintain the growth of cells and distribution of actin, compared to lower concentrations. Additionally, the use of PBS instead of NH_3 fosters the formation of an endothelium-like tissue, with tight intercellular junctions. Overall, the native like fibrils provided in a well-organized collagen network, as well as the smooth topography and the high mechanical properties at the cell length-scale, confirm the ability of these models to promote endothelialization and their potential as reliable biomimetic ECM models.

The above-mentioned results, where extremely high concentrations of collagen are more favorable than the commonly used collagen gel concentrations, contradict the standard practice of using collagen gels for *in vitro* cell culture experiments. Most protocols for the elaboration of collagen gels as cell culture substrates are restricted to low concentrations (typically under 10 mg. mL^{-1}). We show here that the systematic use of low collagen concentration is mostly inherited from long-lasting protocols, but is not backed by actual cell culture experiments, at least not for HUVECs where high concentration (900 mg.mL-1) are more favorable even if this concentration of type I collagen lies out of the range found in native tissues. We can also anticipate that, as shown for different cell culture experiments in our group[30], using highly concentrated type I collagen cell culture substrates will lead to reduced contraction of the matrices and to the possibility to extend the cell culture experiments for longer times.

Future investigations will explore the role of collagen concentration and ultrastructure in directing cell differentiation during tissue morphogenesis, and the control of the migration through imposed concentration gradients. These models may also serve to deepen the understanding of the ECM implications in the development and dissemination of tumor cells, and how the breakdown of the healthy concentration can drive pre-metastatic niches.

5. Materials and methods

Fabrication of the collagen substrates

Type I collagen was extracted from the tendons of young rat tails according to a protocol adapted from Gobeaux *et al*[31]. Tendons were thoroughly cleaned with phosphate buffered saline (PBS) 1X and 4 M NaCl solutions and dissolved in a 3 mM HCl solution. Differential precipitation with 300 mM NaCl and 600 mM NaCl, followed by redissolution and dialysis in

3 mM HCl, provided collagen of high purity. The final collagen concentration was determined using hydroxyproline titration and quantified at 5 $mg.mL^{-1}$. The extracted collagen solution was then concentrated to 40 $mg.mL^{-1}$ by centrifugation. The initial solution was transferred into Vivaspin tubes with 300 kDa filter and centrifuged at 3000g at 10°C, until the final concentration was reached. Handling higher concentrations by centrifugation is technically challenging, since the increasing viscosity that follows collagen concentration hinders its use. To compensate this limitation, samples were concentrated by evaporation at ambient temperature, under sterile conditions, to reach concentrations of 200, 400, and 900 $mg.mL^{-1}$, after deposition on a glass slide using a Doctor Blade® knife. The concentration after evaporation was calculated based on mass difference. The initial deposited volume was determined to reach a final weight of 50 mg of sample for each concentration.

Two conditions were compared (a) collagen fibrillated in ammonia, and (c) fibrillated in PBS buffer. In (a), fibrillogenesis was performed by an increase of the pH up to 9-10 by ammonia vapor diffusion for 24 h, while in (b), samples were immersed in a 10x-PBS sterile buffer bath for 24 h. After a rinsing step with PBS 5x, both gels were placed in 5x-PBS buffer and stored at ambient temperature for 2-weeks, to secure fibrillogenesis. At the end of the process, collagen gels were stored at 4°C.

Compression elastic Young modulus

The compression elastic moduli was assessed by AFM using a Nanowizard 4 BioAFM (PK/Bruker) mounted on a Nikon Eclipse Ti2-U inverted microscope equipped with PetriDish Heater. To cover the wide range of stiffness found in the samples according to the concentration and fibrillogenesis routes, two appropriately matched probes with different spring constants were used for the measurements (qp-BioAC-CI and PPP-FMAuD from NANOSENSORS™). Cantilevers were calibrated using the thermal calibration method in PBS (1X) at 37°C. The Hertz model was applied to fit each force-indentation curve, and stiffness for each scan point was extracted using JPK data processing software. All measurements were made under immersion conditions in PBS (1X) at a physiological temperature of 37°C using a tip with a radius of curvature between 10 and 30 nm.

Transmission electron microscopy

Fibrillated samples were cross-linked with 2.5% paraformaldehyde (PFA), 2% glutaraldehyde, 0.18 M sucrose and 0.1% picric acid for 12 h. The samples were subsequently post-fixed with uranyl acetate in ethanol for 12 h, and dehydrated using baths of increasing concentrations in ethanol. Samples were incorporated in SPURR-S resins prior to sectioning. Ultrathin sections

(70 nm), obtained using a Leica ultramicrotome, were contrasted with uranyl acetate and observed on a transmission electron microscope (FEI Tecnai Spirit G2) operating at 120 kV to observe the ultrastructural collagen features. Images were recorded on a Gatan CCD camera.

Scanning electron microscopy

After fibrillogenesis, matrices devoid of cells were dried by supercritical drying on a EM CPD300 Critical Point Dryer. 5 cycles were performed, at constant stirring, and a slow CO_2 gas out speed (50%). Topography of the collagen substrates (observation plane parallel to the surface), were imaged to depict the morphology of the fibrils. Samples were sputter coated with a 10 nm layer of gold and imaged using scanning electron microscopy on a Hitachi S-3400N microscope at 5 kV. Measurement of the fibril widths were calculated using Ridge detection ImageJ plugin (for resulting fit, see **Appendix B-Fig.S1**)

Cell culture and immunostaining

Human umbilical vein endothelial cells (HUVECs, Lonza) in passages 5-6 were cultured at 37°C and 5% CO_2 in EGM2 cell medium (Lonza). Cells were detached from the adhering surface using TrypLE (Life Technologies, Carlsbad, USA). HUVECs were seeded on the luminal surface of 6 mm diameter discs of the collagen scaffolds (or polystyrene surface as a control) at a density of 1800 cells/sample and cultured for 3 and 5 days. At the end of the culture, samples were fixed with 4% paraformaldehyde, permeabilized with 0.1% Triton X-100, and then incubated with primary anti VE-Cadherin (ratio 1:250, abcam AB33168) for immunostaining, then secondary antibody (ratio 1:400, goat Anti-Rabbit IgG H&L from abcam, Alexa Fluor® 647, ab150077), Phalloidin 488 (ratio 1:2000, Invitrogen A12379), and DAPI (ratio 1:50000, Sigma Aldrich) to visualize VE-cadherin, the F-actin cytoskeleton, and the nuclei.

Confocal microscopy

Cellularized samples with HUVECs cells were observed using a Zeiss LSM 980 upright confocal microscope equipped with W Plan-Apochromat 20x objective. Single and series of images z-stacks were acquired at 0.5 µm intervals to assess cellular morphology.

Widefield fluorescence stereomicroscopy

Cellularized samples with HUVECs were observed using a Macroscope Zeiss apotome (AxioZoom V16) in widefield mode, equipped with PlanNeoFluar Z 1.0X objective, and a detector comprising a Zeiss AxioCam HRc (color camera) and MRm. Cell proliferation was quantified by counting the number of nuclei (based on the DAPI signal) using the LabKit ImageJ plugin.

6. References in Chapter III

1. Dzobo, K. & Dandara, C. The Extracellular Matrix: Its Composition, Function, Remodeling, and Role in Tumorigenesis. *Biomimetics* **8**, 146 (2023).

2. Engler, A. J., Sen, S., Sweeney, H. L. & Discher, D. E. Matrix Elasticity Directs Stem Cell Lineage Specification. *Cell* **126**, 677–689 (2006).

3. Wu, J. *et al.* Gradient biomaterials and their influences on cell migration. *Interface Focus* **2**, 337–355 (2012).

4. Wang, Y. *et al.* Bioengineered Systems and Designer Matrices That Recapitulate the Intestinal Stem Cell Niche. *Cell Mol Gastroenterol Hepatol* **5**, 440–453 (2018).

5. Kyburz, K. A. & Anseth, K. S. Synthetic Mimics of the Extracellular Matrix: How Simple is Complex Enough? *Ann Biomed Eng* **43**, 489–500 (2015).

6. Pajic-Lijakovic, I., Milivojevic, M. & Clark, A. G. Collective Cell Migration on Collagen-I Networks: The Impact of Matrix Viscoelasticity. *Front Cell Dev Biol* **10**, (2022).

7. Elango, J. *et al.* The Molecular Interaction of Collagen with Cell Receptors for Biological Function. *Polymers (Basel)* **14**, 876 (2022).

8. He, Y. J. *et al.* Cell-Laden Gradient Hydrogel Scaffolds for Neovascularization of Engineered Tissues. *Adv Healthc Mater* **10**, (2021).

9. Hirschfeld-Warneken, V. C. *et al.* Cell adhesion and polarisation on molecularly defined spacing gradient surfaces of cyclic RGDfK peptide patches. *Eur J Cell Biol* **87**, 743–750 (2008).

10. Cai, K. *et al.* Regulation of endothelial cells migration on poly(d, l-lactic acid) films immobilized with collagen gradients. *Colloids Surf B Biointerfaces* **79**, 291–297 (2010).

11. Hale, N. A., Yang, Y. & Rajagopalan, P. Cell migration at the interface of a dual chemical-mechanical gradient. *ACS Appl Mater Interfaces* **2**, 2317–2324 (2010).

12. Hu, D. & Shan, X. Effects of different concentrations of type-I collagen hydrogel on the growth and differentiation of chondrocytes. *Exp Ther Med* **14**, 5411–5416 (2017).

13. Ahearne, M. *et al.* Influence of cell and collagen concentration on the cell–matrix mechanical relationship in a corneal stroma wound healing model. *Exp Eye Res* **91**, 584–591 (2010).

14. McKee, T. J., Perlman, G., Morris, M. & Komarova, S. V. Extracellular matrix composition of connective tissues: a systematic review and meta-analysis. *Sci Rep* **9**, (2019).

15. Butcher, D. T., Alliston, T. & Weaver, V. M. A tense situation: forcing tumour progression. *Nat Rev Cancer* **9**, 108–122 (2009).

16. Cox, T. R. & Erler, J. T. Remodeling and homeostasis of the extracellular matrix: implications for fibrotic diseases and cancer. *Dis Model Mech* **4**, 165–178 (2011).

17. McKay, Priyadarsini & Karamichos. Mechanisms of Collagen Crosslinking in Diabetes and Keratoconus. *Cells* **8**, 1239 (2019).

18. Paszek, M. J. *et al.* Tensional homeostasis and the malignant phenotype. *Cancer Cell* **8**, 241–254 (2005).

19. Joshi, I. M. *et al.* Microengineering 3D Collagen Matrices with Tumor-Mimetic Gradients in Fiber Alignment. *bioRxiv* (2023) doi:10.1101/2023.07.09.548253.

20. Vining, K. H. & Mooney, D. J. Mechanical forces direct stem cell behaviour in development and regeneration. *Nat Rev Mol Cell Biol* **18**, 728–742 (2017).

21. Rashidi, H., Yang, J. & Shakesheff, K. M. Surface engineering of synthetic polymer materials for tissue engineering and regenerative medicine applications. *Biomater. Sci.* **2**, 1318–1331 (2014).

22. Van Luyn, M. J. A. *et al.* Relations between in vitro cytotoxicity and crosslinked dermal sheep collagens. *J Biomed Mater Res* **26**, 1091–1110 (1992).

23. Giraud-Guille, M. M. Twisted liquid crystalline supramolecular arrangements in morphogenesis. *Int Rev Cytol* **166**, 59–101 (1996).

24. Giraud Guille, M. M., Nassif, N. & Fernandes, F. M. Collagen-based Materials for Tissue Repair, from Bio-inspired to Biomimetic. in *RSC Smart Materials - Materials Design Inspired by Nature: Function through Inner Architecture* (eds. Fratzl, P., W. C. Dunlop, J. & Weinkamer, R.) vol. 4 107–127 (The Royal Society of Chemistry, 2013).

25. Martinier, I. *et al.* Tunable biomimetic materials elaborated by ice templating and self-assembly of collagen for tubular tissue engineering. *biorXiv* (2023) doi:10.1101/2023.08.30.555553.

26. Critser, P. J., Kreger, S. T., Voytik-Harbin, S. L. & Yoder, M. C. Collagen matrix physical properties modulate endothelial colony forming cell-derived vessels in vivo. *Microvasc Res* **80**, 23–30 (2010).

27. Asgari, M., Latifi, N., Giovanniello, F., Espinosa, H. D. & Amabili, M. Revealing layer-specific ultrastructure and nanomechanics of fibrillar collagen in human aorta via Atomic Force Microscopy testing: implications on tissue mechanics at macroscopic scale. *Adv Nanobiomed Res* **2**, 2100159 (2022).

28. Grant, C. A. & Twigg, P. C. Pseudostatic and Dynamic Nanomechanics of the Tunica Adventitia in Elastic Arteries Using Atomic Force Microscopy. *ACS Nano* **7**, 456–464 (2013).

29. Christensen, M. B., Oberg, K. & Wolchok, J. C. Tensile properties of the rectal and sigmoid colon: a comparative analysis of human and porcine tissue. *Springerplus* **4**, 142 (2015).

30. Parisi, C. *et al.* Porous yet dense matrices: using ice to shape collagen 3D cell culture systems with increased physiological relevance. *Biomater Sci* **10**, 6939–6950 (2022).

31. Gobeaux, F. Phases denses de collagène de type I: transition isotrope/cholestérique, fibrillogenèse et minéralisation. (Université Pierre et Marie Curie, 2008).

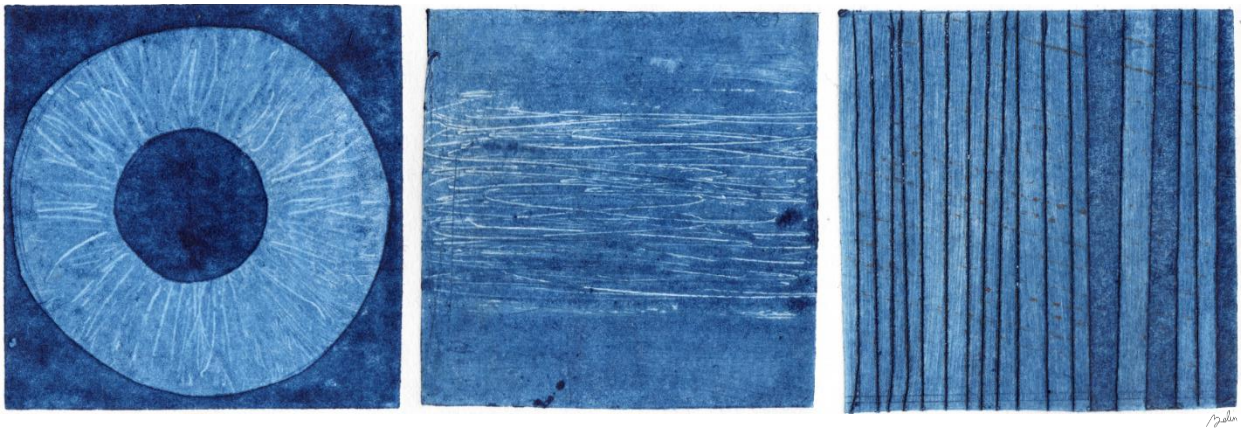

Chapter IV

Porous dense collagen materials elaborated by ice templating and topotactic fibrillogenesis to mimic tissues

"Des petits trous, des petits trous, toujours des petits trous. "

— *Le poinçonneur des lilas*, Serge Gainsbourg

1. Introduction

The preceding chapters have taught us that tubular organs, and the organization of native collagen in particular, are difficult to replicate. On the one hand, as the main component of tubular tissues (§Chapter 1), collagen serves as an optimal core material for any attempt to mimic tubular organs. On the other hand, its practical use is limited by a lack of knowledge about the behavior of this protein during materials processing, as outlined in Chapter 2. The state diagrams proposed in this manuscript aim at partly filling this gap, by detailing the conditions of temperature and concentration controlling collagen integrity and assembly. They illustrate that self-assembly of collagen molecules can be triggered by various mechanisms, such as molecular crowding, or increasing pH and osmotic pressure. We associated these diagrams to various techniques aiming to mimic the features of native collagenous tissues. In particular, these tools provide a deeper understanding of the freezing events occurring during ice-templating of collagen, and enable to measure the concentration yielded by its segregation from a growing ice phase.

The majority of the biomaterials community uses collagen at concentrations below 10 $mg.mL^{-1}$. However, in native tissues, its concentration ranges between 100 to 200 $mg.mL^{-1}$. Our understanding of the interactions of cells with collagen, under physiological conditions, is thus incomplete. Chapter 3 exposes how the concentration and the fibrillogenesis pathways affect the fate of cells, exemplified with endothelial cells (HUVECs). We correlated these findings with the local mechanical properties and the ultrastructure of collagen fibrils. Cells preferentially adhere on materials displaying large fibrils, and proliferate on stiffer substrates. Yet, these 2D materials do not promote cell colonization (taken here in its three-dimensional sense), necessary to favor biointegration in the context of a clinical graft. The only route envisaged for cell migration would be *via* remodeling of the substrate. However, because we have chosen to work at high collagen concentration, this phenomenon is precluded or at least noticeably delayed. Our strategy is to take advantage of the ice-templating technique, and combine it to topotactic fibrillogenesis. This combination enables to generate materials that feature a high degree of hierarchical organization in comparison to the current literature: porous yet dense collagen materials, with native-like fibrils.

Based on previous studies[1,2], these materials combine both the necessary porous network that ensures cell infiltration and access to nutrients; and a local collagen concentration that corresponds to that of native tissues. Commonly, ice templated materials are freeze-dried to generate foams[3–5] Such materials fail to reach native mechanical properties and the fibrillar structure of collagen, a gap often bypassed by chemical or physical cross-linking. In this work, we control the melting of ice and collagen self-assembly by triggering collagen

fibrillogenesis. This topotactic approach is based on imposing fibrillogenesis conditions (pH and/or osmotic pressure increase) at low temperature. It preserves the macroporous structure induced by ice crystals, while simultaneously inducing the self-assembly of collagen molecules into fibrils. We explored and compared here two routes of topotactic fibrillogenesis, using ammonia vapors or immersion in a buffer solution[‡‡].

These techniques are applied to tubular materials featured with different porous structures, resulting in various matrices that present native-like fibrils, highly-organized suprafibrillar architectures, and distinct textural properties. This new family of materials offer mechanical properties in the range of native tissues, without requiring the use of any cytotoxic crosslinkers. Furthermore, *in vivo* studies assessed that they provide a favorable environment for cellular adhesion, colonization and proliferation. By tailoring the freezing and fibrillogenesis conditions, our materials are capable to promote both adhesion of epithelial cells on the lumen to form a monolayer, and the migration of cells from the adventitia. These materials recapitulate composition, structure, biological and mechanical properties akin to tubular tissues ECM.

This chapter describes the preparation and characterization of such materials, as submitted to *Biomaterials Science* journal, given with preliminary results. Additional results detail how the freezing parameters are tailored to obtain specific size and orientations of pores, and how the templating process transposes to other sizes and geometries. Permeable properties are also discussed, and an alternative fibrillogenesis is proposed.

2. Preliminary results

A. Ice templating acidic dense collagen solutions

Originating from the ceramics, ice templating—or freeze-casting—is a common process to form regular porous patterns in three-dimensional structures, by controlling the solidification processes of solution and/or colloidal suspension. Size and periodicity of the patterns correlate directly with parameters such as the thermal gradient, the freezing temperature, the ice front velocity as well as the concentration of the solute and viscosity of the solution. The

[‡‡] Patented work: PCT/FR2023/051232, "Porous collagen material and process for preparing the same by topotactic fibrillogenesis"

control of the solidification front, leading to particles segregation, is the critical factor to tailor the final microstructure. Here we applied this simple process to generate porous biomaterials using type I collagen for future applications in the biomedical field. Pores promote cell infiltration and migration, while the concentrated collagen walls resulting from the phase segregation enhanced cell adhesion and proliferation, as studied in **Chapter 3**.

The rational control of many suspensions by ice templating has been described in the literature, and in particular for biomaterials[6]. A wide variety of compositions have been frozen in a controlled manner, from hydroxyapatite slurries[7] to biopolymer solutions (chitosan[3], collagen[4], among others) targeting the treatment of various pathologies. It is commonly acknowledged that the formation of ice templated materials depends primarily on physical than chemical interactions[8]. It is however important to note that the previous statement holds uniquely in case there are no specific interactions between the solutes and the ice crystal surfaces as in the case of anti-freeze proteins[9]. If no specific interaction is present then the process can be easily transposed to any solution or colloidal suspension, and that the same parameters will result into comparable microstructures. The behavior of type I collagen in this context, and in particular the possibility to establish specific interaction with ice crystals has not been described yet. Theoretical modelling of the behavior of collagen during freezing seems to indicate that no specific interactions occur[10] but few studies investigated unidirectional freezing of concentrated collagen solutions[1,2].Here we describe an extensive rational control of templating a dense collagen solution, and in particular the relationships between the freezing conditions and the final microstructures. We tuned the porosity by varying the **freezing media temperature**, the **freezing dipping speed**, and the **thermal conductivity of the molds** to modulate the thermal gradient. The ice templating of the various collagen materials was followed by sublimation of the frozen phase, leading to porous structures where pores are a replica of ice crystals. Microstructures were analyzed using ImageJ fiji software.

B. Elaboration of the freezing set-up

The experimental set-up to ice-template the tubular collagen scaffolds was built in the laboratory (**Fig.1**). It was designed and assembled using materials found in DIY shops and 3D-printed parts with ABS. The motor was coupled to an Arduino board and a "Nano 33 every" card, to operate the stepper motor that controlled the dipping speed of samples in the freezing media. To do so, a code was adapted from a stepper motor control program and calibrated to freeze materials at 10, 25 and 50 $mm.min^{-1}$ (**Appendix C-Fig.S1**). The tubular scaffolds were mounted on optical steel rails that ensure the straightness and stability of the dipping process.

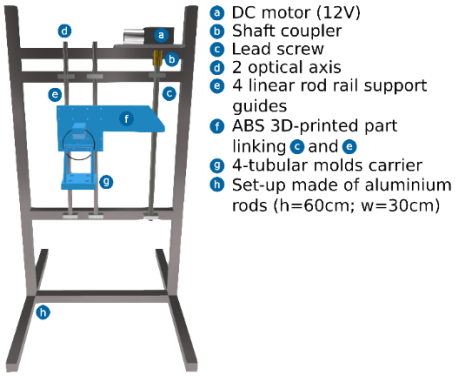

Figure 1. Dedicated ice templating set-up designed and assembled at the LCMCP, used to elaborate biomimetic tubular materials.

C. Tuning the porous network by controlling the freezing conditions

a. Influence of the dipping speed on the anisotropic kinetics

Freezing of aqueous solutions can be split into two major phenomena. The first is the nucleation of ice crystals that occurs from a superccooled state and that generates nanoscopic water aggregates. Nucleation can take place according to two major pathways, homogenous and heterogeneous nucleation[11]. For the work reported in this manuscript, and because only freezing from solutions will be considered, nucleation will be considered as homogeneous. Once the conditions favorable for the accretion of water molecules from the liquid phase to a solid state to form nanoscopic aggregates are gathered—supersaturation of water in a strictly thermodynamic standpoint—the second step occurs, ice growth. In homogeneous nucleation of water, the nucleation rate depends on the supersaturation ratio, which brings a kinetics-dependent dimension to the out-of-equilibrium phenomena. The second step, *i.e.* the ice growth that occurs at equilibrium, depends on the existence of conditions that favor water molecules transport from the liquid phase to a pre-existing solid water aggregate. Simply put, both phenomena are strongly dependent on the thermal boundary conditions of the system and on how these evolve with time.

The experimental set-up that we developed allows to modulate the velocity at which the samples are dipped in the freezing media, thus playing a critical role in both ice nucleation and growth. By adjusting this velocity, we expect to alter the thermal gradient inside the sample during freezing and thus modulate the induction time before nucleation as well as tailor the orientation of the resulting ice crystals. Here, we show that the dipping speed is involved in the formation and growth kinetics of ice in a dense collagen solution. The result of the different sample freezing velocities on ice structure were investigated on 40 $mg.mL^{-1}$ collagen solutions. Collagen was inserted in cylindrical molds composed of aluminum (inner mold), and ABS (outer mold), a set of conditions abbreviated as *Cond.* The combination of

an outer conductive mold and an inner insulating one is expected to orient the thermal gradient axially, from the outer mold to the inner one. Freezing of the samples was then performed by controlled immersion into liquid nitrogen, at 10, 25 and 50 mm.min^{-1}.

At 10 mm.min^{-1}, the sample section is completely covered by a single ice growth "domain" characterized by parallel lamellar pores running radially along the sample wall thickness. At 25 and 50 mm.min^{-1}, an interface is positioned at respectively 27% and 42% from the lumen, calculated as a percentage of the total wall thickness (**Table 1**). The morphological transition from the nucleation-dominated zone to the lamellar ice growth zone can be clearly observed through an interface that lies parallel to the tube walls (dotted lines in **Fig.2-A**), which position shifts with the dipping velocity. At low speed, the balance is in favor of the thermal gradient imposed by the mold conductivity difference, leading to a fast but limited nucleation zone, followed by subsequent lamellar growth. At high dipping velocity, the nucleation of ice covers a larger zone from the external conductive mold (**Fig.2-A**). When a steady state is reached, ice crystals become continuous and grow towards the inner part of the cylinders, with a constant width and following an extended freezing front. At these dipping velocities the longitudinal thermal gradient imposed by the high velocity of the unidirectional dipping competes with the axial thermal gradient imposed by the molds' thermal conductivity. The thermal gradient direction is thus a combination of these parameters that translate to a less well-defined geometry of the ice crystals formed during the growth step. As shown in **Fig.2-B**, for the lowest speed lamellae follow an angle of 11° that corresponds to the orientation of the axial thermal gradient. Using faster freezing rates and this pair of molds, pores display a more longitudinal component. Pores follow a main angle of 32° at 25 mm.min^{-1}, and 63° at 50 mm.min^{-1} (**Table 1**). Additionally, the existence of multiple orientations at higher speeds (-46° at 25 mm.min^{-1}; -25° and 20° at 50 mm.min^{-1}) proves that lamellae are less ordered and do not follow a unidirectional thermal gradient. These data confirm the difficulty to attain a steady growth state at high freezing rates, but these conditions still enable some degree of control over the structure of the porous network.

Table 1. Orientation and dimensions of samples pore, measured in longitudinal sections after freeze-drying. Samples were ice templated at various dipping speeds, including 10, 25 and 50 mm.min^{-1}. Images were acquired by SEM, and measurements were done on the lamellar region using ImageJ.

	Dipping velocity / mm.min^{-1}		
Measurement	10	25	50
Main orientations / °	11	-46, 32	-25, 20, 63
Median Feret / µm	25.95 ± 59.31	24.55 ± 37.56	29.48 ± 49.30
Median MinFeret / µm	14.49 ± 20.78	12.76 ± 14.00	16.11 ± 21.04
Lumen-interface distance / % of the total wall thickness	0	27	42

Differently from the current statements in the literature[12,13], we found that the dipping speed has no dramatic influence on the pore size. All minimum and maximum Feret diameters of pores within the lamellar region are comparable (**Fig.2-C.a,b and Table 1**), with median Feret diameters of 25.95 ± 59.31 µm, 24.55 ± 37.56 µm, and 29.48 ± 49.30 µm for 10, 25 and 50 mm.min^{-1}. These data evidenced that, once in the lamellar regime, the morphology of ice is independent from the imposed initial freezing rate in this set of speeds, and suggests that the local ice growth velocities are equivalent. Extensive studies using thicker materials could provide insights about the stability of the lamellar growth front and the evolution of the ice crystals morphology at high speeds.

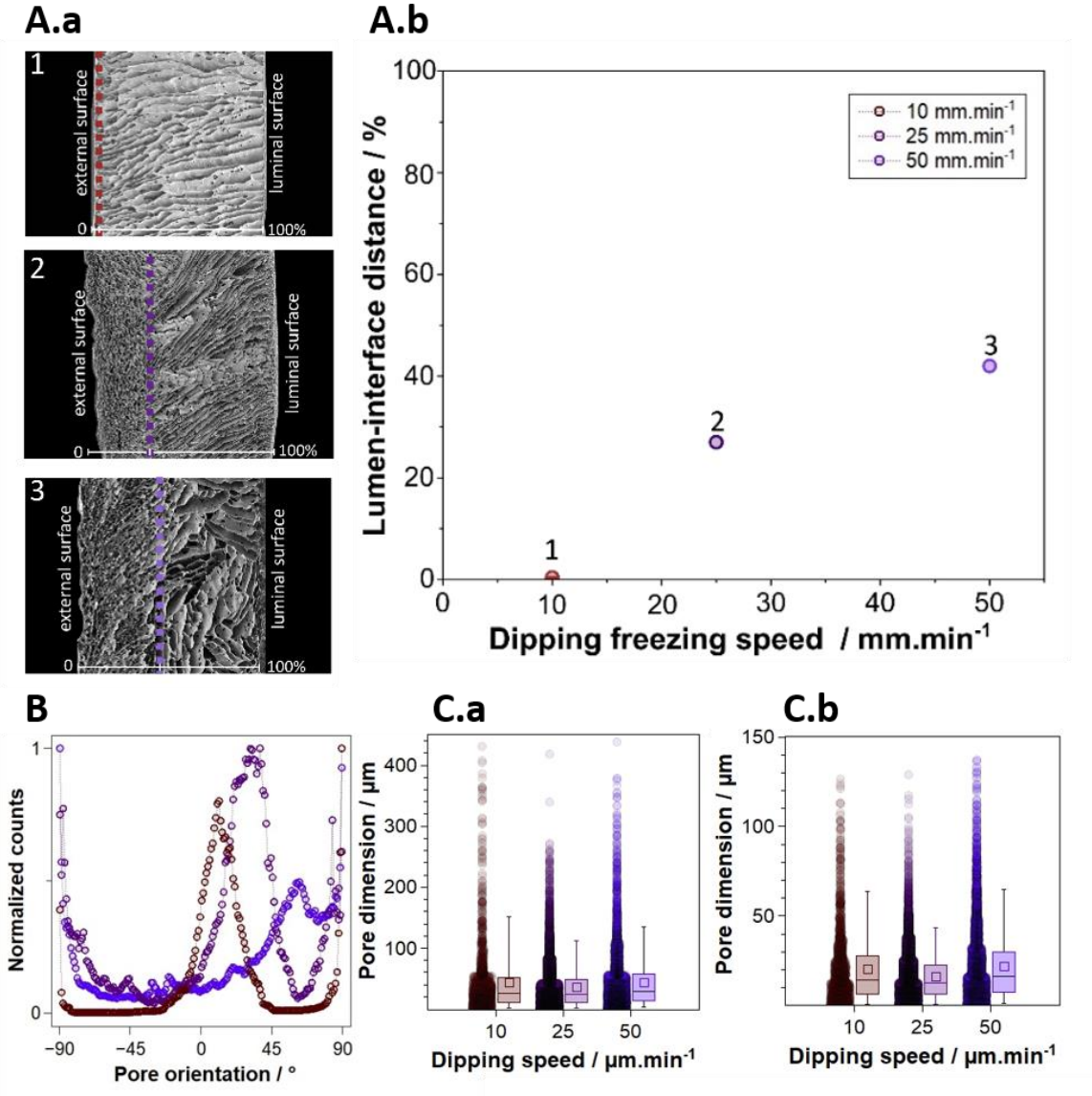

Figure 2. Pore morphology of dense collagen materials ice templated at various dipping speeds, including 10 mm.min^{-1} (in brick red), 25 mm.min^{-1} (in dark purple), and 50 mm.min^{-1} (in light purple). **A.a**) Longitudinal cross sections of samples imaged by SEM. The dotted lines represent the interface

between nucleation dominated and ice growth zones. **A.b**) Correlation between the position of the interface and the dipping velocity. **B**) Orientation of pores measured in the longitudinal cross sections. **C**) Pore dimensions in longitudinal sections, based on the minimum Feret diameter (**a**) and the maximum Feret diameter (**b**). Boxplots are plotted in linear scale and represent the 25th to 75th percentile range of the pore distribution (dots). Top and bottom whiskers indicate the 10th to the 90th percentile range of the distribution, squares denote the mean values, and straight lines represent the medians. This representation stands for the following boxplot graphs in this section. For the methodology of SEM images reconstruction, analysis of the porosity and orientation, see **Appendix C-Fig.S2**.

By simply adjusting the freezing rate, a wide range of structures can be formed. Under the set conditions (molds conductivity and bath temperature), a low freezing rate generates anisotropic structures composed of axially-oriented lamellar pores. Conversely, higher freezing rates induce a shift in the ice front velocity, which leads to the formation of more isotropic structures. These are featured with two distinct porous regions separated by an interface. The first frozen region, corresponding to the ice nucleation close to the conductive mold, displays round planar ice. The second region displays lamellar ice growing with more random orientations. The width of these regions and the position of the interface are directly correlated with the freezing speed. The higher the speed, the closer to the lumen. This short study provides more insights about the ice physics in dense collagen solutions, and the relationships between the freezing rate and the microstructure.

b. Influence of the freezing bath temperature on the macroporous structure

Depending on the pressure and temperature, the crystalline structure of ice changes, particularly at extreme pressures and low temperatures. Under atmospheric pressure conditions, hexagonal ice (Ih) forms when water freezes (**Fig.3-A, B**). In this study, we focused on conditions conducive to hexagonal ice formation, and investigated how varying the temperature of the freezing bath impacts the freezing rate and, consequently, the resulting structures. We compared the effect of two cooling media: liquid nitrogen at -196°C, and dry ice in ethanol at -78°C, for a wide range of materials. Various combinations of molds were tested, using a constant outer brass mold. The inner molds included aluminum, brass, stainless steel, and ABS, yielding different thermal conductivity difference values ($\Delta\lambda$) of -127, 0, 65, and 110 $W.m^{-1}.K^{-1}$, respectively.

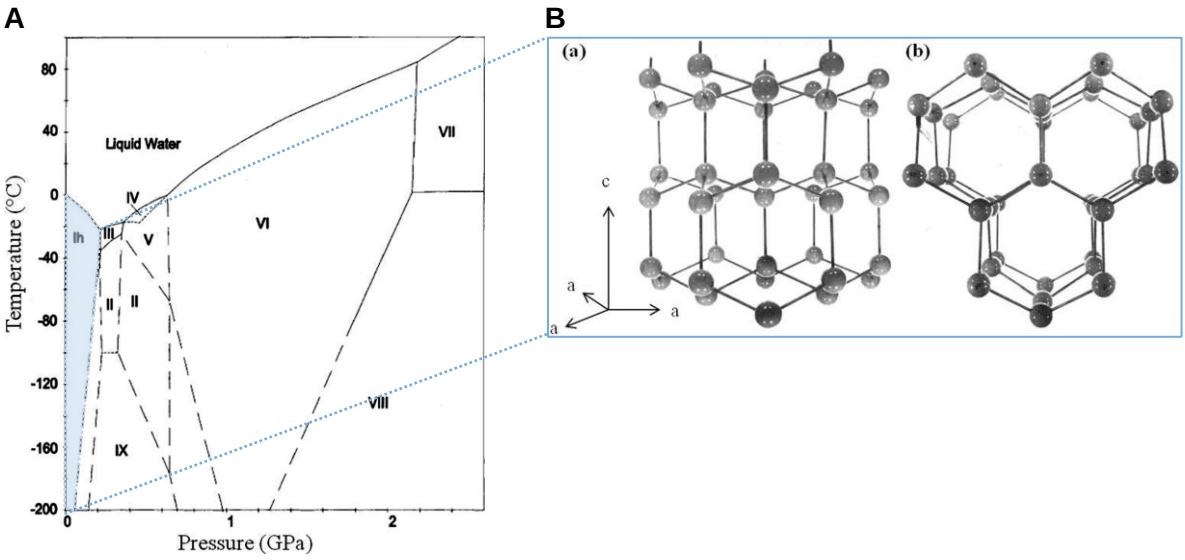

Figure 3. A) The temperature-pressure phase diagram of water. Under normal pressure conditions and at low temperature, ice has a hexagonal structure (Ih). At higher pressure, ice adopts other crystalline structures. **B**) Structure of hexagonal ice, hydrogen bonds are represented with rods. (**a**) Perpendicular to the *c*-axis, and (**b**) parallel to the *c*-axis. Modified reprints from Akyurt *et al.*[14]

As illustrated in **Figure 4**, an interface forms at low **Δλ** values. The bidirectional thermal gradient, imposed here by both conductive molds, induces the growth of ice crystals from the inner mold and from the outer mold. When these two crystalline regions converge, an interface is generated and maintained at a stable position. The formation and stability of that interface is not affected by the different freezing bath temperatures, as it consistently stands at the same distance to the lumen. This suggests that the rate of the ice front velocity remains constant within the materials, regardless the cooling bath temperature. However, with a higher bath temperature, pores tend to be larger (**Fig.4-C,D.a** and **Table 2**).

The main difference between samples frozen at -196°C or -78°C lies in the orientation of pores (**Fig.4-C,D.b**). In samples frozen with liquid nitrogen, pores follow a main angle ranging from -16.5° to -4.5° (**Table 2**). In contrast, when subjected to higher temperatures, we have detected a larger heterogeneity in the pore orientation, with a wider range of angles spanning from -46.5° to -13.5°. While this shift in the orientation between the two freezing baths is not drastic, it is noteworthy that a higher freezing temperature reduces the control over ice formation. It results in larger and more longitudinally-oriented pores that align with the freezing direction along the *z*-axis. By increasing the freezing temperature up to -78°C, the nucleation and growth of ice is not only mediated by the cooling bath temperature, but also by the thermal gradient imposed by the dipping process. This influence is particularly clear when comparing the results obtained using an inner insulating mold. At -78 °C and with **Δλ** = 110 $W.m^{-1}.K^{-1}$, the sole condition for which an insulating mold is used, the dominant ice growth angle is -46.5°. In comparison, samples prepared under equivalent thermal

conductivity conditions but using liquid nitrogen exhibit pores with lower angles centered at -16.5°. This observation reaffirms that at higher temperature, the balance between the gradient along the *z*-axis and the one along the *a*-axis is displaced towards the *z*-axis.

For a low conductivity difference, the presence of an interface in between two lamellar regions translates into the existence of diverse orientations. For **Δλ** values of -127 and 0 $W.m^{-1}.K^{-1}$, pores are respectively oriented at -4.5° plus 40.5°, and -16.5° plus 28.5°, when frozen in nitrogen. Whereas when frozen in dry ice, these same samples display pores oriented at -13.5°, 31.5° plus 41.5, and -14.5° plus 28.5°, respectively.

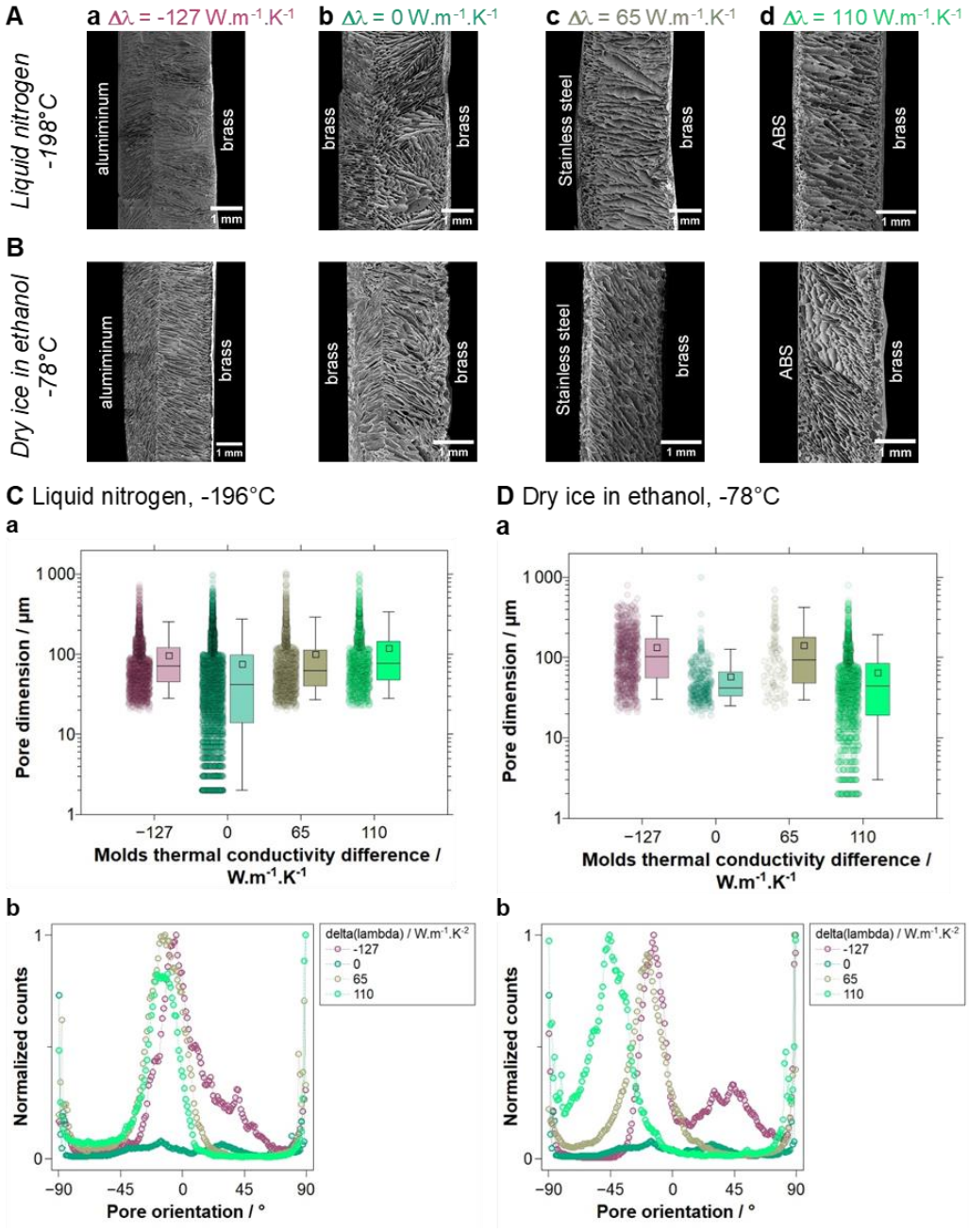

Figure 4. Longitudinal sections of collagen samples ice templated into liquid nitrogen at -196°C (**A**) or dry ice in ethanol at -78°C (**B**), using various combination of mold materials. Images were acquired under SEM after freeze drying. Collagen materials were templated with a constant outer mold of brass (on the right), and various inner molds (on the left) of different thermal conductivity, λ. Inner molds include aluminum, brass, stainless steel, and ABS to yield Δλ values of respectively -127, 0, 65, and 110 $W.m^{-1}.K^{-1}$. Pore dimension and orientation for each combination are compared in the two freezing media (**D.a,b**). Angle color-coded map details of SEM images is available in **Appendix C-Figure S3**.

The higher the freezing bath temperature, the less ordered and isotropic the pores. Equally, the influence of the dipping speed results in longitudinal pores aligned with the freezing direction. However, the process of interface formation between two lamellar regions, is not affected by variations in the freezing bath temperature.

Table 2. Dimensions of the scaffolds pore for longitudinal sections of various samples, after ice-templating and freeze-drying.

		Freezing media	
Molds thermal conductivity difference / $W.m^{-1}.K^{-1}$	Measurement	Liquid nitrogen, -196°C	Dry ice in ethanol, -78°C
-127	Median Feret / µm	71 ± 83.23	102 ± 219.91
	Median MinFeret / µm	33 ± 19.46	45 ± 35.86
	Main orientations / °	-4.5, 40.5	-13.5, 31.5,41.5
0	Median Feret / µm	42 ± 96.23	42 ± 64.56
	Median MinFeret / µm	19 ± 30.40	20 ± 18.07
	Main orientations / °	-16.5, 28.5	-14.5, 28.5
65	Median Feret / µm	62 ± 112.11	93 ± 133.39
	Median MinFeret / µm	33 ± 28.90	32 ± 30.28
	Main orientations / °	-13.5	-18.5
110	Median Feret / µm	77 ± 118.57	44 ± 70.66
	Median MinFeret / µm	42 ± 32.14	24 ± 25.30
	Main orientations / °	-16.5	-46.5

The growth rate of ice crystals and the resulting microstructure are defined by the imposed thermal gradients during the cooling process. In the system presented in the previous section, we used bidirectional thermal gradients to spark lamellar growth and to orient the pores. The gradients were oriented in the *z*-axis, owing to the dipping motion, and in the x-axis of the material due to a difference in the thermal conductivity of the molds. These gradients determine the pores' attributes, *i.e.* their dimension and orientation. The purpose here is to extend the degree of kinetic control over the structuration by ice by

playing on the molds' thermal conductivity and on the bath temperature. In this section, we have introduced multidirectional thermal gradients by using two thermally conductive molds. It induces a competition between two opposing gradients, one from the inner to the outer mold, and the second from the outer to the inner mold, in addition to the gradient associated with the dipping. Consequently, ice growth occurs in opposition to each other in a convergent manner. This results in the formation of an interface corresponding to the plane where these two ice growth fronts meet. Differently from the previously described interface, which arises from a nuclear to growth transition, this interface occurs at the junction of two lamellar (growth) regions. As a result, the choice between a global porous structure that is either anisotropic or isotropic, can be made based on the freezing conditions.

D. Interface formation during ice templating of dense collagen

The section above described the conditions under which an interface arises between two lamellar ice regions. By combining two conductive materials, ice grows from two facing surfaces and form this thin and steady line at their junction. To visualize this event, we froze a collagen solution between two thin sheets of conductive materials in a Hele-Shaw cell (**Fig.5-A**), under the *in situ* cryoconfocal microscope described in Chapter 2, in collaboration with S. Deville at the *Institut Lumière Matière*, Lyon (**Fig.5-B**). We used different conductive materials, including copper and stainless-steel cut from 200 µm-thick sheets, and inserted these strips of metal inside the Hele-Shaw cells. The cells were filled with the same solution of collagen as in Chapter 2, concentrated at 40 mg.mL^{-1} and containing Rhodamine-B. We then imposed a thermal gradient from -15°C to 20°C with a velocity of 10 µm.s^{-1}, and followed the ice front progression under the microscope.

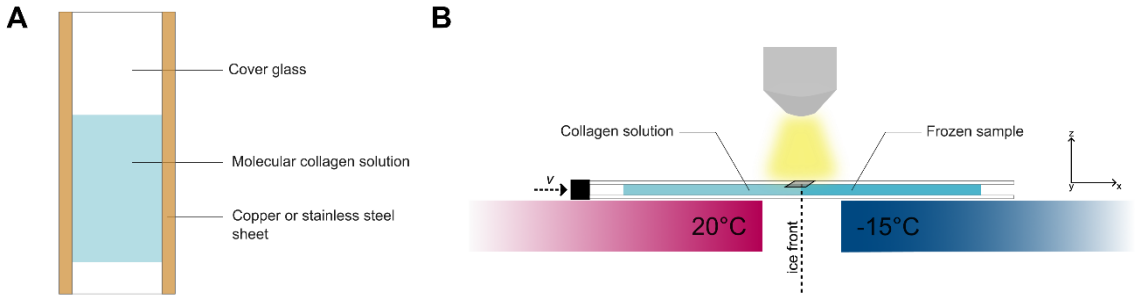

Figure 5. A) Experimental set-up of Hele-Shaw cells, comprising two thin sheets (200 µm) of copper or stainless steel. Collagen solution at a concentration of 40 mg.mL^{-1} was deposited in between two cover glasses, and the overall was sealed with a 100 µm-thick tape on the sides. **B**) The *in situ* cryoconfocal set-up enables to freeze the solution by imposing a controlled thermal gradient from 20 to -15°C and follow the freezing front at the velocity of 10 µm.s^{-1}.

The time-resolved two-dimensional images show a bi-directional growth of ice crystals (in black), that separate from the collagen solution (in light grey at low concentration, white once segregated). Ice growth starts simultaneously from both sides (t=1,6 min), and the two fronts meet at half of the total sample width, which generates an interface. Due to the anisotropy of the boundary conditions, lamellar crystals adopt a tilted angle on each side. On the left section, crystals follow a 59° angle that increases near the interface, up to 78° (**Fig.6-A,B**). On the opposite right side, crystals follow equivalent orientations of -61° and -74°. During freezing, collagen is segregated in small interstices of 6 ± 1.98 µm-median thickness (**Fig.6-C**), between larger ice crystals 14.8 ± 27.79 µm-thick.

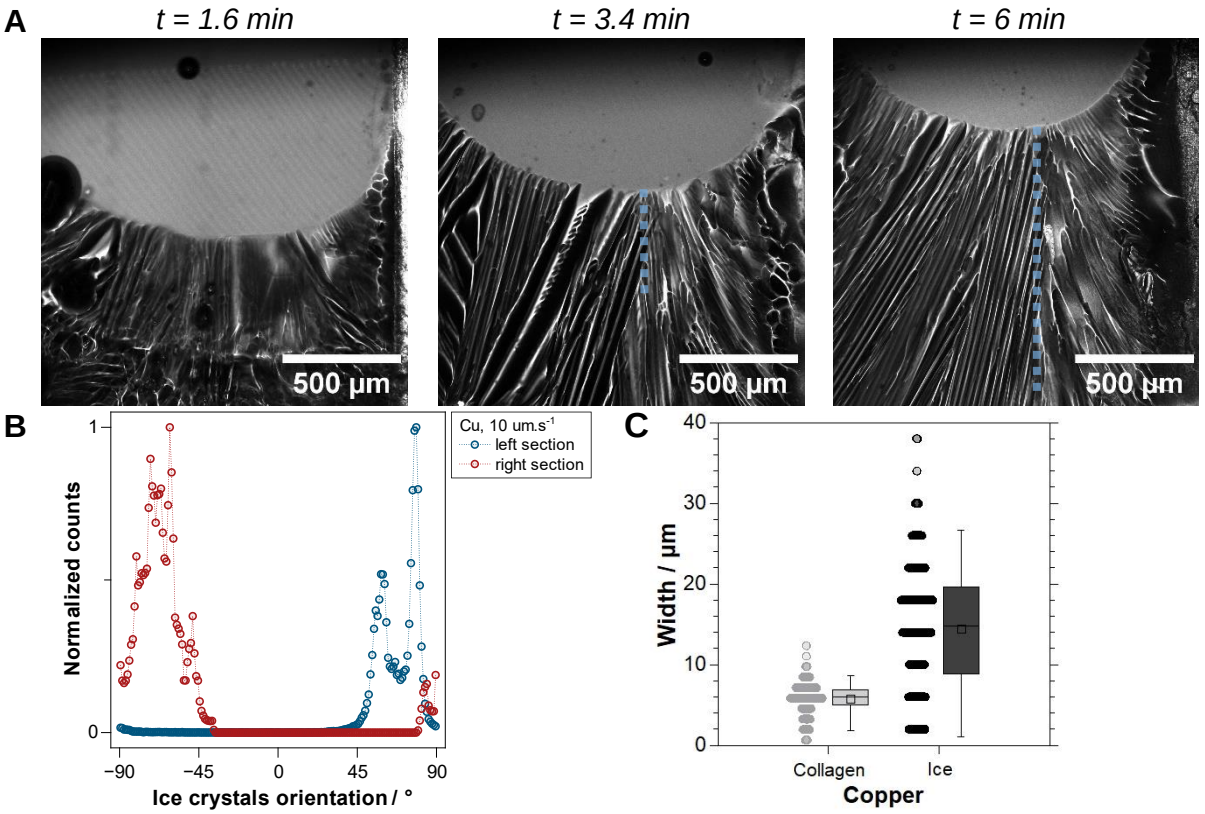

Figure 6. *In-situ* cryoconfocal image analysis of growing ice crystals in a dense collagen solution between two sheets of copper. The freezing front velocity was set at 10 µm.s^{-1}. View is perpendicular to the ice front. **A**) Two opposite growth fronts of lamellar ice give rise to an interface at their meeting point. **B**) Orientations of the ice crystals from the two opposite fronts. **C**) Collagen walls and ice crystals width distributions, analyzed using ridge detection ImageJ plugin (see **Appendix C-Fig.S4**).

When copper is replaced by stainless steel, ice crystals grow with a slightly higher angle of ±81° from both surfaces (**Fig.7-A**). Similarly, the encounter of these two lamellar regions generates an interface, at a steady position over time (**Fig.7-A & Fig.8-A**). The thickness of

the collagen walls is 1.7x higher in steel than in copper, and the ice crystals width 1.2x higher. The median thickness of segregated collagen and ice are respectively of 10.4 ± 2.98 µm and 18.41 ± 8.29 µm. The higher thermal conductivity of copper in comparison to stainless steel—*ca.* 390 and 14 $W.m^{-1}.K^{-1}$—increases the freezing kinetics, which is responsible for smaller pores and phase-segregated walls. This is consistent with the curved profile of the solidification front and the ill-defined nucleation regions in Hele Shaw copper edges, showing that ice runs fast from each surface, with a high local ice front velocity. Near the nucleation region, small bridges are observed, a reminiscence of ice seeds while, after the thermodynamic equilibrium has been reached lamellar ice regions are observed. The formation of the interface is disordered, with a poorly defined line in the early stages of ice growth (**Fig.8-B.a**). Oppositely, using steel results in ice crystals that have a well-defined shape, due to the slower freezing kinetics (**Fig.8-B.b**).

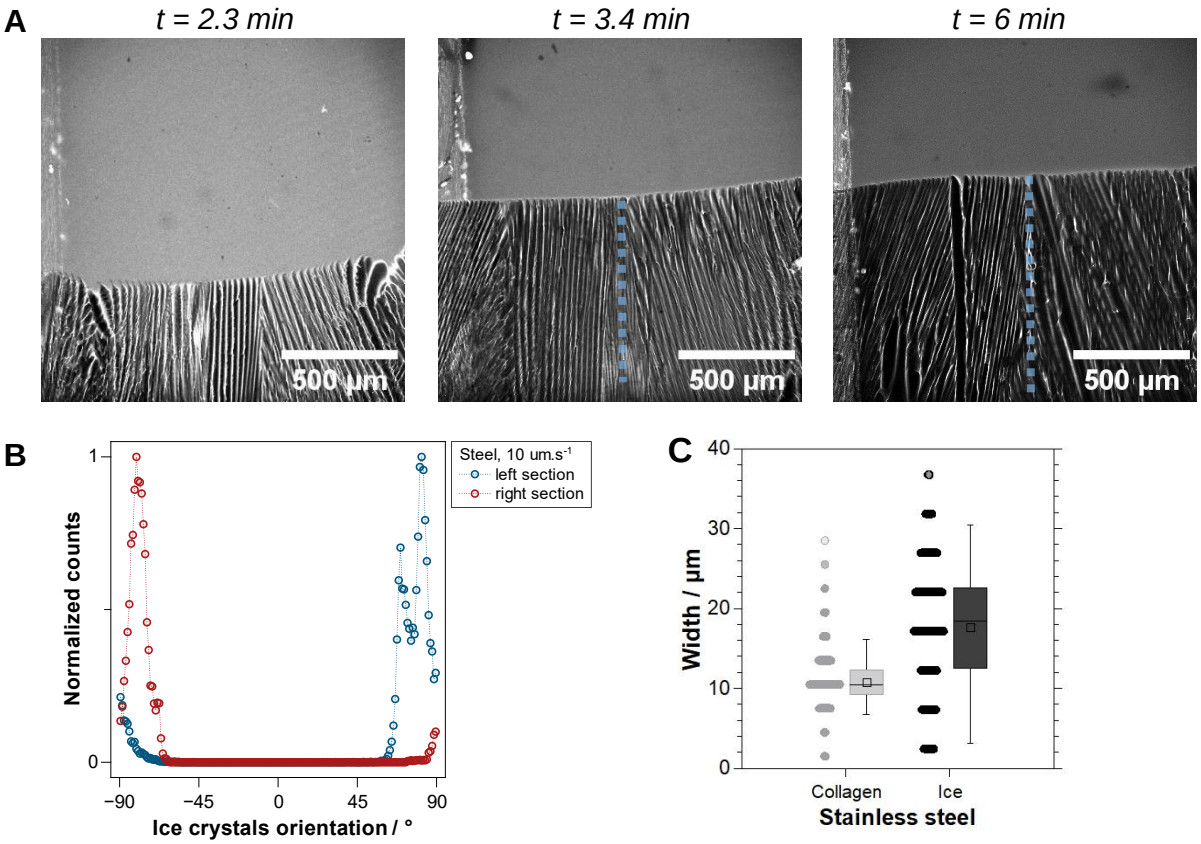

Figure 7. *In-situ* cryoconfocal image analysis of growing ice crystals in a dense collagen solution between two sheets of stainless steel. The freezing front velocity was set at 10 µm.s^{-1}. View is perpendicular to the ice front. **A**) Two opposite growth fronts of lamellar ice give rise to an interface at their meeting point, which position is stabilized over time. **B**) Orientations of the ice crystals from the two opposite fronts. **C**) Collagen walls and ice crystals width distributions, calculated using ridge detection ImageJ plugin (see **Appendix C-Fig.S4**).

We show that the local thermal parameters—in particular the thermal conductivity—controls the formation and structuration of ice during ice templating. Using copper, a highly conductive material, the high local velocity resulted in smaller collagen walls and ice crystal width. The imposed bidirectional gradients generate an interface, which position and formation were not drastically affected by the modification of the thermal gradient. This experiment gave a closer perspective on the control of scaffold architecture through the control of the thermal conduction by the mold. Future work on the influence of the molds design could provide extensive control over the ice nucleation and the resulting anisotropic structures. In the context of biomaterials fabrication, assessing the implications of that interface on the mechanical and biological properties—for instance, cell colonization—may give an additional mean to tailor these properties.

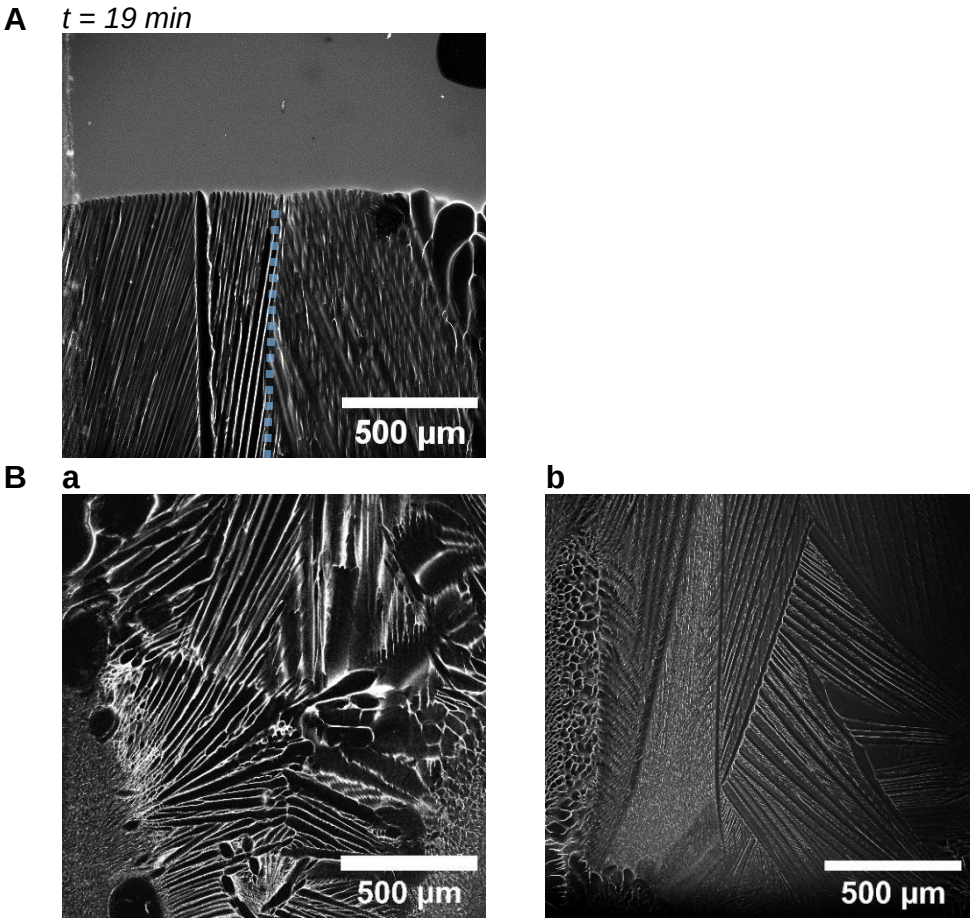

Figure 8. A) Steadiness of the interface position overtime, in the Hele Shaw cells mounted with stainless steel. **B**) Nucleation and growth of ice crystals. Across the sample frozen in copper (**a**), small bridges are observed and the interface is poorly defined. In steel (**b**), crystals are nicely shaped. At the interfaces, an undulating morphology of closed crystals is observed.

3. Manuscript submitted to *Biomaterials Science*

Tunable biomimetic materials elaborated by ice templating and self-assembly of collagen for tubular tissue engineering

Isabelle Martinier[1], Florian Fage[1], Alshaba Kakar[1], Alessia Castagnino[2], Emeline Saindoy[3], Joni Frederick[2], Ilaria Onorati[2], Valérie Besnard[3], Abdul I. Barakat[2], Nicolas Dard[3], Emmanuel Martinod[3], Carole Planes[3], Léa Trichet[1], Francisco M. Fernandes[1]**

[1] Laboratoire de Chimie de la Matière Condensée de Paris, Sorbonne Université, 4 place Jussieu, 75005 Paris, France

[2] LadHyX, CNRS, Ecole Polytechnique, Institut Polytechnique de Paris, Palaiseau, France

[3] Laboratoire Hypoxie & Poumon, Assistance Publique–Hôpitaux de Paris, Hôpitaux Universitaires Paris Seine-Saint-Denis, Hôpital Avicenne, Chirurgie Thoracique et Vasculaire, Université Paris 13, Sorbonne Paris Cité, UFR Santé, Médecine et Biologie Humaine, Bobigny, France

Keywords: collagen, extracellular matrix, tubular grafts, ice templating, fibrillogenesis

Synthetic tubular grafts currently used in clinical context fail frequently, and the expectations that biomimetic materials could tackle these limitations are high. However, developing tubular materials presenting structural, compositional and functional properties close to those of native tissues remains an unmet challenge. Here we describe a combination of ice templating and topotactic fibrillogenesis of type I collagen, the main component of tissues' extracellular matrix, yielding highly concentrated yet porous tubular collagen materials with controlled hierarchical architecture at multiple length scales, the hallmark of native tissues' organization. By modulating the thermal conductivity of the cylindrical molds, we tune the macroscopic porosity defined by ice. Coupling the aforementioned porosity patterns with two different fibrillogenesis routes results in a new family of tubular materials whose textural features and the supramolecular arrangement of type I collagen are achieved. The resulting materials present hierarchical elastic properties and are successfully colonized by human endothelial cells and alveolar epithelial cells on the luminal side, and by human mesenchymal stem cells on the external side. The proposed straightforward protocol is likely

to be adapted for larger graft sizes that address ever-growing clinical needs, such as peripheral arterial disease or tracheal and bronchial reconstructions.

A. Introduction

In mammals, tubular tissues mediate macroscopic transport mechanisms in the vascular, respiratory, digestive and urogenital systems, ensuring that the contents of the lumen travel through the body without uncontrolled leakage to the surrounding environment. Because an important part of their function is to ensure the separation between different compartments in the body, tubular tissues cope with drastic biochemical gradients between the luminal and adventitial sides. In addition, variable pressure, strain at rest and contractile movements require specific mechanical response both under static and cyclic solicitation modes. Taken together, these constraints provide cues to understand the multiscale architecture that characterizes tubular tissues as well as the spatial distribution of the cells that populate them. Early works of Weinberg and Bell suggested that the intrinsic complexity of these tissues could be recapitulated by the elaboration of biomimetic materials usable as tubular tissue grafts.[1] However, the materials currently grafted in clinical practice to replace sections of tubular tissues meet the single purpose of providing mechanical support to the replaced tissue, and fail in most other functions. Mimicking the native tissues' complexity in composition, structure and function, holds the potential to change drastically the materials available to engineer arteries, tracheas and other critical tubular tissues.

In tubular tissues, epithelial cells line the luminal surface, whereas different cell types of mesenchymal phenotype – fibroblasts, smooth muscle cells, or others, depending of the specific tissue in question – populate the inner wall.[2] In addition to the nature and spatial distribution of cells, tubular tissues display a hierarchical arrangement of the extracellular matrix (ECM) components at several length scales, dictating their mechanical properties to a large extent. Type I collagen, the major component of the connective tissues in mammals, is widely responsible for the multiscale mechanical properties of native tissues.[3] Locally, it provides the mechanical support necessary for cell adhesion, migration and proliferation. At the macroscopic level, collagen dominates the tubular tissues' viscoelastic response to the vast range of mechanical loading and ensures their dimensional stability. Moreover, *in vitro* as *in vivo*, type I collagen can be degraded and synthesized by different types of cells, providing a dynamic environment that synthetic counterparts cannot provide. The preceding arguments confirm the relevance of type I collagen as the central component to develop scaffold-based grafts[4] and to recapitulate tissue-like architectures and fibrillar structures, thought to be key for attaining adequate mechanical properties and cell colonization[5].

Although particularly complex to handle in non-denaturing conditions and at relevant physiological concentration[6], several techniques have been developed to elaborate collagen-based tubular materials. Weinberg and Bell proposed a gel-based approach to generate vascular models by casting a suspension of cells in a collagen solution inside a tubular mold[7]. The resulting gel was compacted through a cell-mediated process to reach materials capable of restoring the function and partially reproducing the structure of vascular tissues [8]. However, these materials required mechanical reinforcement by a synthetic sleeve for application. Li *et al.* have reported a different strategy based on drying and crosslinking collagen to modify the elastic properties of the tubular constructs[9]. In a different approach, dense collagen sheets obtained after plastic compression[10] as well as collagen-elastin composite matrices [11] were rolled around a cylindrical mandrel to obtain tubular materials. In the latter case, the obtained vascular grafts demonstrated mechanical properties close to those of native tissues, with encouraging results obtained *in vivo*[11]. Despite their promising results, these techniques fail to produce materials that display both the fibrillar organization of native tissues and the macroporosity required for successful cell colonization.

Materials with accessible pores promote cell colonization[12] inside the material and favor homeostasis due to enhanced diffusion of nutrients and waste. Self-standing porous collagen materials can be obtained by lyophilization of collagen solutions followed by physical[13] or chemical[14] cross-linking. This approach was adapted by Koens *et al.* to provide tubular porous materials displaying three layers[15], but one month after implantation thrombus formation was observed and associated to the porosity of the luminal wall. These results highlight the importance of a precise control over the graft topography for successful graft implantation. Indeed, a *non-porous* luminal surface is required to foster the formation of an endothelium on the internal wall, while an oriented *porous* structure in the external part of the material ensures effective cell colonization from the adjacent tissues.

Here, we introduce a new strategy based on ice templating to tackle the elaboration of materials that are fully composed of type I collagen. Ice templating (equally named freeze casting or ice-segregation-induced self-assembly), a technique initially developed for the elaboration of porous ceramics[16] and adapted to produce scaffolds based on biopolymers[17–19], offers the possibility to precisely tune the materials porosity by playing on different parameters such as solution composition, freezing kinetics, and temperature gradient[20]. Coupling ice templating and topotactic fibrillogenesis, a technique inducing the formation of native-like collagen fibrils during thawing, enables self-assembly of type I collagen to occur, generating biomimetic constructs while maintaining the macroporous patterns defined by the ice templating technique[12,21]. During freezing, the formation of ice crystals induces an increase in concentration of the collagen in solution, due to the insolubility of most solutes in ice[22]. The local concentration of collagen attained by this process reaches the same range of

those observed in biological tissues. The increase in concentration during freezing coupled to the lyotropic behavior of collagen in solution give rise to highly organized domains, which, upon fibrillogenesis, recapitulate the multiscale hierarchical architecture of collagen in native tissues. Compared to other methods, this strategy enables obtaining materials with a controlled and hierarchical structure at different length scales by means of a straightforward protocol, likely to be adapted for larger scale graft production.

In this work, we propose to use this technique to provide tubular materials applicable for tissue engineering purposes. In particular, we explored the effects of processing parameters such as the thermal conductivity of the cylindrical molds and fibrillogenesis routes on the textural and mechanical properties of the biomimetic tubular materials. In addition to the structural characterization we have performed *in vitro* colonization studies with a variety of cell lines to understand the effect of the materials' processing routes on the colonization by human umbilical vein endothelial cells (HUVECs), adenocarcinomic human alveolar basal epithelial cells (A549), as well as human mesenchymal stem cells (hMSC).

The materials reported here combine, for the first time, the hierarchical organization found in native ECM – from the molecular scale up to the tissue level – using type I collagen, the mechanical performance in the range of native tissues as well as the capacity to be colonized by endothelial, epithelial and mesenchymal cell types. These findings open an exciting pathway towards the development of new biomimetic tubular tissue grafts that promise to find applications in pathologies such as peripheral arterial disease (PAD) or tracheal and bronchial reconstructions, for which the currently available materials fail. bular

B. Results

a. Controlled ice growth determines the macroscopic features of biomimetic tubular tissues

To elaborate collagen tubular materials *via* ice templating, we have developed a series of tubular molds that shape collagen into small arteries analogues (5 cm-long, with an inner diameter of 5 mm and a wall thickness of 1.5 mm). The molds were filled with type I collagen solution (40 $mg.mL^{-1}$) and subsequently plunged in liquid nitrogen at a controlled velocity (Figures S1 & 1A). The difference between the thermal conductivity of the inner and outer parts of the mold generates different thermal gradients across the solution and, therefore, allows controlling ice crystal growth.[23,24] This simple approach provides control over the size and the orientation of the ice crystals within the frozen monolith (Figure 1A) that we studied here for a wide range of mold materials. When exposed to a cryogenic liquid such as liquid nitrogen, insulating materials composing the mold delay the nucleation and growth of ice in

the collagen solution, whereas thermally conductive materials promote faster nucleation and growth. The different materials used to study the effect of the thermal conductivity, λ, on the scaffold structure of the tubular matrices include aluminum (λ = 237 $W.m^{-1}.K^{-1}$), brass (λ = 110 $W.m^{-1}.K^{-1}$), stainless steel (λ = 45 $W.m^{-1}.K^{-1}$) and acrylonitrile butadiene styrene (ABS) (λ = 0.17 $W.m^{-1}.K^{-1}$). When the outer mold material displays lower thermal conductivity than the inner part of the mold, the freezing events proceed from the luminal surface towards the outer surface. At the initial moments of the freezing process, due to supercooling, a disordered zone appears close to the internal layer. When the solidification front reaches a steady state, ice crystals grow following the direction of the thermal gradient. Despite its insulating properties, the outer mold is directly in contact with the cooling bath and eventually allows ice to nucleate at its inner surface. This occurs with a delay in comparison to the luminal side, resulting in two frozen regions facing each other. Observed after lyophilization, the porous structure of the collagen matrix is the fingerprint of the ice crystals formed during the cooling process. On both sides, lamellar pores are formed and converge towards an interfacial zone, highlighted with dotted lines on SEM images (Figure 1A). The different pairs of molds, as well as their thermal conductivity difference ($\Delta\lambda = \lambda_{out} - \lambda_{in}$), are displayed in Sup. Table 1. SEM images of the longitudinal cross-sections of the collagen matrices after freeze-drying, fabricated with a variety of mold materials, are shown in Fig. 1B (top).

For the freezing conditions chosen here (dipping speed and mold geometry), and for the materials mentioned above, the position of the interface, x_i, scales linearly with $\Delta\lambda$ and can be adjusted between 5.6% and 62.5% of the tube wall as observed in Fig. 1B and Fig. 1C. The relevance of this interface is multiple since it is expected to play a role in the materials' mechanical performance, the permeability towards cells and fluids, as well as in the regulation of the cellular migration path.

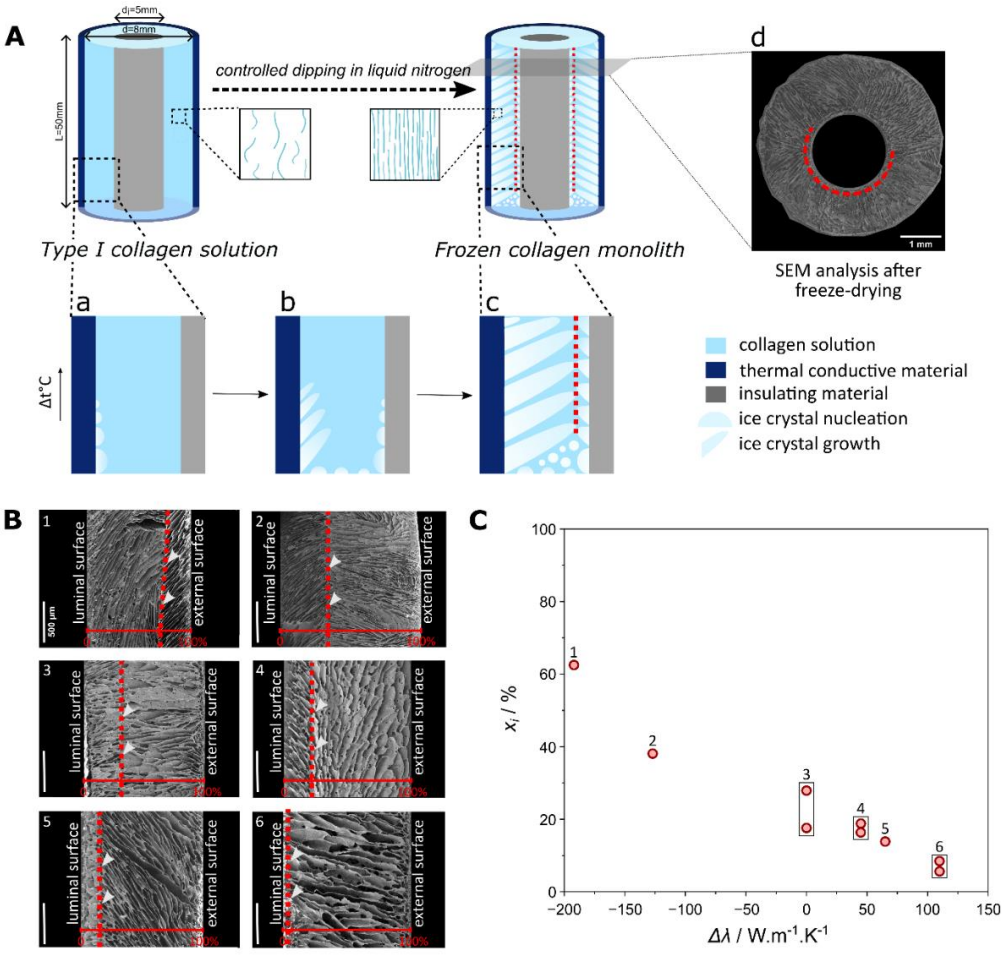

Figure 1. The internal texture of type I collagen materials obtained by ice templating is determined by the thermal conductivity difference between the inner and outer parts of the freezing molds. (**A**) Scheme depicting the ice nucleation and growth events in collagen-based tubular materials leading to the formation of an interface inside the walls of the tubes. SEM analysis of transverse sections of a selected material after freeze-drying showing the concentric position of the interface, highlighted with a red dotted line. (**B**) SEM images of longitudinal sections of freeze-dried collagen materials. The red dotted lines illustrate the position of the interface between the luminal (left) and external (right) surfaces. All scale bars represent 500 um. (**C**) Influence of the difference in molds' thermal conductivities on the position of the interface formed in between the two ice growth regions. Numbers 1 to 6 refer to the SEM longitudinal sections shown in B for specific pairs of materials (displayed in Sup. Table 1). The interface position is defined as the percentage of the distance to the lumen with respect to the total wall thickness of the matrix.

b. Controlling the dimensions and orientation of macropores in collagen scaffolds using ice

The ability to control the size and the orientation of pores in collagen scaffolds is expected to play an important part in cellular adhesion, proliferation and access to nutrients, as well as to promote – or hinder – cell migration within the material. We have selected two different pairs of materials for the inner and outer parts of the mold to maximize or minimize the thermal conductivity difference between them, and thus to impose the widest range of thermal gradient across the sample wall. Materials fabricated with an outer conductive material (aluminum) and an inner insulating one (ABS) are referred to as ***Cond***, while scaffolds prepared with both parts of the mold composed of insulating material (ABS) are referred to as ***Ins***. These conditions yield $\Delta\lambda = 236.83\ W.m^{-1}.K^{-1}$ and $\Delta\lambda = 0\ W.m^{-1}.K^{-1}$, respectively.

Samples were ice templated under equivalent boundary conditions (dipping speed, air and bath temperature) using both mold pairs (*Cond* and *Ins*). After lyophilization, longitudinal and transversal sections of the scaffolds were imaged by SEM to quantify the orientation and dimensions of the pores, as shown in Fig. 2. Pore orientation analysis on longitudinal sections (Figure 2A & B.a.1), showed that the pores are perpendicular (*c.a.* 90°) to the longitudinal axis of the tube for the ***Cond*** freezing conditions (Figure 2A.a.2). Conversely, ***Ins*** conditions favor the formation of axial pores, oriented at 12° with respect to the longitudinal axis of the tube (Figure 2B.a.2). These results confirm the radial thermal gradient imposed by the outer conductive material across the collagen solution. At the initial moment of freezing, ice nucleates in contact with the outer mold and grows towards the lumen, as confirmed by the SEM observation of the transversal cross-section of ***Cond*** (Figure 2A.b.1). ***Ins*** freezing conditions favor the axial thermal gradient imposed by the dipping process, yielding a different pore organization, as shown on both SEM longitudinal and transversal cross-sections (Figure 2B.b.1).

Pore orientation was analyzed on a quarter of each tubular material cross-section (highlighted in gray on Figs. 2A & B.b.1) using the OrientationJ plugin in FIJI[35] (Figure 2A & B.b.2). In ***Cond*** materials, the continuous change of orientation of the pores, observed by the various colors, corresponds to a radial organization. On the contrary, ***Ins*** materials feature pores that are organized in coherent domains that follow one major orientation along the longitudinal axis of the tube. Higher magnification images on other specific parts of the tubular walls confirm this observation (Figure 2A & B.b.3). The striking difference in the internal porosity of these materials is determined solely by the thermal gradient imposed by the mold walls.

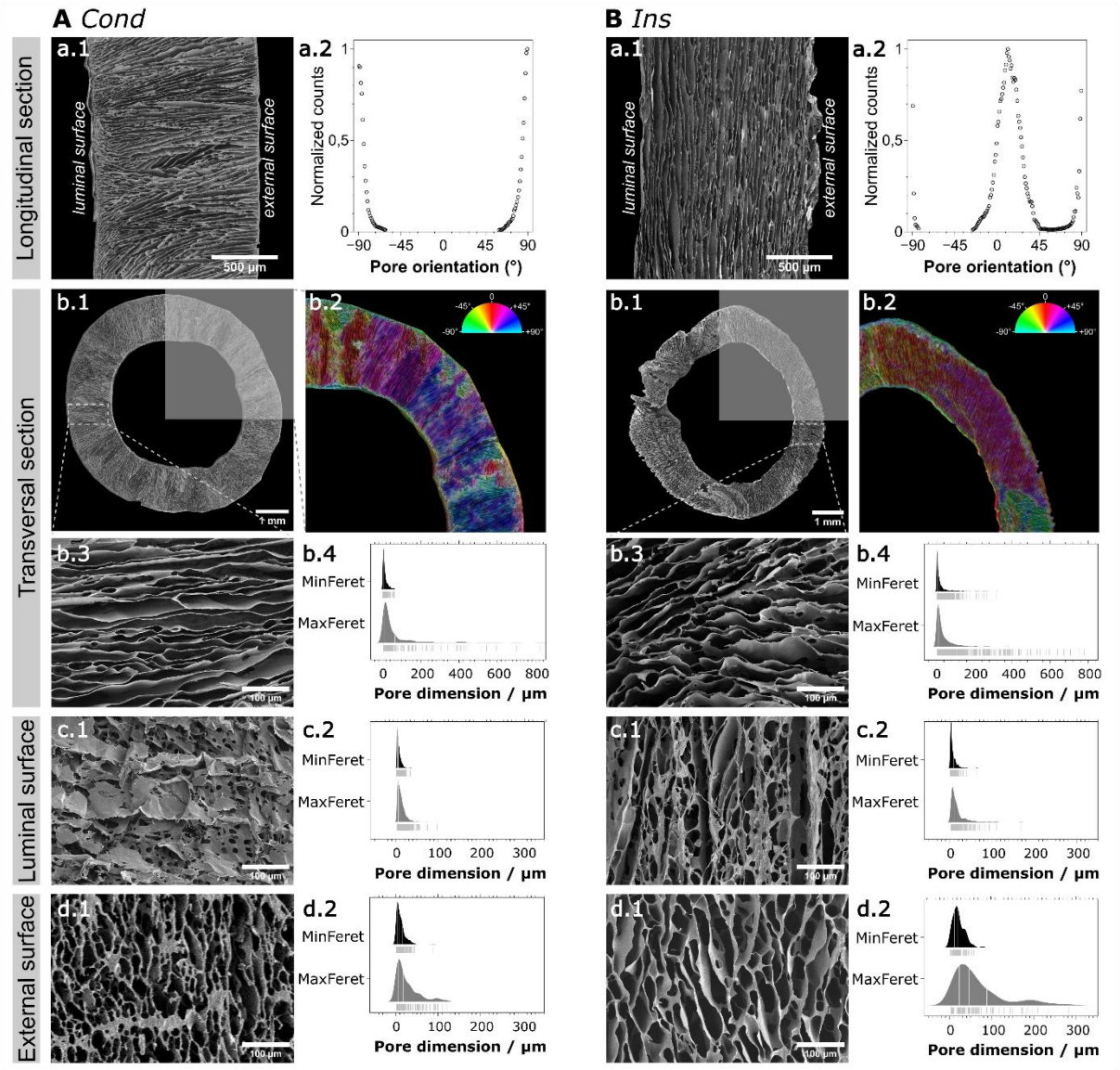

Figure 2. Textural properties of collagen scaffolds obtained with pairs of materials differing in their conductive properties. All images were obtained by SEM. (**A**) Scaffolds fabricated using an outer conductive mold and an inner insulating mold (*Cond*). (**B**) Scaffold fabricated with insulating materials for both outer and inner molds (*Ins*). a.1: longitudinal cross-section of A and B. a.2: pore orientation of the longitudinal cross-section b.1: transversal cross-section of the scaffolds. b2: pore orientation of the transversal cross-section, with an anglecolor-coded map. b.3: high magnification of the zone defined with dotted lines on b.2 images. b.4: analysis of Minimum Feret (MinFeret) and Feret diameters (MaxFeret) of the pores on transversal sections of A and B. c1: luminal surface of the tubular scaffolds. c.2: analysis of MinFeret and MaxFeret diameters of pores on the luminal surface. d.1: external surface of the tubular scaffolds. d.2: analysis of MinFeret and MaxFeret diameters of the pores on the external surface of A and B.

However, the size of the pores observed transversally and at the luminal surface appears to be independent from the molds' thermal conductivity difference. In fact, pores exhibit comparable dimensions with a median Feret diameter of 25.75 µm and 9.77 µm in ***Cond*** scaffolds, and 20.62 µm and 11.36 µm in ***Ins*** scaffolds, for transversal sections and luminal surfaces respectively (Table 1). In contrast, pore formation and dimensions at the external surfaces significantly relate to the thermal conductivity of the outer mold. The median Feret diameter and percentage of surface accessible porosity are both lower in ***Cond***, with a Feret value almost 3 times higher for ***Ins*** (45.83 µm vs 17.32 µm), and a percentage of surface accessible porosity 1.5 times higher for ***Ins*** scaffolds than for ***Cond*** scaffolds (48% vs 63%) (Fig. 2A & B.d,12 and Table 1). These differences are explained by the ice nucleation conditions imposed by the various pairs of mold materials. Since freezing occurs later under ***Ins*** conditions, a wide supercooling zone is formed before freezing. This zone is however minimal in conductive conditions owing to an earlier freezing process, as found in ***Cond***.

Table 1. Dimensions of the scaffold pores for various sections and surfaces, after ice-templating and freeze-drying.

		Freezing conditions	
Analyzed zone	Measurement	*Cond*	*Ins*
Transversal section	Median Feret / µm	25.75 ± 8.43	20.62 ± 2.74
	Median MinFeret / µm	8.71 ± 0.77	9.14 ± 0.80
	Surface accessible porosity / %	59	79
Luminal surface	Median Feret / µm	9.77 ± 0.26	11.36 ± 1.09
	Median MinFeret / µm	5.26 ± 0.12	4.13 ± 0.37
	Surface accessible porosity / %	N/A	53.57
External surface	Median Feret / µm	17.32 ± 2.15	45.83 ± 5.97
	Median MinFeret / µm	8.69 ± 0.86	18.09 ± 1.39
	Surface accessible porosity / %	48	63

The lyophilization of ice templated collagen materials was performed exclusively to observe these textural features, in dry conditions under the SEM. The hydrated fibrillar hydrogels were prepared by a topotactic fibrillogenesis process following ice templating, to induce the self-assembly of collagen molecules into native-like fibrils. The challenge associated with this transformation was to maintain the control over the porosity generated by ice templating, since the self-assembly requires temperatures that initiate the melting of ice.

c. Influence of the topotactic fibrillogenesis pathway on the porous structure

Topotactic fibrillogenesis refers to the ability of inducing fibrillogenesis by a pH rise in a collagen-based material during thawing, while simultaneously keeping the macroporous network developed during freezing[33]. To maintain the shape and dimensions of the tubular scaffolds as well as pores after ice-templating, two fibrillogenesis processes were conducted. One corresponds to the gas-phase ammonia process previously described[23,33] (Figure 3A), while the other uses a concentrated phosphate buffer saline (PBS (10X)) solution (Figure 3B).

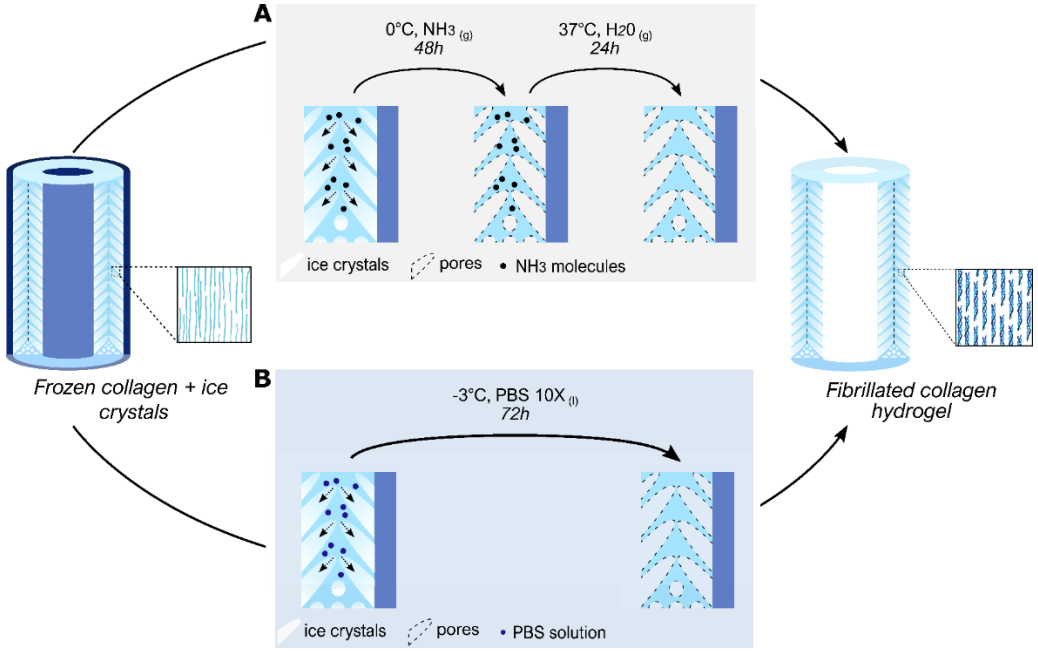

Figure 3. Fibrillogenesis routes applied after ice-templating of the collagen scaffolds and removal of the outer mold. (**A**) Vapor-solid phase process using ammonia vapors at 0°C for 48h, followed by desorption in a water-vapor bath for 24h. (**B**) Liquid-solid based process using PBS (10X) in solution at -3°C for 72h. Both procedures are followed by a 2-week PBS (5X) bath at room temperature to secure the fibrillogenesis. The resulting self-standing hydrogels are highly concentrated in fibrillated type I collagen and display adjustable porosity.

In both cases, the challenge is to use a single step process to achieve a fibrillar yet porous type I collagen tube. Ammonia vapors decrease the freezing point of ice. By exposing the frozen sample to an ammonia atmosphere at 0 °C, we ensured that only ice the crystals exposed to the ammonia vapors were able to melt. Therefore, near the ice crystals being thawed, collagen molecules were exposed to a pH value above their isoelectric point, inducing their self-assembly into native-like fibrils. Changing the fibrillogenesis route towards a liquid-solid interface rather than a vapor-solid interface is challenging. To ensure

that the competition between the kinetics of the ice thawing and the fibrillogenesis in a liquid media were sufficiently balanced to obtain a self-supported material, we have performed the process at a temperature below 0°C, at -3°C (optimization results not shown).

Confocal images of the scaffolds confirm the ability to induce the topotactic fibrillogenesis of collagen scaffolds *via* the ammonia gas-phase route (noted ***Cond*-NH_3** or ***Ins*-NH_3**). Pores formed during freezing remain open and interconnected, and the orientation imposed during the ice-templating process is maintained (Figure 4A.1.a & 2.a). Conversely, the liquid-phase fibrillogenesis pathway induces either the collapse of the pores in the case of ***Cond*-PBS** samples, (Figure 4B.1.a) or a strong reduction of their size for ***Ins*-PBS** samples (Figure 4B.2.a).

Cond*-NH_3** and ***Ins*-NH_3** feature similar pore size in transversal sections (median Feret diameter (Feret) x median minimum Feret diameter (MinFeret)) of (16.12 ± 1.17 µm x 6.31 ± 0.39 µm) and (18.76 ± 1.57 µm x 8.05 ± 0.64 µm), respectively (Figure 4 b.1-2 for A.1 and A.2, and Table 2). Compared to lyophilized samples, the pore size decreases during fibrillogenesis with a reduction of the Feret diameter of 37% and 9% for ***Cond and ***Ins*** conditions, respectively. As ammonia reaches the surface of ice crystals, a competitive process takes place. Thawing of ice crystals induced by the cryoscopic depression at the ammonia-ice interface competes with the self-assembly of collagen molecules. The swelling of the collagen walls is a direct consequence of ice thawing being favored over the fibrillogenesis. In such a case, a partial dilution of the collagen walls in the liquid water generated by the ice melting occurs, before the pH change induces the formation of the fibrillar collagen gel. This leads to a smaller pore size in the hydrogel than in the dried scaffold. We hypothesize that the lower pore diameter reduction for ***Ins*-NH_3** in comparison to ***Cond*-NH_3**, is due to its unidirectional pore structure. It may favor a faster diffusion of ammonia molecules that promote collagen fibrillogenesis over the melting of ice. On the other hand, the isotropic texture of ***Cond*** samples may induce a slower diffusion of ammonia, which leads to faster ice melting and subsequent increased dilution of collagen walls. This observation is confirmed by the proportion of pores giving access to the inner wall in Figures A.1.c.1 and A.2.c.1, where the respective pore coverage for ***Ins*-NH_3** and ***Cond*-NH_3** decreases from 35% to 24%.

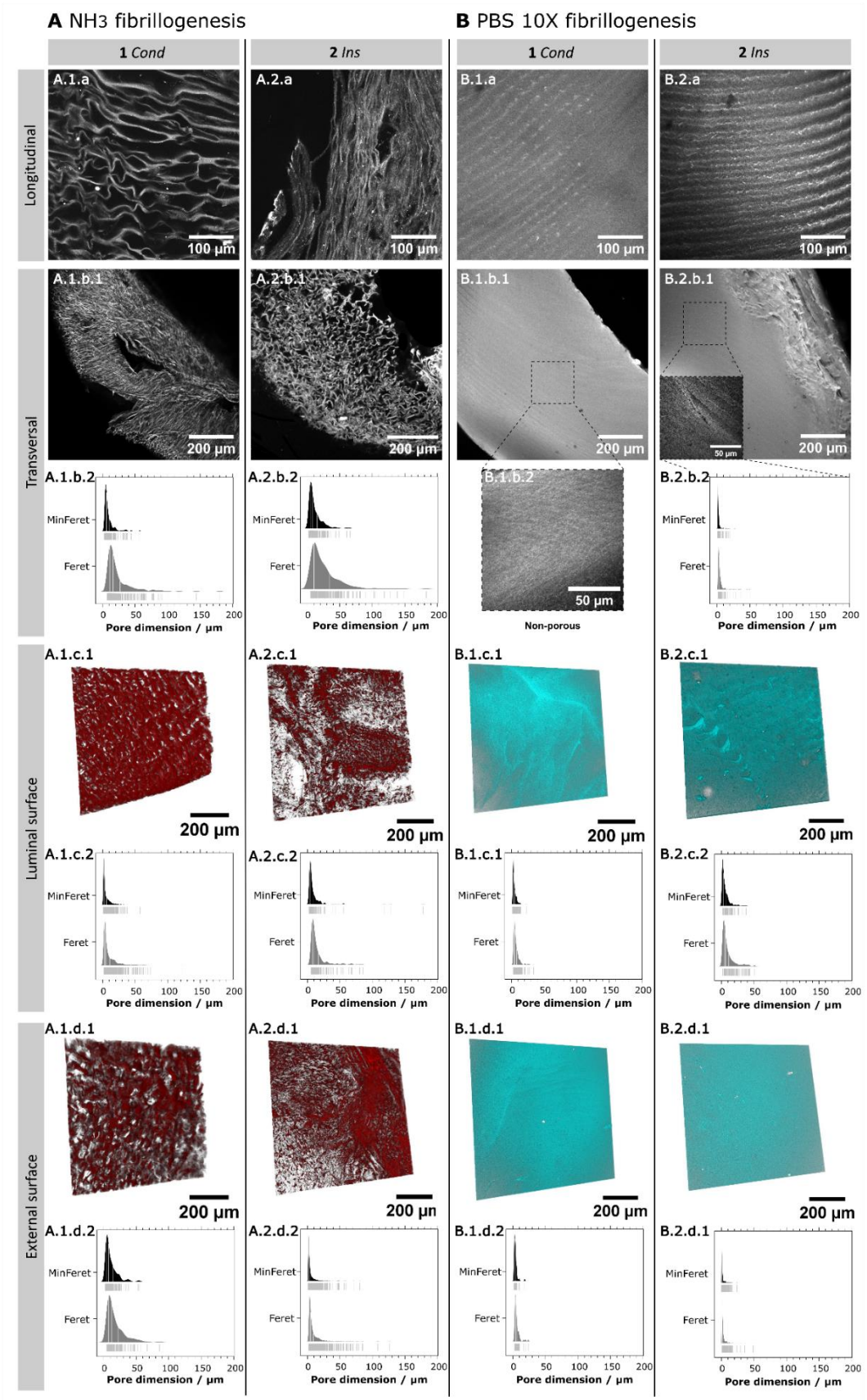
A NH3 fibrillogenesis
B PBS 10X fibrillogenesis
1 Cond
2 Ins
1 Cond
2 Ins
Longitudinal
Transversal
Luminal surface
External surface
A.1.a
A.2.a
B.1.a
B.2.a
100 µm
A.1.b.1
A.2.b.1
B.1.b.1
B.2.b.1
200 µm
50 µm
A.1.b.2
A.2.b.2
B.1.b.2
B.2.b.2
MinFeret
Feret
50 µm
Non-porous
Pore dimension / µm
A.1.c.1
A.2.c.1
B.1.c.1
B.2.c.1
A.1.c.2
A.2.c.2
B.1.c.2
B.2.c.2
A.1.d.1
A.2.d.1
B.1.d.1
B.2.d.1
A.1.d.2
A.2.d.2
B.1.d.2
B.2.d.1

Figure 4. Textural properties of collagen scaffolds after topotactic fibrillogenesis, by gas-phase or liquid-phase pathways, imaged by confocal microscopy. (**A**) Scaffolds fibrillated by the gas-phase method, based on ammonia vapors at 0°C. (**B**) Scaffolds fibrillated by the liquid-phase method, based on a buffer solution of PBS (10X) at -3°C. A.1. A.2. B.1. B.2: (a) longitudinal cross-sections of the scaffolds (b.1) transversal cross-sections of the scaffolds and (b.2) the analysis of Min and MaxFeret diameters of the transversal pores for each. (c.1) 3D-rendering of the luminal surface (100-200 µm) of the tubular scaffolds and (c.2) the analysis of Min and MaxFeret diameters of the pores for each. (d.1): 3D-rendering of the external surface (100-200 µm) of the tubular scaffolds and (c.2) the analysis of Min and MaxFeret diameters of the pores for each.

Table 2. Dimensions of the scaffold pores for various sections and surfaces, after ice-templating and topotactic fibrillogenesis. When available, values are given with the associated standard deviation.

		Freezing and fibrillogenesis conditions			
Analyzed zone	Measurement	NH_3		PBS (10X)	
		Cond	Ins	Cond	Ins
Transversal section	Median Feret / µm	16.12 ± 1.17	18.76 ± 1.57	N/A	3.78 ± 0.27
	Median MinFeret / µm	6.31 ± 0.39	8.05 ± 0.64	N/A	1.78 ± 0.14
	Median aspect ratio	3.04 ± 0.10	2.33 ± 0.08	N/A	1.84 ± 0.05
	Surface accessible porosity / %	24	34	N/A	31
Luminal surface	Median Feret / µm	10.41 ± 2.49	16.00 ± 2.25	5.18 ± 0.26	5.98 ± 0.60
	Median MinFeret / µm	5.56 ± 1.51	7.82 ± 1.18	3.16 ± 0.16	3.32 ± 0.37
	Median aspect ratio	2.03 ± 0.07	1.97 ± 0.97	1.91 ± 0.06	1.47 ± 0.04
	Surface accessible porosity / %	53	21	<1	5
External surface	Median Feret / µm	5.04 ± 0.27	19.35 ± 3.28	4.78 ± 0.54	1.43 ± 0.12
	Median MinFeret / µm	2.68 ± 0.15	10.22 ± 1.54	3.43 ± 0.35	0.79 ± 0.07
	Median aspect ratio	1.99 ± 0.02	1.78 ± 0.10	1.33 ± 0.09	1.46 ± 0.02
	Surface accessible porosity / %	50	28	<1	2

In contrast, PBS (10X)-fibrillated scaffolds demonstrate reduced pore accessibility in the transversal plane (Figure 4B.1.b.1 and B.2.b.1). Surfaces have a smooth appearance, and regardless of the ~20 µm periodic artifacts due to the sample cutting process, the method fails to retain the porous structure (Figure 4B.1.a and B.2.a). ***Cond*-PBS** samples are devoid of pores at the observable length scale. In ***Ins*-PBS**, observable pores are scarce close to the lumen, even at higher magnification (Figure 4B.1.b.2). In the center, small pores can be witnessed in between the formed fibrils (Figure 4B.2.b.1), with a median Feret diameter of 3.78 ± 0.27 µm and an accessible pore surface of 30.5% (Figure 4B.2.b.2). Overall, the conditions imposed by the fibrillogenesis in PBS (10X) favor the melting of ice crystals prior to the self-assembly of collagen. The architecture of ice crystals plays an important role in the

preservation of their shape and the subsequent porosity. Unidirectional pore structures such as those found in ***Ins*** promote faster diffusion of the PBS ions, slightly shifting the kinetics in favor of collagen self-assembly which favors the preservation of the porous structure.

The pore size on the luminal surface is not altered by the gas-phase fibrillogenesis process (Figure 4 c.1-2, d.1-2 for A.1 and A.2). Pores in the lumen present Feret diameters of 10.41 µm and 16.0 µm for respectively ***Cond*-NH_3** and ***Ins*-NH_3** (Table 2), versus 9.77 µm and 11.36 µm in lyophilized scaffolds (Table 1). Pores of the external surface are 2 to 4 times smaller than those of the lyophilized scaffolds, with a mean Feret diameter of 5.04 m and 19.35 µm for respectively ***Cond*** and ***Ins***, compared to 17.32 µm and 45.83 µm in the dry state. However, the degree of surface accessible pores differs from what was observed for lyophilized scaffolds: ***Cond*** provides the highest pore coverage with 53% at the lumen and 50% at the external surface, compared to 21% and 28% for ***Ins***. We can hypothesize that the mismatch between the conservation of the pore size and the reduction of surface accessible is due to a contraction of all pores following fibrillogenesis. The smallest pores observed after freeze-drying may disappear or become too small to be detected, while the largest pores may be reduced due to a slight collagen wall swelling between the dry and the hydrated forms. In contrast, fibrillogenesis in PBS (10X) leads to a significant reduction of the pore size at both the luminal and external surfaces (Figure 4 c.1-2, d.1-2 for B.1 and B.2). At the lumen, pore size is reduced by a factor of ~2 for both ***Cond*-** and ***Ins*-PBS.**, while on the external surface, size is reduced by factors of 4x and 32x, respectively. More importantly, the degree of accessible pores exceptionally decreases in ***Cond*-PBS**. Less than 1% of the luminal and external surfaces is covered by pores, which hinders access of cells to the inner wall of the material upon cellularization. In ***Ins*-PBS**, 5% and 2% of the luminal and external surfaces are covered by pores, corresponding to a 90% size reduction in comparison to lyophilized scaffolds. PBS (10X) route results in the formation of more rounded pores, characterized by a mean aspect ratio ranging between 1.58 and 1.8, in contrast to NH_3 fibrillogenesis that yields values ranging from 2.05 to 2.30. As in any temperature-dependent process, the conditions of topotactic fibrillogenesis determine the final textural characteristics of the scaffolds. The gas-phase route favors the self-assembly of the collagen molecules that stiffen the walls surrounding the ice crystals and subsequently melt the ice crystals to reveal the pores. The resulting materials correspond thus to a fibrillar gel sample whose texture is the fingerprint of the ice crystals formed during ice templating. Conversely, the liquid-phase fibrillogenesis favors first the thawing of ice-crystals, resulting in a dilution of the collagen molecules initially concentrated in the interstices and a partial or complete loss of the texture defined by ice. Shifting the kinetics in favor of self-assembly can enhance the preservation of the porous network, as seen above for anisotropic structures obtained in *Ins* conditions. Such structures lead to faster diffusion rate of the fibrillation media, associated with increased likelihood of keeping the pores and their interconnectivity. However, the evolution of some textural features – such as

the reduction of pore size – induced by liquid route topotactic fibrillogenesis presents advantages. Specifically, the pore dimensions on the luminal surface of tubular constructs obtained through PBS (10X) topotactic fibrillogenesis closely resemble those observed in the tracheal basal membrane, which display an average diameter of 1.76 µm[36]. In this sense, the liquid-phase fibrillogenesis route described here can be seen as a supplementary tool for fine-tuning the porosity of the materials and matching the textural characteristics of a given native tissue. Noteworthy, for both fibrillogenesis routes, the shape and structure of the tubular materials remained stable for at least two years.

d. Influence of the fibrillogenesis pathway on the collagen molecular and supramolecular arrangement

During freezing, collagen molecules in solution are forced to concentrate in the interstitial space created in between ice crystals. Because collagen in solution behaves as a lyotrope, molecular crowding of collagen can lead to the formation of biological analogues of liquid crystals[37]. In specific cases, collagen crowding can also lead to local prefibrillar states, as suggested by Gobeaux *et al.*[38]. Although the results cited above were obtained at room temperature and there are no reports of such mesophases or prefibrillar arrangements near water freezing conditions, it is likely that these semi-ordered states exist in solution close to 0°C. To probe the molecular arrangement of collagen molecules in the obtained fibrillar materials, we examined 200 µm-thick transversal sections of the scaffolds under an optical microscope equipped with cross-polarizers. Each of the samples display birefringent signal along the axis defined by the bisections of the quadrants, formed by the analyzer and polarizer positioned at 0° and 90°, respectively (Figure 5 1-2.a for A and B). The ***Cond*-NH_3** sample features alternating patches of birefringent and extinction zones throughout the entire thickness of the wall (Figure 5A.1.a). These birefringent domains, in the tens of µm across, are dispersed homogeneously throughout the whole thickness of the tubular wall. The ***Ins*-NH_3** sample exhibits a remarkably different behavior, with the presence of a large birefringent domain at the scale of the tube wall. The difference between the birefringence signals among these scaffolds highlights the importance of the freezing conditions in obtaining diverse textures, even when the same fibrillogenesis protocols are employed. Samples fibrillated in PBS (10X) also display a collective birefringent signal spanning the entire thickness of the samples, suggesting the existence of contiguous organized domains of collagen molecules throughout the sample walls. In general, the birefringent signal found at the luminal and external walls suggests a greater degree of order in these zones, possibly resulting from the concentration of collagen molecules in the initial moments of ice templating.

Ordered structures revealed by the birefringence signal emerge from two factors that are difficult to disentangle. On the one hand, molecular crowding can lead to the formation of mesophases, and in some case, to the appearance of pre-fibrillar structures able to produce birefringence signal[38]. On the other hand, since samples are exposed to physicochemical conditions meant to induce fibrillogenesis – ammonia vapors and PBS (10X) solution – even collagen solutions displaying an isotropic molecular arrangement may lead to fibrillar structures able to produce birefringent signal. At the observed scale here, polarized optical microscopy provides clues to understand the global orientation of the collagen molecules within the tubular samples, but is insufficient to describe the formation of biomimetic fibrillar domains.

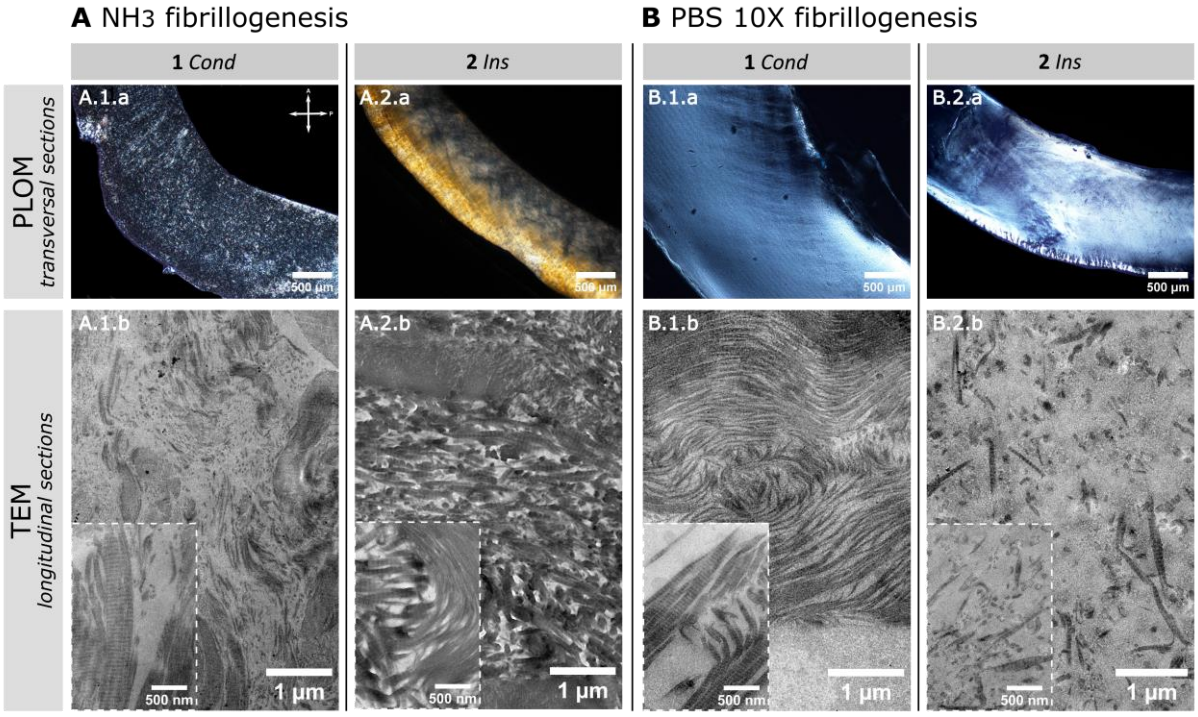

Figure 5. Influence of the processing conditions on the supramolecular organization of collagen in the scaffolds. Materials were fibrillated using ammonia (**A**) or PBS (10X) (**B**), with either conductive (**1**) or insulating (**2**) outer molds. (A & B.1.a, A & B.2.a): under cross-polarizers oriented at 0°, the transversal sections all exhibit a birefringent signal characteristic of liquid crystal-like ordered structures. Transmission electron micrographs of the materials (A & B.1.b, A & B.2.b). Insets display the typical D-banding striation found in the fibrils of each sample.

Ultra-thin longitudinal sections of the scaffolds observed under TEM demonstrate the existence of fibrillar structures for each ice templating/topotactic fibrillogenesis condition, similar to the motifs found in the ECM of arterial tissue. Observed at higher magnification, fibrils present a D-banding pattern along their axis, with distances below the typical 67 nm striations due to their off-plane orientation with respect to the cross-section plane (Fig.S3).

The existence of these features confirms the fact that both fibrillogenesis routes induce the formation of biomimetic fibrils, and follow an arrangement similar to that of native tissues. Exposed to ammonia vapors, collagen molecules form a dense network of small fibrils (Figure 5-A.1.b and A.2.b), both transversal and parallel to the observation plane. Fibrils in ***Cond*-NH_3** are smaller and lie in a looser arrangement than those in ***Ins*-NH_3**, revealing that a simple change of the thermal conductivity of the molds during ice-templating can affect collagen fibril formation. Fibrils in ***Ins*-NH_3** form compact arched patterns, surrounded by denser regions. Conversely, PBS (10X) promotes the formation of a higher number of large striated fibrils, in less tightly packed domains. These results confirm the observations of the texture observed under the confocal microscope, for which the swelling during fibrillogenesis led to narrower – or absent – pores. We hypothesize that during the partial melting of the ice crystals, concentrated collagen solution in the interstitial space is rediluted, which increases the mobility of the molecules and enables the formation of a greater number of supramolecular structures. The high compaction of the fibril network in ***Cond*-NH_3**, ***Ins*-NH_3** and ***Cond*-PBS**, is similar to those of native tissues, suggesting a local concentration ranging between 50 and 200 $mg.mL^{-1}$[39]. The diversity of fibril sizes and arrangement observed here provide a valuable tool to elaborate materials that mimick specific features of a variety of tissues' ECM. To the best of our knowledge, no other tubular biomaterial has reached such a close resemblance to native tubular tissues in terms of collagen supramolecular and network organization.

Although the preceding results confirm the relevance of our elaboration strategy in obtaining biomimetic materials that display structural and textural features of the ECM, they do not provide direct proof of the stabilization effect brought by the fibrillogenesis processes in cold conditions. We have measured the thermal stability of the different materials using Differential Scanning Calorimetry (DSC). The temperature of the endothermic peaks characterizes the thermal denaturation processes of each sample (Fig.S4). Samples fabricated in **-PBS** are more stable, with a mean denaturation temperature (T_d) 2.6°C higher than with **-NH_3** (Table 3). Such a difference can be explained by the prevalence of larger and more mature fibrils in these samples, leading to higher stability. The structural variations induced by the conductive or insulating outer mold do not significantly alter the T_d. In all four conditions, the denaturation temperature is considerably above that of non-fibrillar materials around 37°C.

Two major differences standout regarding the influence of the fibrillogenesis pathways on the collagen texture and microstructure. Ammonia treatment enables the maintenance of the porosity and of the collagen walls' concentration. It leads to the formation of small fibrils, tightly packed in a complex 3D arrangement according to the TEM and PLOM images. In contrast, PBS (10X) favors the thawing of ice that results in less concentrated collagen

domains. These display larger and more mature fibrils than in NH_3, which increase the thermal stability. Regardless of the mold materials conditions, it is evident that a modification of the physico-chemical parameters induces variations in the size and arrangement of fibrils. Unlike other existing tubular biomaterials, we offer here conditions that facilitate the stabilization of the liquid crystal-like mesophases, a key feature of the ECM of native tissues. Given the similarities of our materials to the native cellular microenvironment, we expect them to efficiently promote *in vivo* cellularization after implantation, a necessary process for the long-term biointegration.

Table 3. Thermal stability measurements of the materials demonstrate that PBS (10X) fibrillogenesis leads to a more stable collagen network by the increased denaturation temperature. No significant difference is noted between the materials fabricated with a conductive (***Cond***) or insulating (***Ins***) outer mold. Denaturation temperatures (T_d) of the materials were measured by differential scanning calorimetry (DSC) (Fig.S4).

	NH_3 fibrillogenesis		PBS (10X) fibrillogenesis	
	Cond	*Ins*	*Cond*	*Ins*
T_d ± SD / °C	48.73 ± 3.41	46.76 ± 0.52	49.55 ± 1.09	51.11 ± 0.99

e. Multiscale elastic properties of biomimetic tubular materials

The mechanics of biological tissues and those of their analogues are defined by – at least – two different length scales that correspond to the cell microenvironment and to the full tissue. We have characterized the elastic properties of the biomimetic tubular materials using AFM and quasi-static macroscopic traction tests to describe the material behavior under mechanical loading.

The resistance to macroscopic deformation in both the longitudinal and circumferential directions under quasi-static loading was evaluated for the four different types of obtained tubular materials (Figure 6A and 6B). In the longitudinal direction, ***Ins*-NH_3** samples exhibited the highest stiffness, with a Young's modulus (E) of approximately 58 ± 39 kPa (mean ± SD). Conversely, the circumferential stiffness of ***Ins*-NH_3** samples, as well as the longitudinal and circumferential stiffnesses of ***Cond*-NH_3** samples, were notably lower, ranging between 6 and 10 kPa. These findings indicate that the matrices display anisotropic elastic properties under macroscopic loading, with greater rigidity observed along the longitudinal direction of ***Ins*-NH_3** samples compared to others. Under ***Ins*** conditions, the process of ice templating involves the uniaxial growth of ice crystals, which alignment is preserved through ammonia fibrillogenesis. The longitudinal orientation of pores explains the greatest Young's modulus obtained for ***Ins*-NH_3**, and is coherent with superior elastic properties in the direction of crystal growth but poorer elastic properties in the transverse

directions. In contrast, the thermal gradient imposed in ***Cond*** leads to radially oriented collagen walls and pores. As a consequence, the circumferential and longitudinal directions are perpendicular to the porous structure and show a relatively low Young's modulus. The analogy to the elastic properties of composite materials, here with a collagen matrix populated by zero Young's moduli inclusions – the pores – allows us to rationalize this behavior. One may invoke a Rule of Mixtures (ROM) behavior in case the pores and the walls are aligned with the traction direction, whereas an Inverse Rule of Mixtures (IROM)[40] may explain the lower moduli when the traction is applied perpendicular to the main pore and wall directions.

Contrary to the results obtained using NH_3 as a fibrillogenesis medium, PBS (10X) (Figure 6B) provides the tubular materials with isotropic elastic properties. Regardless of the orientation of the pores initially developed through ice templating, elastic moduli remain close to 20 kPa. This behavior is ascribed to the fact that PBS (10X) favors faster ice melting over the self-assembly of collagen, resulting in poorly preserved porosity, small pore size and low anisotropy compared to NH_3-fibrillated samples (Figure 4). Instead of having a composite material with highly distinct mechanical properties in the longitudinal and circumferential directions, as seen in NH_3-fibrillated samples, we obtain a material with similar mechanical properties in both deformation directions. This difference in elastic properties depending on the direction of stress between the two types of fibrillogenesis could allow mimicking a large range of tissues with orthotropic properties (such as bone, cartilage, tendon...) as well as tissues with isotropic properties (adipose tissue, connective tissue, spongy bone...).

The elastic properties earlier discussed describe the behavior of the materials at the tissue level. However, their local elastic properties – at the cell length scale – are equally important to ascertain their relevance as tissue grafts. The local Young's modulus was measured in compression on the luminal and transverse surfaces of -**PBS** and -**NH_3** samples using an Atomic Force Microscope (AFM). Unlike the tensile measurements that provided the macroscopic stiffness of the samples, these local stiffness measurements focused on the stiffness of the walls within the samples. Results depicted in Figure 6 demonstrate that the -**NH_3** samples exhibited a significantly higher average stiffness of approximately 300 kPa compared to the -**PBS** samples, which had an average stiffness of around 50 kPa. Furthermore, the ammonia-fibrillated samples exhibited a broader distribution, characterized by increased variability in the 25th and 75th percentile values when compared to the -**PBS** fibrillated samples. Additionally, the violin plots suggest the co-existence of two populations of elastic local environments for the -**NH_3** samples, while the -**PBS** sample displays a Gaussian distribution indicative of a single population.

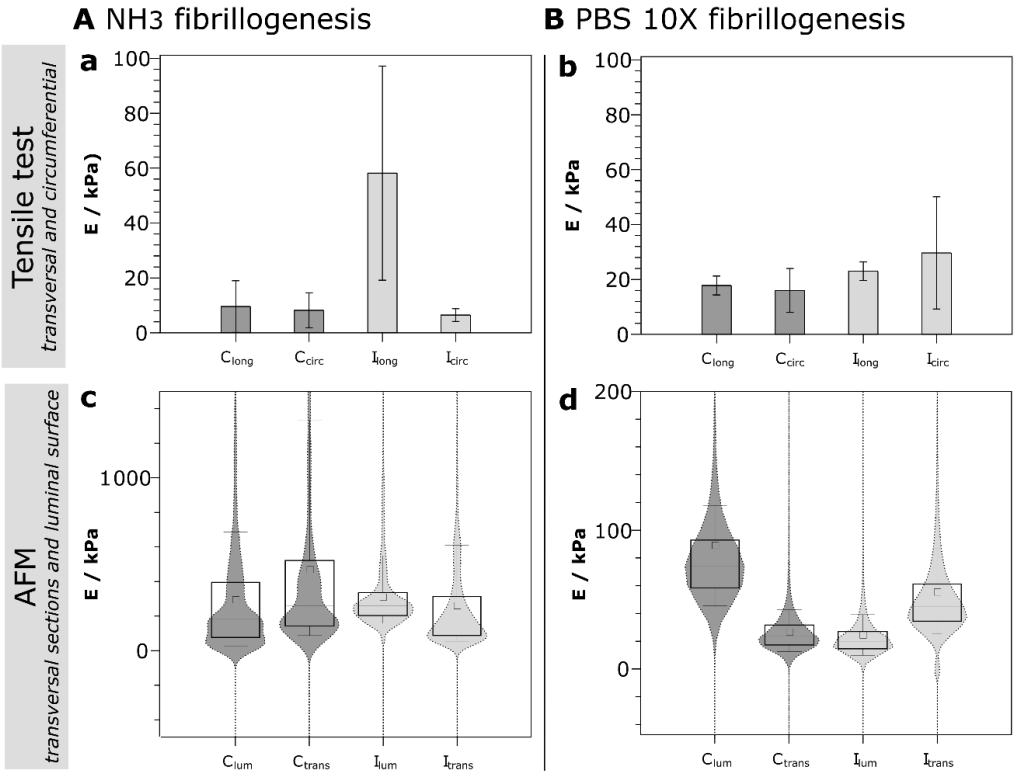

Figure 6. Influence of the processing conditions on the mechanical properties of the scaffolds. Materials were fibrillated using ammonia (**A**) or PBS (10X) (**B**), with either conductive (*Cond* - **C**) or insulating (*Ins* - **I**) outer molds. (a, b) Longitudinal (long) and circumferential (circ) traction Young's moduli for each sample. Error bars represent standard deviations. (c, d) Luminal (lumen) and transversal (trans) compression Young's moduli for each sample. Box plots represent the 25th to 75th percentile range of the modulus distribution, with the whiskers indicating the 10th to the 90th percentile range of the modulus distribution. The squares denote the mean values, and the straight lines represent the medians.

Taken together, these results confirm the observations arising from the microscopy techniques (TEM and confocal microscopy) that suggested a partial dilution of the collagen walls during (10X) PBS-induced topotactic fibrillogenesis, whereas NH_3 tends to preserve highly concentrated collagen domains in the internal walls of the scaffolds. The ability to tune the collagen concentration in our scaffolds through different fibrillogenesis protocols presents an interesting aspect. Cells are significantly impacted by the collagen concentration in their microenvironment[41], directly influencing the stiffness and mechanical properties of the surrounding extracellular matrix, as demonstrated by our AFM experiments. This crucially affects cellular adhesion, migration, differentiation, and tissue development. Consequently, tailoring local collagen concentration with our different fibrillogenesis

protocols could result in adapted substrates for grafting at different locations with diverse surrounding cell types.

f. In vitro cellularization of biomimetic tubular materials

Endothelialization and epithelialization of the luminal surface of tubular scaffolds

Functional epithelia and endothelia play a key role in tubular tissues because they provide the semi-permeable character that mediates transport from the luminal to the adventitial sides of the tissues. Human alveolar basal epithelial cells (A549) and human umbilical vein endothelial cells (HUVECs) were seeded on the luminal side of the different materials to ascertain the effect of the topography and the fibrillogenesis pathway on their suitability to host cells. The cellularization was studied in time and compared to a simplified model of basal lamina (*i.e.* PDMS substrates coated with type IV collagen) as a control. Observations under confocal microscopy of immunostained cells demonstrate that luminal surfaces of all materials promote cell proliferation after a few days of culture (Figure 7), suggesting their potential to facilitate endothelium formation *in vivo* A549 display a homogenous covering of ***Cond*-NH_3** surface at day 3 while the distribution of cells seems more erratic on other surfaces at that time, suggesting that ***Cond*-NH_3** is more compatible for A549 adhesion. However, at day 11 for a given material, cell densities reach comparable levels in between the two fibrillogenesis and cell spatial distribution becomes more homogeneous, although ***Cond*** surfaces seem more suitable than ***Ins*** ones.

The trends of epithelial cellularization observed for these materials using A549 cells were equally confirmed by seeding HUVECs. As depicted in Fig. 7B, ***Cond*** surfaces generally provide a more favorable substrate for HUVECs adhesion than ***Ins*** surfaces with the cells exhibiting a more homogeneous distribution and more complete surface coverage regardless of the cell culture time and the fibrillogenesis pathway (with the exception of ***Cond*-PBS** at day 3). ***Cond*-NH_3** cell density follows that of the biomimetic control at days 3, 5 and 7. At day 7 cell densities are steady compared to the previous time point, suggesting that confluence has been attained.

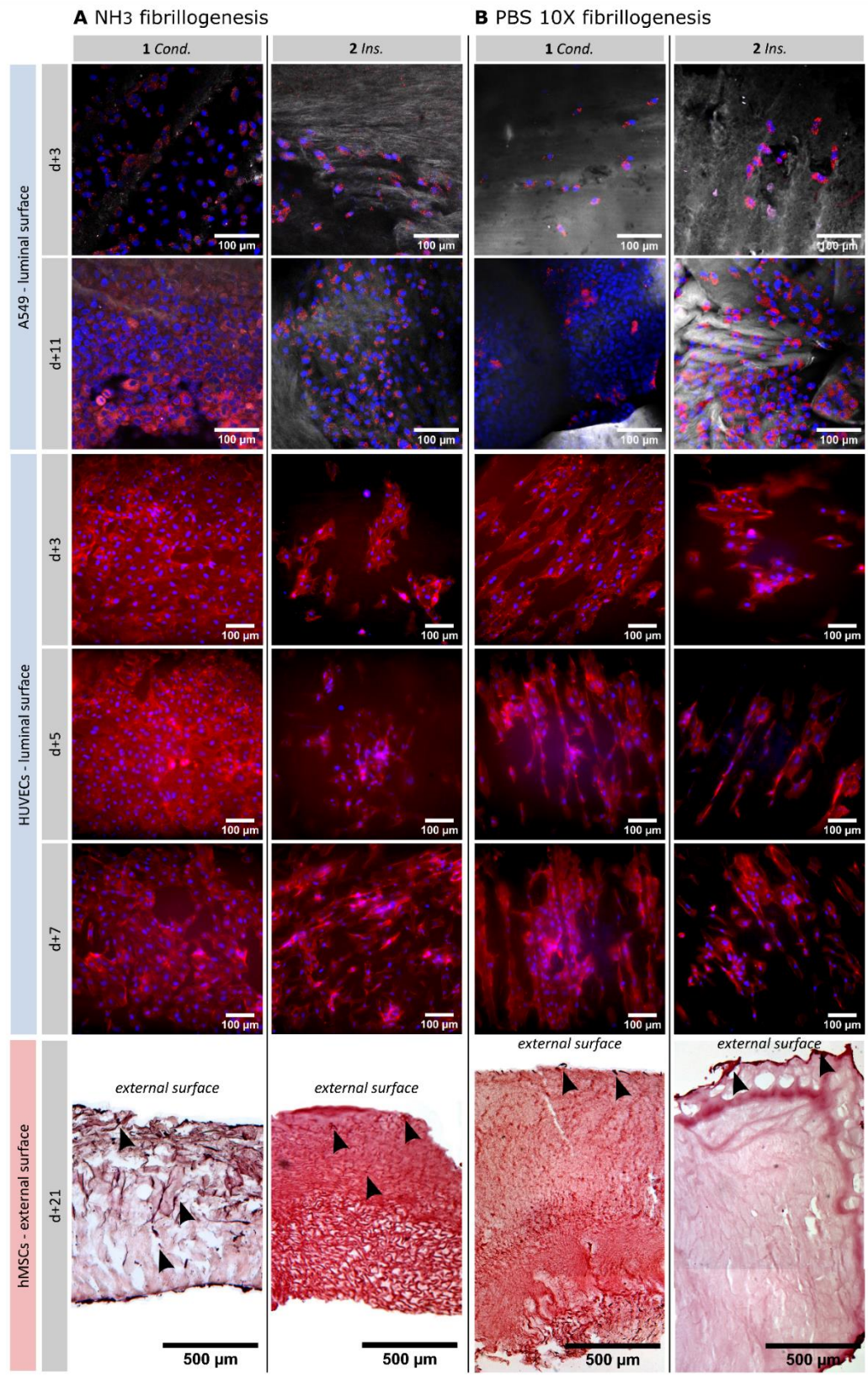
A NH3 fibrillogenesis
B PBS 10X fibrillogenesis
1 Cond.
2 Ins.
1 Cond.
2 Ins.
A549 - luminal surface
d+3
d+11
HUVECs - luminal surface
d+3
d+5
d+7
hMSCs - external surface
d+21
100 µm
external surface
500 µm

Figure 7. Cell colonization of biomimetic type I collagen materials for the studied mold materials and fibrillogenesis routes. Epithelium formation was studied with luminal seeding of two different cell lines, A549 cells (days 3 and 11) and HUVECs (days 3, 5 and 7). The ability of cells to colonize the adventitial part was demonstrated with hMSC and observed at day 21. Observations of epithelial cells were performed under confocal microscopy, with immunostaining of the nuclei (blue: DAPI), actin (red: phalloidin) and collagen (grey: FITC). Observations of the colonization by hMSC were performed under microscope on cryosections stained with hematoxylin (nucleus) and eosin (cytosol) dyes.

Materials prepared by PBS (10X) fibrillogenesis display slower cellularization kinetics as compared to materials fibrillated in ammonia. Despite the initial differences, the cell density in PBS (10X) fibrillogenesis materials does evolve positively over time as can be observed from Figs. 7 and 8. These results demonstrate that it is possible to direct the cell-material interactions by an adequate choice of the mold thermal conductivity parameters and the fibrillogenesis route. The highest density was obtained for ***Cond***, which coincides with the low porosity of the lumen previously observed under confocal microscopy. Combined with NH_3 fibrillogenesis, ***Cond*-NH_3** surfaces present the highest cell densities at early cell culture time points, but as mentioned earlier cell density appears to decrease once confluence is attained.

Migration of hMSCs into the tubular scaffolds from the external surface

Materials were seeded with human mesenchymal stem cells (hMSCs) on their external surface and cultured for three weeks in order to evaluate their ability to be colonized. Cryosections stained with hematoxylin and eosin dyes (Figure 7) indicate that hMSCs deeply migrate in ***Cond*-NH_3** at day 21, while only partial colonization is observed in other materials. Since porosity is poorly preserved in **-PBS**, cells lie on the top surface and do not migrate into the materials. Moreover, ***Ins*** materials seem less favorable for colonization compared to ***Cond*** ones, may be due to the looser collagen density within the walls observed at the TEM.

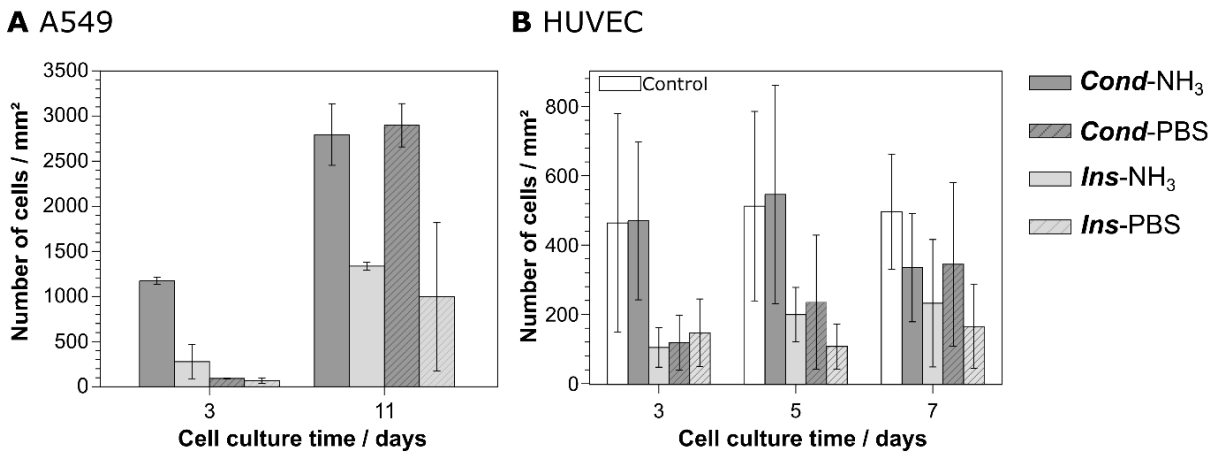

Figure 8. Ability of the materials to promote epithelium formation. Two epithelial cell lines (A549 cells and HUVECs) were seeded on the luminal surface. (**A**) A549 cell density at days 3 and 11 on each material's lumen. Error bars: ± SD, (**B**) HUVECs density at day 3, 5 and 7 on each material's lumen. Error bars: ± SD.

C. Conclusions

We describe here a strategy to replicate the composition, the structure, as well as the mechanical and biological functions of native tubular tissues' ECM using exclusively type I collagen.

Ice-templating has proven versatile as a shaping technique to fine-tune the materials porosity by adjusting the thermal boundary conditions imposed by molds. This simple method allows orienting pores in either longitudinal or radial directions, a tool to tailor the accessibility of cells to the scaffold. The topotactic fibrillogenesis conditions provide further control over the porosity while triggering the self-assembly of collagen molecules into biomimetic fibrils. Our materials offer cellular micro-environments closely resembling those of biological tissues, a lacking feature in materials currently used in the clinic. In particular, one material stands-out as a potential graft, ***Cond*-NH3**, which meets the requirements initially set regarding the structure of tubular tissues. It provides a luminal surface that promotes a rapid endothelium formation, as well as a porous outer layer that enables cell colonization.

Using only type I collagen and in the absence of any cytotoxic cross-linkers, the elastic properties at both the tissue and the cellular length scales, reach those of native tissues. This exceptional combination of native composition and mechanical properties, is given by our precise control over the porosity and orientation. It directs the anisotropic *versus* isotropic

character of the materials' elastic properties, offering the opportunity to mimic mechanical behaviors of a wide range of biological tissues.

Interactions between the materials and different cell lines – ECs and MSCs – demonstrate their potential to serve as biologically relevant substrates. On the basis of hMSCs migration experiments, ammonia fibrillogenesis proves more suitable to preserve pores and to facilitate cell colonization, ensuring a successful graft implantation. Epithelial and endothelial cells adhere well to the materials and proliferate until confluence is reached in all conditions, demonstrating their potential to promote endothelialization *in vivo*.

Overall, we introduce a new family of tubular collagen materials, exhibiting a unique combination of high concentration and porosity, with unprecedented resemblance to native tissues. Through their textural and compositional features, they promote both cell adhesion on the luminal surface and cell migration from the external surface, associated with mechanical performances suitable for functional replacement. We anticipate that these are central to a new range of grafts, whose biomimetic features secure assimilation by the body of the patient.

Beyond their role as tissue grafts, our materials are expected to act as organotypic models of tubular tissues. These may answer a vast range of open questions – from cell-cell and cell-matrix interactions up to drug treatment response – bridging current gaps for improved patient care in respiratory, vascular, gastrointestinal and urinary tracts pathologies.

D. Experimental section

Fabrication of the collagen scaffolds

Collagen I was extracted from young rat tail tendons. After thorough cleaning of tendons with phosphate buffered saline (PBS; 1X) and 4 M NaCl, tendons were dissolved in 3 mM HCl. Differential precipitation with 300 mM NaCl and 600 mM NaCl, followed by redissolution and dialysis in 3 mM HCl, provided collagen of high purity. The final collagen concentration was determined using hydroxyproline titration with a spectrophotometer. To attain a high fibrillar collagen density in the model, the remaining collagen solutions were concentrated at 40 $mg.mL^{-1}$ by centrifugation. The solutions were transferred into Vivaspin tubes with 300 kDa filter and centrifugated at 3000 g at 10°C, until the final concentration was reached.

Concentrated collagen is introduced in between two cylindrical molds (inner mold: 3x5 mm; outer mold: 8x10 mm: length: 50 mm) whose ends are hermetically sealed by caps. For removal of air bubbles, sample is centrifuged at 1 rpm and 10°C for 10 minutes. The sample is placed onto a home-made set-up that allows a continuous and regulated dipping of the

sample in liquid nitrogen. It is composed of: 2 optical axes, 4 linear rod rail support guides, a lead screw, a DC motor (12 V), a speed controller, a transformer and an ABS 3D-printed part linking the support guide and the lead screw (Figure S1).

The sample is ice-templated at a dipping speed of 10 $mm.min^{-1}$. Once frozen, the outer mold is quickly removed and a topotactic fibrillogenesis condition is applied. At low temperature, two conditions are compared: (a) exposure to ammonia vapors or (b) PBS (10X: 1.37 M, KCl 26.8 mM, Na_2HPO_4 80.7 mM, and NaH_2PO_4 14.7 mM). Pre-fibrillogenesis for (a) consists of exposing the sample to ammonia vapors at 0°C in an ice-water bath for 48 h, followed by removal of ammonia using distilled water vapors for 24 h at 37°C in a heat room. For (b), the sample is simply maintained in PBS (10X) at -3°C in a thermostatic bath for 72 h. For both (a) and (b), fibrillogenesis is completed by keeping the sample in PBS (5X: NaCl 685 mM, KCl 13.4 mM, Na_2HPO_4 40.35 mM, and NaH_2PO_4 7.35 mM) for 14 days at room temperature.

Scanning electron microscopy

After ice-templating, the frozen matrices were freeze-dried for 24h, and the resulting dried foams were cut into different sections to determine crystallization mechanism and pores alignment of the scaffold. Two sections were cut horizontally (perpendicular to the ice front growth direction), at the top and bottom. Two sections were cut longitudinally (parallel to the ice front growth direction), to depict the lumen and the intima-adventitia-like layers of the tubular construct. Samples were imaged using scanning electron microscopy (SEM), with prior sputter coating with a 10nm layer of gold. Observations were performed at 10 kV at various levels of magnification using a Hitachi S-3400N microscope.

Porosity quantification

Porosity was quantified using ImageJ Fiji (Fig.S2). Images were first binarized by adjusting the threshold for transversal sections or using the *LabKit segmentation* plugin for the surfaces. Porosity was quantified using the ImageJ plugin *Analyze particles* which detects particles or round structures in images by analyzing intensity variations and identifying groups of pixels with high gradient values. Feret diameter (MaxFeret), minimum Feret diameter (MinFeret), aspect ratio and area were the set measurements. The Feret diameter corresponds to the diameter of the smallest circle enclosing the pore, whereas MinFeret corresponds to the diameter of the biggest circle enclosed within the pore. Data are expressed as mean ± SE (standard error).

Pore orientation was quantified using the ImageJ plugin *OrientationJ*. Pore surface coverage was determined as the percentage of accessible pores on a given surface.

Confocal microscopy

After fibrillogenesis, semi-thin sections (200 µm-thick) were cut. Collagen was labelled with fluorescein isothiocyanate (FITC, 0.05 mg/mg of collagen) at 4°C overnight. Cellularized samples with A549 cells were fixed in between a glass slide and a coverslip with a handmade set up to maintain it, and imaged at the end of the culture. Observations were conducted on using a Zeiss LSM 980 upright confocal microscope.

Transmission electron microscopy

Hydrated samples were cross-linked with 2.5% paraformaldehyde (PFA), 2% glutaraldehyde, 0.18M sucrose and 0.1% picric acid for 12 h. The samples were subsequently post-fixed with uranyl acetate in ethanol for 12h, and dehydrated using baths with increasing concentrations of ethanol. Samples were incorporated in SPURR-S resins prior to sectioning. 70 nm ultrathin sections (Leica microtome) were contrasted with uranyl acetate and observed on a transmission electron microscope (FEI Tecnai Spirit G2) operating at 120 kV to observe the ultrastructural collagen features. Images were recorded on a Gatan CCD camera.

Polarized light microscopy

Samples were incorporated in 2,5% agarose and 200 µm semi-thin sections were cut with a vibratome (Compresstome), and observed under a Nikon Eclipse E600Pol microscope equipped with 4X, 10X and 40X objectives, a DXM 1200 CCD camera, and cross-polarizers to observe the birefringence of the sections.

Axial and circumferential Young's modulus measurement

Uniaxial traction testing of porous collagen tubes was performed on a homemade stage with a 10 N load cell (ME-Meßsysteme GmbH, Germany). The tubes were first cut open and unfolded toward a flat geometry. Rectangular strips measuring 2 cm x 1 cm were then cut from the samples in both circumferential and longitudinal directions. To measure the thickness of the samples, a compression rheometer (MCR 302. Anton Paar) was used: the base of a cylindrical probe was approached at a constant speed toward the sample until a force was detected, corresponding to the thickness of the sample. For the uniaxial tests, each strip was held in place with serrated jaws blocking the ends. The initial distance between the jaws was adjusted until each strip was flattened with non-zero force measured, and this

distance was set as the unloaded sample length. To ensure consistency and accuracy of the results, two pre-conditioning cycles were performed to produce a consistent force-elongation curve for each strip. Each strip was subjected to cyclic testing, and data from the third cycle's loading phase were used for analysis. The deformation rate, $k = {}^{v}/_{L}$, with v being the deformation speed and L the unloaded sample length, was maintained for each sample at a constant value of 0.8%. This protocol was followed for all tests. The resulting stress/strain curves were used to calculate the Young's modulus, and only the linear portion of these curves was utilized (Fig.S5). All measurements were carried out under immersion conditions in PBS (1X) at the physiological temperature of 37°C. Three tubes for each condition were used for statistical relevance.

Compression elastic Young modulus

The compression elastic modulus (Young's modulus) was assessed by AFM using a Nanowizard 4 BioAFM (PK/Bruker) mounted on a Nikon Eclipse Ti2-U inverted microscope equipped with PetriDish Heater. Due to the difference in stiffness between the PBS (10X) and NH_3 fibrillated samples, two appropriately matched probes with different spring constants were used for the measurements (qp-BioAC-CI and PPP-FMAuD from NANOSENSORS™). Cantilevers were calibrated using the thermal calibration method in PBS (1X) at 37°C. In order to locate the walls of our sample (i.e. to ensure we were not scanning within a pore), initial blind 2D scans were performed. Subsequently, appropriately sized scans were conducted in these identified regions (Fig.S5). The Hertz model was applied to fit each force-indentation curve, and stiffness for each scan point was extracted using JPK data processing software. All measurements were made under immersion conditions in PBS (1X) at a physiological temperature of 37°C.

Tubular matrix cellularization

Sample sectioning for cellularization

Collagenous tubular materials were prepared for cellularization as described above. After longitudinal sectioning, circular sections of the tube wall were cut using a 6 mm-diameter skin biopsy punch. For the cellularization with the different cell lines, samples were supported by the extremities using two thin needles on a PDMS substrate, with either the luminal or the external surface exposed.

HUVECs

Human umbilical vein endothelial cells (HUVECs, Lonza) in passages 5-8 were cultured at 37°C and 5% CO_2 in EGM2 cell medium (Lonza). Cells were detached from the adhering surface using TrypLE (Life Technologies, Carlsbad, USA). HUVECs were seeded on the luminal surface of 6 mm diameter discs of the collagen scaffolds (or PDMS coated with Collagen IV as control) at a density of 5,000 cells/sample and cultured for 3, 5 and 7 days. At the end of the culture, samples were fixed with 4% paraformaldehyde, permeabilized with 0.1% Triton X-100, and then incubated with DAPI (Sigma Aldrich) and Phalloidin 495 (LifeTechnologies) to visualize nuclei and the F-actin cytoskeleton. A series of images z-stacks were acquired at 1 µm intervals using an inverted microscope (Nikon Eclipse Ti-U, Japan) equipped with a CCD camera (Orca AG; Hamamatsu, Japan) and a motorized x-y stage equipped with a 20X Plan Apo λ Ph2 DM objective. Cell proliferation was quantified by counting the number of nuclei (based on the DAPI signal) using the FIJI plugin Cell counter.

Epithelialization with A549

Discs of 6 mm diameter were seeded on the luminal surface with 1'500 A549 cells (equivalent to 5300 cells/cm^2), and then grown in DMEM containing 25 mM D-glucose, 10 mM HEPES, 23.8 mM $NaHCO_3$, 1 mM sodium pyruvate, 2 mM L-glutamine, 100 U/ml penicillin, 100 µg/ml streptomycin, 10 µg/ml gentamycin, and 10% FCS in a 3% O_2, 5% CO_2 and 92% air atmosphere. The medium was changed every 48h hours.

Samples were fixed at days 3 and 11 after seeding with 4% formaldehyde in PBS (1X) for 16 hours at 4°C, then rinsed in PBS. After permeabilization with 0.1% Triton-X100 in PBS (1X) for 10 minutes and BSA-blockage in 3% BSA/0.1% Tween-20 in PBS, samples were stained with 1 µg/mL TRITC-conjugated phalloidin (Sigma) for 15 min at room temperature. They were rinsed several times in PBS (1X), stained with DAPI and placed in aqueous mounting medium (Citifluor AF1) for confocal microscope analysis.

External surface seeding with human mesenchymal stem cells (hMSC)

Six mm diameter discs were seeded on their external surface with 50'000 hMSCs (equivalent to 176'000 cells/cm2), and then grown for 3 weeks in DMEM containing 25 mM D-glucose, 10 mM HEPES, 23.8 mM $NaHCO_3$, 1 mM sodium pyruvate, 2 mM L-glutamine, 100 U/ml penicillin, 100 µg/ml streptomycin, 10 µg/ml gentamycin, and 10% FCS in a 5% CO_2 – 95% air atmosphere. The medium was changed every 48h hours.

After 3 weeks of culture, samples were fixed with 4% formaldehyde in PBS (1X) for 16 hours at 4°C, then rinsed in PBS. Samples were successively transferred in 15%, 30% sucrose in PBS (1X) and then in 50% OCT / 30% sucrose mixture at 4°C until equilibration. Finally,

samples were progressively embedded in 100% OCT on dry ice and conserved at -80°C until cryosections were performed. Ultrathin cryo-sections (10 µm-thick) were cut and post-fixed in ice-cold acetone for 15 minutes. Samples were then stained with haematoxylin and eosin dies for 5 minutes and placed in aqueous mounting medium for microscope analysis.

E. Acknowledgements

The authors kindly acknowledge the help from F. Lam and C. Chaumeton with confocal fluorescence microscopy. C. Djédiat is equally acknowledged for the preparation of samples for TEM observations. The authors gratefully acknowledge the contribution of C. Parisi and E. Budimirovic for their initial contributions on the subject.

F. Supporting Information

Tunable biomimetic materials elaborated by ice templating and self-assembly of collagen for tubular tissue engineering

by

Isabelle Martinier[1], Florian Fage[1], Alshaba Kakar[1], Alessia Castagnino[2], Emeline Saindoy[3], Joni Frederick[2], Ilaria Onorati[3], Valérie Besnard[3], Abdul I. Barakat[2], Nicolas Dard[3], Emmanuel Martinod[3], Carole Planes[3], Léa Trichet[1], Francisco M. Fernandes[1]**

Table S1. The different pairs of mold materials and their corresponding thermal conductivity differences used for the study of the interface position during ice-templating of a collagen solution. The difference was calculated by subtracting the inner material thermal conductivity from the outer one. Interface position is given in percentage as the distance to the lumen relative to the total wall thickness. The materials include aluminum (237 W/(m.K)), brass (110 W/(m.K)), stainless steel (45 W/(m.K)), acrylonitrile butadiene styrene (ABS) (0.17 W/(m.K)) and high impact polystyrene (HIPS) (0.11 W/(m.K)).

Number	Outer material	Inner material	Thermal conductivity difference (W/(m.K))	Interface position (%)
1	Stainless steel	Aluminum	-192	62.5
2	Brass	Aluminum	-127	38.1
3	Brass	Brass	0	27.9
3	Stainless steel	Stainless steel	0	17.6
4	Stainless steel	ABS	44.8	16.4
4	Stainless steel	HIPS	44.9	18.8
5	Brass	Stainless steel	65	13.9
6	Brass	ABS	109.8	8.5
6	Brass	HIPS	109.9	5.6

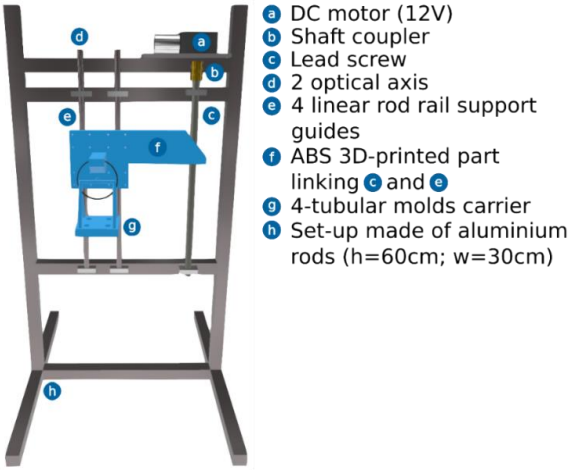

Figure S1. Homemade set-up for unidirectional controlled ice templating.

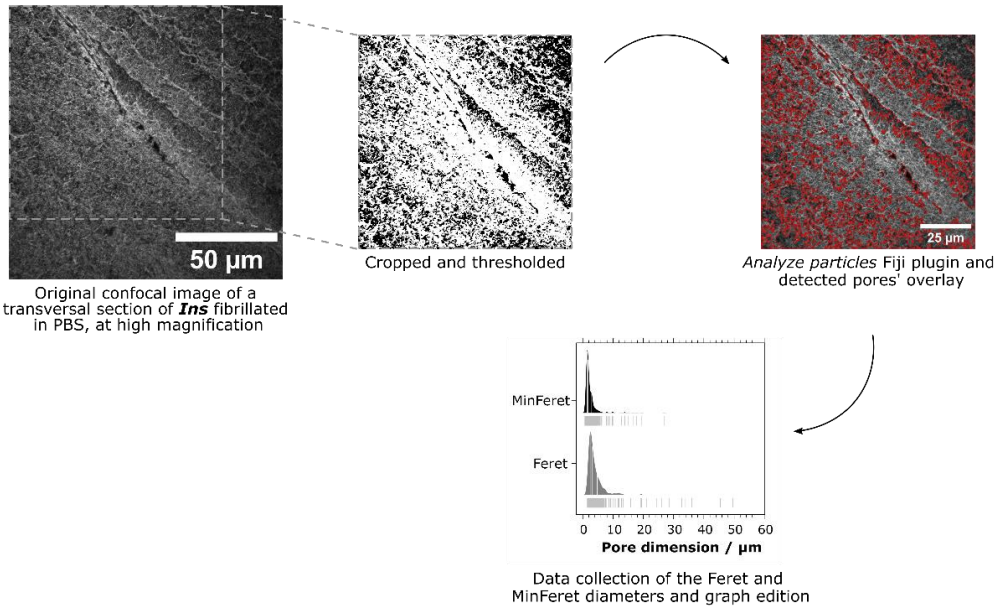

Figure S2. Pores dimensions analysis using ImageJ Fiji of ***Ins*** scaffold fibrillated in PBS (10X) and imaged by confocal microscopy at high magnification.

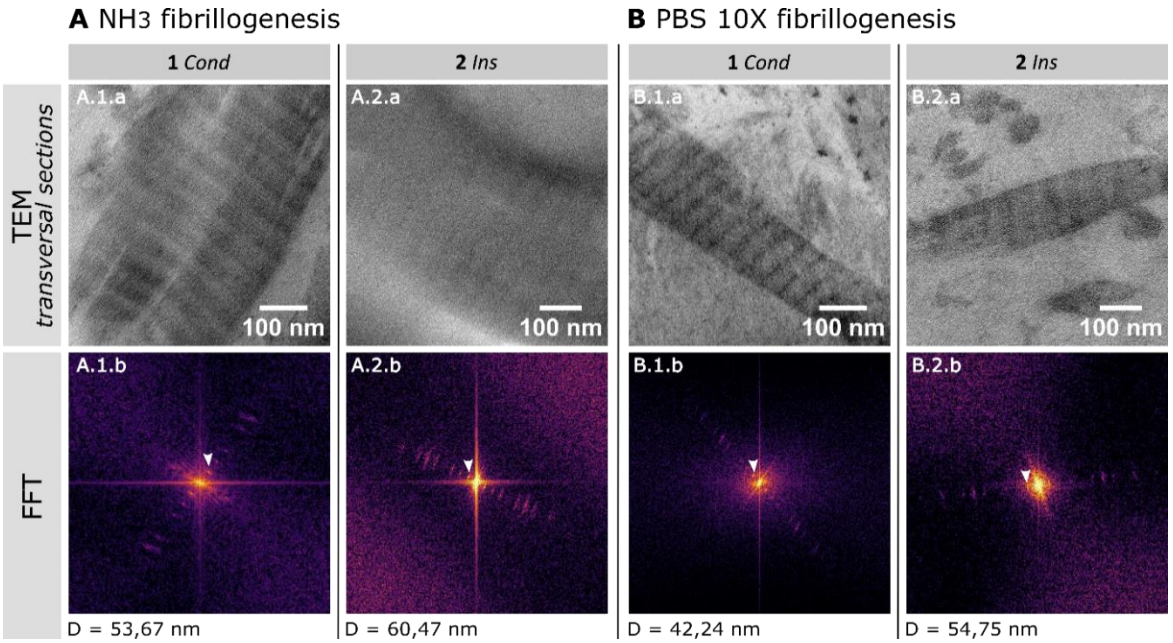

Figure S3. (**A.1.a, A.2.a, B.1.a, B.2.a**): High magnification of the fibrils' striation for each scaffold, imaged by transmission electron microscopy. (**A.1.b, A.2.b, B.1.b, B.2.b**): Corresponding fast Fourier transforms (FFT) and the measured D-bandings.

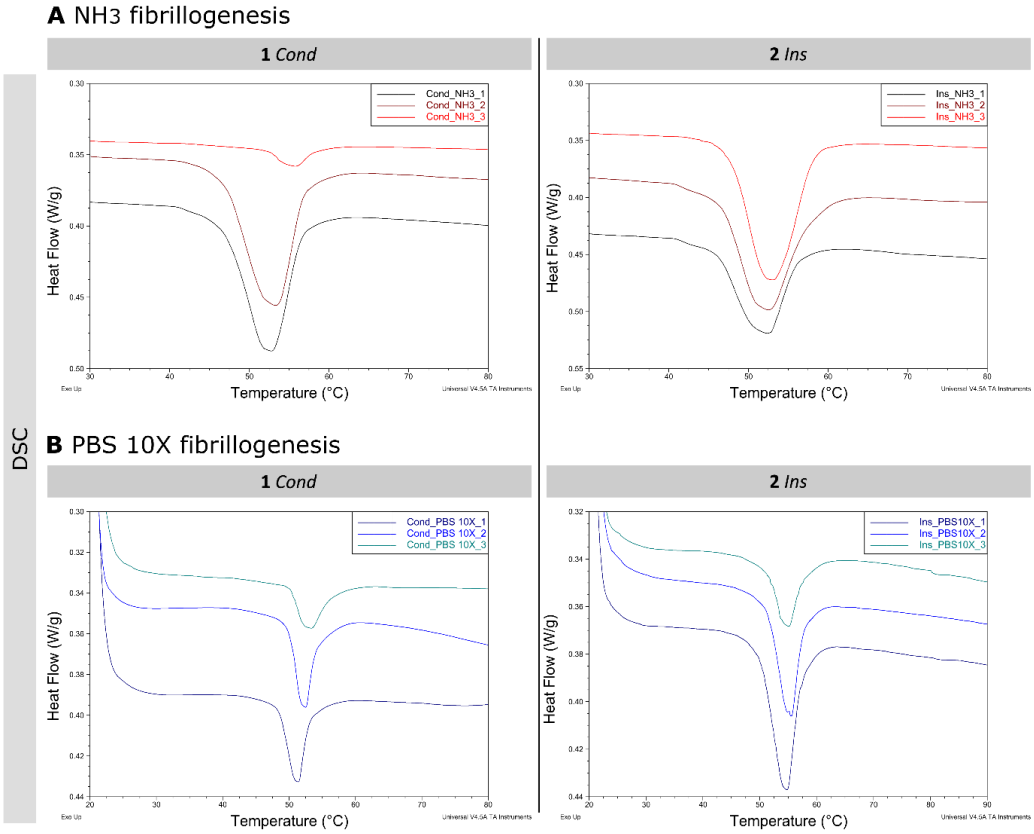

Figure S4. Detailed thermograms of the denaturation temperature measurements for each scaffold. Samples were heated from 20 to 120°C at a rate of 5°C.min^{-1})

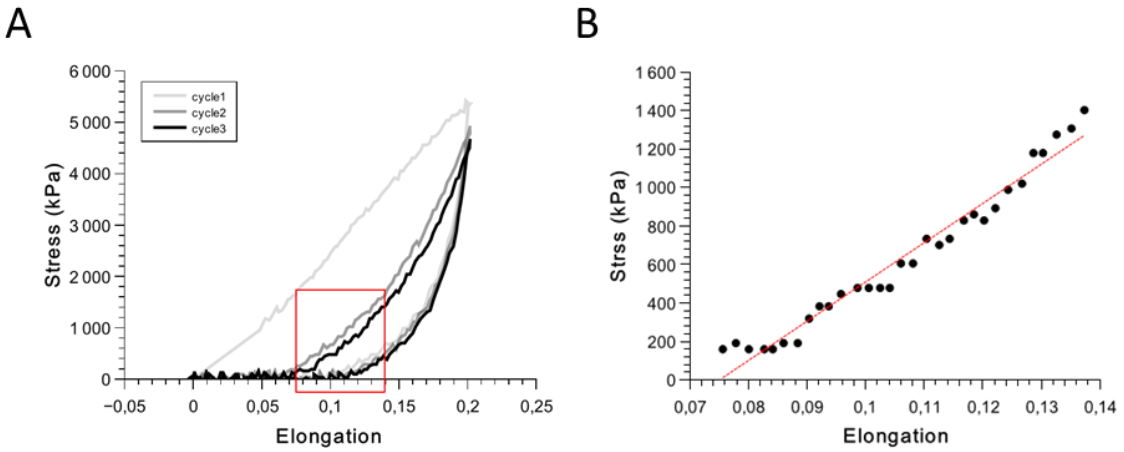

Figure S5. (**A**) Representative stress/strain curves for traction cycles. Each cycle is color-coded with Cycle 1 shown in light grey, Cycle 2 in grey, and Cycle 3 in black. (**B**) Illustration of stress-strain fitting for the linear region of the third cycle.

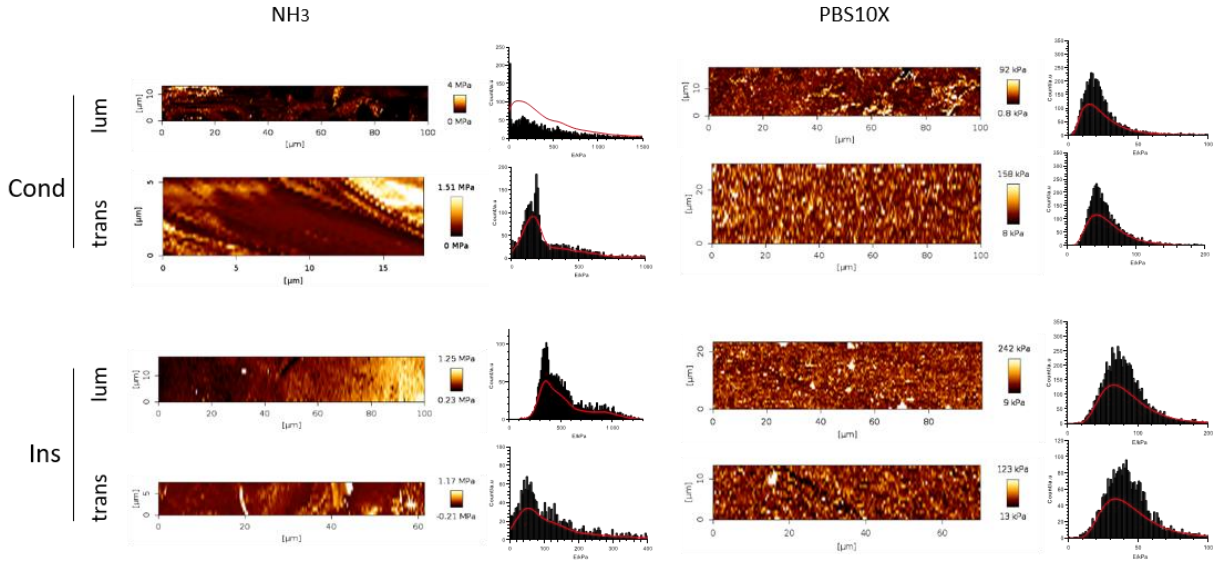

Figure S6. Typical Young's modulus maps extracted from AFM measurements and their corresponding statistical distributions. The distributions are smoothed using the kernel density estimation method (in red).

4. Additional results

A. Scaling the ice templating technique to a broader range of biomaterials

The materials fabricated above by means of ice templating followed by topotactic fibrillogenesis were designed to reproduce tubular tissues, which vary in size and thickness throughout the human body. In our study, the initial materials matched the dimensions of medium-sized arteries, with internal and external diameters of respectively 5 mm and 8 mm. However, in the context of tubular tissue grafts, the transposition of the technique to different dimensions could address a wider range of pathologies. Trachea has an inner diameter of 16 mm with a thickness of 1.5 mm[42]. Arteries vary strongly in size according to the anatomic zone; small arteries possess an outer diameter of ca. 5 mm with a thickness of 1.5 mm[43] while aorta, the largest artery, has dimensions comparable to those of the trachea[44]. This approach includes not only other tubular organs (trachea, esophagus, gastrointestinal and urinary tract), but also extends to two-dimensional tissues such as skin for which new *in vitro* platforms or skin grafts could be developed. The porosity could facilitate both the adhesion and migration of fibroblasts whereas a dedicated non-porous zone could favor the formation of the epidermis, within a type I collagen-rich matrix resembling native skin. This versatility in accommodating various dimensions and applications underscores the promising potential of our materials in addressing a broad spectrum of medical needs.

Here, we studied how ice-templating conditions, which define the microstructure, could be translated from our initial model to other sizes and geometries. Using the same technique, we adapted the molds to generate square flat materials, and tubular materials with an internal diameter of either 2 or 15 mm. These dimensions correspond to the dimensions of small-diameter arteries, the aorta, and the trachea, with all samples displaying a thickness of 1.5 mm (**Fig.9-A**). Two sets of mold materials were compared, with different thermal conductivity properties. The first set, named earlier *Cond*, combined aluminum and ABS to generate a high thermal conductivity difference between the outer and inner molds. The second set, referred as *LC*, used brass and aluminum to yield low conductivity difference between the outer and inner molds (**Fig.9-A**). Following ice templating in liquid nitrogen at 10 $mm.min^{-1}$, the outer mold is removed and materials were freeze-dried for 24 h. Longitudinal section were imaged under scanning electron microscope and porosity is analyzed using ImageJ (see methodology in **Appendix C-Fig.S2**). Orientation analysis was performed on pores that are perpendicular to the cross-section plane where pores and walls are clearly distinct. Analysis were done using a local window of 12 pixels, a gaussian distribution, and the histogram of the orientation was built with pixels of at least 2%-normalized energy.

Using *Cond* molds, the various geometries resulted in pores of equivalent median Feret and minimum Feret diameters, with values of respectively 14.49 ± 59.31, 14.78 ± 138.42, and 16 ±

90.21 µm for tubular materials of 2- and 15-mm internal diameter and the flat sample (**Fig.9-B,D,E** and **Table 6**). Only the smallest geometry presents an interface, surely a transition between nuclei to ice growth, whereas the others display a monodomain composed of lamellar ice crystals. In *LC* materials, the small tubular material and the flat material are alike, characterized by comparable median Feret diameters (17.58 ± 45.99 µm and 18 ± 120.36 µm, respectively), interface position, and main orientation angle (**Fig.9-C, D, E** and **Table 3**). In this set of conditions, ice crystals adopt an axial orientation of 6.5 and -3.5° for small tubular and flat geometries, respectively. However, an exception is made for the tubular material with a 15 mm-diameter, for which the microstructure is not symmetric to other geometries. The interface is not centered but rather close to the luminal surface, and longer pores are measured, with a median Feret diameter of 53.03 ± 114.08 µm. Additionally, these pores have a more longitudinal orientation of 50.5°. The displacement of the interface, as well as the longer pores and their longitudinal orientation, indicate a variation in the imposed thermal gradient that can only result from the change in mold size. This requires more experiments to confirm this singular observation.

This dataset shows that, for most part, the microstructure resulting from the freezing conditions (freezing bath temperature, dipping speed, mold conductivity, and solution properties) can be scaled up.

Table 3. Dimensions of the scaffold pores for longitudinal sections of various samples, after ice-templating and freeze-drying.

		Freezing conditions	
Dimension	Measurement	High conductivity delta (*Cond*)	Low conductivity delta (*LC*)
Tubular, $\varnothing_i$ = 2 mm	Median Feret / µm	25.95 ± 59.31	17.58 ± 45.99
	Median MinFeret / µm	14.49 ± 20.78	9.76 ± 18.38
	Main orientations / °	50.5	-27.5, -7.5, 11.5
Tubular, $\varnothing_i$ = 15 mm	Median Feret / µm	14.78 ± 138.42	53.03 ± 114.08
	Median MinFeret / µm	6.79 ± 25.22	22.48 ± 20.10
	Main orientations / °	6.5	-27.5, -12.5, 4.5
Flat	Median Feret / µm	16 ± 90.21	18 ± 120.36
	Median MinFeret / µm	8 ± 16.17	7 ± 17.04
	Main orientations / °	-3.5	6.5

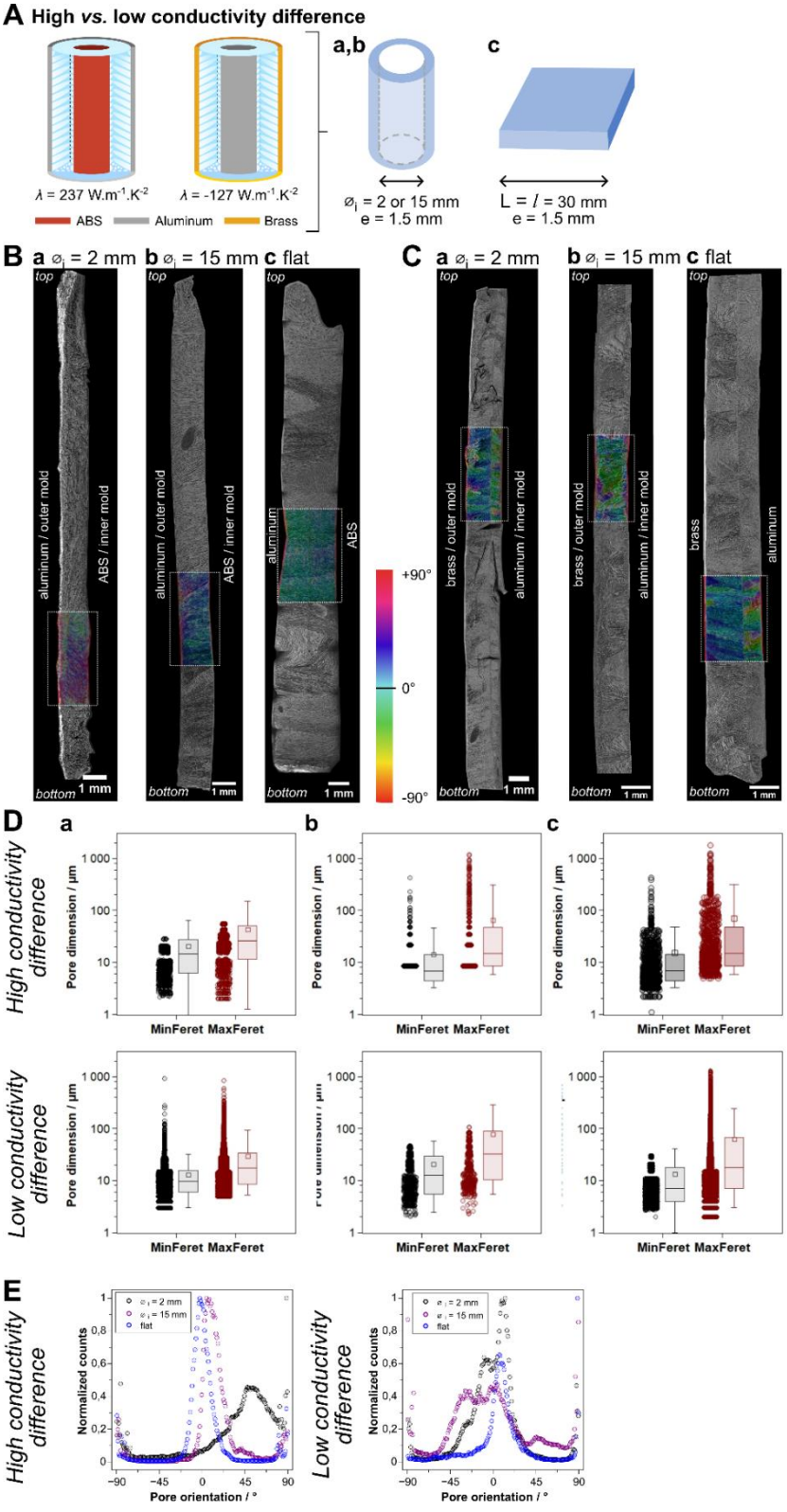

Figure 9. Textural properties of collagen scaffolds obtained with pairs of materials differing in their thermal conductive properties and fabricated in various dimensions. **A**) Scaffolds fabricated using a high or low conductivity difference (*Cond*, outer aluminum conductive mold and an inner ABS

insulating mold, or *LC*, outer brass mold and inner aluminum mold) in various geometry and size ((**a,b**) tubular, internal diameter of 2 or 15 mm or (**c**) flat). **B**) Longitudinal sections of *Cond* scaffolds imaged by SEM. Analysis of the pore orientation is defined by a dotted line, with indication of angle orientation based on color-coded map. Several dimensions were investigated, including tubular materials with an inner diameter of 2 mm (**a**) and 15 mm (**b**), and flat materials. **C**) Longitudinal sections of *LC* imaged by SEM. Analysis of the pore orientation is defined by a dotted line, with indication of angle orientation based on color code mapping. Several dimensions were investigated, including tubular materials with an inner diameter of $\varnothing_i$ = 2 mm (**a**) and 15 mm (**b**), and flat materials. **D**) Analysis of MinFeret and MaxFeret diameters of the pores in the zone delimited by the dotted line for each scaffold and dimensions (tubular, (**a**) $\varnothing_i$ = 2 mm and (**b**) 15 mm, and (**c**) flat).

B. In the beginning, they were four... A larger family of "tunable biomimetic materials elaborated by ice templating and self-assembly of collagen for tubular tissue engineering"

The materials described in the manuscript submitted to Biomaterials Science were selected from an initial larger family of materials, with a wider array of freezing conditions (**Fig.10**). Two other combinations of mold materials were studied, including medium thermal conductivity difference referred as *MC* ($\Delta\lambda$ = 110 $W.m^{-1}.K^{-1}$), and of negative thermal conductivity difference referred to as *NC* ($\Delta\lambda$ = -127 $W.m^{-1}.K^{-1}$). *MC* are constituted by brass and ABS for the outer and inner molds, respectively, while for *NC* an aluminum counterpart replaced the inner ABS mold. In this section, we detail the textural properties of *MC* and *NC*, both before and after NH_3 or PBS fibrillogenesis, and the few mechanical and biological properties that we evaluated. Based on these findings, we discuss the rationale behind selecting *Cond* and *Ins* for the complete study of tubular collagenous matrices.

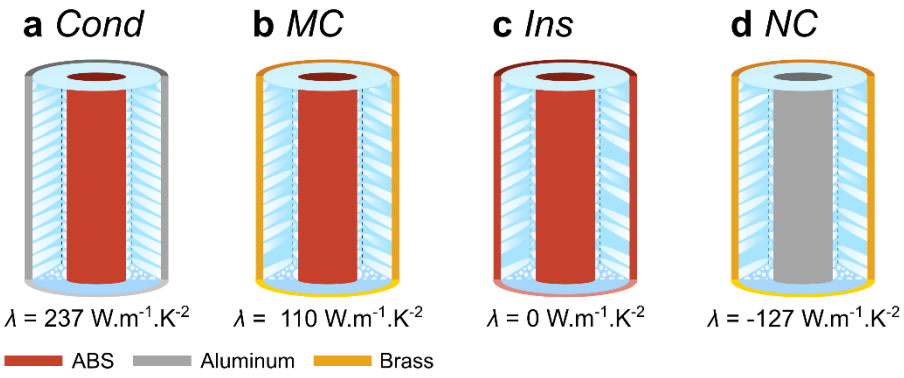

Figure 10. Elaboration of collagen samples with various porous structures, resulting from ice-templating in different combinations of molds and their thermal conductivities. Conductive properties are abbreviated as follows: *Cond* for conductive, *MC* for medium conductivity, *Ins* for insulating, and *NC* for negative conductivity (the inner mold being more conductive than the outer one).

After freeze-drying, *MC* exhibits larger pores compared to *NC*, with a median Feret diameter of 80.94 ± 134.86 µm compared to 62.76 ± 41.29 µm in transversal sections (**Fig.11** and **12-A,B**, and **Table 4**). Similar to *Cond* and *Ins*, the pore diameter is reduced during fibrillogenesis due to the swelling of the collagen walls. Using PBS, the diameter is reduced by 82% for both *MC* and *NC*, with median Feret diameters of 14.27 ± 21.37 µm and 11.48 ± 18.71 µm, respectively. Using ammonia, an equivalent pore reduction of 81% was observed for *MC*, with a median Feret diameter of 15.71 ± 22.89 µm. For *NC*, pores in the transversal section could not be visualized under the confocal microscope. Despite using the same conditions—fabrication parameters, thickness of the section, fluorophore concentration, and microscope settings—obtaining clear images was not possible. We attempted transparization protocols using urea-based amino-sugar mixture, termed UbasM[45], but we did not succeed to improve the observation. This was one of the reasons for excluding this sample from the complete study. In particular, neither the investigation of the cellular migration by confocal imaging or the correlation between porosity and mechanical properties would have been possible. We hypothesized that the diffusion of the matrix, coupled to autofluorescence of collagen combined to a very small pore size, may have hindered imaging due insufficient resolution and excessive signal intensity. Decreasing the thickness of the section below 200 µm may have offered a solution, but collagen samples are too fragile to be cut to such thickness by the vibratome technique. Cryosectioning, carried-out by a Dr. N. Dard, a collaborator at the Hypoxia & Lung laboratory (*Université Sorbonne Paris Nord*, Bobigny), revealed that the sample is in fact, porous (**Fig.13-B.b**). For practical reasons, we chose to keep that technique for assessment of cell colonization ability, rather than for structural analysis.

All external surfaces are porous (**Fig.11-C.e** and **f**). Particularly in *MC*, pores significantly cover the surface, with a coverage of 53% for NH_3 and 18% for PBS fibrillogenesis, in contrast to 11% and 10% in *NC*. Most importantly, choices of *Cond* and *Ins* were directed by the high pore size and coverage of the luminal surfaces for *MC* and *NC* (**Fig.11-C.c** and **d**). For NH_3-fibrillated samples, *MC* and *NC* exhibit pores with a median Feret diameter of 27.61 ± 19.52 µm and 11.60 ± 42.43 µm, covering 43% and 12% of the surface, respectively. Surprisingly, in PBS these values were also high. We measured a pore fraction of 20% with a median pore size of 7.36 ± 12.91 µm in *MC*, and 38.7% of the surface was covered by pores of 6.75 ± 25.99 µm median Feret diameter in *NC*. We can infer this high pore coverage to the use of an inner conductive material, which triggers the nucleation of ice and results in a large number of small, isotropic pores on the luminal surface.

The local arrangement of collagen fibrils within the four samples was evaluated by imaging ultrathin sections under TEM. At the suprafibrillar level, dense networks of packed nanofibrils are visible in all samples. Pores are found across the samples, devoid of any specific collagen motifs (**Fig.13-A,B.a**). Interestingly, we observed that the self-assembly of

larger cross-striated fibrils seems facilitated at the periphery of the pores, where an increasing number of fibrils was formed (**Fig.13-A,B.a**, transversal sections).

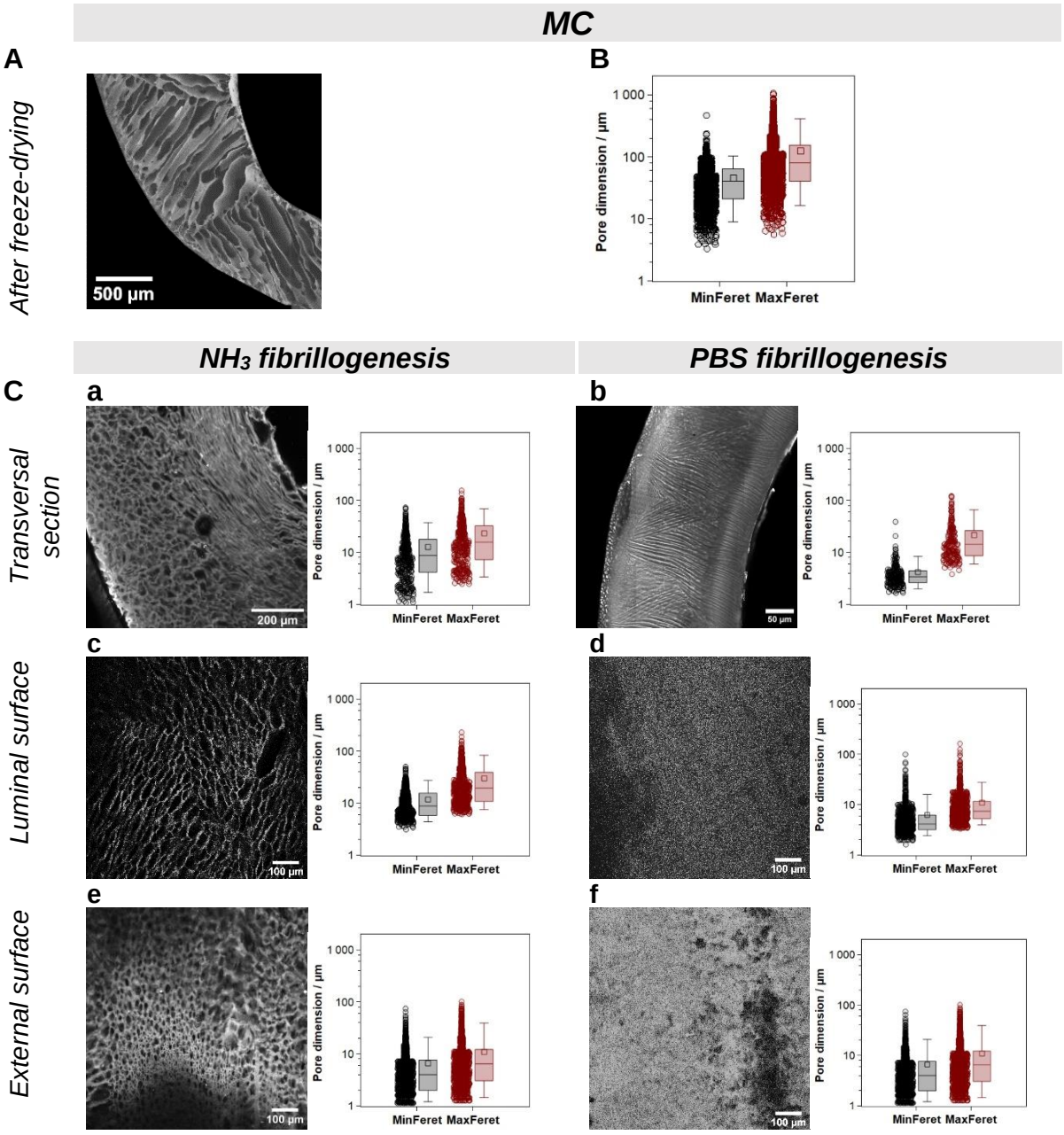

Figure 11. Textural properties of collagen scaffolds obtained with a pair of materials differing in their conductive properties, composed of an outer mold of brass and an inner mold of ABS (λ= 110 $W.m^{-1}.K^{-1}$). **A)** SEM image of a transversal section of the sample, after freeze-drying. **B)** Pore dimensions in the transversal section of the scaffold after freeze-drying. Variations of the pore dimensions after fibrillogenesis were investigated for transversal sections, luminal and external surfaces, using ammonia (**C-a, c and e**) or PBS (**C-b, d, and f**).

Re-dilution of the walls during fibrillogenesis gives greater mobility to collagen molecules and pre-fibrils, resulting in the formation of larger supramolecular structures. These comprise an increased number of repeated units, evidenced by the typical D-banding pattern. Throughout the samples, structural heterogeneities are observed, in particular in *NC* (**Fig.13-B.a**). The latter is composed of randomly oriented cross-striated fibrils that coexist with tightly packed networks of nanofibrils. This observation demonstrates local variations of the concentration. Looser regions may correspond to the borders of swelled walls, which recover the initial concentration of 40 mg.mL^{-1}, while denser regions correspond to segregated collagen walls, with a concentration close to the *critical concentration* calculated in Chapter 2.

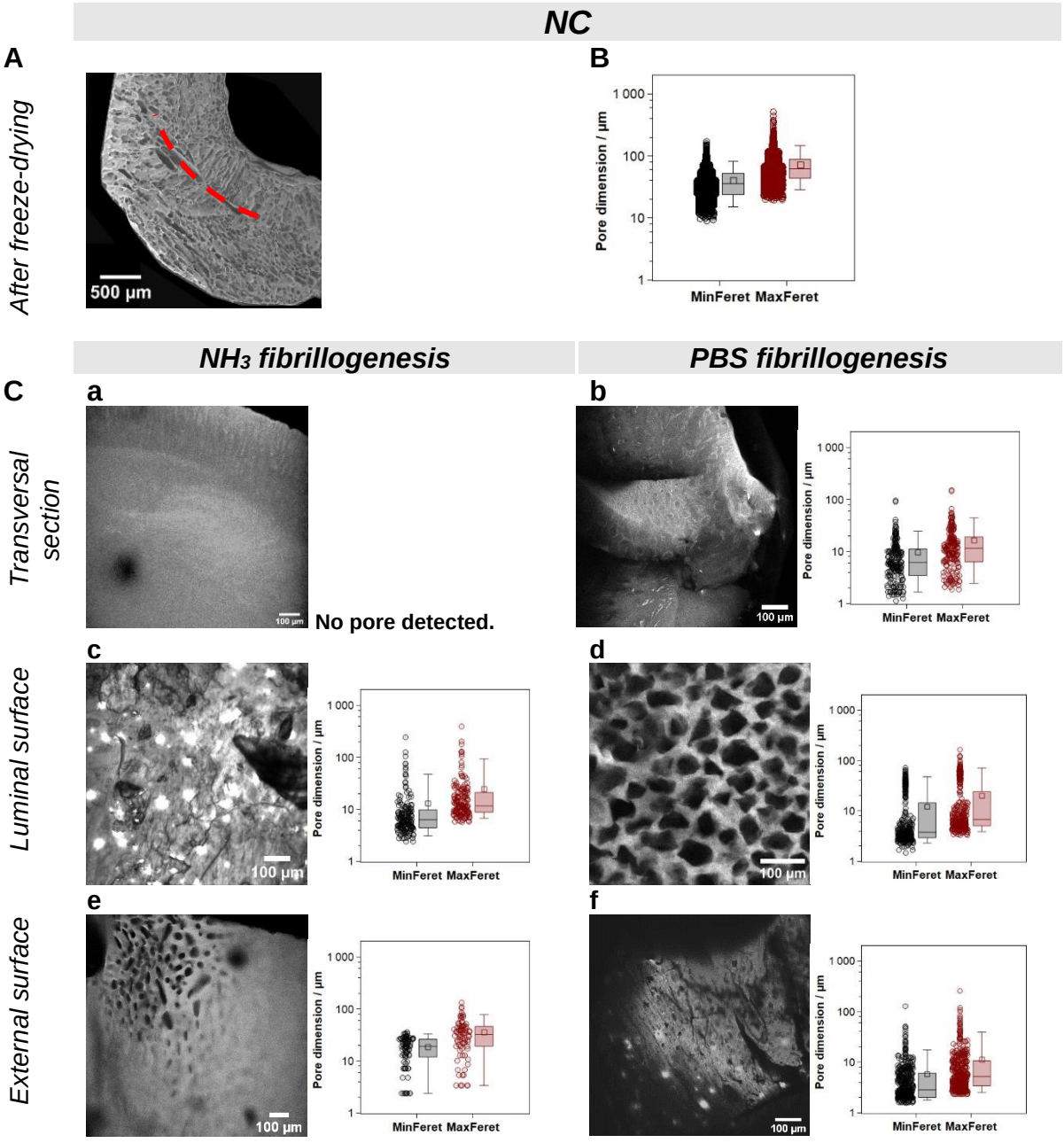

Figure 12. Textural properties of collagen scaffolds obtained with a pair of materials differing in their conductive properties, composed of an outer mold of brass and an inner mold of aluminum (λ= -127 $W.m^{-1}.K^{-1}$). **A**) SEM image of a transversal section of the sample, after freeze-drying. **B**) Pore dimensions in the transversal section of the scaffold after freeze-drying. Variations of the pore dimensions after fibrillogenesis were investigated by confocal microscopy for transversal sections, luminal and external surfaces, using ammonia (**C-a, c and e**) or PBS (**C-b, d, and f**).

Table 4. Dimensions of the scaffold pores for various sections and surfaces, after ice-templating and topotactic fibrillogenesis. When available, values are given with the associated standard deviation.

		Freezing conditions			
Cross-sections	Measurement	*MC*		*NC*	
Transversal	Median Feret / µm	80.94 ± 134.86		62.76 ± 41.29	
	Median MinFeret / µm	40.55 ± 32.94		35.25 ± 21.81	
Fibrillogenesis conditions		NH_3	PBS	NH_3	PBS
Transversal	Median Feret / µm	15.71 ± 22.89	14.27 ± 21.37	N/A	11.48 ± 18.71
	Median MinFeret / µm	8.66 ± 12.32	3.37 ± 3.41	N/A	5.8 ± 6.60
Luminal surface	Median Feret / µm	27.61 ± 19.52	7.36 ± 12.91	11.60 ± 42.43	6.75 ± 25.99
	Median MinFeret / µm	7.66 ± 8.76	4.39 ± 6.06	6.31 ± 25.65	3.73 ± 15.58
	Pore fraction / %	43	20	12	38.7
External surface	Median Feret / µm	16.89 ± 12.65	13.45 ± 6.42	32.24 ± 25.28	5.18 ± 19.77
	Median MinFeret / µm	9.52 ± 7.46	7.66 ± 3.98	19.05 ± 9.31	2.82 ± 9.28
	Pore fraction / %	53	18	11	10

In a few regions of the samples we found particles that may result from parallel reactions between the aluminum or brass molds and HCl in the collagen solution, or in contact with ammonia vapors during fibrillogenesis (**Fig.13-B.a**, outlined by white dotted circles). Although we did not conduct specific analysis to clarify the nature of these particles, there is a strong possibility that the side reactions conduct to the formation of $CuO_{(s)}$, $Cu(OH)_{2(s)}$ or $Zn(OH)_{2(s)}$ in presence of ammonia, whereas PBS (which composition contains 81 mM Na_2HPO_4 and 15 mM NaH_2PO_4) could lead to the formation of metal phosphates. Copper is a

trace element in the body, critical for the function of many enzymes, in both its oxidation states (Cu^{I} and Cu^{II})[46]. It acts as a cofactor in redox reactions of enzymes, mitochondrial respiration, iron absorption and elastin cross-linking. The concentration of copper in human blood plasma is evaluated between 10^{-18} and 10^{-13} M. An excess of copper ions leads to unbalanced copper homeostasis that triggers cellular cascades, resulting in the formation of reactive oxygen species (ROS) and potential cellular damage. Aluminum level in normal individuals is estimated at 10 $\mu g.L^{-1}$, [47], and increased levels exceeding 200 $ug.L^{-1}$ are associated with poisoning. Given its widespread presence in daily life (hygiene products, medications food, pollution, etc), we are already exposed to large amounts of aluminum which poses a risk factor for several pathologies, in particular to bones[48,49]. Whatever the nature of these particles, their presence hinders the use of the resulting materials in the context of vascular grafts.

In summary, the TEM observations reveal the similar of the fibrillar networks in the collagen walls, resulting from the four elaboration conditions. It confirms the reliability of the PBS process in formulating fibrillar networks akin to those resulting from NH_3 fibrillogenesis, despite the important swelling of the walls observed in confocal microscopy images. TEM also revealed the presence of potentially toxic components, reinforcing our decision to pursue with *Cond* and *Ins* conditions for the fabrication of our collagenous biomaterials.

Mesenchymal stem cells (MSCs) were seeded on the adventitial surface of the materials, and their colonization was observed by day 2 (**Fig.13-A,B.b**). At the end of the culture, the MSCs had already started to migrate through the porous structure of the samples. The migration extended over distances up to 930 µm, 780 µm, and 560 µm, for *MC*-PBS, *NC*-NH_3, and *NC*-PBS, respectively. These results highlight the key role of the controlled porosity induced by ice-templating, which triggers the colonization of samples by MSCs. We noted that the topotactic fibrillogenesis of these samples seems to smoothen the luminal surface, more than for *Cond* and *Ins*. This textural difference could be advantageously used to direct different cellular migration kinetics in the samples. Unfortunately, these were not investigated, and the preliminary tests for endothelialization were performed only with matrices fibrillated by ammonia.

A	MC	
	NH_3	PBS
a	Not imaged	*Longitudinal* 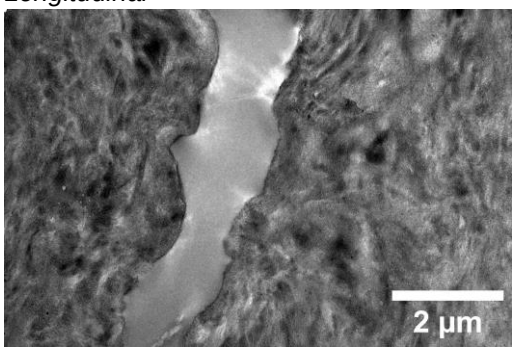
TEM		*Transversal* 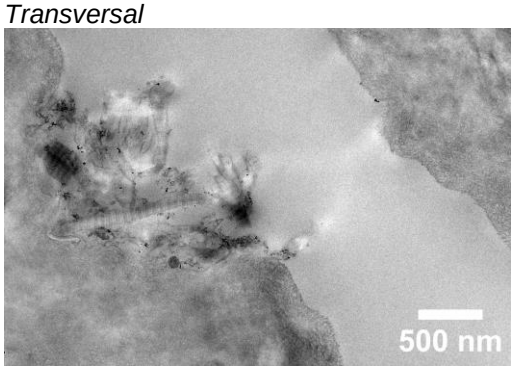
b	Not cellularized	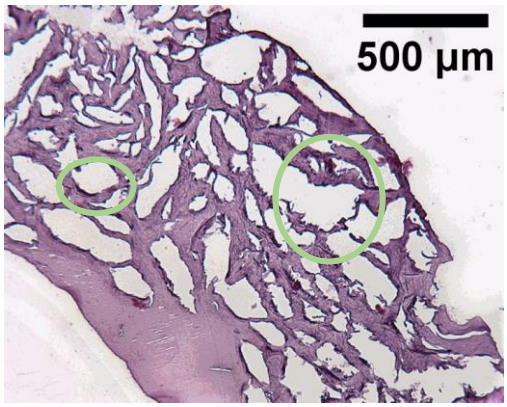
MSCs – day 2[§§]		

§§ Cell culture of MSCs, cryosections and image acquisition were performed by N. Dard (Hypoxia & Lung laboratory, Université Sorbonne Paris Nord, Bobigny).

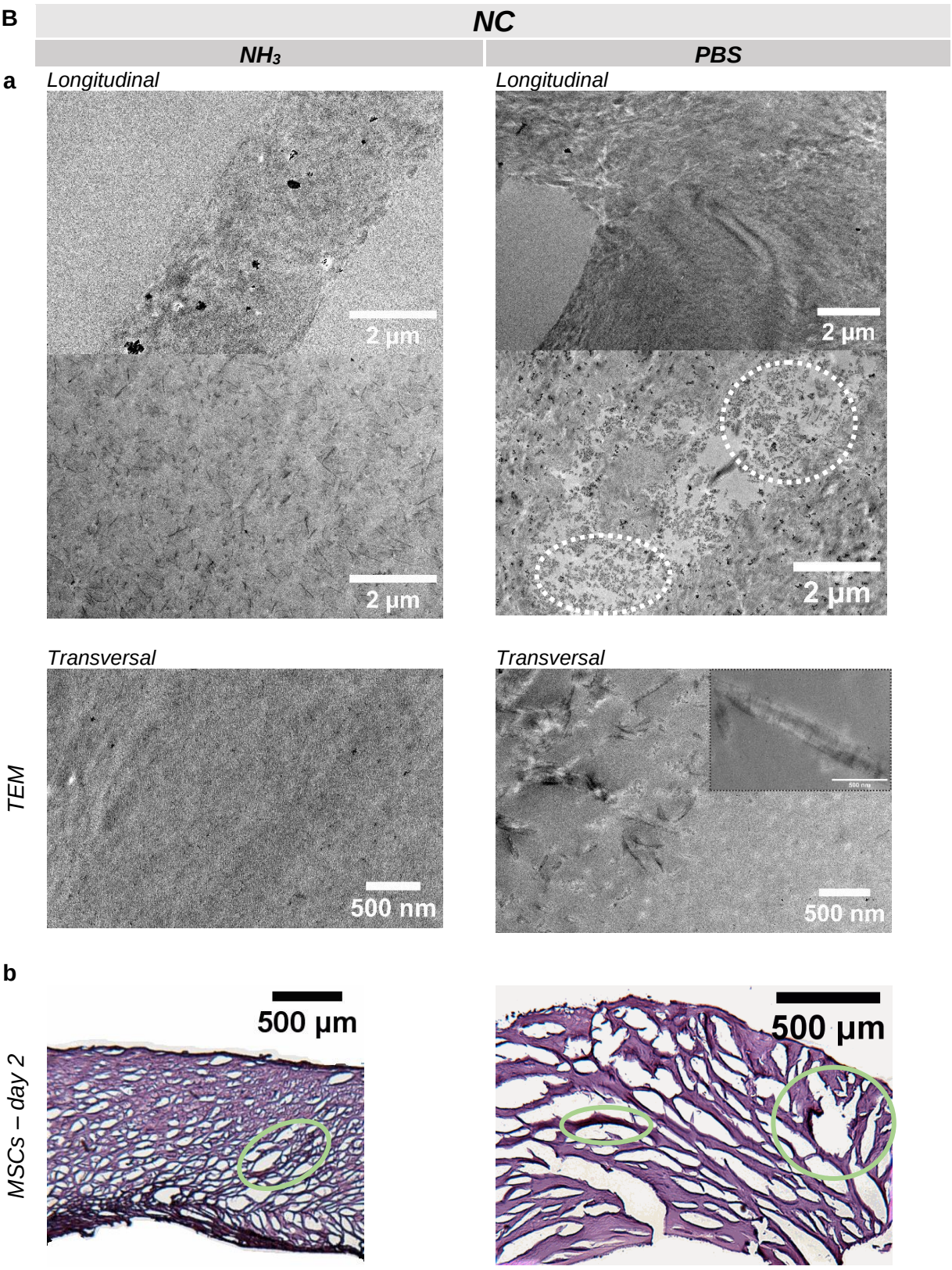
B
NC
NH3
PBS
a
Longitudinal
Longitudinal
2 µm
2 µm
2 µm
2 µm
Transversal
Transversal
TEM
500 nm
500 nm
b
500 µm
500 µm
MSCs – day 2

Figure 13. Properties of various collagen samples, fabricated in molds of different conductivity differences (*MC* (**A**) and *NC* (**B**)) followed by ammonia or PBS fibrillogenesis. **a**) Transmission electron micrographs of longitudinal and transversal cross-sections of the materials. **b**) Mesenchymal stem cells were cultured on the outer surface of samples for 2 days. Their ability to colonize the samples was assessed by light microscope of cryosections, stained with hematoxylin (nucleus) and eosin (cytosol) dyes. Green circles show cells migrating in the samples.

Preliminary endothelialization tests were conducted by seeding HUVECs cells on the luminal surface of *MC* and *NC* materials, fibrillated solely with ammonia. After 3 days, a tight layer of cells covers the surface of *MC*, similar to an epithelium (**Fig.14-A**). In contrast, on *NC* substrate, cells adhered and proliferated less (**Fig.14-B**). These results were compared to a substrate coated with fibronectin (Fn) that mimics the basal membrane (**Fig.14-C**). Similar to the non-coated *MC* material, the Fn coating promoted the development of an endothelium-like layer. As in chapter 3, this underscores that the high concentration reached by ice templating foster the adhesion and proliferation of cells, by providing a native-like environment. In this sense, a coating may not be needed. This assertion may be nuanced by tests in flow conditions or using plasma where the presence of Fn could provide a supplementary advantage. Moreover, the coating strategy could reduce thrombogenicity by limiting the direct contact between blood and collagen—thrombogenic—for future application as vascular grafts.

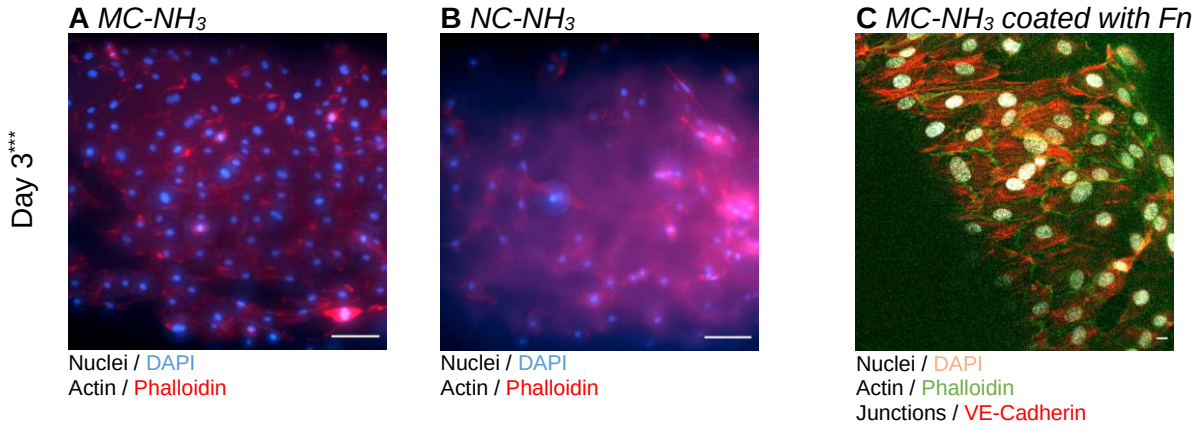

Figure 14. First study of the epithelium formation with luminal seeding of HUVECs up to 3 days, observed under confocal microscopy. Seeded materials were fibrillated in ammonia, and ice templating in *MC* (**A**) or *NC* (**B**) molds. A coating of Fn was studied as a control on *MC* material (**C**).

*** Cell culture of HUVECs and image acquisition were performed by A. Castagnino (*Laboratoire d'Hydrodynamique de l'X (LadHyX)*, Ecole Polytechnique, Palaiseau).

Immunostaining of the nuclei (DAPI), actin (phalloidin) and with Fn, junctions (VE-cadherin). (**A,B**) Scale bar = 100 µm (**C**) Scale bar = 10 µm.

C. Permeability of the interface in fibrillated scaffolds

The formation of an interface at a certain position during the solidification process is a tunable feature in tubular materials, and more generally for any geometry during freezing processes. By playing on the temperature and the dipping speed, we have shown that various structures can be obtained, either single-layered or dual-layered. However, the implications of that interface over the mechanical properties and in the cellular migration remain unknown. These may be of particular importance to create a barrier between the *outer muscular* and the *inner endothelial* layers discussed in **Chapter 1**, and avoid the migration of endothelial cells into the collagen wall (**Fig.15-A**). By mimicking the function of the basal membrane, this interface could play a major role in the endothelialization process by ensuring the compartmentalization of cells. Additionally, the presence of an interface acts as a mechanical reinforcement element in the collagen wall. The existence of a thicker layer in the wall combined to the pores' axial orientation responsible for its formation is expected to provide more resistance to the materials. We describe here a permeability assay of tubular collagenous materials, using microparticles of relevant diameter. Based on the diffusion of these labelled particles and in conjunction with intensity quantification, permeability data for collagen samples were determined. We discuss the relationships between the experimental results of the diffusion and the porous structure imposed by ice templating and the topotactic fibrillogenesis method. The kinetics of fibrillogenesis, either in ammonia vapor or phosphate buffer solution, lead to different preservation of the porous structure. PBS results in smaller pores and less concentrated collagen walls, while NH_3 maintain the porous network. Using *Cond* molds described above, we compared the ability of microparticles to diffuse through samples fibrillated by ammonia or PBS.

Effect of the fibrillogenesis route on permeability

Transversal thick sections of the samples were cut (*ca.* 400 µm-thick) using a Vibratome, and sealed on a glass slide using silicon grease. The external part of the samples was in contact with a PBS solution to avoid dehydration. Microparticles with a diameter of 3.6 µm were dispersed in DI water, at a concentration of 4%vol, and injected via a needle in the lumen under a widefield stereomicroscope. Diffusion of the particles was recorded over time (**Fig.23-B to E**). The acquired time-lapse movies show the evolution of the fluorescence signal throughout the samples that was subsequently analyzed using ImageJ. Intensity was

normalized in % by the maximum fluorescence intensity values over time, defined as the normalized fluorescent intensity (NFI). Two different measurements were conducted. *i)* The median NFI for the whole sample wall shortly after injection, at 2.8 minutes of diffusion (**Fig.15-F.a**), and *ii)* the evolution of the NFI, measured every 3300 ms, at a given distance to the luminal surface (100 µm) (**Fig.15-F.b**).

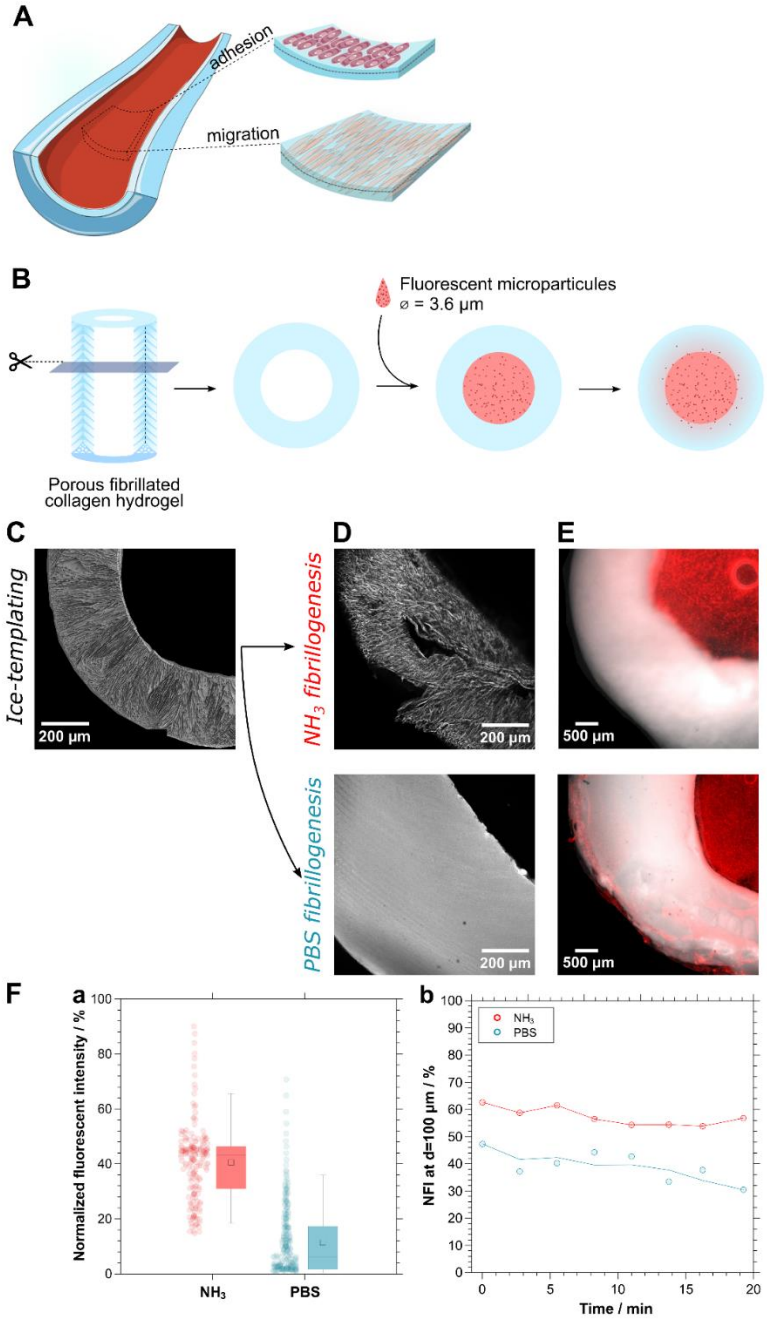

Figure 15. **A**) Simplified dual layer model for tubular tissue engineering, showing the different cellular behaviors and cell types populating the layers. **B**) Experiment design to evaluate the permeability of the collagen materials. **C**) Structure of the freeze-dried *Cond* scaffold, imaged by SEM in transverse

section. **D**) Porous structure of the material after fibrillogenesis by NH_3 or PBS, imaged by confocal in transverse section. **E**) Fluorescent microparticles were infused into the samples' lumen. Diffusion over time is quantified by fluorescence intensity under a macroscope (time-lapse imaging), as an indicator of the permeability to the microparticles. **F**)(**a**) Normalized fluorescence intensity distribution (NFI) measured in the samples wall at t=2,8 min. (**b**) NFI at a distance of 100 µm from the lumen for each sample over time. Lines represent the moving average.

At t=2.8 min, the median NFI is 7x higher for samples fibrillated in NH_3 than for samples fibrillated in PBS, with values of 43.12 ± 14.09 % and 6.05 ± 13.10 % (**Fig.15-F.a**). This result is in good agreement with the porous structure of the materials (submitted paper – section 2.3) that revealed significant differences between *Cond*-NH_3 and *Cond*-PBS (**Fig.16-C**). The porosity is, for all measurements, higher in NH_3. Pore median Feret diameter is 16.12 ± 1.17 µm and 10.41 ± 2.49 µm in transverse and luminal sections, respectively, while for PBS no pore was detected in transverse. At the luminal surface, pores have a median Feret diameter of 5.18 ± 0.26 and cover less than 1%, compared to 53% using ammonia. The structural differences correlate directly with the median NFI measured for each sample.

Overtime, the NFI measured at 100 µm from the lumen remains stable for NH_3, which suggests a longer and continuous diffusion of the particles through the sample thickness. The diffusion profile of particles in *Cond*-PBS, however shows that intensity slightly decreases overtime, with an initial intensity of 47% that decreases down to 30% at t=19.2min. Based on the luminal porosity, we did not expect particles to penetrate the wall. We can infer that they may be able to diffuse through pores that are undetectable under the confocal microscope, due to a tight network and the auto-fluorescence of collagen. The reduction of the fluorescence signal overtime could correspond to a concentrated wave of particles that diffuses through the sample thickness resembling of a coffee stain effect (although no evaporation is expected in the current setup).

Table 5. Relationships between the luminal permeable properties and the dimensions of the scaffold pores in transversal sections of collagen samples, depending on the fibrillogenesis route. Samples were fibrillated with either ammonia (***Cond*-NH_3**) or 10x-phosphate buffer solution (***Cond*-PBS**). Both were ice templated in molds with a high thermal conductivity difference (***Cond***). Diffusion of 3.6 µm particles was followed through time under a confocal microscope, and quantified using ImageJ.

		Fibrillogenesis conditions	
Characteristics	Measurement	Ammonia (*Cond*-NH_3)	10x PBS (*Cond*-PBS)
Structural	Transversal median Feret / µm	16.12 ± 1.17	N/A
	Luminal median Feret / µm	10.41 ± 2.49	5.18 ± 0.26
	Luminal pore fraction / %	53	<1
Permeability	Maximum distance to the lumen / µm	234	156

Effect of the freezing boundary conditions on permeability

Besides the influence of the fibrillogenesis pathway on the permeable properties, we studied the impact of distinct freezing boundary conditions, and respective porous structures, on permeability. The analysis was conducted using the same experimental conditions described above, for samples prepared using the PBS fibrillogenesis route. The combinations of materials were previously described, and include *Cond* (237 $W.m^{-1}.K^{-1}$, aluminum (outer) and ABS (inner)), *MC* (110 $W.m^{-1}.K^{-1}$, brass-ABS), *Ins* (0 $W.m^{-1}.K^{-1}$, ABS-ABS), and *NC* (-127 $W.m^{-1}.K^{-1}$, brass-ABS) (**Fig.10**).

Cond sample provides the most impermeable luminal surface of the studied samples (**Fig.16-A.a** and **Appendix C-S5-A,B.a**). At a distance of 100 µm from the lumen, the NFI decreases over time. The mean NFI measured at t=2.8 min represents the lower value of the set, with a value of 11.29±13.09 % (**Table 6**). This directly correlates to the poor accessibility of the inner wall, due to a luminal pore fraction inferior to 1%, together with the smallest luminal pores found across the samples. At a similar time point, *MC* exhibits a higher mean NFI of 16.39±20.67 %, due to a higher pore fraction of 20.5 %. Time-lapse movies also reveal a slow increase in the fluorescent intensity over time, until reaching a plateau of 64% NFI at 8 min. The maximum distance yielded by microparticles was measured at 212 µm, which could correspond to the shift in the pore morphology observed in the sample after fibrillogenesis (**Fig.16-B.b**). The limited transport of particles at that junction suggests that pores are not interconnected at the interface, which corresponds to an impermeable wall. Similar results were obtained for *Ins*, despite its low luminal pore fraction of 5%. The mean NFI of 24.53±11.13 %, and the increasing intensity over time, show that the porosity at the luminal surface seems responsible for the enhanced transport of fluorescent microparticles. This is confirmed by the results obtained for *NC*, the most permeable samples of all four, for which the difference with *MC* is its highest pore fraction of 38.7%. Particles diffuse immediately, and reach a mean NFI 1.5x time higher than *MC*, of 37.21±27.96 %.

Interestingly, the relationship between the mean NFI measured on the whole sample thickness seems to be directly controlled by the difference in thermal conductivity of the molds, illustrating the relevance of this simple parameter over the functional properties of the collagen tubes (**Fig.17**).

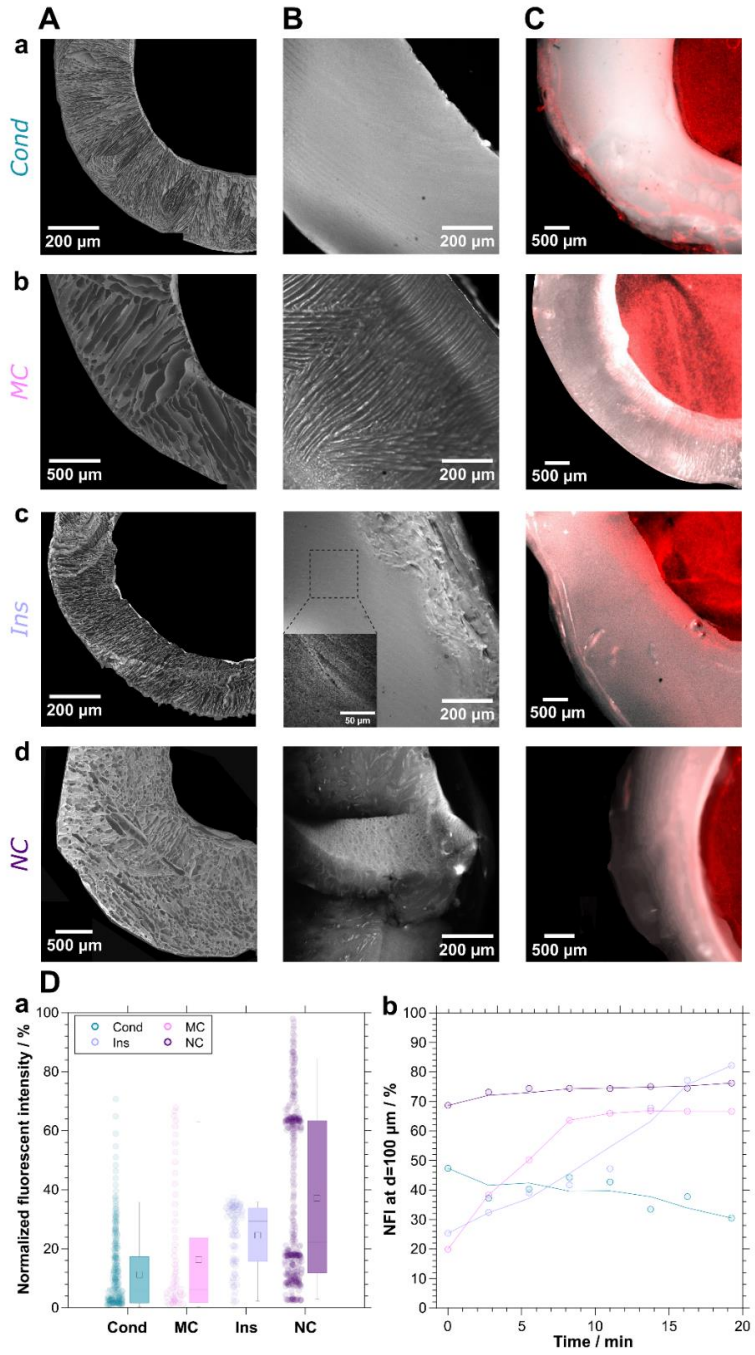

Figure 16. A) Textural properties in transversal sections of collagen scaffolds obtained with pairs of molds differing in their conductive properties, imaged by SEM after freeze-drying. **B**) Variations of the pore dimensions after fibrillogenesis were assessed by confocal microscopy on transversal sections. **C**) Fluorescent microparticles were infused into the samples' lumen. Diffusion over time is quantified by fluorescence intensity under a macroscope (time-lapse imaging), as an indicator of the permeability degree. Photos presented here were acquired at the end of the experiment, for t=19.2 min. **D**)(a) Normalized fluorescence intensity distribution (NFI) measured in the samples wall at t=2,8 min. (b) NFI at a distance of 100 µm from the lumen for each sample over time. Lines represent the moving average.

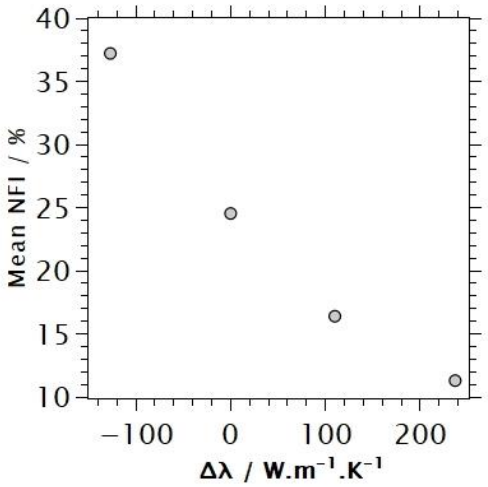

Figure 17. Relationship between the mean NFI at 2.8 mins and the difference of thermal conductivity of the inner and outer parts of the cylindrical molds for tubular samples fibrillated in PBS.

Table 6. Relationships between the luminal permeable properties and the dimensions of the scaffold pores in transversal sections of collagen samples, depending on the internal porous structure. Structural features result from the ice templating conditions, using mold pairs with different thermal conductivities. Following ice templating, all samples were fibrillated with 10x-PBS. Diffusion of 3.6 µm particles was followed through time under a confocal microscope, and quantified using ImageJ.

		Ice templating conditions			
Characteristics	Measurement	*Cond*	*MC*	*Ins*	*NC*
Thermal conductivity difference ($W.m^{-1}.K^{-1}$)	N/A	237	110	0	-127
Structural	Lumen-interface distance / µm	0	0	0	550
	Transversal median Feret / µm	10.83 ± 17.37	14.27 ± 21.37	3.78 ± 0.27	11.48 ± 18.71
	Luminal median Feret / µm	5.18 ± 0.26	7.36 ± 12.91	5.98 ± 0.60	6.75 ± 25.99
	Luminal pore fraction / %	<1	20.5	5	38.7
Permeability	Mean NFI at t = 2,8 min / %	11.29 ± 13.09	16.39 ± 20.67	24.53 ± 11.13	37.21 ± 27.96

Taken together, we present here a short study of the luminal permeability towards microparticles on collagenous materials, and underscore the possibility to tune it by

controlling the characteristics of the porous network. We found that the lower porosity yielded by PBS fibrillogenesis, in comparison to ammonia fibrillogenesis, advantageously increases the impermeability. Within the framework of PBS, we also demonstrated the influence of the freezing conditions on the diffusion rates of particles. An increased thermal conductivity difference in the molds equally increases the pore fraction of the lumen, which favors particle diffusion. Interfaces may serve as impermeable barriers in samples, a feature that requires further investigations.

We acknowledge the current limitations of our system. In this setting, the microparticles were not dissolved in a physiological fluid analogue—*i.e.* BSA or simulated body fluid—which might affect the permeability properties. Moreover, these trials were not optimized, and the bath limiting drying around the samples may be improved to avoid any variation of the dimensions of the tubes' section. Using larger microparticles, more extended duration, and permeability assessment under flow could also provide more accurate data.

5. Perspectives

The combination of ice templating and fibrillogenesis of collagen presented in this chapter leaves many doors open to optimization and for further studies. Our ice templating method offer precise control over the formation of axial to longitudinal pores, and over their respective dimensions. Additionally, we introduce bidirectional and multidirectional thermal gradients by manipulating the thermal conductivity of the molds, and adjusting the dipping speed in the freezing bath. We show that an interface can be generated between two ice fronts of opposite directions, and that this structure could provide an effective barrier to the transport of particles—and possibly of cells—inside the thickness of the tubular walls.

Some aspects could not be investigated in depth, due to time constraints and to the lengthy optimization steps required in the early stages of the study. One example is the limited exploration of achieving tangentially oriented pores, as found in arteries, to host smooth muscle cells (SMCs). *In vivo*, SMCs are distributed in the media with a spiral orientation, in planes perpendicular to the direction of the blood flow. Highly interconnected and circumferentially oriented pores may have been possible by a controlled rotation of the samples, while being immersed in liquid nitrogen. As a proof of concept, we manually rotated samples of collagen in *Ins* materials, at 10 µm.s^{-1}, as shown on SEM images (**Fig.18**) of the transversal mid-section.

Color-coded orientation map of the middle section of the sample displays regions shifting from green (-45°) to purple (+45°). It evidences the feasibility of the process to create

circumferential porous structures, but require further experiments to refine the control of the rotation and confirm these observations.

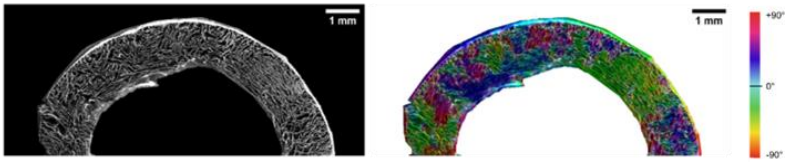

Figure 18. Assay to yield a porous circumferential structure in tubular collagen sample, by rotation during ice templating. Transversal mid-sections of the sample were observed by SEM. Orientation was analyzed by angle color-coded map with ImageJ.

Following ice templating, the topotactic fibrillogenesis conditions do not only provide further control over the porosity, but also triggers the self-assembly of collagen molecules into biomimetic fibrils. The resulting materials recapitulate the features of native tissues, by providing a porous network that promotes cell colonization in a local collagen-rich environment, and offers physiological mechanical properties. Nevertheless, both fibrillogenesis conditions raise challenges. The use of PBS reduces the porosity created during ice templating, impeding the migration of cells from the adventitia. In contrast, NH_3 preserves the porous network and promote cell migration. However, it also facilitates the migration of epithelial cells towards the tubes' walls, which may delay endothelialization of the lumen. Furthermore, materials fibrillated with PBS yield mechanical properties closer to native tissues. These distinct properties create a dilemma when selecting a material for future grafting applications. In other words, the ideal candidate would combine properties of both fibrillogenesis. With this idea in mind, we started to develop a novel approach termed "hybrid fibrillogenesis". It aims to harness the materials properties found with ammonia fibrillogenesis routes – pores on the adventitial surface and in the sample–and PBS–to smoothen the luminal surface and lower mechanical properties. Two protocols were elaborated, *simultaneous fibrillogenesis* and *successive fibrillogenesis*.

Simultaneous fibrillogenesis. We conceived this idea of using a permeable outer membrane, to expose the material to ammonia vapor while simultaneously insert PBS in the luminal space. In our initial trials, we used either dialysis membranes or expanded polytetrafluoroethylene (ePTFE). Briefly, a dense collagen solution (40 $mg.mL^{-1}$) was introduced in between two cylindrical molds, the external one being made of expanded polytetrafluoroethylene or a dialysis membrane, the internal one of ABS (**Fig.19**). After ice templating in liquid nitrogen, the internal mold is removed and 10x PBS is inserted inside the lumen space to induce the topotactic fibrillogenesis step at the luminal surface. Meanwhile, the material is placed in a chamber at -3°C under ammonia vapors for 48h to perform concomitantly a topotactic fibrillogenesis step on the outer surface of the tube. Ammonia is

further removed using distilled water vapors for 24h at 37°C in a heat chamber. The fibrillogenesis is then completed in a consolidation step, by keeping the sample in 5x PBS for 14 days at room temperature.

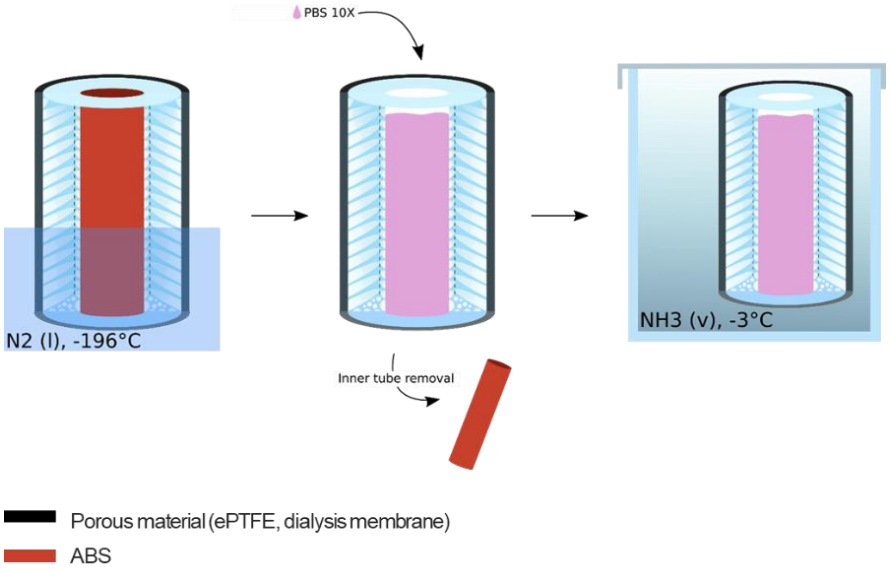

Figure 19. Description of the materials fabricated by hybrid simultaneous fibrillogenesis. After ice templating in a porous outer material and insulating inner mold, the inner tube was removed and replaced by 10x PBS. The sample was then exposed to ammonia vapors at -3°C.

Dialysis membranes are composed of capillary fibers arranged in a tight meshwork, selectivity permeable. It retains high molecular weight entities, eg. proteins, while permitting the passage of salts and molecules of low molecular weight. Here, we used a 4 kDa membrane as an outer mold for ice templating collagen. After freeze-drying, the material was observed by SEM to assess the macroporous structure. As shown in **Figure 20-A**, pores are oriented parallel to the wall. Luminal and external surfaces are porous (**Fig.20-B,C**), with median Feret diameter values of 9.43 ± 40.51 µm and 12.43 ± 35.70 µm, respectively (**Appendix C-Fig.6**), lower than those observed in *Ins* and *Cond*. Interestingly, the texture of the membrane imprinted a regular pattern onto the outer surface of our material. While it would have been interesting to compare if these attributes were preserved through fibrillogenesis, the process did not succeed. After exposure to ammonia vapors, the frozen collagen resulted in a material that lacked self-standing properties and was highly viscous. Despite a whiter color, suggesting the self-assembly of collagen molecules into fibrils, the loss of mechanical properties in comparison to our standard methods indicated that the melting of ice was occurring prior to fibrillogenesis. Adjusting the membrane size or the duration of fibrillogenesis may resolve this issue, but this procedure was not pursued any further.

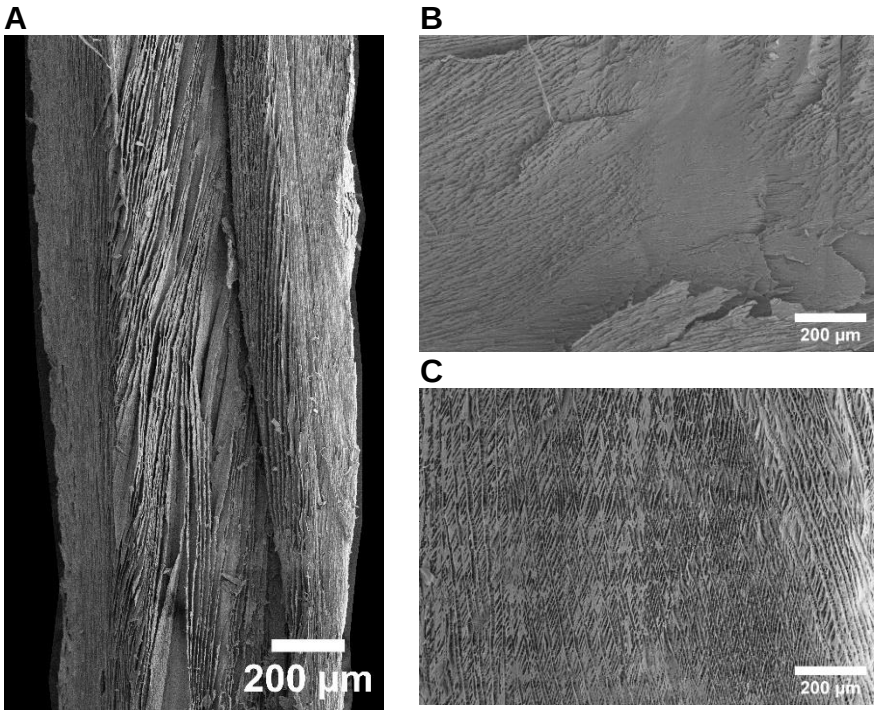

Figure 20. Structural analysis by SEM of a collagen sample ice templated with an outer dialysis membrane. **A**) Longitudinal section. **B**) Luminal surface. **C**) External surface.

Next, we applied the same protocol using ePTFE instead of a dialysis membrane. The resulting matrix, obtained by this concomitant fibrillogenesis process, was examined under cross-polarizers (**Fig.21**). The material displays a birefringent signal indicative of supramolecular ordering, with a structure of dense collagen walls and pores that confirms the topotactic fibrillogenesis using ePTFE. By lack of time, we were unable to delve deeper into this experiment, although it promises interesting results.

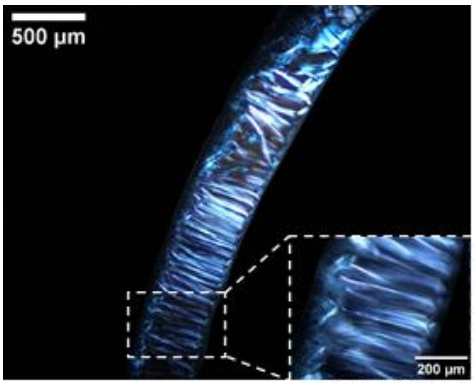

Figure 21. Structure and supramolecular organization of collagen in the sample fabricated with an outer mold of ePTFE (external surface on the left, luminal surface on the right side), imaged by PLOM. Under cross-polarizers oriented at 0° and 90°, the transversal section displayed a birefringent signal, characteristic of liquid crystal-like ordered structures.

Successive fibrillogenesis. An alternative protocol was evaluated, involving a short exposure to ammonia vapor before immersion into the 10x PBS bath. Collagen was introduced in *MC* molds and ice templating was carried out in liquid nitrogen. Subsequently, the external mold was retrieved and the material was subjected to ammonia vapor at 0°C for 24h. The material was then poured into 10x-PBS at -3°C for 48h, followed by a consolidation step in 5x PBS for 2 weeks. The obtained self-standing material exhibited a translucent appearance, in contrast to the opaque white and translucent yellow resulting from PBS or NH_3 fibrillogenesis (**Fig.22**). Under cross-polarizers, the bi-refringent signal reveals a supramolecular ordering, with no significant change in the collagen orientation (**Fig.23-A**). Confocal images of transversal sections show a structure akin to *MC* fibrillated solely in PBS, with the difference of pores present on the external surface (**Fig.23-B.a,b**). Again, further exploration of this was not pursued due to time constraints.

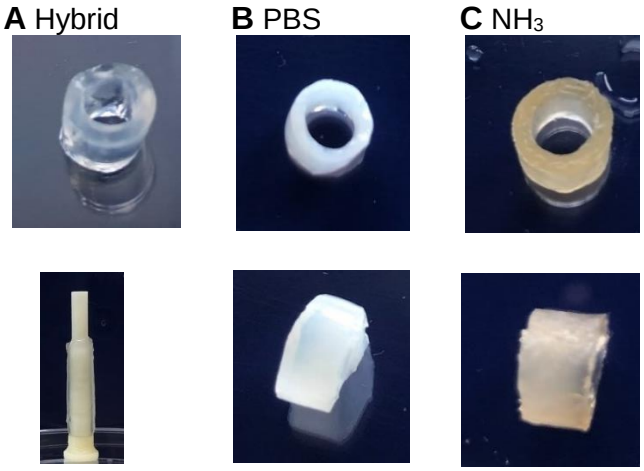

Figure 22. Photos of materials ice templated in the same conditions, and fibrillated by (**A**) hybrid *successive fibrillogenesis* comprising 24h in NH_3 vapors at 0°C and 48h in 10x PBS at -3°C, (**B**) 72h in a 10x PBS bath at -3°C, or (**C**) 48h under ammonia vapors at 0°C. Materials have an inner diameter of 5 mm.

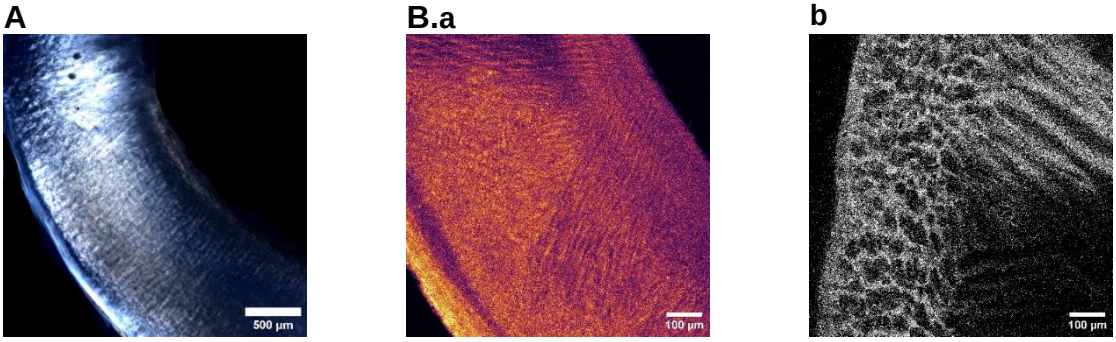

Figure 23. Structural and textural properties of collagen scaffolds after hybrid *successive fibrillogenesis.* Transversal sections were imaged under cross-polarizers at 0° and 90° (**A**), and confocal microscopy (**B**), with a focus made on the external surface (**B.b**).

6. Conclusions

We describe here strategies to replicate the microstructure of porous tissues, prone to colonization by the host cells in the context of an implantation. Using exclusively type I collagen, we yield the morphology, the mechanics and the functions of native tissues' ECM. We focused on the particular case of tubular tissues, a challenging two-layered structure to recapitulate.

Ice-templating is a shaping approach enabling to fine-tune the materials porosity, providing a mean to tailor access of cells to the scaffold and to modulate the materials' mechanical properties. By adjusting the thermal boundary conditions, this simple method allows orienting pores in either longitudinal or radial directions, modulating the pore size, and directing the choice of an isotropic or anisotropic structure. An interface can be generated between either a isotropic and a anisotropic region, or between two opposing anisotropic porous regions. The first correlates with the dipping speed, while the second is controlled by the molds' thermal conductivity difference. These parameters are adaptable to a vast array of sizes and geometries, providing a reliable method for the development of biomaterials that target the treatment of several pathologies.

The topotactic fibrillogenesis conditions provide further control over the porosity while triggering the self-assembly of collagen molecules into biomimetic fibrils. Our materials offer cellular micro-environments close to those of biological tissues, a lacking feature in materials currently used in the clinic. The seeding of different cell lines—ECs and MSCs—demonstrate their potential to serve as biologically relevant substrates. On the basis of hMSCs migration experiments, ammonia fibrillogenesis proves more suitable to preserve pores and to facilitate cell colonization, ensuring a successful graft implantation. Epithelial and endothelial cells adhere well to the materials and proliferate until confluence is reached. However, materials fibrillated in PBS 10X provide mechanical properties akin to native tissues, along with a more impermeable luminal surface.

Doubts may be raised about the endothelialization potential under physiological flow conditions, especially concerning contact with blood, since collagen triggers thrombus formation. The surgical gesture of suturing to the material to the anastomosis during grafting procedures, has not been evaluated either. These questions will be addressed in the upcoming months, and will involve assessing the ability of HUVECs to form a tight layer under flow, and suturing tests performed by both a homemade mechanical set-up and by surgeons.

Overall, we introduce a new family of tubular collagen materials, exhibiting a unique combination of high concentration and porosity, with unprecedented resemblance to native

tissues. Beyond their role as tissue grafts, our materials are expected to act as *in vitro* models of tubular tissues. These may answer a vast range of open questions—from cell-cell and cell-matrix interactions up to drug treatment response—bridging current gaps for improved patient care in respiratory, vascular, gastrointestinal and urinary tract pathologies. We believe that these materials hold promise as efficient replacement grafts, with planned evaluation by *in vivo* studies for both tracheal and vascular applications in the months ahead.

7. References in Chapter IV

1. Parisi, C. *et al.* Porous yet dense matrices: using ice to shape collagen 3D cell culture systems with increased physiological relevance. *Biomater Sci* **10**, 6939–6950 (2022).

2. Rieu, C. *et al.* Topotactic Fibrillogenesis of Freeze-Cast Microridged Collagen Scaffolds for 3D Cell Culture. *ACS Appl Mater Interfaces* **11**, 14672–14683 (2019).

3. Yin, K., Divakar, P. & Wegst, U. G. K. Freeze-casting porous chitosan ureteral stents for improved drainage. *Acta Biomater* **84**, 231–241 (2019).

4. Divakar, P., Yin, K. & Wegst, U. G. K. Anisotropic freeze-cast collagen scaffolds for tissue regeneration: How processing conditions affect structure and properties in the dry and fully hydrated states. *J Mech Behav Biomed Mater* **90**, 350–364 (2019).

5. Christoph, S. *et al.* Ice-templating beet-root pectin foams: Controlling texture, mechanics and capillary properties. *Chemical Engineering Journal* **350**, 20–28 (2018).

6. Qin, K., Parisi, C. & Fernandes, F. M. Recent advances in ice templating: from biomimetic composites to cell culture scaffolds and tissue engineering. *J Mater Chem B* **9**, 889–907 (2021).

7. Deville, S., Saiz, E. & Tomsia, A. P. Freeze casting of hydroxyapatite scaffolds for bone tissue engineering. *Biomaterials* **27**, 5480–5489 (2006).

8. Deville, S., Saiz, E. & Tomsia, A. P. Ice-templated porous alumina structures. *Acta Mater* **55**, 1965–1974 (2007).

9. Baskaran, A. *et al.* Anti freeze proteins (Afp): Properties, sources and applications – A review. *Int J Biol Macromol* **189**, 292–305 (2021).

10. Cyr, J. A., Husmann, A., Best, S. M. & Cameron, R. E. Complex architectural control of ice-templated collagen scaffolds using a predictive model. *Acta Biomater* **153**, 260–272 (2022).

11. Kashchiev, D. & van Rosmalen, G. M. Review: Nucleation in solutions revisited. *Crystal Research and Technology* **38**, 555–574 (2003).

12. Deville, S. Freeze-Casting of Porous Ceramics: A Review of Current Achievements and Issues. *Adv Eng Mater* **10**, 155–169 (2008).

13. Ghorbani, F., Zamanian, A., Kermanian, F. & Shamoosi, A. A bioinspired 3D shape olibanum-collagen-gelatin scaffolds with tunable porous microstructure for efficient neural tissue regeneration. *Biotechnol Prog* **36**, (2020).

14. Akyurt, M., Zaki, G. & Habeebullah, B. Freezing phenomena in ice-water systems. *Energy Convers Manag* **43**, 1773–1789 (2002).

15. Carrabba, M. & Madeddu, P. Current strategies for the manufacture of small size tissue engineering vascular grafts. *Front Bioeng Biotechnol* **6**, 1–12 (2018).

16. Cen, L., Liu, W., Cui, L., Zhang, W. & Cao, Y. Collagen tissue engineering: development of novel biomaterials and applications. *Pediatr Res* **63**, 492–496 (2008).

17. Giraud Guille, M. M., Nassif, N. & Fernandes, F. M. Collagen-based materials for tissue repair, from Bio-inspired to biomimetic. in *Materials design inspired by nature: function through inner architecture* (eds. Fratzl, P., W.C. Dunlop, J. & Weinkamer, R.) 107–127 (The Royal Society of Chemistry, 2013). doi:10.1039/9781849737555-00107.

18. Weinberg, C. B. & Bell, E. A blood vessel model constructed from collagen and cultured vascular cells. *Science (1979)* **231**, 397–400 (1986).

19. Hirai, J. & Matsuda, T. Venous reconstruction using hybrid vascular tissue composed of vascular cells and collagen: tissue regeneration process. *Cell Transplant* **5**, 93–105 (1996).

20. Li, X., Xu, J., Nicolescu, C. T., Marinelli, J. T. & Tien, J. Generation, endothelialization, and microsurgical suture anastomosis of strong 1 mm-diameter collagen tubes. *Tissue Eng Part A* **23**, 335–344 (2017).

21. Ghezzi, C. E., Marelli, B., Muja, N. & Nazhat, S. N. Immediate production of a tubular dense collagen construct with bioinspired mechanical properties. *Acta Biomater* **8**, 1813–1825 (2012).

22. Kumar, V. A. *et al.* Acellular vascular grafts generated from collagen and elastin analogs. *Acta Biomater* **9**, 8067–8074 (2013).

23. Parisi, C. *et al.* Porous yet Dense matrices: using ice to shape collagen 3D cell culture systems with increased physiological relevance. *Biomater Sci* **10**, 6939–6950 (2022).

24. Madaghiele, M., Sannino, A., Yannas, I. V. & Spector, M. Collagen-based matrices with axially oriented pores. *J Biomed Mater Res A* **85**, 757–767 (2008).

25. Pawelec, K. M., Husmann, A., Wardale, R. J., Best, S. M. & Cameron, R. E. Ionic solutes impact collagen scaffold bioactivity. *J Mater Sci Mater Med* **26**, 91 (2015).

26. Koens, M. J. W. *et al.* Vascular replacement using a layered elastin-collagen vascular graft in a porcine model: One week patency versus one month occlusion. *Organogenesis* **11**, 105–121 (2015).

27. Cavallaro, J. F., Kemp, P. D. & Kraus, K. H. Collagen fabrics as biomaterials. *Biotechnol Bioeng* **43**, 781–791 (1994).

28. Magnan, L. *et al.* Human textiles: A cell-synthesized yarn as a truly "bio" material for tissue engineering applications. *Acta Biomater* **105**, 111–120 (2020).

29. Deville, S. Freeze-casting of porous ceramics: A review of current achievements and issues. *Adv Eng Mater* **10**, 155–169 (2008).

30. Qin, K., Parisi, C. & Fernandes, F. M. Recent advances in ice templating: From biomimetic composites to cell culture scaffolds and tissue engineering. *J Mater Chem B* **9**, 889–907 (2021).

31. Gutiérrez, M. C., Ferrer, M. L. & Del Monte, F. Ice-templated materials: Sophisticated structures exhibiting enhanced functionalities obtained after unidirectional freezing and ice-segregation- induced self-assembly. *Chemistry of Materials* **20**, 634–648 (2008).

32. Pawelec, K. M., Husmann, A., Best, S. M. & Cameron, R. E. Ice-templated structures for biomedical tissue repair: From physics to final scaffolds. *Appl Phys Rev* **1**, 021301 (2014).

33. Rieu, C. *et al.* Topotactic fibrillogenesis of freeze-cast microridged collagen scaffolds for 3D cell culture. *ACS Appl Mater Interfaces* **11**, 14672–14683 (2019).

34. Thibert, E. & Dominé, F. Thermodynamics and kinetics of the solid solution of HCl in ice. *Journal of Physicial Chemistry B* **101**, 3554–3565 (1997).

35. Schindelin, J. *et al.* Fiji: An open-source platform for biological-image analysis. *Nat Methods* **9**, 676–682 (2012).

36. Knight, D. A. & Holgate, S. T. The airway epithelium: Structural and functional properties in health and disease. *Respirology* **8**, 432–446 (2003).

37. Bouligand, Y. Liquid crystals and biological morphogenesis: Ancient and new questions. *Comptes Rendus Chimie* **11**, 281–296 (2008).

38. Gobeaux, F. *et al.* Fibrillogenesis in dense collagen solutions: a physicochemical study. *J Mol Biol* **376**, 1509–1522 (2008).

39. Giraud-Guille, M. M. *et al.* Liquid crystalline properties of type I collagen: Perspectives in tissue morphogenesis. *Comptes Rendus Chimie* **11**, 245–252 (2008).

40. Ashby, M. F. & Bréchet, Y. J. M. Designing hybrid materials. *Acta Mater* **51**, 5801–5821 (2003).

41. Critser, P. J., Kreger, S. T., Voytik-Harbin, S. L. & Yoder, M. C. Collagen matrix physical properties modulate endothelial colony forming cell-derived vessels in vivo. *Microvasc Res* **80**, 23–30 (2010).

42. Breatnach, E., Abbott, G. C. & Fraser, R. G. Dimensions of the Normal Human Trachea. *American Roentgen Ray Society* **141**, 903–906 (1984).

43. Moore, D. H. & Ruska, H. The fine structure of capillaries and small arteries. *Journal of Biophysical and Biochemical Cytology* **3**, 457–475 (1957).

44. Martinod, E. *et al.* Tracheal regeneration following tracheal replacement with an allogenic aorta. *Annals of Thoracic Surgery* **79**, 942–948 (2005).

45. Chen, L. *et al.* UbasM: An effective balanced optical clearing method for intact biomedical imaging. *Sci Rep* **7**, 12218 (2017).

46. Tapiero, H., Townsend, D. M. & Tew, K. D. Trace elements in human physiology and pathology. Copper. **57**, 386–398 (2003).

47. Mcguigan, M. A. Chronic Poisoning. in *Goldman's Cecil Medicine* vol. 1 88–95 (Elsevier, 2012).

48. Malluche, H. H. & Faugere, M.-C. Aluminum-Related Bone Disease. *Blood Purif* **6**, 1–15 (1988).

49. Klein, G. L. Aluminum toxicity to bone: A multisystem effect? *Osteoporos Sarcopenia* **5**, 2–5 (2019).

Conclusions

"Sashay away"

— RuPaul

Conclusions

Biological tissues are mainly composed of type I collagen. The formation of this protein *in vivo* has been partially unveiled, with a description from the amino-acid sequences, the formation of procollagen and tropocollagen molecules, up to the growth of fibrils and their assembly in tissues. The analogy between the organization of these tissues and the liquid crystal mesophases of collagen has been described first by Y. Bouligand. Such work was pursued by M-M. Giraud-Guille, among others, who studied the mesophases of collagen in solution and their impact on the architecture of connective tissues. In parallel, part of the biomaterials' community has focused on developing strategies to reproduce and to replace native tissues based on *biomimetism*, i.e. the reproduction of the structural and compositional features of biological entities.

Given the high incidence of pathologies affecting tubular tissues—circulatory system, esophagus, trachea, gastrointestinal and urinary tract—we focused on the understanding of their structure and composition. In Chapter 1, we underline how they can be united in a simplified model. We propose a dual-layer model comprising an epithelial inner layer, and a muscular outer layer. The strategies to achieve this structure rely on a *biomimetic composition* and a *biomimetic structure*, which can be placed in a two-axis graph. This graph guides the fabrication and can be used as a tool to compare the biomimetic nature of materials in the literature.

To foster epithelialization in biomaterials, we identified three luminal surface strategies (ECM-derived, bioactive, and textured surfaces), while techniques providing the muscular layer rely on either a porous network (*via* decellularization, textile-inspired techniques, electrospinning, ice-templating, 3D-printing, or cryoprinting) or on dense materials (through cell-mediated ECM fabrication, densification or bioprinting). Among these strategies, type I collagen-based biomaterials have gathered increasing attention, due to its prevalence in tubular tissues. However, the processing of collagen raises fundamental questions:

How to preserve the collagen structure and its ability to form native-like fibrils and fibrillar assemblies throughout the harsh processing conditions?

How to ensure that the native concentration regime found in native tissues is achieved?

This thesis aims at filling this gap, partially, by a detailed study of the influence of key materials processing parameters—temperature and concentration—on the collagen state. In chapter 2, we evidenced the impact of the concentration, temperature, and the fibrillogenesis pathway on the state of collagen, and contextualized it for various materials processing techniques. We concentrated collagen at various densities of 40, 200, 400 and 900 mg.mL^{-1} *via*

evaporation, and paired it with two different fibrillogenesis routes (NH_3 and PBS). The use of X-ray, coupled to thermal experiments, rheology and microscopy observations (PLOM and TEM), allowed to describe the boundaries between the denatured, vitreous, gel and sol states in acidic collagen solutions. The thermal analysis enabled us to establish the *liquidus*, *solidus*, *vitrification* and *denaturation* lines in the state diagram. We extended this methodology to analyze fibrillar collagen materials. Additionally, SAXS measurements evidenced the absence of harmonics at 400 $mg.mL^{-1}$ for both self-assembly routes. This could be interpreted as a different arrangement of the molecules, potentially displaying a different D-period. The formation of these structural defects has already been observed, notably in pathological and embryogenic tissues. Further investigations are required to confirm this interpretation and to clarify the conditions under which different patterns form, and to what extent they may be considered proxies to tissue pathologies.

The establishment of these state diagrams opens new perspectives in the elaboration of biomimetic materials, in particular in the concentration range of native tissues (100-200 $mg.mL^{-1}$). However, the relationships between collagen concentration in a fibrillar state and the fate of cells has never been studied in this range of values, which covers both healthy and pathological tissues. In Chapter 3, we undertook the challenge of modelling these situations, by creating cellular micro-environments that provide different collagen concentrations (from 40 to 900 $mg.mL^{-1}$), fibrillar topography (from 95 to 390 nm in width), and local elastic modulus (from 23 to 1432 kPa). Endothelial cells (HUVECs) were seeded and observed at day 3 and 5 by widefield and confocal microscopy. High concentrations, in particular at 900 $mg.mL^{-1}$, have proven favorable to actin spreading and cell proliferation, whereas the presence of large fibrils is responsible for enhanced cell adhesion. The obtention of these large cross striated fibrils on the surface occurs at different concentrations in NH_3 and PBS, of respectively 200 and 900 $mg.mL^{-1}$, owing to the different fibrillogenesis media. Furthermore, the observation of a higher occurrence of cadherin between cells that were seeded on PBS surfaces, suggests that this route is preferential to foster epithelialization.

Proving that a high collagen concentration promotes cell adhesion, proliferation, and enhances local mechanical properties, has driven us to adopting fabrication techniques that result in increased collagen concentration. In this context, ice templating is particularly efficient. Due to the porous network created by ice, these materials are prone to cell colonization, a critical factor for biointegration after surgical implantation. Considering these elements, we prepared collagen materials under controlled conditions of temperature, concentration, and compared the two fibrillogenesis routes described earlier (Chapter 4). The challenge resided in replicating the ECM of tissues using collagen alone, within the peculiar two-layered structures of tubular tissues. By tailoring several parameters, we demonstrate that adjusting the dipping speed, the thermal boundary conditions, and the freezing bath temperature allows orienting the pores in either longitudinal or radial directions, modulating the pore size, and directing the isotropic *vs* anisotropic character of the pores. Moreover, the

choice of the topotactic fibrillogenesis conditions implies different kinetics, which direct the self-assembly of collagen molecules and the preservation of the porous network. We further assessed the biological properties of the materials, by seeding different cell lines, including epithelial, endothelial, and mesenchymal stem cells. We confirmed what was observed in chapter 3, which is that PBS provides a smoother surface fostering epithelial cell proliferation over time. In contrast, ammonia fibrillogenesis favors structural maintenance and hence facilitates the migration of hMSCs into the material. The two fibrillogenesis routes are thus both promoting proliferation, but induce different cell behavior; adhesion or colonization. One set of conditions stands out for achieving both adhesion and proliferation of cells, as well as for displaying the relevant mechanical properties to serve as a tubular graft. Overall, we believe that the combination of ice templating and topotactic fibrillogenesis yield a promising new family of grafting materials. They offer a unique combination of high concentration and porosity in wet state, with unprecedented resemblance to native tissues. Evaluation by *in vivo* studies will be conducted in the months ahead for several tubular tissue applications—tracheal and vascular.

Perspectives

The state diagrams that we drew describe the state of collagen as a function of the concentration and temperature. However, we did not place the mesophases in these diagrams, that require being able to observe liquid crystal-like transitions by birefringence. The development of an *in situ* cryomicroscope equipped with cross-polarizers could unveil such transitions. Increasing our level of understanding and precise the guidelines to design biomimetic materials, are also expected to act in favor of better *in vitro* models.

In the future, the dense collagen models developed here could also be used to evaluate the implications of collagen concentration and organization on the cell differentiation during tissue morphogenesis, and to study the control of the migration through concentration gradients. These studies could answer a vast range of questions, from cell-cell and cell-matrix interactions up to drug treatment responses, in either pathological or healthy conditions. In particular, they could provide cues in how tumor cells develop and disseminate, and how shifting away from the physiological concentration regime can drive pre-metastatic niches.

The tubular materials that we designed require further experiments to confirm their potential as clinical tissue grafts. The behavior of epithelial cells may be different under physiological flow conditions, especially concerning contact with blood since collagen triggers thrombus formation. The materials could also serve as a platform to answer

questions regarding the collective behavior of ECs under flow, and how they respond to chemical stimuli or mechanical constraints. Finally, the act of suturing the material to perform anastomosis shall be performed to confirm the possibility to graft it onto animal models. If these materials have pushed the basic knowledge and the engineering of collagen forward, we hope that they will also translate into improved patient care for respiratory, vascular, gastrointestinal and urinary tract pathologies.

Appendices

"Everything is some kind of a plot, [hu]man."
— Thomas Pynchon

Appendix A

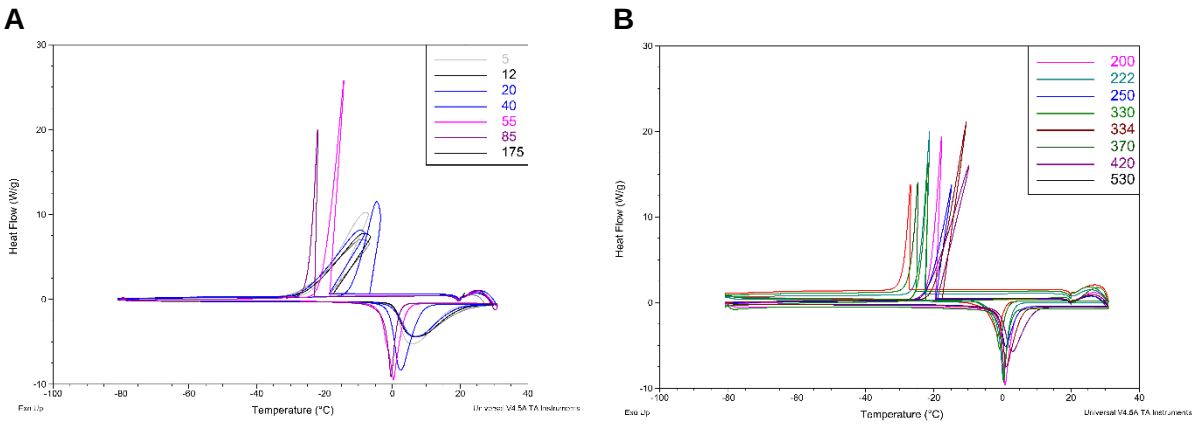

Figure S1. Analysis of the free water fusion enthalpy in collagen solutions of various concentrations. All measurements were performed by DSC at a speed of 5°C.min^{-1}. **A)** From 5 to 175 mg.mL^{-1}. **B)** From 200 to 530 mg.mL^{-1}.

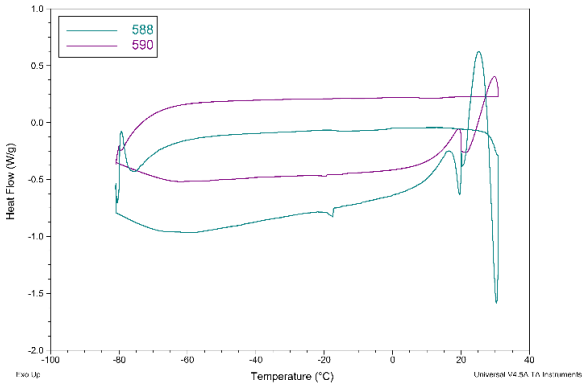

Figure S2. Analysis of the free water fusion enthalpy in collagen solutions above 530 mg.mL^{-1}, at 588 and 590 mg.mL^{-1}. Measurements were performed by DSC at a speed of 5°C.min^{-1}.

Mass fusion enthalpy $\Delta H_{fus\ (solution)}$: measured on the thermogram

Free water fraction $\Phi_{w,f}$:

$$\Phi_{w,f} = \frac{\Delta H_{fus\ (solution)}}{\Delta H_{fus\ (solvent)}}$$

If $\Delta H_{f(solution)} > \Delta H_{f(solvant)}$, $\Phi_{w,f} > 1$

with ΔH_{fus} (HCl 3 mM) = 319.3 J.g^{-1}

Initial fraction of collagen c_i :

$$c_i = \frac{collagen\ concentration\ (mg.mL^{-1})}{collagen\ concentration\ (mg.mL^{-1}) + 1000}$$

Initial concentration of collagen (%):

$$c = c_i * 100$$

Total water fraction $\Phi_{w,T}$:

$$\Phi_{w,T} = 1 - c$$

Bound water fraction $\Phi_{w,b}$:

$$\Phi_L = \Phi_{w,T} - \Phi_{w,f}$$

Local concentration of collagen (in the interstices, %):

$$c_L = \frac{c_i}{c_i + \Phi_{w,b}} * 100$$

Figure S3. Calculations of the fraction composing the solution of collagen upon cooling, as a function of the collagen initial concentration (c_i) and the fusion enthalpy of water ($\Delta H_{fus(solution)}$).

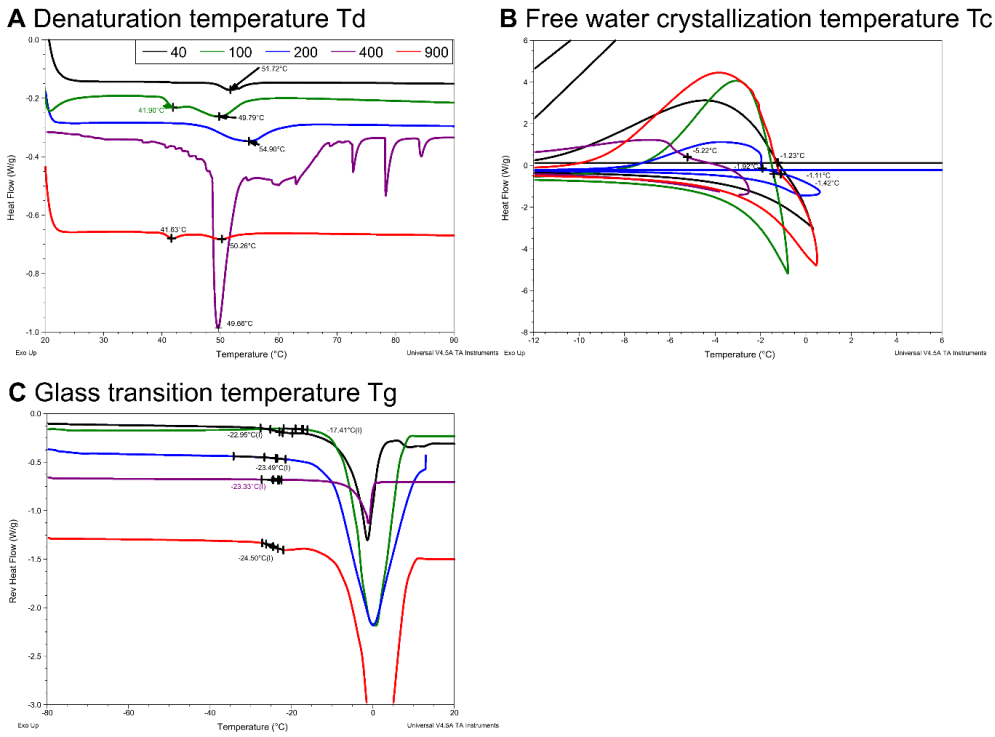

Figure S4. Analysis of the thermodynamic phase boundaries by DSC and mDSC of collagen samples fibrillated by ammonia vapors. All measurements were performed at a rate of 5°C.min^{-1}. (**A**) Denaturation temperature T_d, (**B**) free water crystallization temperature T_c, and (**C**) free water melting temperature measurements used to determine the *critical collagen concentration*.

Video S1. Sequential 2D fluorescence imaging of the ammonia fibrillogenesis medium diffusion front in the previously ice-templated collagen solution, at a constant temperature of -5°C. The first front corresponds to the diffusion of NH_3 that induce the self-assembly of collagen molecules within the wall (purple-yellow), which occurs before the melting of ice (black, 2nd front). Link: https://dropsu.sorbonne-universite.fr/s/HaANNBL6zQr6r5S

Appendix B

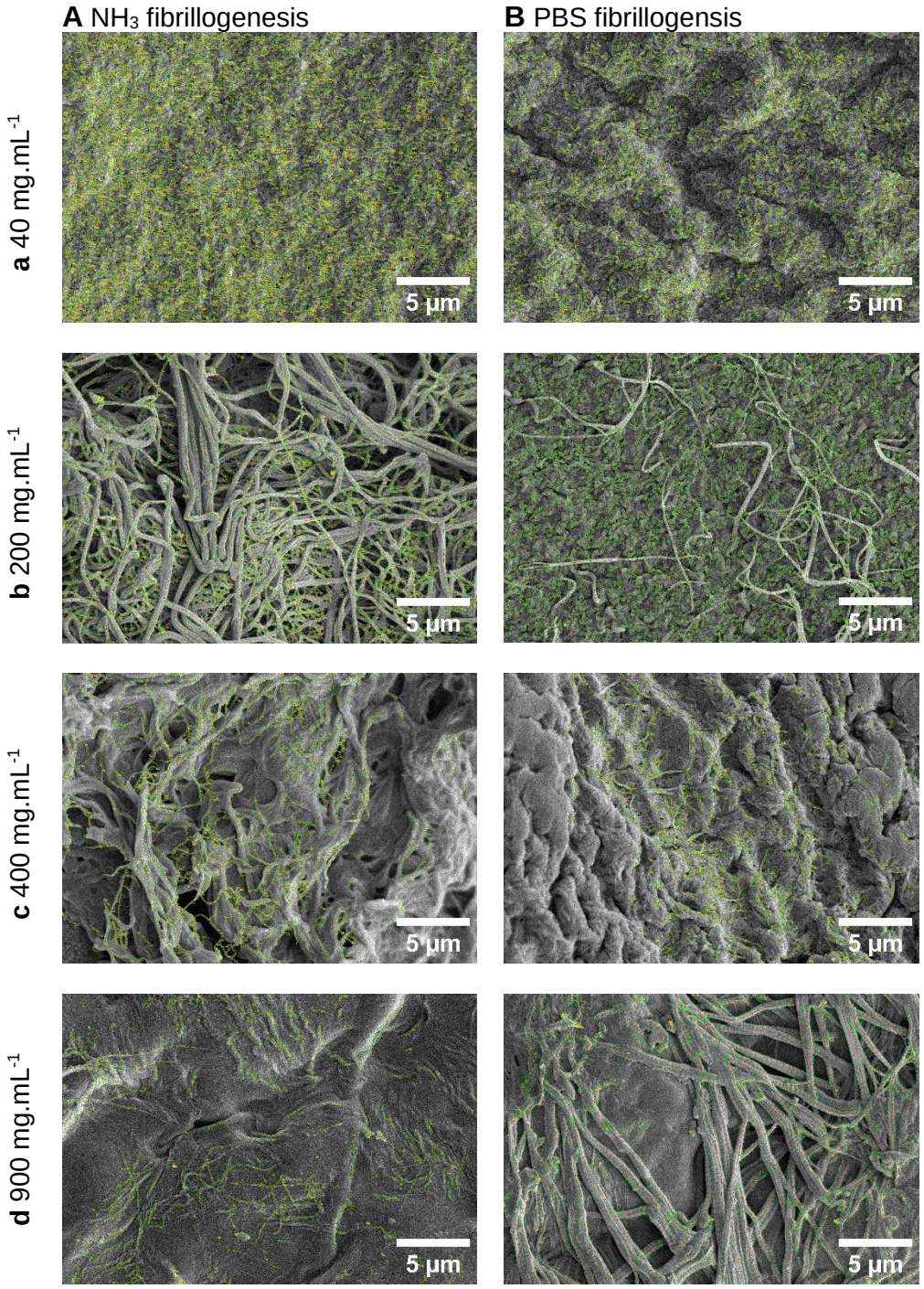

Figure S1. Fibril width measurement for each sample, performed on SEM images with Ridge detection ImageJ plugin.

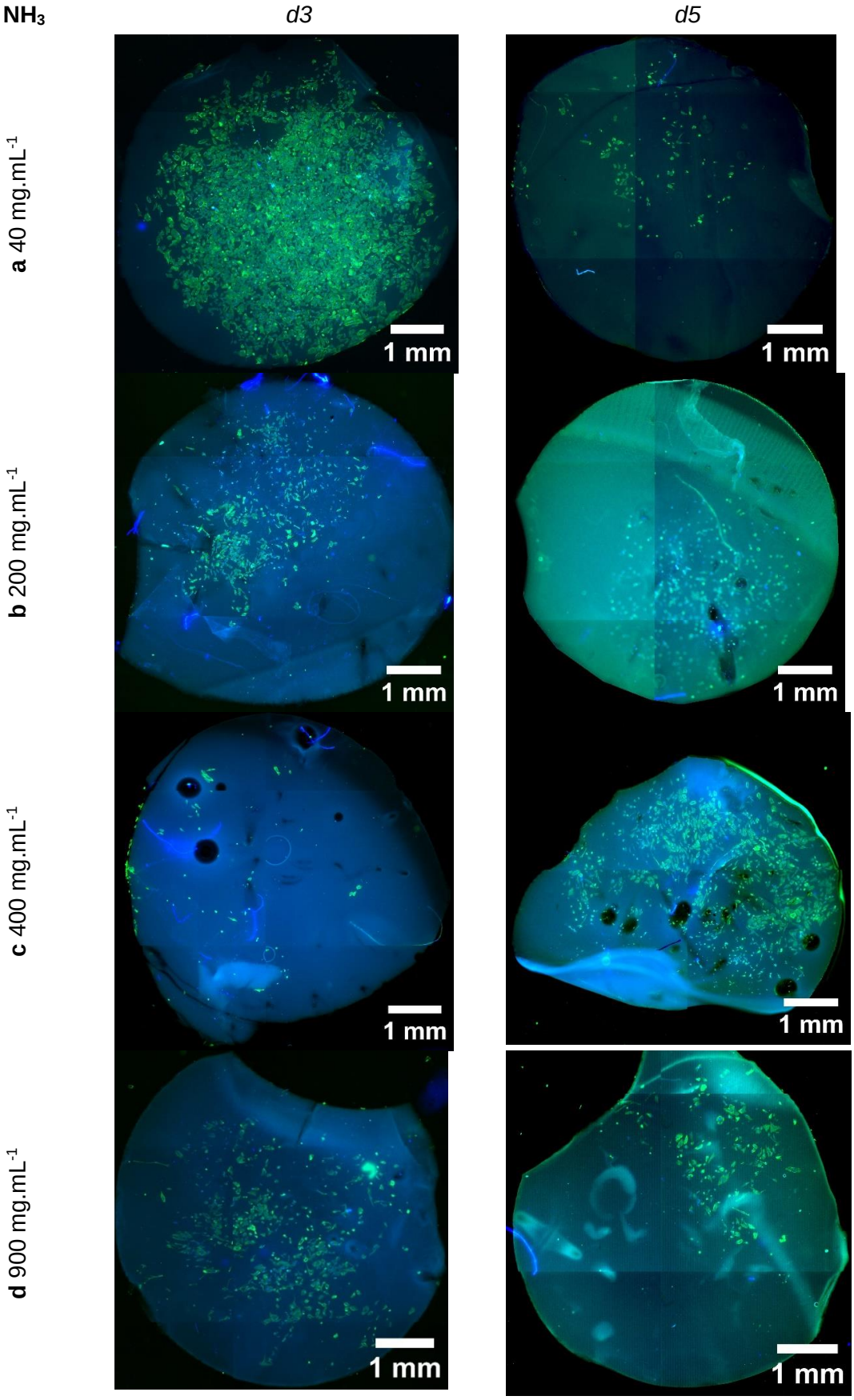
NH3
d3
d5
a 40 mg.mL-1
b 200 mg.mL-1
c 400 mg.mL-1
d 900 mg.mL-1
1 mm

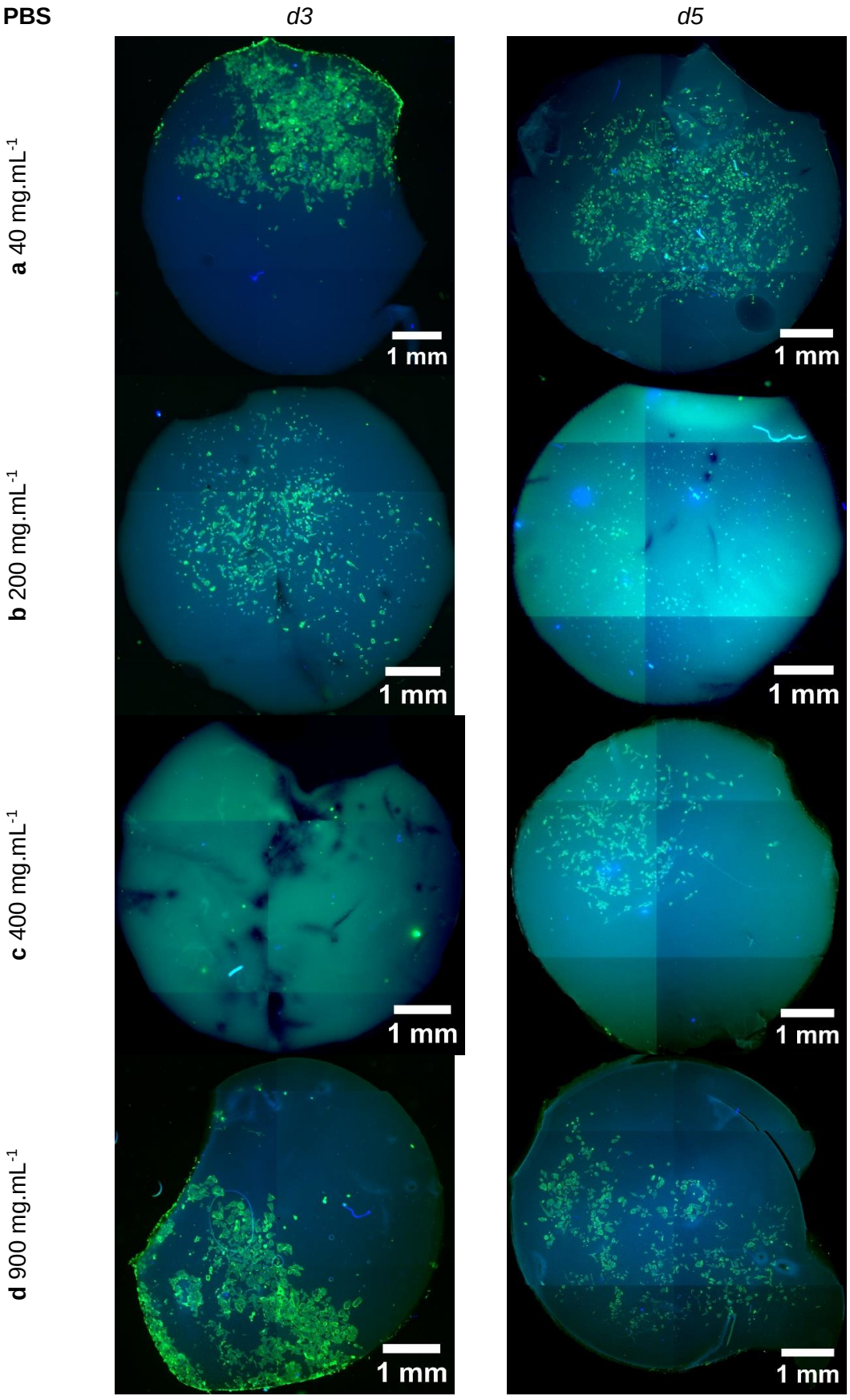
PBS
d3
d5
a 40 mg.mL-1
b 200 mg.mL-1
c 400 mg.mL-1
d 900 mg.mL-1
1 mm

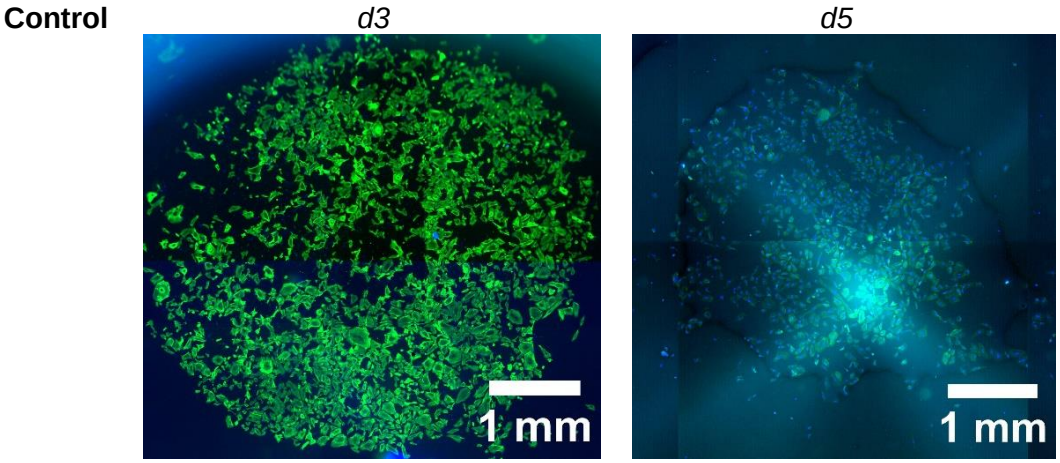

Figure S2. Cellular proliferation and spreading assessment for the various fibrillogenesis conditions (NH_3 and PBS) and concentrations (40, 200, 400, and 900 $mg.mL^{-1}$), and the controls, overtime. Images were acquired using a macroscope in tile mode, with a 20x objective, actin (phalloidin, in green) and nuclei (DAPI, in blue). For all conditions (except controls), three substrates were imaged. The image presented here are the most representative.

Appendix C

```
#include <AccelStepper.h>

AccelStepper stepper(AccelStepper::DRIVER,9,8);

int sign = 0;       // Either 1, 0 or -1
int spd = 10;     // The current speed in steps/second


void setup()
{
  Serial.begin(9600);
  stepper.setMaxSpeed(1000);
  stepper.setSpeed(0);
}

void loop()
{
  char c;
  if(Serial.available()) {
    c = Serial.read();
    if (c == 'f') {  // forward
      sign = 1;
    }
    if (c == 'r') {  // reverse
      sign = -1;
    }
    if (c == 's') {  // stop
      sign = 0;
    }
    if (c == '1') {  // standard speed 10mm/min
      spd = 33;

    }
    if (c == '2') {  // 25 mm/min
      spd = 82;
    }
    if (c == '3') {  // 50 mm/min
      spd = 165;
    }


    stepper.setSpeed(sign * spd);
  }
  stepper.runSpeed();
}
```

Figure S1. Arduino code to control the dipping speed in the freezing media for the ice templating process. The standard command for the elaboration of the materials described above were "f1", corresponding to *forward* and a speed of 10 mm.min^{-1}.

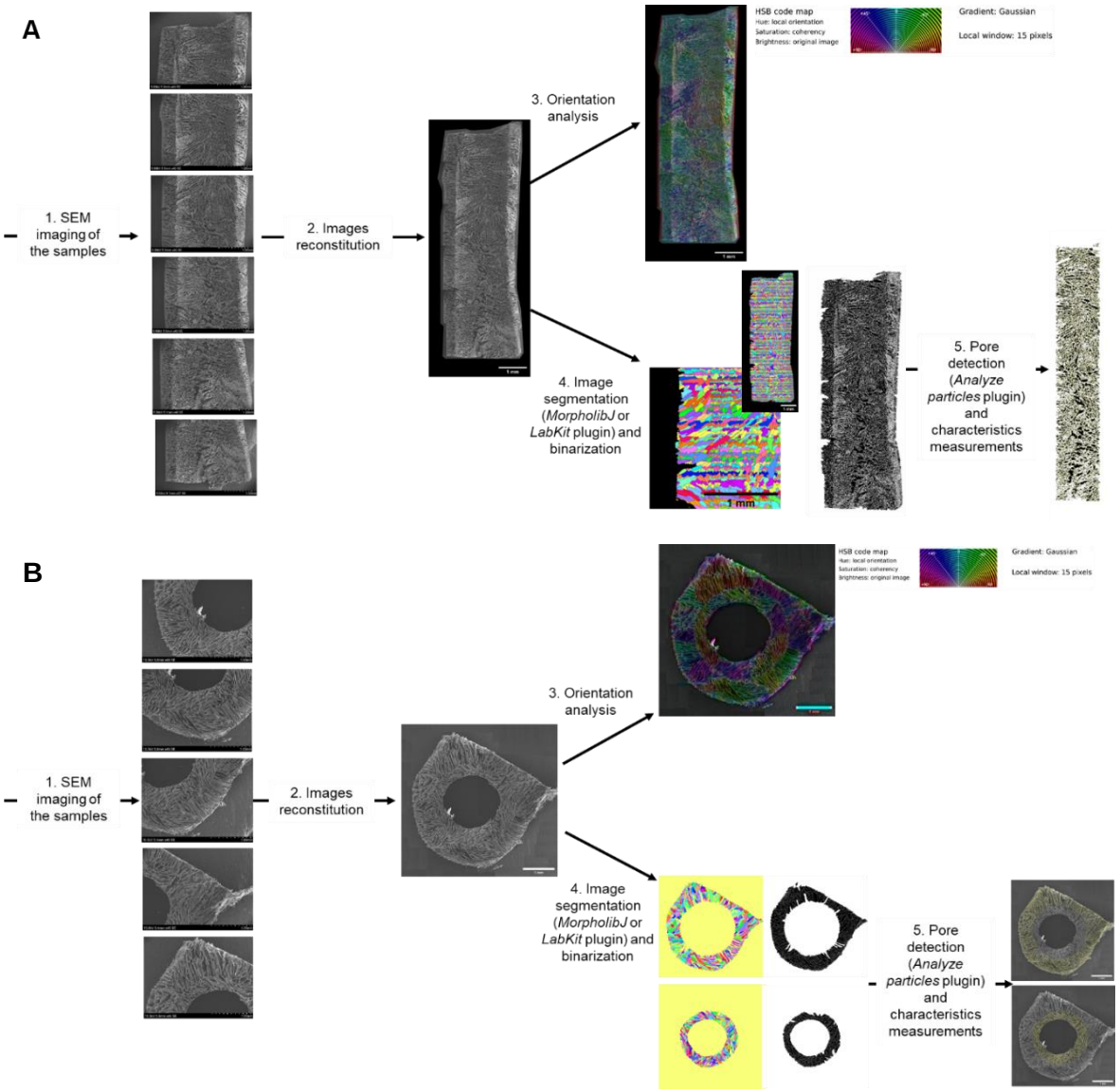

Figure S2. Analysis of the pore dimension base on SEM images and using ImageJ plugins, for longitudinal (**A**) and transversal (**B**) cross-sections. **Figure S3.** Color-mapping of pore angles in SEM images of samples ice templated in various conditions.

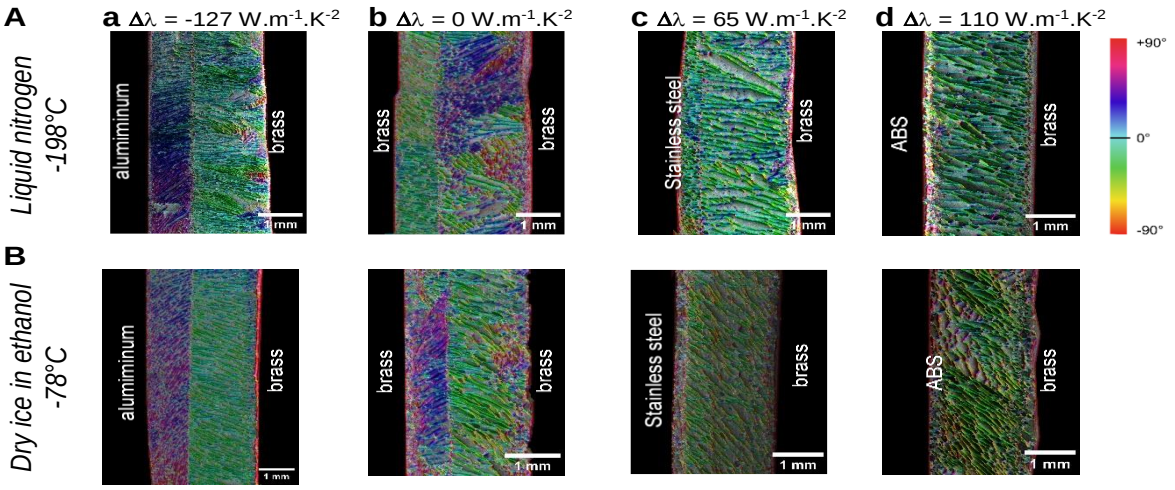

Figure S3. Color-mapping of pore angles in SEM images of samples ice templated in various conditions.

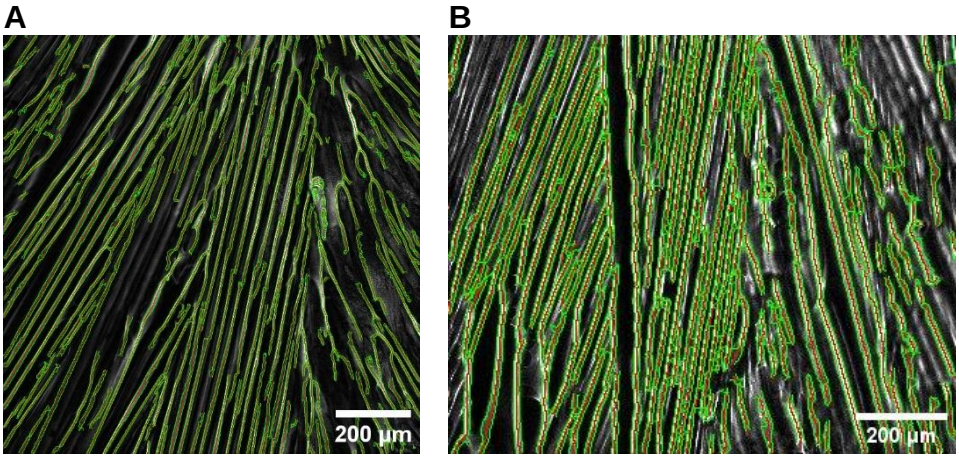

Figure S4. First analysis steps, using ImageJ, of collagen walls width following ice templating of collagen solution under the cryoconfocal. Contrast was adjusted and background was subtracted to enhance the width detection by Ridge Detection plugin. Images are the results of the ridge detection results for collagen frozen in copper (**A**) or steel (**B**).

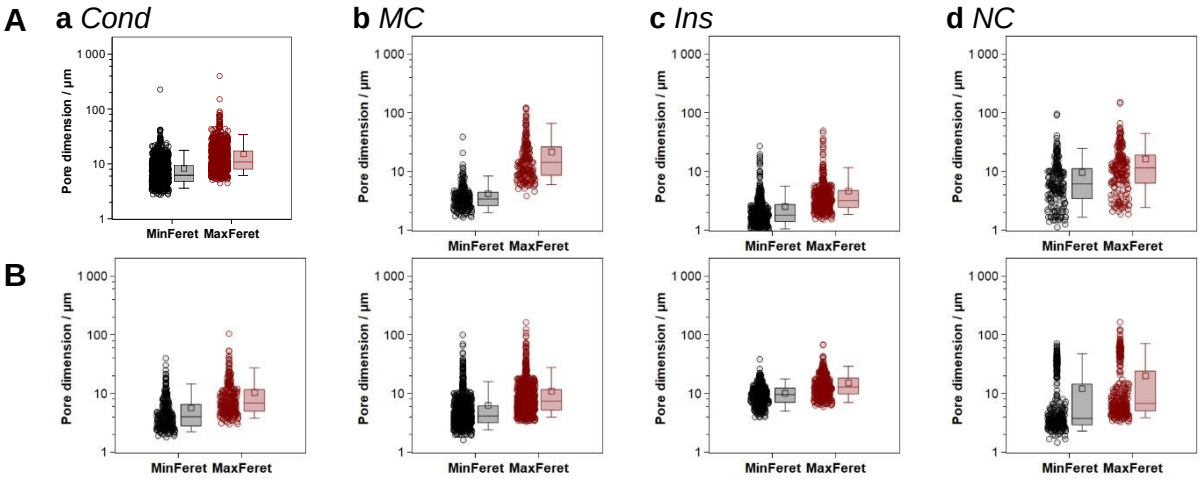

Figure S5. Dimensions of pore in transversal sections (**A**) and at the luminal surface (**B**) based on the MinFeret and MaxFeret diameters, for various porous structures (**a** *Cond*, **b** *MC*, **c** *Ins*, and **d** *NC*). Box plots represent the 25th to 75th percentile range of the modulus distribution, with the top and bottom lines indicating the 10th to the 90th percentile range of the modulus distribution (dots). Squares denote the mean values, and the straight lines represent the medians.

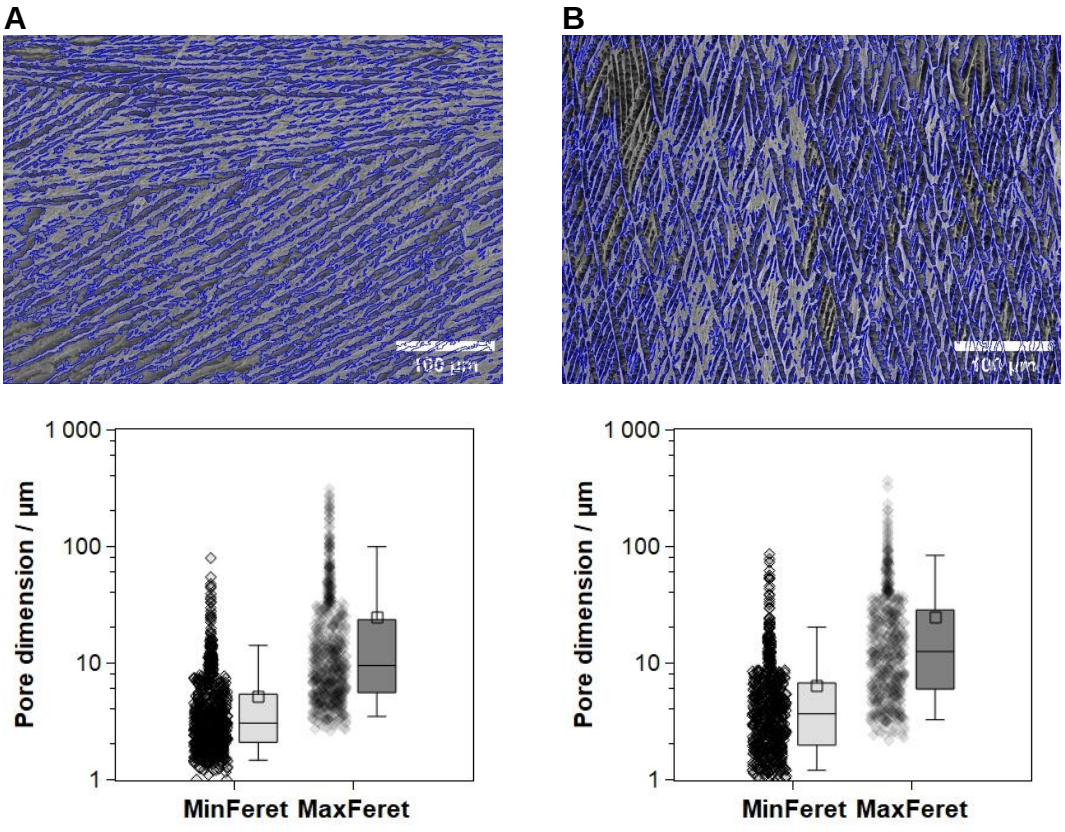

Figure S6. Pore dimensions of the sample ice templated with a dialysis membrane for the outer mold. Porosity was analyzed on thresholded images, using analyze particles ImageJ plugin. Detected pores on the luminal surface (**A**), and external surface (**B**), given with the pore distribution.